ISSN 0915-6348

NATIONAL INSTITUTE FOR FUSION SCIENCE

Physics and Applications of High Energy Density Plasmas Produced by Pulsed Power

Edted by H. Akiyama and S. Katsuki

(Received - Sep. 22, 2004)

NIFS-PROC-62 Apr. 2006

RESEARCH REPORT
NIFS-PROC Series

TOKI, JAPAN

This report was prepared as a preprint of work performed as a collaboration research of the National Institute for Fusion Science (NIFS) of Japan. The views presented here are solely those of the authors. This document is intended for information only and may be published in a journal after some rearrangement of its contents in the future.

Inquiries about copyright should be addressed to the Research Information Office, National Insitute for Fusion Science, Oroshi-cho, Toki-shi, Gifu-ken 509-5292 Japan.

E-mail: bunken@nifs.ac.jp

<Notice about photocopying>

In order to photocopy any work from this publication, you or your organization must obtain permission from the following organizaion which has been delegated for copyright for clearance by the copyright owner of this publication.

Except in the USA

Japan Academic Association for Copyright Clearance (JAACC)
6-41 Akasaka 9-chome, Minato-ku, Tokyo 107-0052 Japan
Phone: 81-3-3475-5618 FAX: 81-3-3475-5619 E-mail: jaacc@mtd.biglobe.ne.jp

In the USA

Copyright Clearance Center, Inc.
222 Rosewood Drive, Danvers, MA 01923 USA
Phone: 1-978-750-8400 FAX: 1-978-646-8600

Physics and Applications of High Energy Density Plasmas Produced by Pulsed Power

Edited by Hidenori Akiyama and Sunao Katsuki

March 9-10, 2004
National Institute for Fusion Science
Toki, Japan

Abstract

This is the proceedings of the meeting on "Physics and Applications of High Energy Density Plasmas Produced by Pulsed Power", which was held at the National Institute for Fusion Science in March 9-10, 2004. The meeting topics cover z-pinch plasmas, plasma focus, charged particle beams, high power discharges and their applications to radiation sources, high power microwave, inertial confinement fusion and shock waves in addition to pulsed power technologies. The papers reflect the present status and trends in the research field of high energy density plasmas generated by pulsed power.

Keywords: z-pinches, plasma focus, charged particle beam, X-ray sources, extreme ultraviolet, inertial confinement fusion, high power microwave, material processing, shock waves, gas decomposition, fragmentation

PREFACE

The collaborative research meeting entitled "Physics and Applications of High Energy Density Plasmas Produced by Pulsed Power" was held at National Institute for Fusion Science (NIFS), Toki, in March 9-10, 2004. 22 papers were presented at the meeting and totally 41 scientists attended from universities, institutes and companies. These proceedings contain most of the papers.

As the field of high energy density plasma has a multi-disciplinary nature, the extensive discussion of related subjects is difficult in conventional scientific meetings. The purpose of the meeting has been to provide a forum to discuss important technical developments, some applications, increased understandings, new trends, and also the future prospects in the field of high energy density plasmas. The meeting was successful from such view points.

We would like to express our sincere thank to all of the authors, participants and National Institute for Fusion Science

Hidenori Akiyama
Sunao Katsuki
Department of Electrical and Computer Science
Kumamoto University

CONTENTS

Low inductance gap-less pulsed current generator to drive Z-pinch plasmas for EUV light source · · · · · · · · · · · · 1
A. Kimura, S. Katsuki, H. Akiyama (Kumamoto University)

EUV spectral characteristics of argon and xenon Z-pinch plasmas · · · · 10
F. Kobayashi, K. Takasugi (Nihon University)

Study of xenon capillary Z-pinch extreme-ultraviolet light source for lithography · · · · · · · · · · · 16
A. Kitade, I. Song, M. Okamoto, Y. Hayashi, M. Masnavi, M. Watanabe, A. Okino, K. Yasuoka, K. Horioka, E. Hotta (Tokyo Institute of Technology)

High current generator for EUV-source development · · · · · · · · · · · 24
N. Ohshima, T. Yokoo, W. Jiang, K. Yatsui K. Shimada*, A. Tokuchi* (Nagaoka University of Technology, *Nichicon Corporation)

Development of miniature pulse X-ray source - Electrical characteristics and basic performance - · · · · · · · · · · · · 30
Y. Kiriyama, M. Nakajima, M. Shiho, K. Horioka, K. Kanno*, E. Tanabe* (Tokyo Institute of Technology, *AET Japan, Incorporated)

Efficient energy input in creation of microplasma with a copper powder particle · · · · · · · · · · 37
T. Yokoyama, K. Takano, T. Amano, S. Ibuka, K. Yasuoka, S. Ishii (Tokyo Institute of Technology)

Development of bipolar-pulse accelerator for intense pulsed ion beam acceleration · · · · · · · · · · 44
K. Masugata, Y. Shimizu, Y. Fujioka, I. Kitamura, H. Tanoue, K. Arai (Toyama University)

Characteristic of high energy ions produced in plasma focus · · · · · · · · 52
Y. Kawaguchi, K. Takao, M. Shiotani, T. Honda, I. Kitamura, K. Masugata (Toyama University)

Generation of intense pulsed heavy ion beam by a B_y type MID with pulsed plasma gun · · · · · · · · · · · · 60
J. Kawai, R. Tejima, I. Kitamura, K. Masugata, H. Tanoue*, K. Arai* (Toyama University, *National Institute of Advanced Industry Science and Technology)

Droplet generation mechanism by intense pulsed ion-beam evaporation · · · 69
H. Shishido, H. Kawahara, H. Yanagi, T. Suzuki, T. Yunogami*, H. Suematsu,

W. Jiang, K. Yatsui (Nagaoka University of Technology, *Doshisha University)

Diesel flue gas treatment by pulsed, intense relativistic electron beam · · · · 78
G. Imada, T. Sakurai, K. Yatsui (Nagaoka University of Technology)

Pulsed operation of an inertial electrostatic confinement fusion device and its application · · · · · · · · · · · · 86
K. Tomiyasu, K. Yamauchi, A. Tashiro, M. Watanabe, A. Okino, T. Kohno, E. Hotta (Tokyo Institute of Technology)

Development of compositionally gradient thin films by intense, pulsed ion-beam evaporation · · · · · · · · · · · · 93
M. Hirai, T. Honzawa, N. Honda, T. Suzuki, H. Suematsu, T. Yunogami*, W. Jiang, K. Yatsui (Nagaoka University of Technology, *Doshisha University)

C-band intense microwave radiation with cylindrical corrugated waveguide · · 105
K. Ishibana, T. Nishiguchi, N. Tomizawa, K. Yamamoto, R. Ando, K. Kamada (Kanazawa University)

Development of virtual cathode oscillator for high-power microwave generation · · · · · · · · · · · 113
S. Ohno, K. Kanbara, N. Shimada, W. Jiang, K. Yatsui (Nagaoka University of Technology)

Modeling and characterization for low temperature operation of power MOSFET · · · · · · · · · · · 119
M. Io, T. Kikuchi, M. Nakajima, K. Horioka (Tokyo Institute of Technology)

Breaking of ice using pulsed power · 125
S. Ihara, C. Yamabe (Saga University)

Rail gap switch using porous metal as electrodes · · · · · · · · · · · · 135
S. Furuya, H. Tanaka, S. Takano, J. Irisawa (Nagaoka University of Technology)

Pressure measurement of the shock waves due to pulsed streamer discharges in water · · · · · · · · · · · · 142
K. Tanaka, M. Jikuya, T. Fudamoto, T. Namihira, S. Katsuki, H. Akiyama (Kumamoto University)

LIST OF PARTICIPANTS

Ihara, Satoshi	(Saga University)
Hotta, Eiki	(Tokyo Institute of Technology)
Tomiyasu, Kunihiko	(Tokyo Institute of Technology)
Kitade, Keita	(Tokyo Institute of Technology)
Horioka, Kazuhiko	(Tokyo Institute of Technology)
Io, Miho	(Tokyo Institute of Technology)
Kiriyama, Yuji	(Tokyo Institute of Technology)
Ishii, Shozo	(Tokyo Institute of Technology)
Yokoyama, Takuma	(Tokyo Institute of Technology)
Masugata, Katsumi	(Toyama University)
Kawaguchi, Yoshikazu	(Toyama University)
Kawai, Jun	(Toyama University)
Tomita, Takayuki	(Toyama University)
Higashiyama, Masayoshi	(Toyama University)
Yatsui, Kiyoshi	(Nagaoka University of Technology)
Jiang, Weihua	(Nagaoka University of Technology)
Imada, Go	(Nagaoka University of Technology)
Hirai, Makoto	(Nagaoka University of Technology)
Oshima, Nobuaki	(Nagaoka University of Technology)
Sakurai, Tomoki	(Nagaoka University of Technology)
Kawahara, Hideki	(Nagaoka University of Technology)
Ohno, Shuhei	(Nagaoka University of Technology)
Furuya, Seizo	(Nagaoka University of Technology)
Kamada, Keichi	(Kanazawa University)
Ishibata, Keichi	(Kanazawa University)
Nishiguchi, Takashi	(Kanazawa University)
Sato, Morihiko	(Gunma University)
Kobayashi, Fuminari	(Nihon University)
Sirota, Moriki	(Nihon University)
Hayashi, Takuya	(Nihon University)
Yamaguchi, Yoshitomo	(Nihon University)
Maejima, Takahiro	(Nihon University)
Akiyama, Hidenori	(Kumamoto University)
Katsuki, Sunao	(Kumamoto University)
Maeda, Daisuke	(Kumamoto University)
Kimura, Akihiro	(Kumamoto University)
Tanaka, Keiichi	(Kumamoto University)
Kato, Yoshihide	(Kumamoto University)
Sonoda, Tadayasu	(Kumamoto University)
Ikuta, Kazunari	(The Japan Steel Works, Ltd.)
Tazima, Teruhiko	(National Institute for Fusion Science)

Low inductance gap-less pulsed current generator to drive z-pinch plasmas for EUV light source

Akihiro Kimura, Sunao Katsuki and Hidenori Akiyama
(*Dept. Electrical and Computer Engineering, Kumamoto University*)

Abstract

This paper describes a compact z-pinch device driven by a low inductance gap-less pulsed current generator, which is developed for an extreme ultraviolet (EUV) source. A magnetic switch was installed to eliminate the reverse current and to achieve the high repetition rate operation. The z-pinch discharge chamber is placed at the center of the toroidal ferromagnetic core and is connected to a capacitor bank. A magnetic pulse compressor (MPC), which operates with the repetition rate of 200 Hz, is used for the rapid charging of the capacitor bank. The main circuit with an inductance of 30 nH is capable of delivering the current up to 35 kA in 110 ns to the short-circuit load. The EUV emission from the z-pinched xenon plasma is characterized with respect to in-band light energy (13.5 nm, 2% bandwidth), spectrum, and angular distribution as well as temporal behavior of the emission.

Keywords: pulsed current generator, low inductance, gap-less, z-pinch, extreme ultraviolet

1. INTRODUCTION

Discharge produced plasmas (DPP) are presently the most powerful extreme ultraviolet (EUV, 13.5 nm 2% bandwidth) source for the 45 nm or less rule photolithography process. Industrial requirements are the average EUV power of hundreds of watts and 24 hours operation. There are several discharge schemes to produce the high energy density plasmas for the EUV emission, such as a dense plasma focus[1], capillary discharge[2], z-pinches[3], a hollow cathode discharge[4]. Generally, EUV emission energy from these pinched plasmas tends to be proportional to the square of the peak current amplitude. On the other hand, the increase in electrical energy input to the discharge causes the ablation of electrodes and insulator wall, which results in the generation of large amount of debris and the impurity contamination in the target plasmas.

Shortening the discharge current pulses is one of the key techniques to reduce the thermal problems and to improve the conversion efficiency from the discharge energy to the EUV emission. Also the plasma is expected to behave more dynamically while pinching, which brings about the increase in the plasma temperature and the decrease in the source size.

We have developed a compact z-pinch device for the EUV light source. The device is driven by a 110 ns duration pulsed current delivered by a low inductance gap-less pulsed power generator. This paper describes the structure and the operation of the pulsed current generator. Also the characteristic of the EUV emission from the z-pinch plasma are presented.

2. EXPERIMENTAL SETUP

A. Fast z-pinch device

FIG 1 shows the cutting illustration of the z-pinch discharge chamber and its main electrical circuit, which consists of a 42 nF capacitor bank, a toroidal ferromagnetic core, and a z-pinch discharge chamber. They are sandwiched with two circular metal plates. FIG 2 shows the appearance of the main part of the system. One of the metal plates is directly bolted on the vacuum chamber, which is evacuated to 10^{-3} torr. The other is provided with negative 10s of kilovolts. The z-pinch discharge chamber, which consists of a hollow Cu-W alloy cathode, a ring anode and a rounded alumina ceramic ring with the minimum diameter of 5 mm, is located in the center of the coaxial structure. Mass flow of xenon gas fed into the chamber is controlled in the range from 2 to 100 cc/min.

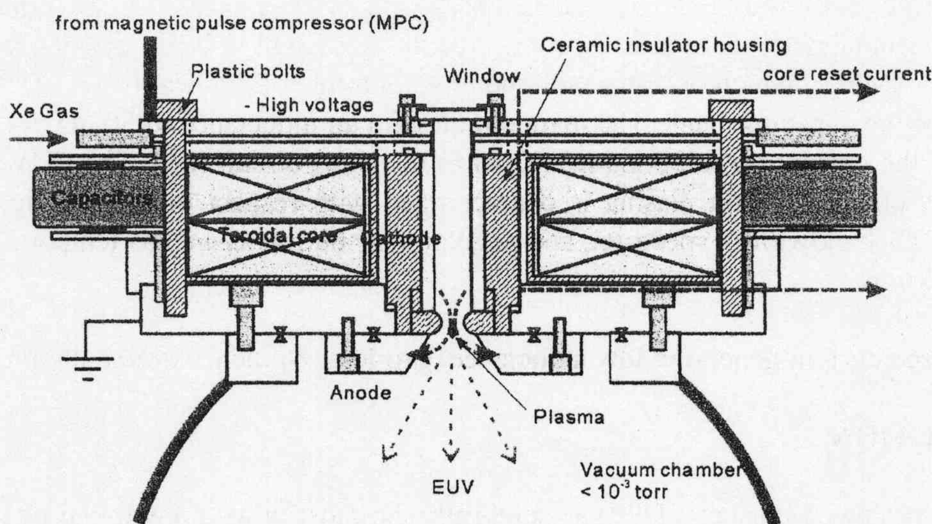

FIG 1. Cutting view of the z-pinch device for the EUV source.

B. Driving Circuit

FIG 3 shows the equivalent circuit of the system including the z-pinch electrodes and a magnetic pulse compressor (MPC). The MPC contains three saturable inductors. SL_0 works as a secondary switch assisting the thyristor to reduce its switching loss. SL_2 and SL_3 work as switches for the pulse compression. After SL_0 is saturated, energy stored in the capacitor C_0 is transferred to the high voltage capacitor C_1 through a step-up transformer. When the capacitor C_2 in the main circuit is charged up to a certain voltage, the energy is quickly released to the z-pinch load through SL_2 being saturated. The energy efficiency of the MPC exceeds 90%. The voltage and the energy per pulse delivered to the 42 nF capacitor bank are 30 kV and 20 J, respectively.

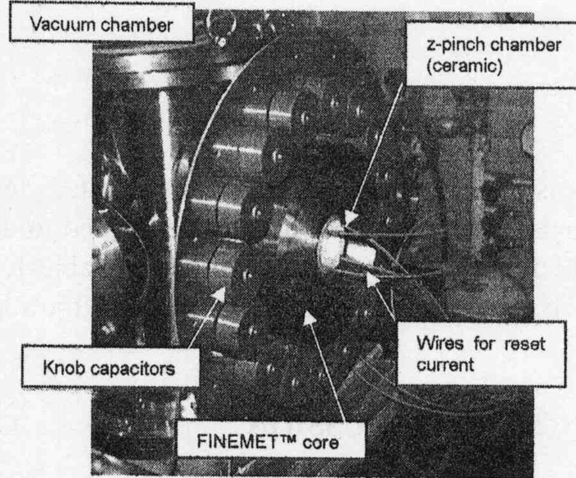

FIG 2. External appearance of the low inductance gap-less pulsed current generator for z-pinch discharge based EUV source. High voltage circular plate is removed in the photograph.

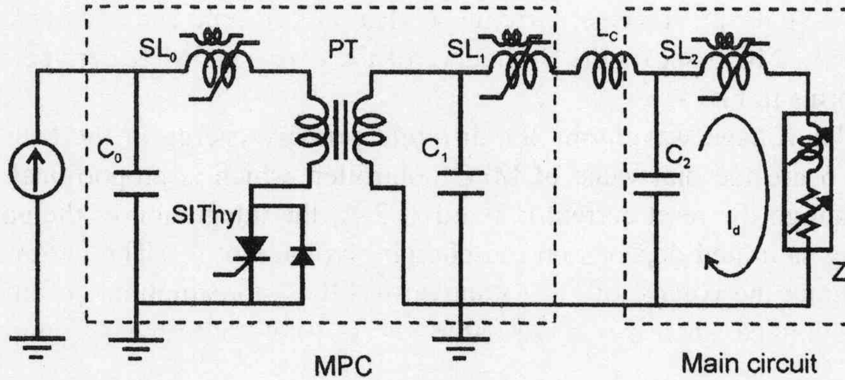

FIG 3. Equivalent circuit of the pulsed current generator including the z-pinch load. $C_0 = 3$ μF, $C_1 = 42$ nF, $C_2 = 42$ nF, SL_0, SL_1 and SL_2 are saturable inductors, PT is a step-up transformer (1:10). L_C is the inductance due to the connection between the MPC and the z-pinch device. Z is the electrical expression of the z-pinch plasma.

Because of using the magnetic switch, the maximum charging voltage is limited by the cross section of the toroidal core. If the magnetic flux density of the core is "reset" to B_R in advance, the voltage of the capacitor V_c is determined by

$$N(B_R + B_S)S = \int_0^T V_C dt \;, \qquad (1)$$

where N (=1), B_R and B_S are the number of winding, the residual and the saturation magnetic flux density of the core, respectively. T is the time when the core is saturated. Therefore, the capacitor bank has to be charged up as quickly as possible in order to obtain higher voltage of the capacitor or to minimize the core cross section, which determines the inductance of the main circuit. The charging time t_{ch} is determined by

$$t_{ch} = \pi\sqrt{(SL_{1S} + L_C)C} \qquad (2)$$

where $C = C_1C_2/(C_1+C_2)$, SL_{1S} is the inductance of SL_1 when saturated. The t_{ch} is mainly dependent on SL_{1S} and L_c. Multi-staged pulse compression is usually performed to decrease t_{ch}. FINEMET™ FT-1H (Hitachi Metals), of which the property is summarized in Table 1, was selected as the core material because of its large Bs and Br in addition to the fast transition from unsaturated to saturated status.

3. EXPERIMENTAL RESULTS AND DISCUSSION

A. Circuit operation (Short circuit load)

FIG 4 shows the typical waveforms of the charging voltage of the capacitor C_2 and the current through the short circuit load placed in the z-pinch discharge chamber. The capacitor C_2 is charged up to 34 kV in approximately 600 ns through the connection using two parallel plates. When the magnetic switch is turned on, the pulsed current with 110 ns duration is delivered to the load. The magnetic switch prevents the reverse current, so that the current ends at a half period of the sinusoidal waveforms. FIG 5 shows the B-H curve of the core at 5MHz derived from the voltage and current waveforms in FIG 4.

FIG 6 shows the voltage waveforms for different primary energy in the MPC. The numbers shown in the FIG 6 are the dial value of MPC controller, which is proportional to the charging voltage of C_0. Although the reset current is fixed at 2 A, the integration of the voltage waveform until the core being saturated depends on the charging voltage of C_2. The current amplitude was adjusted with changing the voltage of C_2. As shown in FIG 7, the amplitude of the current peak is proportional to the voltage when the core is saturated, V_{c0}, but not to the maximum voltage of the C_2.

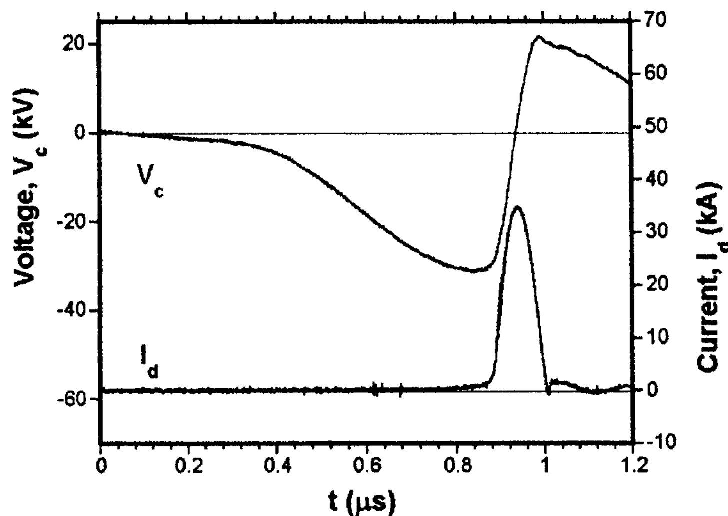

FIG 4. Voltage of the capacitor C_2, V_2, and the discharge current, I_d.

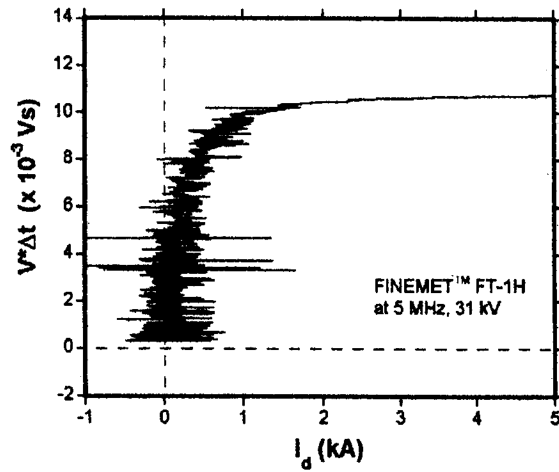

FIG 5. B-H curve derived from the voltage and current waveforms in FIG 4.

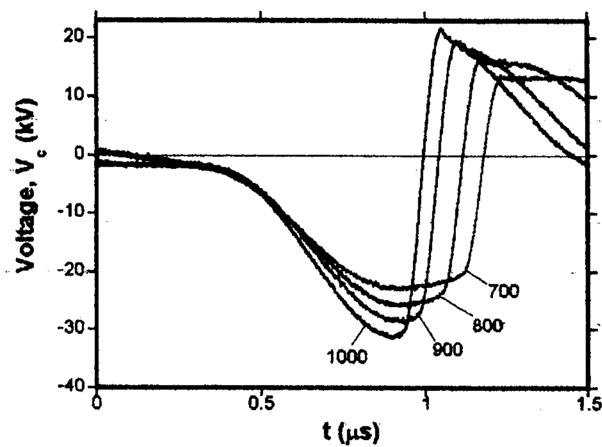

FIG 6. Voltage of the capacitor C_2, V_2, and the discharge current, I_d.

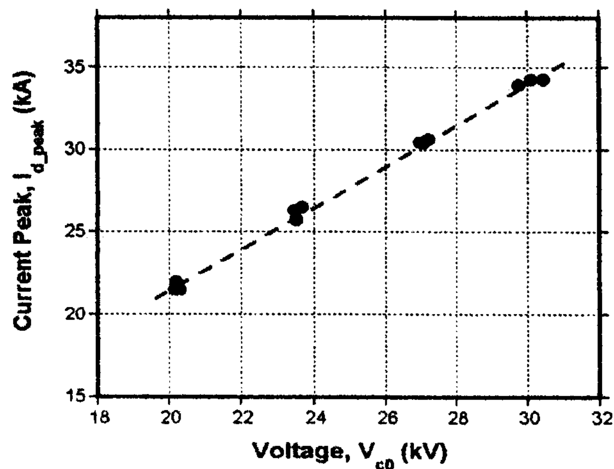

FIG 7. The plasma current peak as a function of the voltage in the capacitor when the magnetic switch turns on.

TABLE 1. Specifications of FINEMET™ FT-1H

Structure,	nano crystalline
Ribbon thickness	18 μm
Saturation magnetic field, B_S	1.35 T
Residual magnetic field, B_R	1.20 T
Coercivity, H_c	0.8 A/m
Relative magnetic permeability, μ_r	5000 (at 1kHz) 1500 (at 100 kHz)
Loss, P_{CV}	950 kW/m^3 (100 kHz)

B. EUV emission from z-pinch plasma

Temporal behavior of the relative EUV emission intensity is monitored by a fast PIN photodiode (Hamamatsu, 3883, 300 MHz) covered with a 150 nm thick Zr filter (Luxel). The transmission band of the filter is from 7 to 18 nm. FIG 8 shows the typical waveforms of the plasma current and the EUV intensity in the case of xenon gas flow rate of 25 cc/min, which is the best condition for the 5 mm insulator wall with respect to the in-band EUV energy. The current in the order of 100's A flowing through the discharge before the main current plays a role of the pre-ionization of the xenon gas. A couple of tens ns after the main current starts to flow, the EUV emission suddenly occurs and increases rapidly. However the EUV emission decays quickly after the peak. The temporal development of EUV emission drastically varies with the xenon flow rate. At the larger flow rate (> 40 cc/min) both intensity and energy tend to decrease with an increase in the flow rate and the maximum emission is delayed.

The transmission grating spectrometer (TGS, 1000 L/mm, Ø50 μm) was employed to obtain EUV spectra. FIG 9 shows the typical spectrum of the z-pinch plasma in EUV region. A bunch of line associated with 4d-5p transition of Xe^{10+} is much smaller than 4d-4f transition of Xe^{11+}. Our experiments show the spectrum depends on the plasma current and the xenon gas flow rate. Several studies on EUV spectrum of discharge produced plasmas reported that the 4d-4f transition of Xe^{11+} becomes stronger as the electron temperature is increased. The amplitude of the current and the gas flow rate is influenced on the temperature.

The relative EUV energy at 13.5 nm with 2% bandwidth is measured using a device, which consists of an x-ray Si photodiode (AXUV100Ts, IRD), a Si/Mo multilayer mirror, and a Zr filter. The Si/Mo multilayer mirror determines the spectrum range to detect. The Zr filter excludes visible light. FIG10 shows the angular distribution of the in-band EUV energy. There are two possible reasons why the emission is not isotropic. One is the source size effect. Since the 4d-5p transition in Xe^{10+}, which is associated with 13.5 nm, is optically thin in the pinched plasma, the source size seen from the detector should be significant. According to the EUV source images taken by a pinhole camera placed at 15° off-axis, the source appears to be a filament, of which the dimension is approximately 500 μm in diameter and 3 mm in length. However, the decreased in the energy at 30° cannot be explained by this. The second reason might be the absorption by dense xenon gas existing in front of the plasma.

FIG 11 shows the in-band EUV energy as a function of the amplitude of the plasma current. The optimum gas flow rate tends to be larger for the larger plasma current, so that the number of emissive particles might be different for the different current amplitude. The EUV energy is

proportional to the 2.5th power of the plasma current. The power number exceeding 2.0 indicates the increase in the conversion efficiency from discharge energy to the EUV energy. One of the possible reasons is that the number of the emissive particles confined in the pinch plasma might be changed. We need further investigation including EUV spectra, source size, and electron density to understand its physics more clearly.

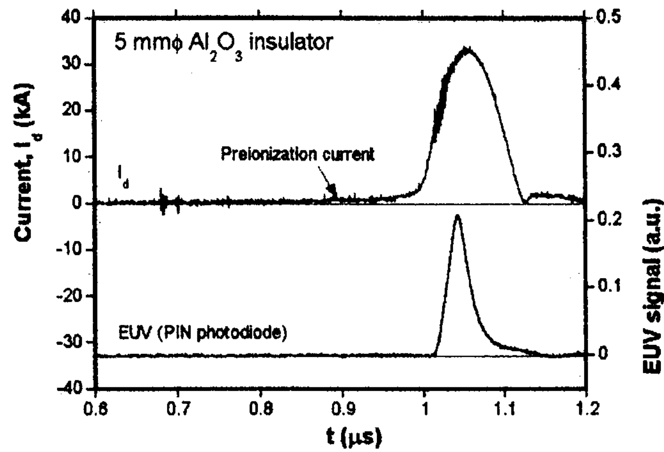

FIG 8. The plasma current and the relative EUV power monitored by a fast PIN photodiode with a 150nm thick Zr filter.

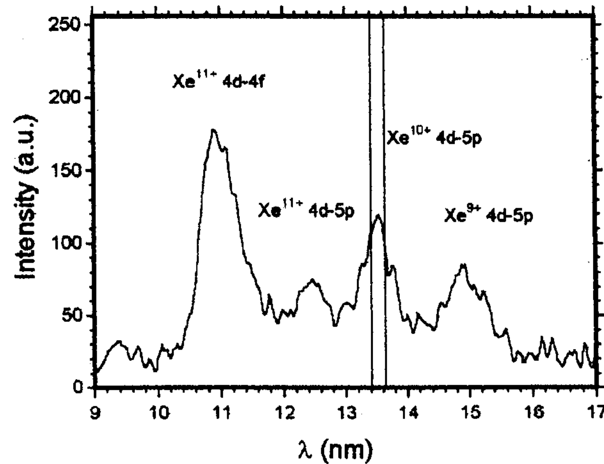

FIG 9. Emission spectrum of the z-pinch plasma in EUV region. Strip indicates the spectrum range that will be used for the photo lithography in semiconductor fabrications.

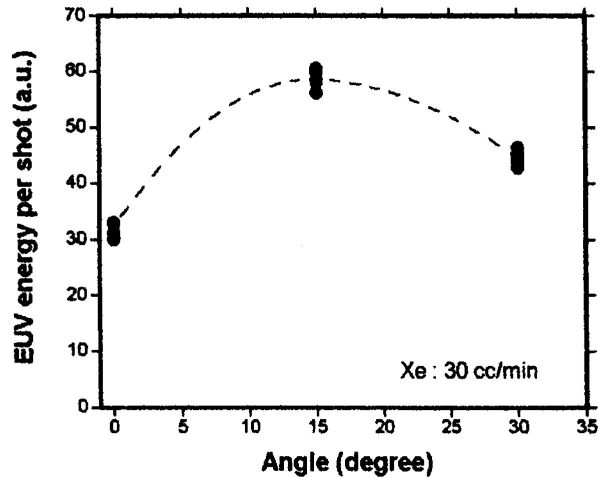

FIG 10. Angular distribution of in-band EUV energy.

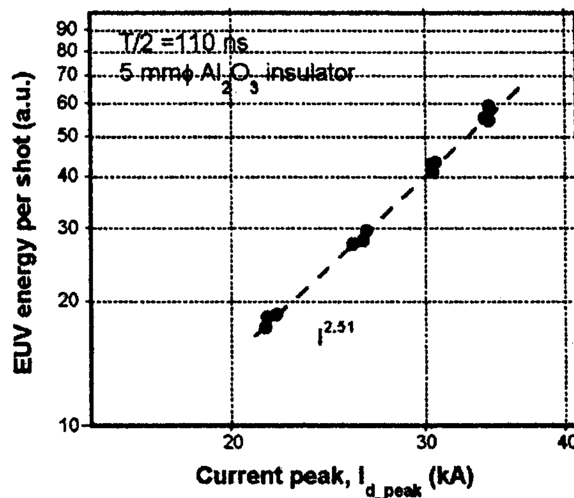

FIG 11. In-band EUV energy of the z-pinch plasma as a function of the plasma current amplitude.

4. CONCLUSION

A gap-less low inductance pulse current generator was built and tested. The current delivered to the short circuit load was 34 kA in 110 ns. A z-pinch plasma was driven by the pulsed current generator and the EUV emission from the pinched plasma was detected. Experiments showed that the larger driving current contributes on the improvement of the conversion efficiency from the discharge to EUV energy.

ACKNOWLEDGEMENTS

This study is supported by the New Energy and Industrial Technology Development (NEDO) and the 21st Century COE Program being conducted at Kumamoto University.

REFERENCES

[1] V. Banine, J.P. Benschop, M. Leenders, R. Moors, "Relationship between EUV lithographic system," Proc. SPIE 3997, 126-135 (2000)

[2] W.T. Silfvast, M.A. Klosner, "Xenon-emission spectra identification in the 5-20 nm spectral region in highly ionized xenon capillary-discharge plasmas," J. Opt. Soc. Am. B: Optical Physics, 17(7), 1279-1290 (2000)

[3] M. McGeoch, "High-power extreme ultraviolet source based on a z-pinch," Appl. Optics 37, 1651-1658 (1998)

[4] W.N. Partlo, I.V. Fomenkov, R. Oliver, D.L. Birx, "Development of an EUV (13.5 nm) light source employing a dense plasma focus in lithium vapor," Proc. SPIE 3997, 136-156 (2000)

[5] K. Bergman, G Schriever, O. Rosier, M. Mueller, W. Neff, R. Lebert, "Highly repetitive extreme ultraviolet radiation source based on a gas-discharge plasma, Appl. Opt., 38, 5413-5417 (1999)

[6] N. Bowering, M. Martins, W.N. Partlo, I.V. Fomenkov, "Extreme ultraviolet emission spectra of highly ionized xenon and their comparison of model calculations," J. Appl. Phys., 95(1), 16-23 (2004)

EUV SPECTRAL CHARACTERISTICS OF ARGON AND XENON Z-PINCH PLASMAS

F. Kobayashi and K. Takasugi

College of Science and Technology, Nihon University
1-8-14 Kanda-surugadai, Chiyoda-ku, Tokyo 101-8308, JAPAN

ABSTRACT

Spectroscopic measurements of EUV light emitted from Ar and Xe gas-puff z-pinch plasmas have been carried out. Spectral lines of Ar IX and Ar X were observed in the Ar z-pinch. The tendency of spectral ratio Ar X/Ar IX is consistent with the energy distributed to each particle. He gas was examined for the dilution of target gas, and the possibility of controlling the EUV spectrum has been demonstrated for Ar and Xe z-pinch plasmas. Strong radiation at the wavelength of 11 nm was observed in the He-diluted Xe z-pinch plasma.

I. Introduction

Gas-puff z-pinch is an efficient system for generating high temperature and high density plasma.[1] X-ray point sources called "hot spots" are generated on the axis of the pinch column, and intense pulsed soft x-ray is radiated. X-ray spectroscopy shows that the electron temperature of those spots is nearly 1 keV.[2] The temperature has increasing tendency with the delay time of discharge from gas-puffing, which is opposite tendency to the bulk plasma characteristics. As the strong contraction is driven by $m = 0$ mode of instability, the plasma temperature is considered to be spatially distributed. As the pulse width of emission is different between soft x-ray and EUV light, the temperature is distributed both spatially and temporally.[3] EUV radiation from electrode material has been observed,[4] and this implies possibility for new source of radiation.

Recently, EUV light source of wavelength region 11 - 13 nm is strongly demanded for the next generation semiconductor lithography. The development of the light source using Xe or Sn has been undergoing. The control of plasma parameter is essential for obtaining optimum radiation spectrum. In this experiment the characteristics of EUV radiation from Ar gas-puff z-pinch have been investigated depending on the delay time of discharge from gas-puffing. And the effect of diluting by He gas for the control of EUV radiation from Ar or Xe z-pinch plasma has also been examined.

II. Experimental Setup

Schematic diagram of the SHOTGUN z-pinch device is shown in Fig. 1. The storage section consists of 24 μF fast capacitor bank which is charged up to 25 kV (7.5 kJ). Pressurized gas is injected through a hollow nozzle mounted on the anode. The plenum pressure is 0.5 MPa during the experiment. The cathode has many holes in order to prevent stagnation of gas. The spacing between the electrodes is 30 mm. Both electrodes are made of Al. Rogowski coils are used for the measurement of discharge currents. The anode coil measures the input current from the power supply, and the cathode coil measures the current

that flows between the electrodes. The input energy to the z-pinch system can be evaluated by analyzing the discharge current waveform.

A scintillation probe is used to detect time dependent signal of soft x-ray emitted from the plasma. The probe is filtered by a 10 μm Be window, and it is sensitive to x-ray whose energy is above 1 keV. The sensitive range contains both K-shell radiation of Ar ions and K_α radiation of impurity metals coming from Hot Spots. The EUV light emitted from the plasma is detected by an x-ray diode (XRD) with Al photocathode. The sensitive range of XRD is spreading from UV to soft x-ray (1 – 100 nm). The XRD signal mainly shows L-shell and M-shell radiations of Ar ions.

A glazing incidence spectrometer is used for the measurement of EUV light. The grating has the groove density 1200 lines/mm, and it is coated by Au. The spectrometer is designed at the incident angle $\theta = 87^\circ$. Kodak BioMax-MS film is used for recording EUV spectra. Since there is no filter between the plasma and the film, all light can be led to the film without loss. The distance between the grating and the film is 235 mm. The available range of EUV light in the spectrometer is 4 - 20 nm.

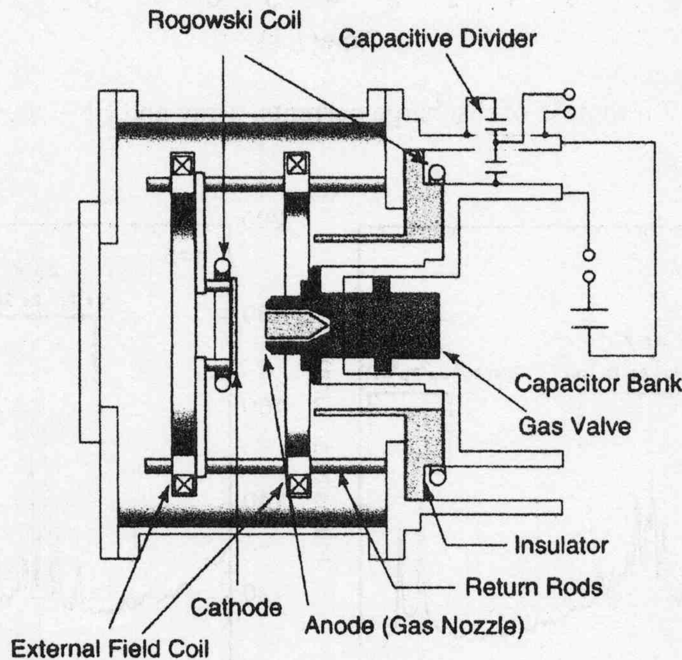

Fig. 1 Schematic diagram of the SHOTGUN z-pinch device.

III. Delay Time Dependence

Delay time of discharge from gas-puffing is a key parameter of the gas-puff z-pinch. Gas pressure between the electrodes monotonically increases with the delay time. An example of discharge currents, scintillation probe and XRD signals at the delay time τ_d = 0.35 ms are shown in Fig. 2. Two currents are almost the same up to maximum pinch, and the discharge is in the typical z-pinch operating region. At the maximum pinch, a dip in the current waveform is generated due to rapid increase of load inductance, and soft x-ray emission occurred in connection with this. The scintillation probe signal is in sharp pulses. The signal mainly comes from K-shell radiation of Ar ions and K_α radiation of impurity metal atoms. Pulse width of XRD signal is wider than that from the scintillation probe, and this shows that the EUV radiation lasts longer than the soft x-ray radiation.

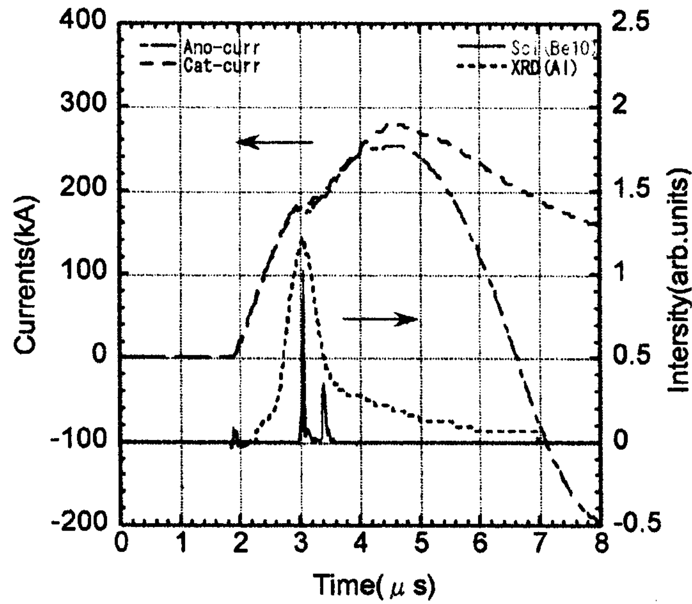

Fig. 2 Example of discharge currents, x-ray and EUV signals

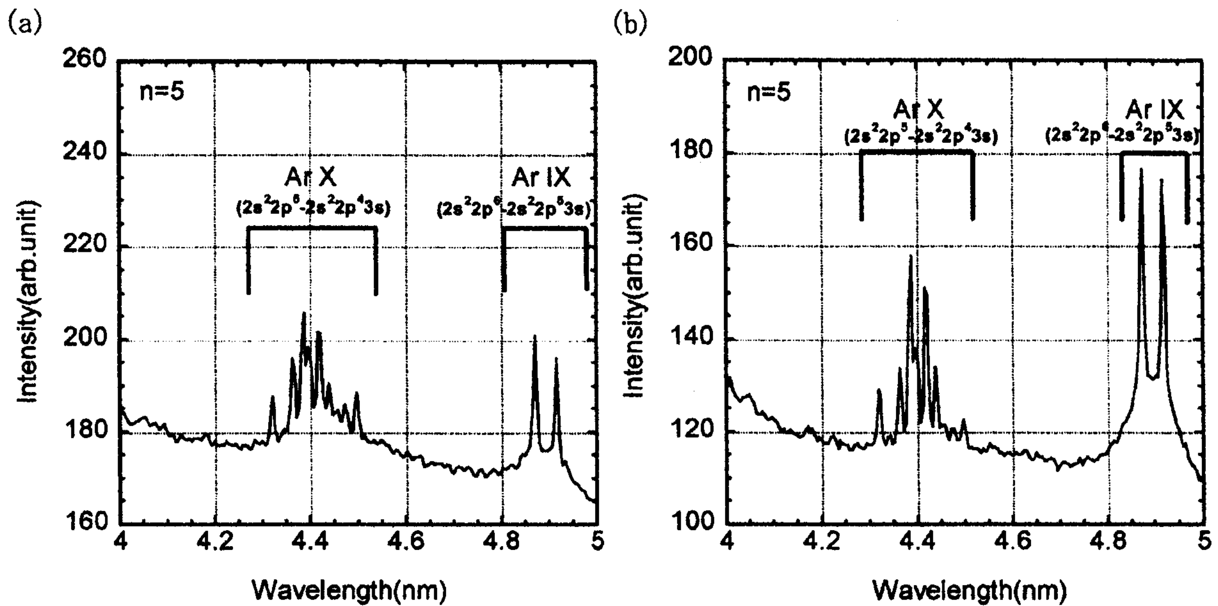

Fig. 3 EUV spectra of Ar z-pinches at (a) $\tau_d = 0.2$ ms and (b) $\tau_d = 0.4$ ms.

Figure 3 shows EUV spectra of Ar gas-puff z-pinch plasma at the delay time (a) $\tau_d = 0.2$ ms and (b) $\tau_d = 0.4$ ms. The number n shown in the figure is the order of refraction. Two groups of spectral lines are observed. Both lines correspond to L-shell radiations of highly ionized Ar ions. By the comparison of (a) and (b), the intensity of lines, especially Ar IX lines, increases with the delay time. Figure 4 shows the delay time dependence of spectral intensities of Ar X and Ar IX. Although the data is rather dispersive, the increasing tendency with the delay time is reconfirmed. The intensity ratio of Ar X/Ar IX decreases with the delay time. This indicates that the electron temperature decreases with the delay time.

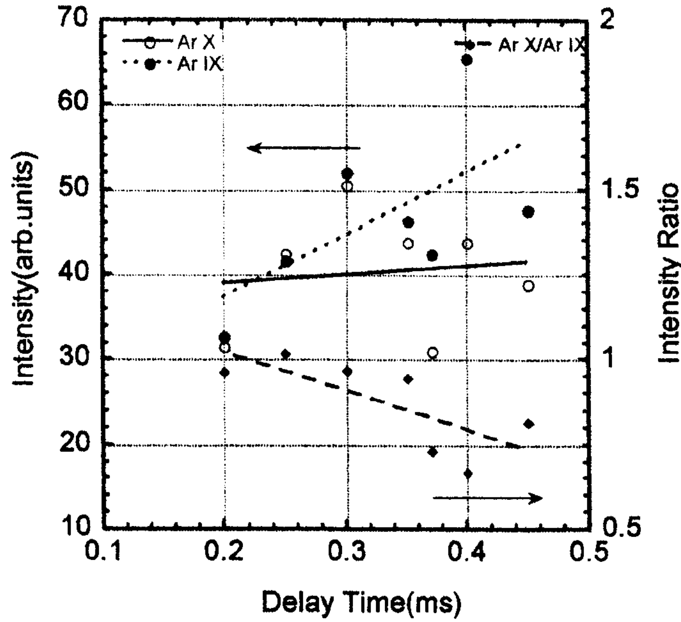

Fig. 4 EUV spectral intensities v.s. delay time.

Delay Time	[ms]	0.25	0.40
Pinch Time	[μs]	0.80	1.38
Pinch Current	[kA]	151	201
Pinch Mass	[ng]	17.5	49.0
Input Energy	[J]	241	294
Energy per Ptl.	[keV]	5.71	2.50

Table 1. Plasma parameters at each delay time.

Plasma parameters at the delay time of 0.25 ms and 0.40 ms are compared in Table 1. The pinch time and the pinch current are the measured values. The pinch time increases with the delay time due to the increase of amount of gas. As a result, the pinch current increases. The net input energy to the z-pinch plasma is evaluated by analyzing the current waveform. The energy increases the delay time. However, the energy divided by the number of particles decreases with the delay time.

IV. Dilution with He Gas

The ionization potential of He ion is relatively low, and it is easily fully ionized in the z-pinch plasma. Figure 5 shows EUV spectrum of pure He gas-puff z-pinch plasma. Highly ionized Al ions (Al IX, Al X and Al XI) are observed in the spectrum. Diluting target gases with He gas would be an effective method for controlling the plasma temperature.

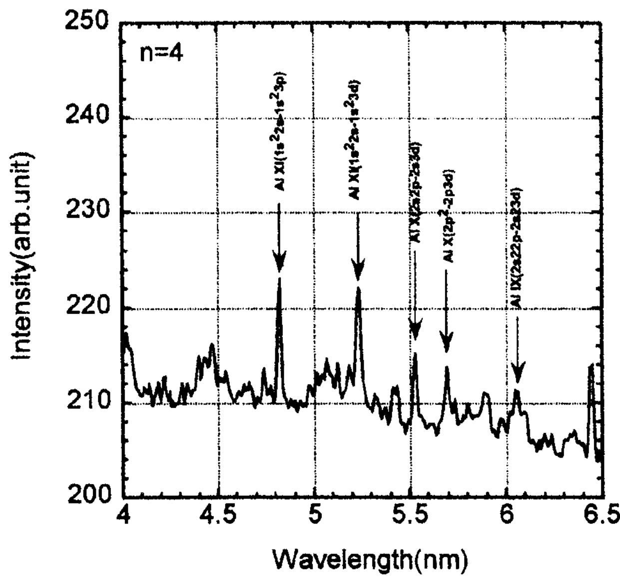

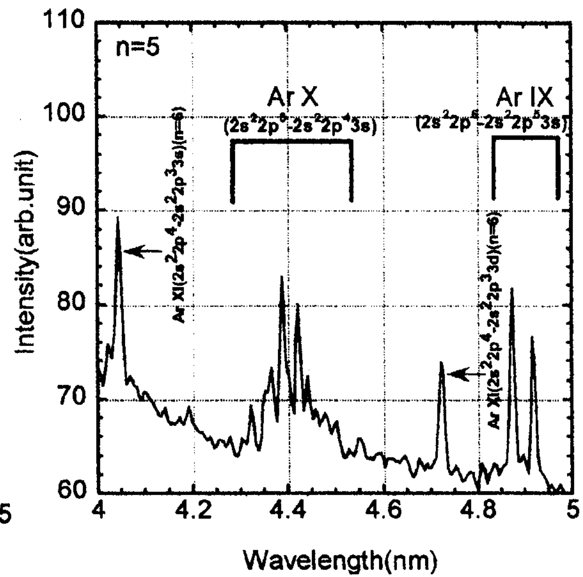

Fig. 5 EUV spectra of He z-pinch plasma.

Fig. 6 EUV spectra of He-diluted Ar z-pinch plasma.

(a)

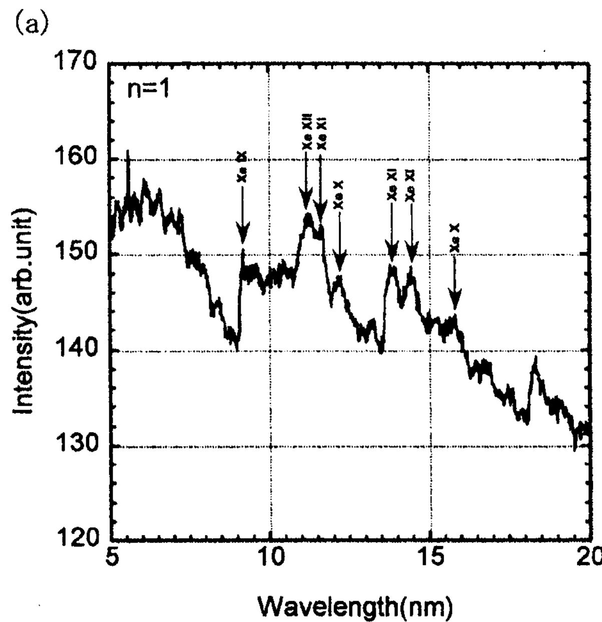

(b)

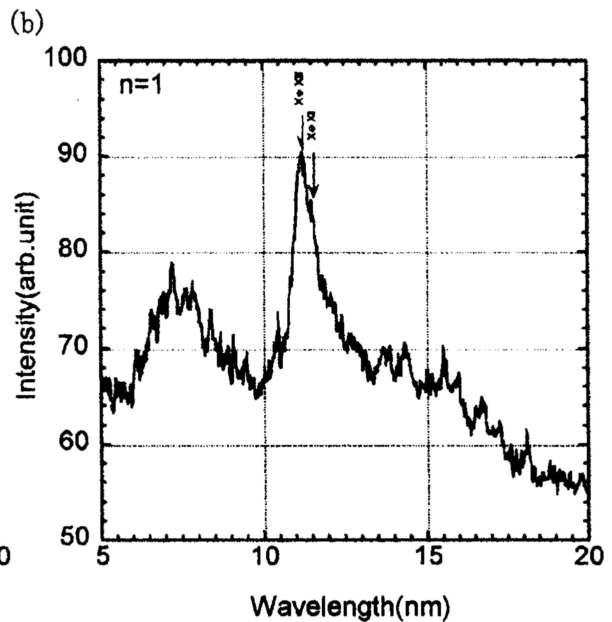

Fig. 7 EUV spectra of (a) pure Xe and (b) He-diluted Xe z-pinch plasmas.

Figure 6 shows the spectrum of He-diluted Ar z-pinch plasma (He:Ar = 500:1). Ar XI lines which have not been observed in Fig. 3 are observed. This indicates the increase of electron temperature, although the intensities of other lines are weak.

EUV spectrum of pure Xe z-pinch plasma is shown in Fig. 7 (a). Highly ionized Xe ions (Xe X, Xe XI and Xe XII) are observed in the spectrum, but the intensities of those lines are not intense. Dilution with He is also examined for Xe z-pinch. Figure 7 (b) shows the spectrum of He-diluted Xe z-pinch plasma (He:Xe = 500:1). A strong line of Xe XII at the wavelength of 11 nm is observed. Other lines are not intense, and this indicates the increase in

electron temperature.

V. Summary and Discussion

Ar IX and Ar X lines were observed in the Ar z-pinch plasma. Assuming thermal equilibrium, the electron temperature is in the range of 30 – 40 eV, if those ions are dominating. The temperature has decreasing tendency with increasing the delay time of discharge. It is consistent with the decreasing tendency of input energy distributed to each particle as shown in Table 1. The value and tendency of electron temperature are consistent with the average plasma characteristics, and we can say that this is the bulk plasma.

In the He z-pinch plasma Al IX, Al X and Al XI lines were observed. The electron temperature is estimated in the range of 40 – 80 eV assuming thermal equilibrium. The Al ions may be originated from electrode material. The temperature range of the plasma is higher than the Ar z-pinch plasma, and the contamination of He possibly controls the temperature of the plasma. Actually Ar XI lines were observed in the He-diluted Ar z-pinch plasma, and we can confirm the increase in the electron temperature.

In the Xe z-pinch plasma Xe X, Xe XI and Xe XII lines were observed. The electron temperature is estimated in the range of 20 – 30 eV, if the plasma is in thermal equilibrium. In the He-diluted Xe z-pinch plasma the strong line of Xe XII at the wavelength of 11 nm was observed. The dilution of target gas with He gas is effective method of controlling plasma parameters and the resulting EUV spectra.

References

[1] K. Takasugi, H. Suzuki, K. Morioka and T. Miyamoto: Jpn. J. Appl. Phys. **35**, 4051 (1996).
[2] N. Akiyama and K. Takasugi: NIFS-PROC-51, 17 (2002).
[3] K. Takasugi, T. Miyamoto, K. Moriyama and H. Suzuki: AIP Conf. Proc. **299**, 251 (1994).
[4] F. Kobayashi and K. Takasugi: NIFS-PROC-54, 70 (2003).

Study of xenon capillary Z pinch extreme-ultraviolet light source for lithography

Keita Kitade*, Inho Song, Mitsuo Okamoto, Yasushi Hayashi, Majid Masnavi, Masato Watanabe, Akitoshi Okino, Koichi Yasuoka, Kazuhiko Horioka and Eiki Hotta

Department of Energy Sciences, Tokyo Institute of Technology, Nagatsuta, Midori-ku, Yokohama, 226-8502, Japan.

ABSTRACT

Extreme-ultraviolet (EUV) lithography is regarded as the potential candidate for technology under 50 nm node optical lithography after 2007. In TITech EUV group, we have developed a capillary Z pinch EUV light source which uses xenon gas discharge produced plasma. The *4d-5p* transition of Xe XI has strong emission characteristic around 13.5 nm. For getting high efficiency of EUV emission around 13.5 nm, design of discharge part is important and capillary needs a current which has a risetime of less than one μs and a peak value up to several tens kA. Therefore, we have devised electrode structure and a pulse power circuit with a magnetic switch and SI thyristors, which has a discharge current risetime of 500 ns [1]. To shorten the current risetime, a high voltage pulse transformer was applied and we got the discharge current risetime of 160 ns. In this paper, we have investigated the characteristics of xenon gas capillary Z pinch plasma for lithography, which is powered by two types of pulse power supply, using a high speed camera, a spectrometer and an EUV photodiode. From the results, we confirm the 13.5 nm emission and that the fast discharge current has better characteristics compared with the slow one in plasma dynamics, EUV power and debris generation. The high EUV power and low debris generation make this light source system attractive for a 13.5 nm EUV lithography application.

1. Introduction

The apparently unstoppable advance of miniaturization continues in silicon chip industry. However, the inexorable advance of miniaturization is limited by the wavelength of the light sources used. The semiconductor manufacturers were long in moving on from mercury lamps, which produce visible light of 436 nm wavelength. In successive production the industry currently uses ultraviolet lasers with a wavelength of 248 nm and then with a shorter wavelength of 193 nm for 90 nm linewidth. The intention is to deploy 157 nm lasers as from 2005. But the light source too quickly may reach the lower limit of 70 nm. The semiconductor industry, however, is aiming in the next generation to achieve structure size of less than 65 nm in order to obtain higher storage density and switching speed. Therefore, new processes should be found for the production of finer structures, which could be used to the end of the era of optical lithography. Until a short time ago, a whole series of processes appeared to be possible candidates for next-generation

lithography: extreme ultraviolet (EUV) lithography, electron beam lithography, ion-beam lithography and x-ray lithography. After the start of International SEMATECH in 2000, the choice was narrowed down to EUV lithography. The application of EUV lithography to large-scale semiconductor chip manufacturing requires the availability of high power EUV radiation sources with 13.5 nm wavelength. The combination of the mirrors used in the illumination and imaging system results in the fact that only an effective bandwidth of 0.27 nm around the wavelength of the reflectivity peak of the EUV radiation, which is 2 % bandwidth of the emission wavelength, can be used for wafer exposure. Tool manufacturers demand EUV in-band power of 115 W to achieve a throughput of 80 wafers per hour for production lithography. This requirement in combination with the related lifetime issues of source components and optics makes the EUV source the most critical issue in the development of EUV lithography. The various EUV source parameters for production are summarized in table 1[2].

Table 1. Requirements for EUV source parameters to be installed in EUV lithography high volume production tools. Most of the requirements are given in intermediate focus behind the first collector optics.

Source parameter	Requirement
Central wavelength	13 – 14 nm
EUV power (in-band) at intermediate focus	115 W
Repetition frequency	> 7 kHz – 10 kHz
Integrated energy stability (3σ, over 50 pulses)	< 0.3 %
Maximum solid angle input to illuminator	0.03 – 0.2 sr
Etendue (area × solid angle)	~ 1.0 – 3.3 mm^2sr
Condenser lifetime	30,000 hours
Spectral purity	
10 – 40 nm	< 100 %
40 – 130 nm	< 100 %
130 – 400 nm	< TBD _ 7 %
400 – 800 nm	TBD
> 800 nm	TBD
Spatial stability	< 2 % of size

The gas-filled discharge produced plasma (DPP) sources have the competitive advantages in low cost, compactness and high power. But they have to achieve higher conversion efficiency and low debris generation for industrial use of DPP EUV light sources. Firstly, conversion efficiency is of major importance because this minimizes the demand on driving power for required EUV power. The driving power influences directly the cost of ownership of the source with respect to both investment costs and operational costs, so that a source with higher conversion efficiency has more chances for technical realization. Secondly, discharge plasma sources tend to generate particulate debris resulting from the interaction between the plasma and the electrodes and/or capillary. Deposition of debris on the collector surface or etching of mirror by debris degrades the reflectance of condenser optics in lithography system.

Therefore, debris generation must be reduced to satisfy condenser lifetime requirement in table 1.

We know that a very thin xenon plasma column of high temperature and high density inside a capillary is a source to generate EUV radiation. Therefore, we have to pump much electrical energy into the gas-filled capillary in an efficient manner from an electrical source. High voltage is required to initiate breakdown inside the capillary and a fast rising current is needed to heat and compress the charged particles to produce such a plasma. At the beginning of discharge, a faint plasma layer (current sheet) is formed on the wall surface and it drives a shock wave ahead of itself and they implode inward. It propagates toward the axis with the Alfven velocity V_A. Axial confinement time is defined such as $\tau_C = l/2V_A = l/2B_\theta/\sqrt{\mu_0 \rho_m}$ (l: plasma length, B_θ: magnetic flux density, ρ_m: mass density) and is about 147 ns on the condition of 0.2 mm plasma radius, 3 mm plasma length, 10 kA discharge current, and 0.1 Torr xenon initial pressure. To produce the desired density and temperature plasma with high EUV conversion efficiency, we should give the maximum energy within the confinement time. After the pinch, the input energy heats the electrodes and the capillary, and this leads to generation of particulate debris. Therefore, we should reduce the input energy after the confinement as fast as possible for achievement of debris-free operation in EUV lithography. In this paper results obtained with a slow pulse power supply, which has the discharge current with slow risetime and long duration, and a fast pulse power supply, which has the current with fast risetime and short duration, in xenon-filled capillary Z pinch EUV light source for lithography are presented. We will discuss the research results on long and short pulse discharges for EUV light source that generates high EUV output power with low debris. Also, we will show the spectrum result of our source measured by EUV monochromator.

2. Experimental setup

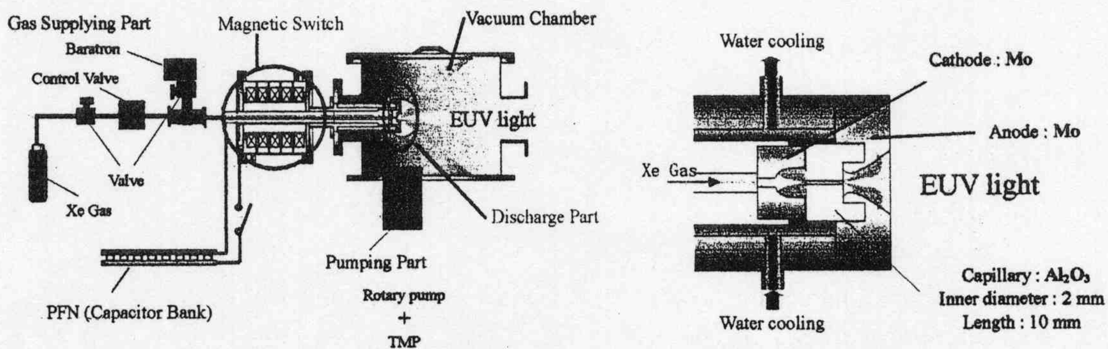

Fig. 1. Schematic drawings of system and discharge section.

Schematic drawings of the entire system and the discharge section are presented in Fig. 1. The discharge head consists of molybdenum anode/cathode and an alumina capillary of 2 mm inner diameter and 10 mm length. The features of electrode structure are to reduce the surface current density and to get enough EUV light flux [1]. The xenon gas, which is fed through a mass flow controller, flows into the capillary through the hollow cathode and was differentially pumped out of the system by use of the capillary itself as the

differential pumping tube. The pressure of the xenon gas near the electrode is estimated to be controlled up to several hundreds mTorr while the chamber pressure is maintained less than several mTorr. A magnetic switch is connected in series with the capillary cathode electrode. The magnetizing current leaking through the magnetic switch during the holding phase is used as the preionization current. Figures 2 and 3 show two types of pulse power supply circuit and each discharge current waveform. The pulse power system is composed of all solid-state components. The slow pulse power supply without magnetic pulse compression shown in Fig. 2 (a) has a discharge current of 500 ns risetime and 3 μs pulse width. On the other hand, the fast pulse power supply with pulse compression shown in Fig. 2 (b), which adopts a high voltage pulse transformer and 40 nF capacitor, can produce a current with 160 ns risetime and 320 ns pulse width [3].

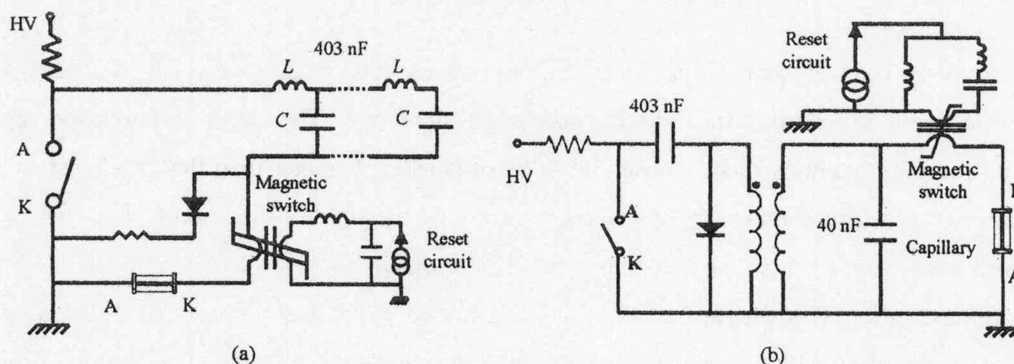

Fig. 2. Pulse power supply system for EUV light source; (a) a slow pulse power supply without magnetic pulse compression and (b) a fast pulse power supply with magnetic pulse compression.

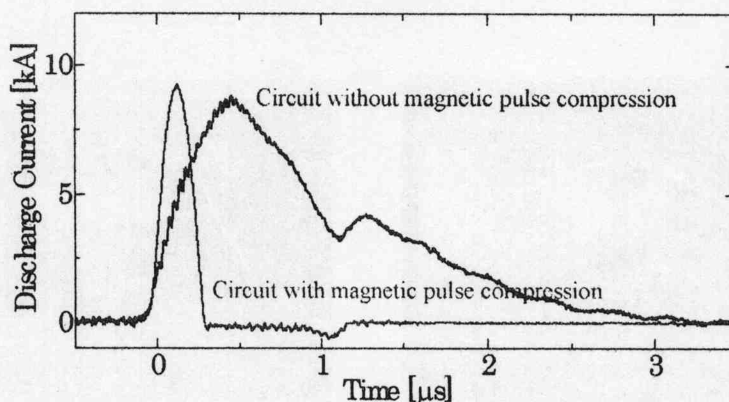

Fig. 3. Discharge current waveforms of each pulse power supply.

In order to measure a time evolution of EUV photon output over the wavelength range of approximately 5 ~ 15 nm, an EUV photodiode (IRD, AXUV-100) with Zr/C filter (thickness 200/50 nm) is used. Streak photographs of capillary plasma in visible region are taken by using a high-speed image converter camera (IMACON 468) for investigating plasma dynamics in a capillary. The spectral emission of this source is analyzed by using a multi-channel spectroscope (Ocean Optics, HR2000) and a monochromator (SHIMADZU: 1800 lines/mm and $\Delta\lambda$ = 0.027 nm, HAMAMATSU: R928) in visible range and a grazing incidence monochromator (McPHERSON, 248/310G) which is equipped with a 600 gr/mm grating and has a measurable wavelength region from 1 nm to 300 nm and the maximum resolution of 0.08 nm. The

radiation dispersed by the grating is recorded by BrightView (XUV-2010) consisting of a microchannel plate (MCP) and a phosphor-coated fiber optic reducer. We used an ICCD camera as a detector. The MCP together with grating is placed under high vacuum (<10^{-4} Torr) by employing another turbo molecular pump. The spectra is recorded by accumulating data for several pulses and calibrated by comparison with previous results obtained for He discharge and with known line positions of Xe [4].

3. Results and discussions

Dynamics of pinching plasma is observed with a high-speed camera in the visible region. The streak photographs of each pinch process with current waveform are presented in Fig. 4. Streak images demonstrate that the plasma inside the capillary rapidly collapses and heats up. After stagnation, the plasma column expands to the wall and the luminous region extends. Fast pulse power supply system produces better plasma symmetry with respect to the axis than slow one. The rapid compression produces a high-density plasma column, which is observed to be of smaller diameter than that produced by a longer current pulse on the same conditions. We have demonstrated the stable generation of hot, dense capillary plasmas with a diameter of less than 0.22 mm, which corresponds to $\delta = 0.11$ ($\delta = 0.36$ for slow one), by fast discharge excitation. δ is the ratio of the pinch plasma radius to the capillary radius at the maximum current. This is consistent with theoretical studies, which indicate that the region of minimum instability for pinch discharges is in the neighborhood of $\delta = 0.1$ [5]. We can see that the expanded plasma generated by the slow pulse power supply contacts with capillary wall for a long time compared with that by the fast one. This contact heats the wall of the capillary and thus produces particles from the wall material.

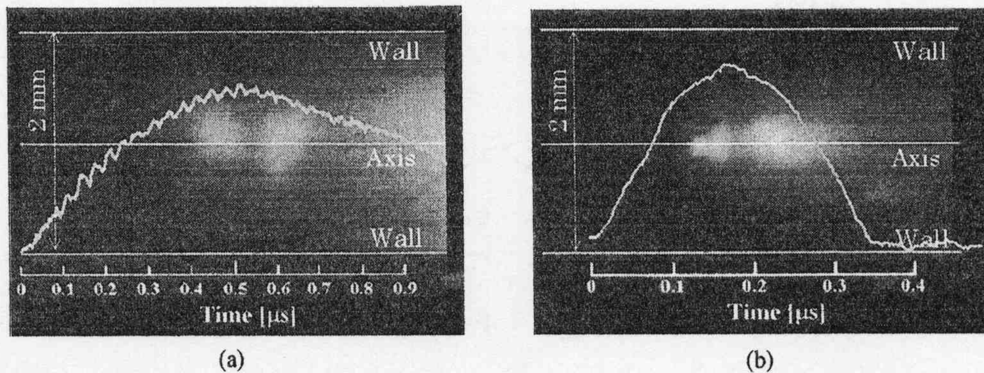

Fig. 4. Streak photographs of capillary discharge plasmas (a) slow pulse power supply, (b) fast pulse power supply. Current waveforms are superimposed.

Waveforms of the discharge current as well as photodiode output are presented in Fig. 5. Each EUV photodiode signal appears first (around 40 ns for fast pulse power supply) after the initiation of the discharge inside the capillary and it reaches a maximum at the time of maximum compression of the plasma. The maximum compression time was inferred from Fig. 4. During the early phase of discharge, EUV output energy for fast pulse power supply is larger than that shown in Fig. 5 (a). And the photodiode signal for slow pulse power supply lasts after the peak of the discharge current. Two mechanisms can

explain the phenomena: first, peak EUV output energy for fast pulse power supply is greater than that for slow one. The total conversion efficiency can be factorized to take into account the relevant processes $\eta_{total} = \eta_{driver} \cdot \eta_{coupling} \cdot \eta_{plasma} \cdot T$, where the efficiencies of generation of suitable driver pulses η_{driver}, the efficiency of coupling the driver pulse to the plasma $\eta_{coupling}$, the efficiency of the conversion of the plasma to the EUV η_{plasma} and the transmission coefficient in the beamline T are discussed separately. The most effective coupling of the electrical energy to the emitting plasma is achieved when all the stored electrical energy is consumed in the emitting pinch plasma. If the plasma load is mainly an inductive load and the generator would be pulsed, a rough estimate of the coupling efficiency is $\eta_{coupling} = L_P/(L_0+L_P)$, where L_P is the pinch inductance and L_0 the driver inductance. Thus, up to 50 % can be achieved in our case. In view of $\eta_{coupling}$, the efficiency of fast pulse power supply, which has small driver inductance with respect to the slow one, is high. We can get the higher EUV output energy for fast pulse power supply. However, with pulsed discharge system the fast temporal development of the pinching plasma which leads to a rapid change of the dominating electrical properties load resistance and load inductance requires a more subtle optimization of driver parameters with respect the plasma dynamics; second, the photodiode signal for slow pulse power supply lasts after the peak of the discharge current. Compared with the photodiode signals after the end of discharge current in Fig. 5, the ablation process is still active when the current decreases and provides more EUV emitters in case of Fig. 5 (a). Emission from ablation seems to be the more efficient process for EUV production. However, it results in a limited lifetime of the capillary, a generation of spectral impurities Al and O and debris from the source [4]. Therefore, we will discuss this with the results of spectroscopic analysis.

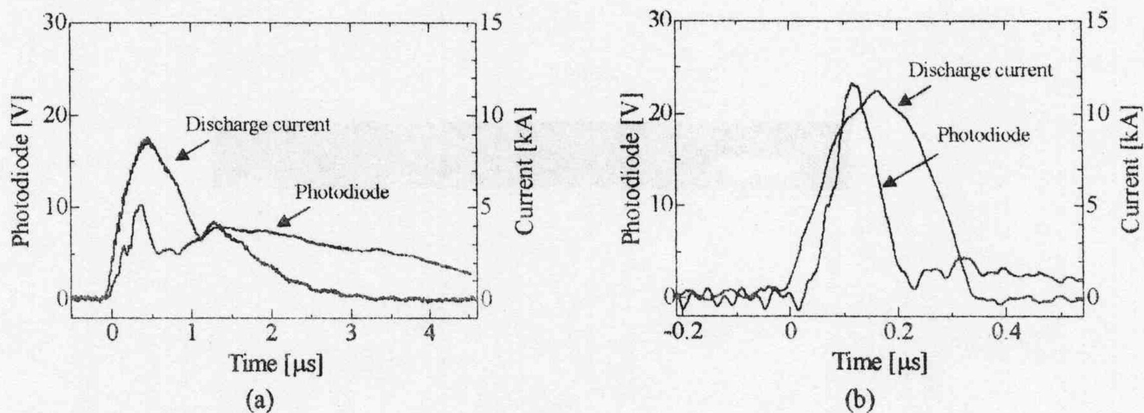

Fig. 5. Measured discharge current and photodiode signal waveforms (a) slow pulse power supply, (b) fast pulse power supply.

Figure 6 (a) shows spectral results of the visible emission lines from plasma identified for the each pulse system. The impurities O and Al observed in slow discharge come mostly from the capillary, while Mo impurities of the electrode cannot be detected. We speculate that the contact time between the plasma and the capillary in fast discharge is not long enough to allow the impurities ablated from the capillary. Examination of the time variation of specific impurity lines with a monochromator reveals that the contact of plasma with the capillary causes such impurities. Figure 6 (b) shows the starting timeof signals of Xe II

(487.65 nm), Xe III (392.25 nm), Al III (452.91 nm) and O III (559.22 nm) lines for slow pulse system. For the results of fast pulse power system, the beginning point of impurity lines relative to the discharge current and kinds of impurities are the same as those for slow discharge, but the intensities of impurities are much lower. It shows that after the plasma expands and heats the wall of capillary, the impurity lines are generated. This unwanted effect of the instreaming of ablated wall material is to cool the plasma and reduce the EUV production efficiency. Also, it affects the spectral purity of EUV source and makes debris. The spectral purity of EUV source is one of the factors, which influence the lifetime of optics mirror and generate a heating problem of it. To achieve a long capillary lifetime it is essential to stay the surface below a melting point. This requires a choice of material with high melting temperature and good thermal conductivity. Also, the longer lifetime can be achieved by reducing the contact time of plasma with in the capillary wall by using such a fast pulse power system.

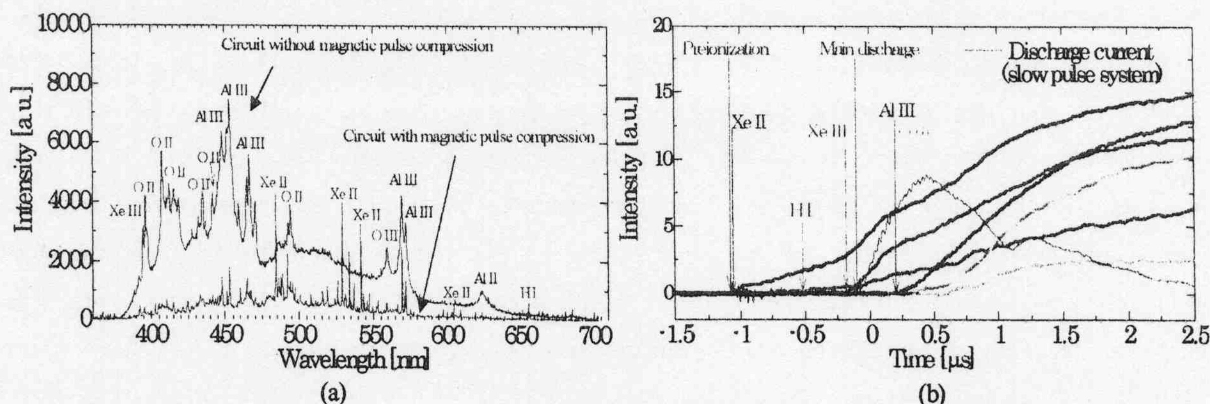

Fig. 6. (a) Timeintegrated spectra and (b) the time variation of Xe and specific impurity lines in visible range.

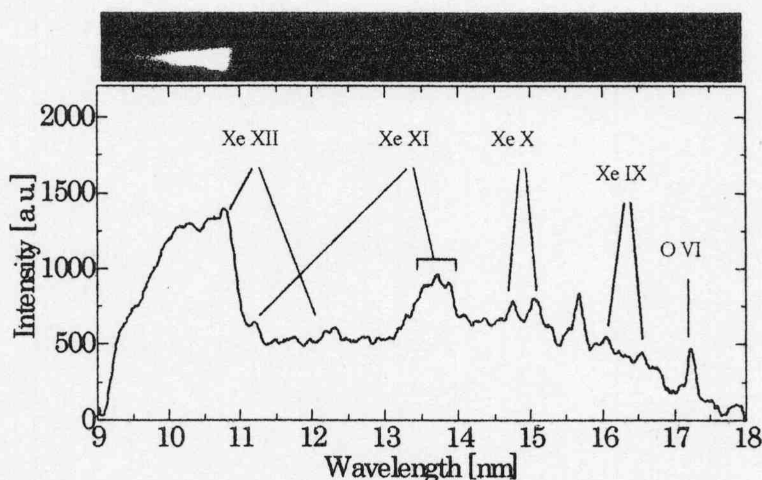

Fig. 7. Timeintegrated spectra for a slow pulse power supply, $\Delta\lambda = 0.08$ nm.

Using the grazing incidence monochromator, xenon spectra for a slow pulse system were recorded in the wavelength region from 9 to 18 nm. Figure 7 shows the photograph and the corresponding spectrum obtained at a xenon supplying pressure of 6 Torr and charging voltage of 9 kV. Four broadband emission

peaks can be observed. The peaks are centered at 11 nm, 13.5 nm, 15 nm and 16.1 nm. These peaks could be identified as transitions in Xe XII, Xe XI, Xe X and Xe IX ions. Besides these broadband peaks a line from oxygen impurity at 17.2 nm also appears [6]. This line O VI is attributed to the emission of impurity from wall of capillary. According to M. A. Klosner and W. T. Silfvast, the observed ionization state Xe XII corresponds to an electron temperature of at least 50 eV [4]. While the entrance slit of monochromator and an aperture, which has 2 mm slot width and is installed at 450 mm from the capillary end, have been used for elimination of stray light, the stray light cannot be completely removed. Therefore, we are now planning an improvement of situation.

4. Summary

We have preformed streak camera and photodiode measurements and spectroscopic analysis of a xenon-filled capillary Z pinch source within the visible and 9 ~ 18 nm wavelength region. Our experiments and comparison of slow and fast pulse power system show that a short pulse current with fast risetime is better for producing higher EUV output and lower spectral impurities and debris. EUV calorimeter (designed by TITech and corrected by Emon) measurements, a elaborate time-resolved spectroscope and a EUV pinhole camera analysis that are beyond of this project could lead to a more accurate analysis and finally study of their dependence.

In order to characterize the EUV emission properties of xenon capillary Z pinch, we study the emission under various conditions of gas pressure, discharge current and capillary radius and length. The variable parameters affect the plasma temperature and density, which are key properties that influence the ionization balance and hence the spectral emission. By observing how the emission changes with respect to the operating parameters, we can gain an insight into the EUV light source for lithography.

5. Acknowledgement

This work is partly supported by New Energy and Industrial Technology Development Organization (NEDO).

References

[1] T. Kasao, M. Okamoto, I. H. Song, M. Watanabe, A. Okino, K. Horioka, E. Hotta, NIFS-PROC-53 (2003), p. 75-81

[2] U. Stamm, et all, Proceedings of SPIE, Vol. 5037 (2003), p. 119-129

[3] I.H. Song, et all, Technical meeting on Pulsed Power Technology, IEE Japan, PPT-04-4, p. 21-25

[4] M. A. Klosner and W. T. Silfvast, J. Opt. Soc. Am. B, Vol. 17, No. 7 (2000), p. 1279-1290

[5] T. D. Arber, P. G. F. Russell, M. Coppins and J. Scheeffel, Phys. Rev. Lett. 74 (1995), p. 2698

[6] M. A. Klosner and W. T. Silfvast, Optics Letters, Vol. 23, No. 20 (1998), p. 1609-1611

HIGH CURRENT GENERATOR
FOR EUV-SOURCE DEVELOPMENT

Nobuaki Oshima, Tomoyuki Yokoo, Weihua Jiang and Kiyoshi Yatsui

Extreme Energy-Density Research Institute, Nagaoka University of Technology
Nagaoka, Niigata 940-2188, Japan

Kazuya Shimada and Akira Tokuchi

Nichicon Corporation
2-3-1, Yagura, Kusatsu, Shiga, 525-0053

ABSTRACT

A repetitive pulsed high current generator has been constructed. It has been developed for generation of high-density plasma as extreme ultraviolet (EUV) source. This generator has peak output current over 40 kA with pulse width of less than 400 ns. The generator consists of a semiconductor switch and a magnetic pulse compression (MPC) unit. This paper reports the design details of circuit composition and the magnetic switches.

I. Introduction

The semiconductor technology is supporting our advanced information society in the recent years. In semiconductor manufacturing process, lithography is necessary in order to exposure the circuit pattern on the wafer surface. The light source used by lithography has been evolving from mercury lamp to excimer lasers. The wavelength of the light source has become shorter and shorter, following the requirement of the resolution R in the lithography processes which is given by the following equation [1].

$$R = k_1 \frac{\lambda}{NA} \quad (1)$$

where, k_1 is constant determined by the resist process conditions, λ is the wavelength of the light source, NA is the numerical aperture of the optics.

Now, the next generation light source for lithography is demanded by the semiconductor industry. Among several potential candidates, extreme ultraviolet (EUV) light at 13.5 nm is attracting great attention and various R and D are carried out all over the world.

The EUV emission can be obtained from high temperature and high density plasma [2]. There are basically two approaches to pulsed EUV generation, laser produced plasma (LPP) and discharge produced plasma (DPP).

In LPP, Xe gas jet is blasted out from a nozzle and irradiated by pulsed high-brightness lasers [3), 4)]. In DPP, pulsed high-current discharge is carried out in the source gas [5), 6)]. This paper reports the design and test of a pulsed high-current generator development for DPP applications.

In DPP, the plasma is generated by high-current pinch of pulsed discharge. For the pulsed power generator, high-current capability and short rise-time are required. Therefore, very low output-inductance is necessary. The minimum peak current calculated by the Bennett equation is on the order of 10 kA.

In order to study EUV generation by DPP, we have developed a pulsed high-current generator of which the designed output parameters are shown in Table 1.

Table 1 Output parameters of the generator

Output current	> 30 kA
Pulse width	< 600 ns
Repetition rate	200 Hz (continuous operation) 1 kHz (burst operation)

II. Circuit Design

In order to achieve the parameters listed in Table 1, the circuit composition is determined as shown figure 1. The capacitance of the capacitor are determined as following, C_{DC} = 55 mF, C_0 = 16.8 μF, C_1 = 1.33 μF, and C_2 = 1.11 μF. The parameters of the discharge current from the capacitors and the inductance of the transmission line are determined as shown Table 2.

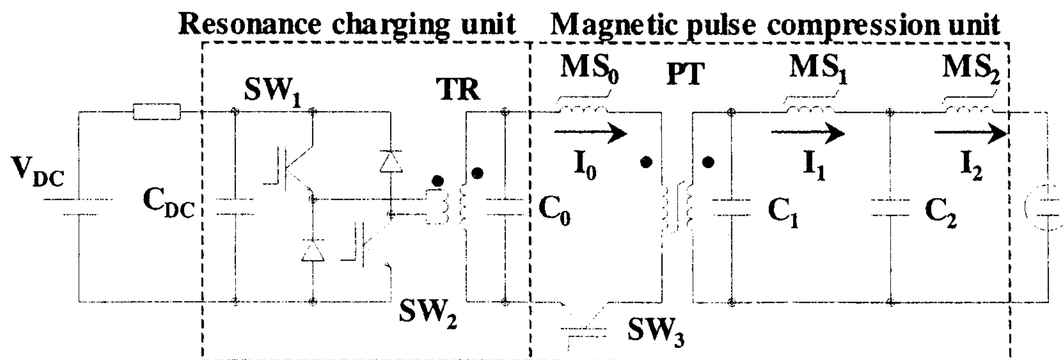

Fig.1 A schematic diagram of the designed generator.

Table 2 Circuit parameters and expected values of peak current

Energy Transfer (Current)	Duration, μs	Peak Current, kA	Inductance, nH
$C_0 \rightarrow C_1$ (I_0)	4.4	2.6 (2nd)	2580 (2nd)
$C_1 \rightarrow C_2$ (I_1)	1.0	9.4	160
$C_2 \rightarrow$ load (I_2)	0.55	30	28

The generator basically consists of two units, the resonance charging unit and magnetic pulse compression unit (MPC) [7), 8)]. The capacitor C_{DC} is charged by DC voltage supply V_{DC} to 350 V. When SW_1 and SW_2 are closed, the discharge current flows via C_{DC}-SW_1-TR-SW_2 so that the capacitor C_0 is charged to 1500 V. When the energy transfer is completed, SW_3 is triggered, the voltage applied on MS_0. After that, the current I_0 flows via C_0-MS_0-PT-SW_3, and C_1 is charged to 4800 V. The energy stored in C_1 is compressed by MS_1 and MS_2 before being released to the load.

SW_1 and SW_2 are IGBTs connected in series, so the switching voltage is only half of the operating voltage. SW_3 is a stack of 28 IGBTs, in order to withstand applied voltage and increase current capability. The generator uses three magnetic switches (MS) and a pulse transformer that has a magnetic core of toroidal structure. These magnetic cores are made of same material. Their parameters are shown in Table 3. MS_0 is not used for the pulse compression. It is used as magnetic assistance to decrease the switching loss in SW_3. PT is the step-up transformer, which has a turn ratio of 3:10. MS_1 and MS_2 are used for pulse compression, where the compression rate is 4.4 and 1.8, respectively.

Table 3 Parameters of magnetic cores

Parameter	Unit	MS_0	PT (2nd)	MS_1	MS_2
Charge voltage, V	kV	1.5	4.8	4.8	4.8
Outer diameter, b	m	0.108	0.152	0.332	0.366
Inner diameter, b	m	0.09	0.09	0.286	0.286
Thickness, d	m	0.0254	0.0254	0.035	0.035
Cross section, S	m^2	0.00023	0.00079	0.00081	0.00140
Number of winding, n	—	4	10	8	1
Magnetic flux swing, ΔB	T	1.7	1.7	1.7	1.7
V × t, $V \cdot t$	Vs	0.00155	0.01339	0.01095	0.00238
Saturation time, t	μs	1.036	—	4.428	0.992

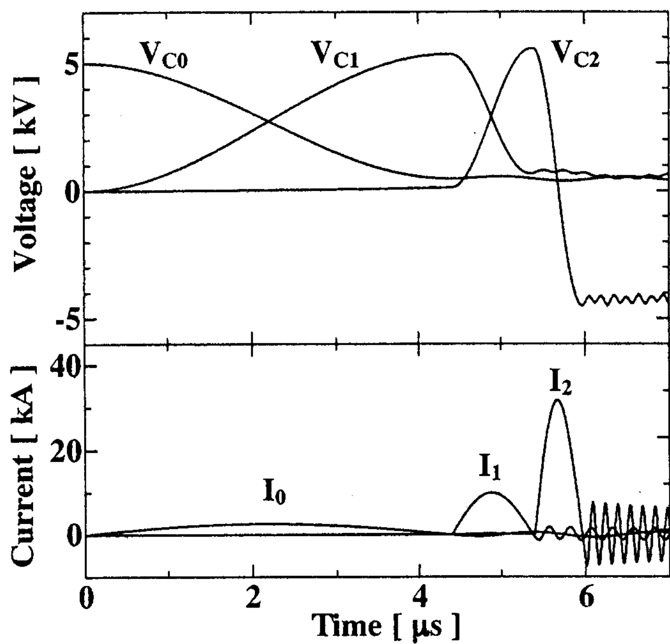

Fig. 2 Waveforms of voltage and current of each sections.

Numerical simulations are used to study the circuit behavior and to confirm the output parameters. The calculated voltage and current waveforms are shown in Fig.2. The directions of I_0, I_1 and I_2 are indicated in Fig.1. It is seen that the peak value of I_0 reaches ~ 2.6 kA in the secondary winding of PT, with pulse width of ~ 4.4 μs. In addition, I_1 has a peak value of 9.9 kA and pulse width of 1 μs. It is noticed that the output current (I_2) reaches 34 kA, with pulse width of 550 ns.

Figure 3 shows the generator designed with the above considerations taken into account. The MPC unit has a coaxial structure with diameter of 575 mm. The tank, where the MPC is located, is filled by transformer oil.

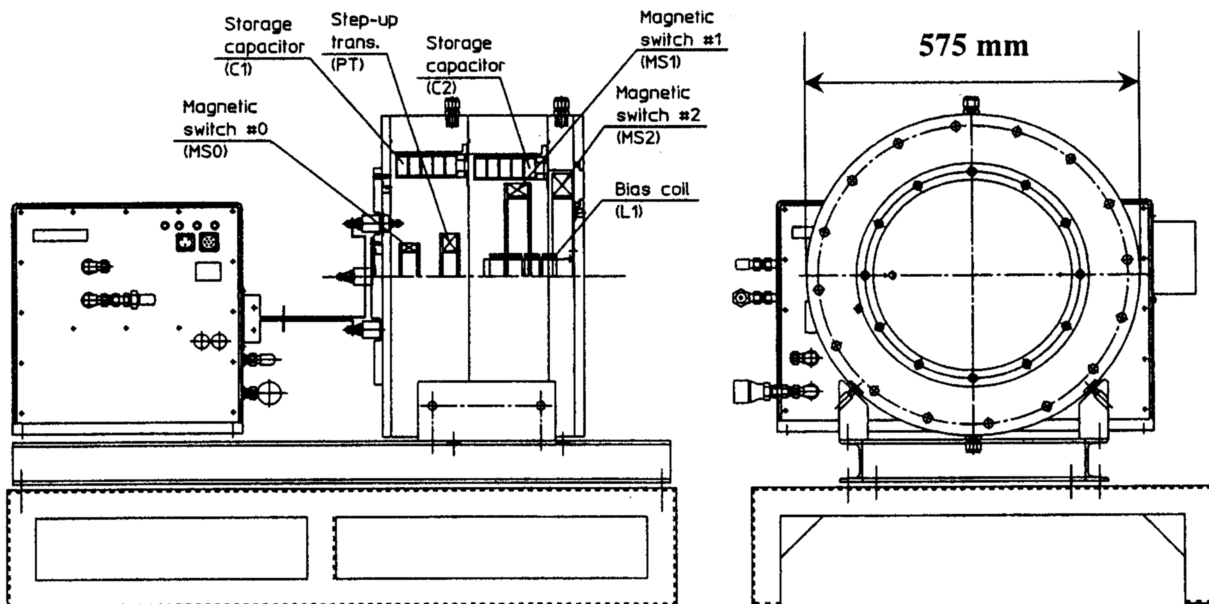

Fig.3 Cross-sectional view of the generator.

III. Operation Results

Test operation of the generator has been carried out with short circuit between the output electrodes.

Figure 4 shows the waveform of output current (I_2) on the shorted load. It was detected by a Rogowski coil installed after MS_2 and recorded by a digital oscilloscope (LT264 : LeCroy). It has a peak value of 40.2 kA and a full-width of 397 ns. The current rise rate is approximately 200 kA/μs. From this waveform, the inductance after C_2 is calculated to be 14 nH. Figures 5 and 6 show the waveforms of charging voltage of C_0 when the generator is operated at repetition rates of 200 Hz and 1 kHz (burst), respectively. The reason to use the charging voltage waveform to confirm the repetitive operation is that the output pulse is too narrow to be seen in the time scales of Figs. 5 and 6. From these results, it is seen that the generator can operate at 200 Hz continuously and 1 kHz in burst mode.

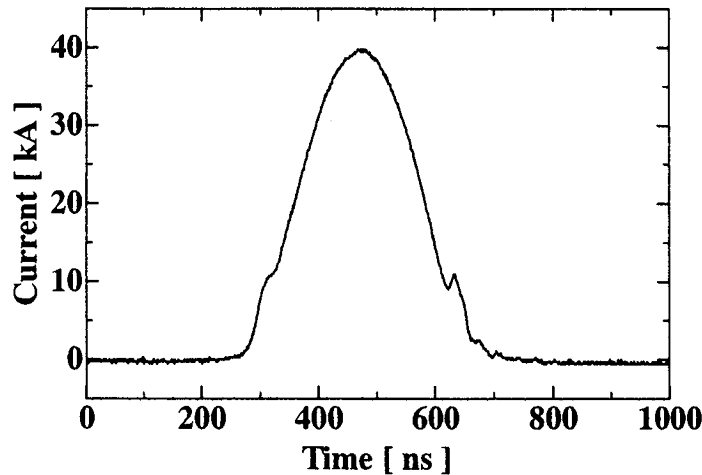

Fig.4 Waveform of output current

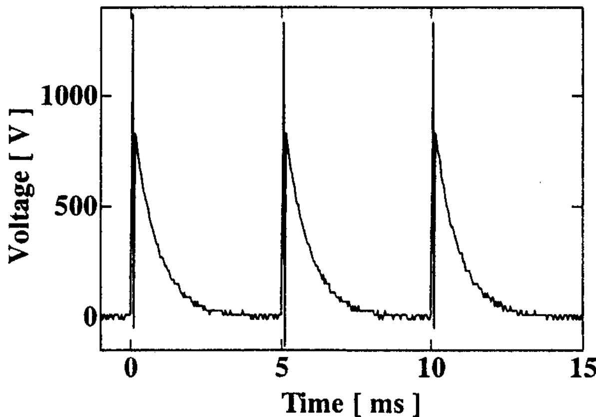

Fig.5 Waveform of V_{C0} in 200 Hz operation

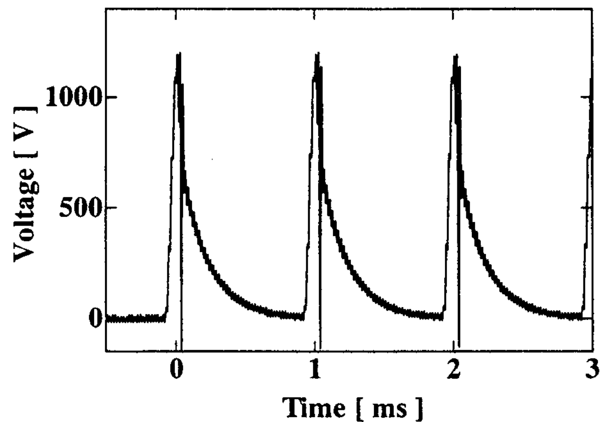

Fig.5 Waveform of V_{C0} in 1 kHz operation

IV. Conclusions

A pulsed high-current generator has been developed for EUV source applications. The design and test of the generator were carried out, and the following conclusions were obtained.

(1) The generator is successfully operated by using combination of semiconductor switch and magnetic pulse compression.

(2) The saturated inductance of the last magnetic switch is found to be lower than 14 nH, which resulted in the peak current of 40.2 kA on a shorted load, with pulse width of ~ 400 ns.

(3) The generator can be operated at repetition rates of 200 Hz continuously, and 1 kHz in burst mode.

References

1) K. Murakami, T. Oshino, H. Kinoshita, T. Watanabe, M. Niibe, M. Ito, H. Oizumi and H. Yamanashi: Jpn. J. Appl. Phys. Vol.37, 6750-6755 (1998)
2) H. Yoneda: J. Plasma Fusion Res. [in Japanese] vol.79, No.3 226-233 (2003)
3) Richard H. Moyer, Harry Shields, Armondo Martos, Steven W. Fornaca, Randall J. St. Pierre, Michael B. Peach: Proc. of SPIE, vol.4343, 249 (2001)
4) A. Endo: J. Plasma Fusion Res. [in Japanese], vol.79, No.3, 240-244 (2003)
5) W. N. Partlo, I. V. Fomenkov, R. M. Ness, R. I. Oliver, S. T. Melnychuk, J. E. Rauch: Proc. of SPIE, Vol.4343, 232 (2001)
6) Igor V. Fomenkov, William N. Partlo, Richard M. Ness, I. Roger Oliver, Stephan T. Melnychuk, Oleh V. Khodykin, Norbert R. Böwering: Proc. of SPIE. vol.4688, 634 (2002)
7) W. S. Melville: Proc. of IEE, 98, 185 (1951)
8) K. Kurihara, S. Kobayashi, I. Satoh, K. Shibata, M. Shigeta, K. Masugata and K. Yatsui: Rev. Sci. Instrum. 63, 2138 (1992)

DEVELOPMENT OF MINIATURE PULSE X-RAY SOURCE

-ELECTRICAL CHARACTERISTICS AND BASIC PERFORMANCE-

Yuji Kiriyama, Mitsuo Nakajima, Makoto Shiho and Kazuhiko Horioka
(Department of Energy Sciences, Tokyo Institute of Technology)
Kouichi Kanno and Eiji Tanabe *(AET Japan, Inc.)*

Abstract

For radiotherapy, a miniature pulse X-ray source is developed. The X-ray source is capable of in-situ irradiation and repetitive operation. The miniature X-ray tube is driven by a high voltage pulser through a thin coaxial cable with 25nsec/40kV/50Ω and 2m in length. About 1Gy dose irradiation is obtained by the miniature source with pulsed operation of 4000 shots. The basic concept, technological issues, and a proof-of-principle experiment are briefly described.

I. Introduction

Radiation sources are widely used in industrial, scientific, and medical fields. Especially, irradiation X-ray sources are playing significant roles in recent medical field. It is thought that the role of the radiation source in cancer treatment continues to grow with the increase of cancer patients.[1][2] Conventionally, efforts for miniaturization of an accelerator or the X-ray source have been made, focusing on the object for medical treatments.[3] However the management and their handling are still difficult in medical sites. The equipment cost is still high, and the danger of contamination outside of the regulated area still remains in the spot of medical treatment application.

In order to overcome the above-mentioned problems, we set the target to be the development of a pulsed miniature X-ray tube, which is driven by a flexible cable, with the size of less than a few cm. Compared with conventional X-ray sources or direct e-beam irradiation methods, expected merits of the miniature X-ray tube are as follows;

- Small and lightweight equipment is expected.
- Capability of in-situ irradiation of required dose, only into a required place.
- Raise in X-ray energy, miniaturization and a long life are expected.
- Controllability of the dose rate by adjusting the operation voltage and repetition rate of the pulser.[4]
- Ease of handling and reduction of the operational cost.

A conceptual figure of the miniature X-ray source is shown in Fig.1. The miniature X-ray source currently drawn is a prototype for medical treatments for direct irradiation, which is expected to be applied in-the living-body like a catheter. In the R&D of the miniature pulse X-ray source, shortening of the electric power pulse used for X-ray generating is essential point to attain compactness and long-life operation of the X-ray tube.[5][6]

For that purpose, development of the pulse power generator, efficient power transmission technology and selection of suitable electron beam source for earning the required amount of X-rays is indispensable. In this report, a proof-of-principle experiment of the miniature pulse X-ray source is described, and its possibility is discussed.

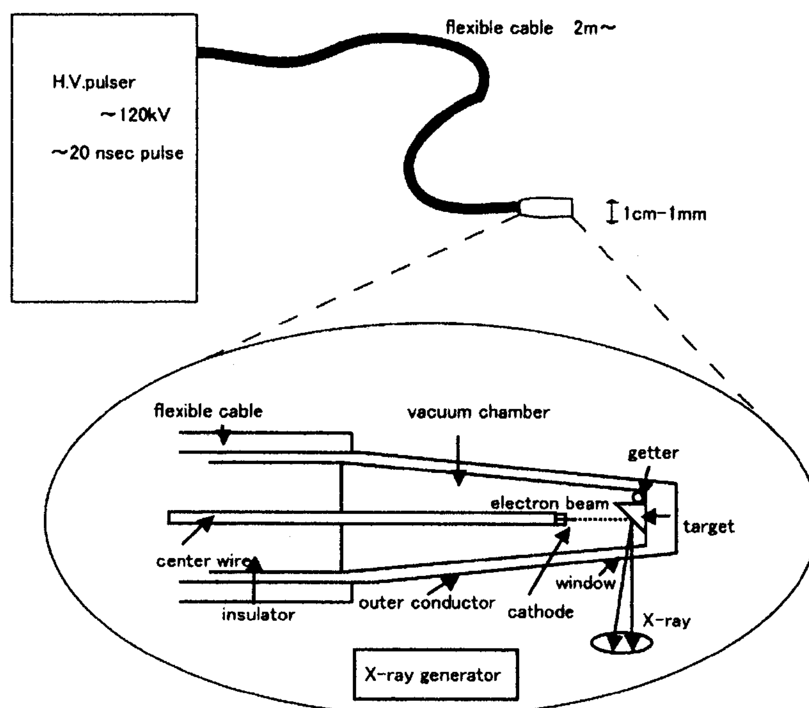

Fig.1 Conceptual figure of the miniature X-ray source

II. Experimental set up

The expected operating parameters for medical application of this kind of device are shown in Table 1.

Item	Target value
X-ray tube size	～ϕ5mm
X-ray energy	30-120keV
Pulse width	～20nsec
Transmission cable length	1m～
The rate of a repetition	～10Hz
Dose	8～10Gy

Table.1 Expected operating parameter of miniature X-ray tube

II-1. High-voltage-pulse power supply

The equivalent circuit of the developed high-voltage-pulse power supply is shown in Fig.2. This pulse power generator consists of a capacitor bank, a primary switch, a pulse-forming-line (PFL), and a secondary switch through a (1:10) pulse set-up transformer. The transformer is made of Ferrite cores and amplifies the voltage pulse. Through the process of energy transfer between C_1 and C_2, and the operation of secondary switch, pulse compression is carried out. The spice circuit simulation predicts that, for 20nsec pulse formation, the inductance of secondary switch should be less than 0.2μH. Therefore, we have developed a coaxial type high-pressure switch. The operational characteristic of coaxial high-pressure switch is shown in Fig.3.

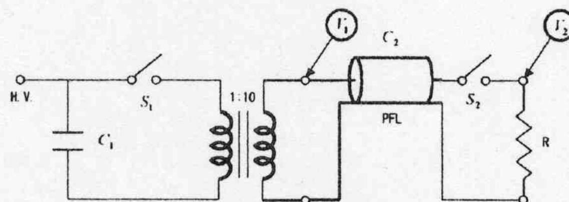

Fig.2 Equivalent circuit of high-voltage-pulse power supply

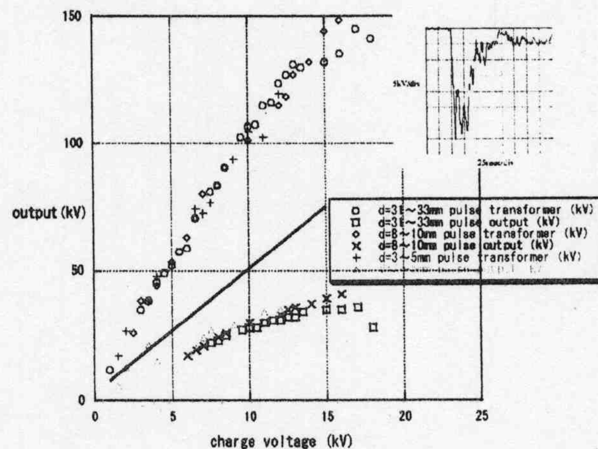

Fig.3 Operational characteristic of Coaxial high-pressure switch

Ⅱ-2. Electron sources

We tested two-types of field emission cathodes for the candidate of the electron beam source. The field emission type cathode is advantageous for the miniaturization because it can operate at room temperature.[7][8][9] We used cathodes made of a tungsten (W) needle and carbon nanotube. The needle cathode was manufactured by the electrolysis etching method. Fig.4 is the microphotograph of each cathode. First, we checked the characteristics of electron emission at D.C. voltage condition and, from the obtained Fowler-Nordheim plots, we assured that each cathode was operating with field emission mode in the low-voltage-region. (Fig.5)

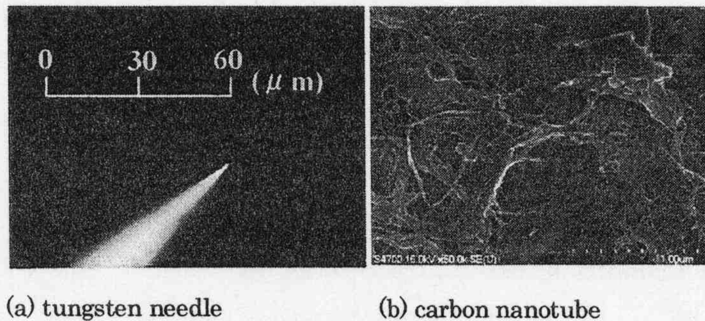

(a) tungsten needle (b) carbon nanotube

Fig.4 Microphotographs of each cathode

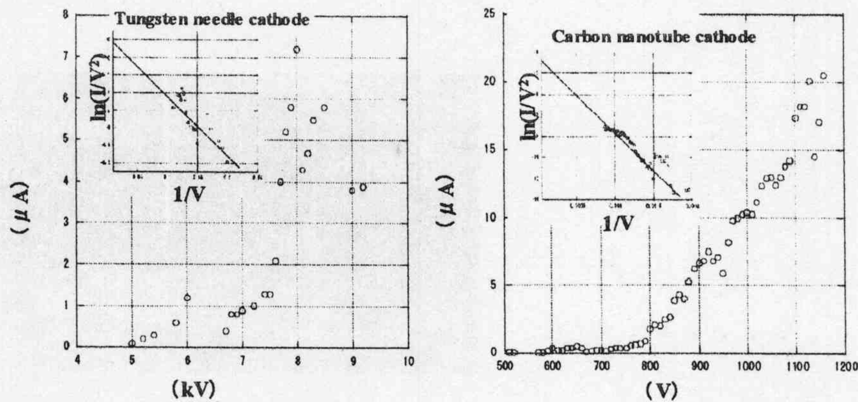

Fig.5 Field emission characteristic

Ⅱ-3. X-ray detection experiment

The experimental arrangement for X-ray generation is shown in Fig.6. With a vacuum system composed of a rotary, a turbo, and a sputter ion pump, the vacuum chamber was evacuated less than 10^{-8} Torr and the tantalum (Ta/Z=73) with 0.1mm in thickness was

installed as the anode target. The distance between cathode-anodes was 22mm. To demonstrate the X-ray emission, 4000 pulses with 40kV/25nsec were applied on the cathode using the high-voltage pulser. After 4000 shots irradiation, we evaluated the X-ray dose by an X-ray film (GAFCROMIC MD55).

Ⅲ. Experimental results

The electron beam current obtained by the pulse voltage application is shown in Fig.7, and a dose distribution of the X-ray film after operation of 4000-shots is shown in Fig.8. As shown, about 1Gy dose irradiation was assured from the X-ray film. Here, the result shown in Fig.8 is obtained using tungsten needle cathode. When 40kV/25nsec pulse was applied at the same condition, using carbon nanotube cathode, the X-ray film was not exposed, probably because it was destroyed in the early stage.

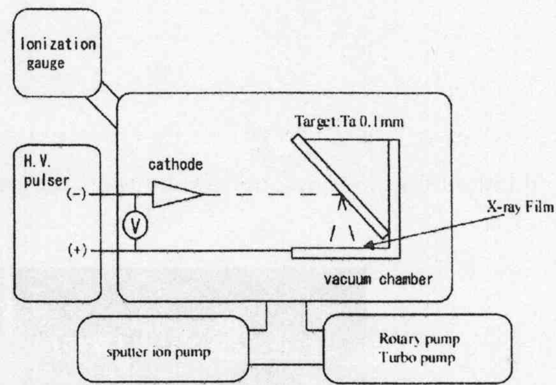

Fig.6 Schematic of X-ray detection

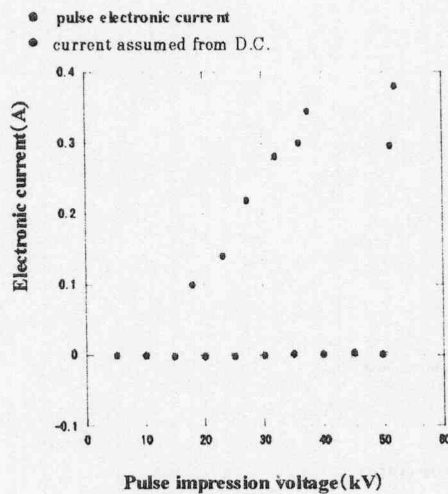

Fig.7 Electronic beam current obtained acquired by pulse impression

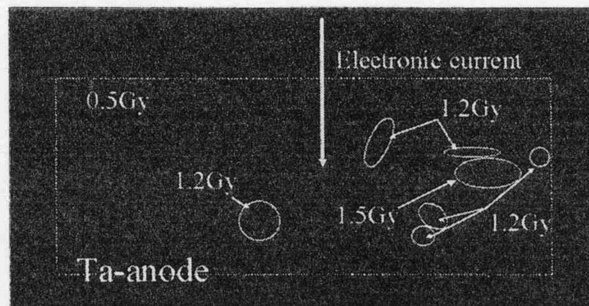

Fig.8 Dose distribution (GAFCROMIC MD55)

IV. Conclusion and discussion

A 40kV/25nsec/50Ω high-voltage pulser was developed using a step-up transformer and a cable pulse-forming-line driven by a coaxial type low-inductance switch. Based on the development of these components engineering, a proof-of-principle experiment for the pulsed X-ray source was performed with tungsten needle cathode. In case of carbon nanotube cathode, although the electron emission was much more efficient at low voltage region compared with the needle cathode, the surface was broken at high voltage operation. This result indicates that carbon nanotube cathode may become a source of a large current electron, if its structure is modified and the current-voltage scaling is extrapolated to a high-voltage region.

The conversion efficiency η from an electronic beam to bremsstrahlung X-ray is approximately expressed as

$$\eta = KZV \quad (K = 1.3\times10^{-6}\ [\mathrm{kV}^{-1}])$$

where, V is the accelerating voltage. Then the X-ray power P can be expressed as

$$P = \eta VI = KZV^2 I$$

where, I is the electron beam current.

Experimentally observed electron beam current for pulsed, high voltage operation was far larger than that for DC operation. This may be caused by plasma formation at the tip of cathode. The cause of localized dose distribution of the film in X-ray detection is not yet understood well. Therefore, it may be necessary to evaluate the energy spectrum of X-ray dose, and the trajectory of electron beam.

In this report, we were able to clarify the future issues of the miniature pulse X-ray source development through the proof-of-principle experiment. To increase the accelerating voltage and the beam current, and to upgrade the repetition capability including the lifetime of components, are the future subjects for the enhancement of the X-ray dose. For the application to the treatments at a medical site, efforts are still required to exactly evaluate the irradiation effect, safety level of each component, and the conformability of the catheter-like power cable to the human body. Cooperation with persons in life science and medical filed is inevitable for the clinical testing.

References

[1] Development and application of compact electron sources;
Proceedings of Workshop on ultra-compact accelerators and X-ray sources, Edited by K.Horioka, Tokyo Institute of Technology (in Japanese) (2000)

[2] B.M.Coursey, R.Nath : "Radio-nuclide Therapy", Physics Today 4, p.25 (2000)

[3] C.J.Karzmark,C.S.Nunan and E.Tanabe : *"Medical Electron Accelerators"* (MeGrawHill, Inc, 1993)

[4] J.M.Pouvesie, C.Cachoncinlle, E.Robert, Viladrosa, C.B.Collins and F.Devanloo : "Compact flash x-ray source producing high average powers in nanosecond pulses", Rev. Sci. Intsrum., **64**, No.8, p.2320 (1993)

[5] K.Hiraoka, E.Tanabe, M.Nakajima, M.Shiho, K.Horioka : "Development of Medical Miniature X-ray source", IEEJ(The INsitute of Electrical Engineers in Japan), Pulse Power Meeting, **PPT-01**, p.27 (2000)

[6] K.Horioka, F.Maejima, M.Nakajima, M.Shiho K.Hiraoka, E.Tanabe : "Short-Pulse Miniature X-ray Source", IEEJ Pulse Power Conf., **PPT-01**, p.5 (2001)

[7] G.Z.Yue, Q.Qiu and Bo Gao, Y.Cheng, J.Zhang, S.Chang, J.P.Lu andO.Zhou : "Generation of continuous and pulsed diagnostic imaging x-ray radiation using a carbon-nanotube-based field-emission cathode" , Applied Physics Letters, **Vol.81**, No.8, p.355 (2002)

[8] H.Sugie, M.Tanemura, V.Filip, K.lwata, K.Takahashi : "Carbon nanotubes as electron source in an x-ray tube" Applied Physics Letters, **Vol.78**, No.17, p.2578 (2001)

[9] Bo,Gao, Guozhen Z.Yue, Q.Qiu, Y.Cheng, H.Shimoda, L.Fleming, O.Zhou : "Fabrication and Electron Field Emission Properties of Cabon Nanotube", Advanced materials, **13**, No.23, December 3 (2001)

Efficient energy input in creation of microplasma with a copper powder particle

T. Yokoyama, K. Takano*, T. Amano, S. Ibuka, K. Yasuoka, and S. Ishii

Department of Electrical and Electronic Engineering
Tokyo Institute of Technology
2-12-1-S3-9 O-okayama, Meguro-ku, Tokyo, Japan

ABSTRACT

A copper powder particle with a diameter of 100μm is used to create a dense microplasma. The early stage of pulsed discharges with it is investigated to establish efficient energy delivering into the powder plasma, where the particle becomes a plasma state through the phase transition from solid to gas. The plasma is created in the atmospheric condition. The evolution of phase transition is verified by voltage and current characteristics and a laser shadowgraph technique. The resistance component between the electrodes in which the copper particle is placed increased drastically after the vaporization. The impedance matching using a pulse transformer is effective to improve energy input into the particle.

I. Introduction

Microplasmas are small-scale plasmas with the size of hundreds microns. The plasmas will be formed in the required position and with the amount of only necessary volume. By utilizing the feature of microplasmas as a miniaturized plasma source, there is a variety of applications such as plasma display panels: PDPs[1], microelectromechanical systems, short wavelength light sources, and micro-reactors in chemistry. Many methods to form the microplasmas have been proposed and examined experimentally. The discharges are usually operated in atmospheric pressure to obtain high-density plasma.

The methods of creating the microplasmas are classified roughly into three modes as follows. A microplasma is generated at a sharp tip of thin electrode due to high electric fields. We call it as an energy-concentrated mode. The plasmas are formed also in micro-cells or capillaries to limit the plasma volume. The PDP discharge is an example of a space-limited mode. Dielectric barrier discharges are commonly used to make such plasmas. Since the ratio of the surface area for the plasma volume is extensively larger in comparison with that of the conventional plasmas, the discharge characteristics are affected by the surface of the micro-cells and the capillaries. Electron emission from the electrodes and the dielectric surface plays an important role for the discharge development in the small space. Electrons and ions easily recombine at the surface of walls, which causes the particle loss. Fast

electrical energy input is required to form the microplasma in the space-limited mode because energy and particle losses occur in the very short time. To overcome these drawbacks, we will eliminate the wall to limit the volume. This is realized that pulsed electrical discharges through a microdrop or a powder particle can create the dense microplasmas in a mass-limited mode.

The microplasma is often generated using gases for continuous operation with high controllability and a high repetition rate. When a solid substance is used as an initial matter, high-density microplasmas will be formed at any required position. We reported the pulsed high current discharge of powder which is transiently injected between the electrodes by the electrostatic force in vacuum[(2)(3)]. The discharge resembles the well-known vacuum sparks. In this scheme, any materials in the periodic table of the elements will become plasmas as far as they can be made to powder. In this paper we proposed to use a single powder particle as an initial matter to form the microplasma. A copper powder particle with a diameter of about several hundred microns is placed between discharge electrodes with a small diameter. Then it is heated resistively by a pulsed discharge current. Since the initial matter is a solid material, it is required to make the phase transition from solid to vapor efficiently.

II. Experimental Setup

The copper powder particle employed is 100μm in diameter as shown in Fig.1. The particles are spherical and their diameters are almost the same in the powder. It is hard to determine the initial resistance of the copper particle. However, when we consider a 100μm diameter copper cylinder with the length of 100μm, the resistance of it is 0.15mΩ. We will use this value for the discussion.

The experimental setup is shown in Fig. 2. A copper particle was placed between tungsten electrodes with the diameter of 300μm in the air. The particle manipulation was carried out by observing under a magnifying optical system with the combination of lenses and a CCD camera. Since the melting point of tungsten, 3660K, is higher than that of the copper, 1357K, the electrodes can endure even if the temperature of copper particle reaches its melting point. The electrical contact between the particle surface and the electrodes was confirmed by

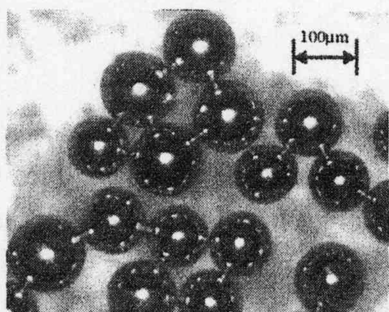

Fig.1. Spherical copper powder particles with a diameter of 100μm.

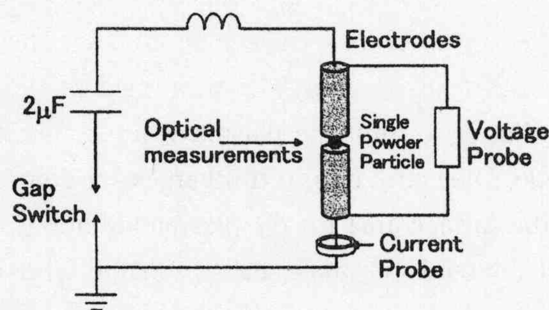

Fig.2. Experimental setup of a single powder particle discharge.

measuring the resistance between the electrodes.

The pulsed discharges were powered by a capacitor of 2μF charged to 1kV with the stored energy of 1J. The residual inductance in the circuit is 190nH. The voltage appearing between the electrodes was measured with a resistive voltage divider. The current was measured with a current probe (Pearson Current Monitor; 110A). Excitation and ionization states were characterized by optical emission spectroscopy. Temporal change of the visible light emitted from the discharge was also observed. A laser shadowgraph technique was used to observe the discharge development of the copper particle. The second harmonic wavelength of 532nm of a Nd:YAG laser with a pulse-width of 6ns was used as a probing laser.

III. Results and Discussion

The discharge current reaches its peak value of 2.3kA in 1μs. Although the current distribution in the copper particle is complicated because of its spherical shape, the skin depth of copper is 100μm for the current with the frequency of 250kHz. Therefore, the current will flow through whole region in the particle. Fig. 3 summarizes the results on the temporal change of voltage, current, input energy, visible light emission, and copper atomic line emission of 522nm in the early phase of the discharge. At the beginning of the discharge, Joule heating takes place in the solid copper particle. Weak jump in the voltage signal appears at 0.2μs. This is caused by the resistance increase of the particle when it has been vaporized. If we assume that the resistance has increased from 0.15mΩ to 10mΩ, the circuit analysis with the P-Spice shows the similar voltage jump characteristics. The initial resistance before the discharge depends on contact condition of the surface between the particle and the electrode. The timing of the voltage jump changes shot by shot and fluctuates randomly. This means that melting and vaporization of the particle do not occur uniformly and reproducibly.

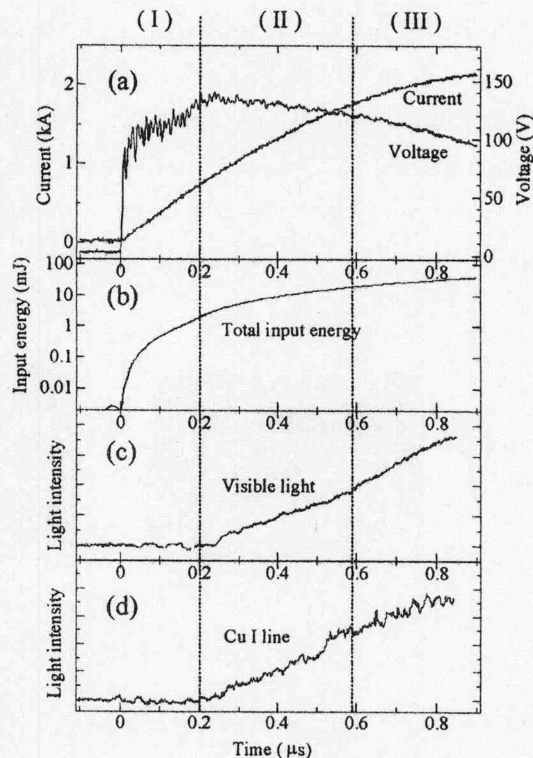

Fig.3. The temporal change of (a) voltage, current, (b) input energy, (c) visible light emission, and (d) copper atomic line 522 nm in the early phase of the discharge.

Table.1. Energy necessary for phase transition of the copper particle.

	Melting point	Heat of fusion	Heat of vaporization	Ionization energy
Energy	1.96 mJ	3.08 mJ	28.5 mJ	83.3 mJ

No visible light emission is observed until 0.2μs. During this period, the particle is heated resistively so that its phase transition from solid to liquid develops. When the particle temperature reaches the melting point of copper, 1357K, at the end of phase (I), the particle start to melt(4)(5). At this moment the input energy amounted to 1.92mJ as shown in Fig. 3(b). It agrees with the theoretical value of 1.96mJ, which is listed in Table.1 that describes the energy calculated theoretically when the temperature reaches the critical points of phase transition, namely the melting point, the boiling point, and the ionization.

The vaporization develops from the surface of the particle that is confirmed by both the visible light and copper atomic line emission of 522nm as shown in Fig. 3(c) and (d). The energy of 3.08mJ is required to melt the whole copper particle. The input energy amounts to 18mJ at 0.6 μs that is less than 28.5mJ necessary for complete vaporization of the particle. Consequently, the particle has not been fully vaporized at this time.

Macroscopic behavior of the copper particle discharge development observed by the laser shadowgraph is shown in Fig. 4. Since the deformation of the spherical particle advances at 300 ns in which the voltage jump does not start yet, the melting process in the copper particle progresses before the voltage jump. Radial expansion of copper vapor is remarkable at 400ns. The discharge characteristics resemble that of the exploding wire on which many papers have been published. However, differences from the exploding wire are as follows. The electrical energy to create the plasma is low, which is order of tens mJ because the size of conducting

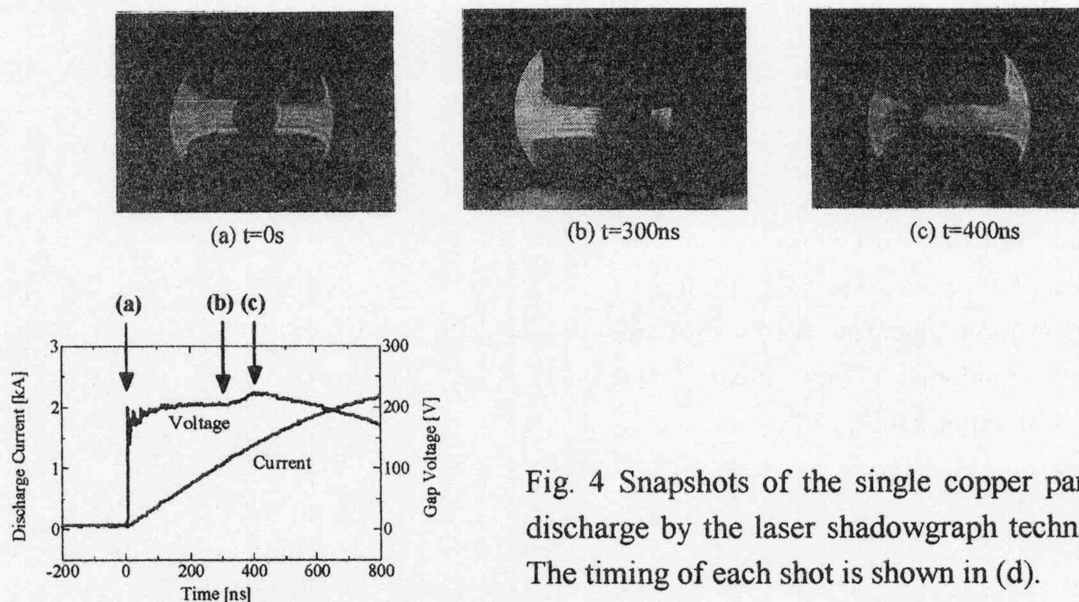

Fig. 4 Snapshots of the single copper particle discharge by the laser shadowgraph technique. The timing of each shot is shown in (d).

materials is extremely small. Although the exploding wire is described in a two-dimensional phenomenon, the copper particle discharge is a three-dimensional one.

The discharge was carried out in the air; therefore we observed formation of shock waves originating from the particle surface. The discharge will be greatly affected by the surrounding gases that are chosen for the applications. An advantage of the microplasmas is that the energy is not necessary to be high to power the discharge in comparison with the conventional plasma apparatuses. However, the circuit parameters for the discharge are not optimized yet, because our experiment is in preliminary state. Although there is no energy loss to the wall in the mass-limited mode, the energy loss to the electrodes and to the surrounding gas cannot be disregarded. The energy loss depends also on the amplitude and the rise-time of the pulsed current in the early phase of the discharge.

The particle has to be vaporized efficiently, which is quite different from the situation in gas discharges. Fast high current discharges are often employed to create the microplasmas. In the copper particle discharge, a fast high current is not desirable during the vaporization process from the viewpoint of the energy efficiency. When the rate of current rise is higher, the voltage drop across the inductance in the circuit becomes also higher. In other word, the

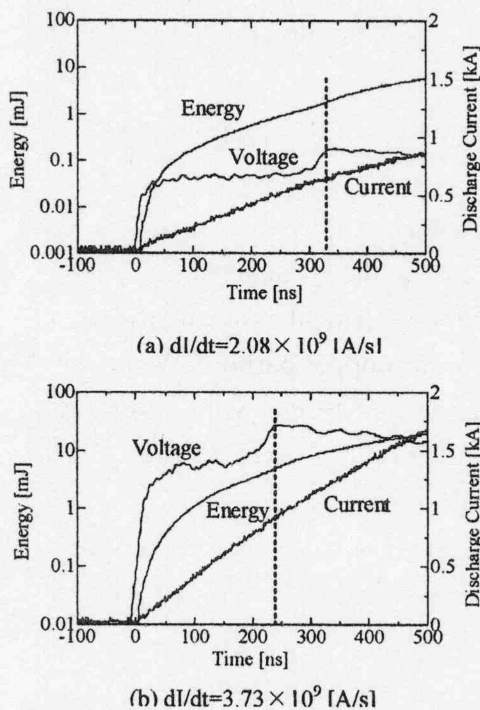

Fig. 5 The dependence of volage, current, and energy on the rate of current rise: dI/dt. The charging voltages of the 2μF capasitor are 600V for (a) and 1kV for (b), respectively.

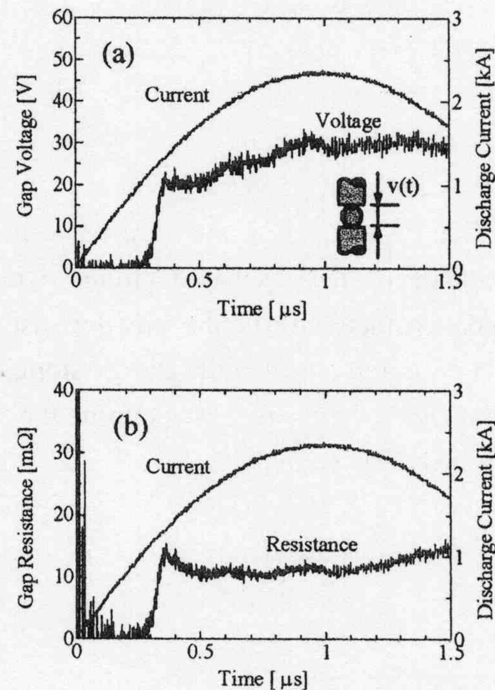

Fig. 6 Temporal change of the voltage across the copper particle: (a) and the resistance between the tungsten electrodes: (b).

ratio of the resistive drop across the particle for the inductive drop in the discharge circuit becomes smaller, which means the energy dicipated in the particle decreases.The phase transition process from solid to vapor was examined by varying the rate of current rise as shown in Fig.5. The energy used for vaporization until the voltage jump is smaller for the discharge with the slower current rise. Fast high current pulses are necessary after vaporization as required for the gas discharges. Temporal control of the discharge current pulse is needed to establish efficient creation of the microplasma with the conducting particles. The measured voltage signals described so far contain both the resistive and inductive drop across the tungsten electrodes. They have to be eliminated to obtain the effective voltage drop across the particle. The effective voltage drop is shown in Fig. 6(a) for the charging voltage of 1kV. The resistive component changes temporally as shown in Fig. 6(b). The resistance of the order of 10 mΩ agrees with that used in the P-Spice analysis.

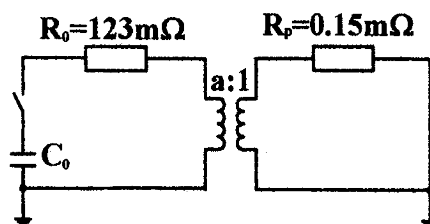

Fig.7 A testing circuit for power coupling with a pulse transformer.

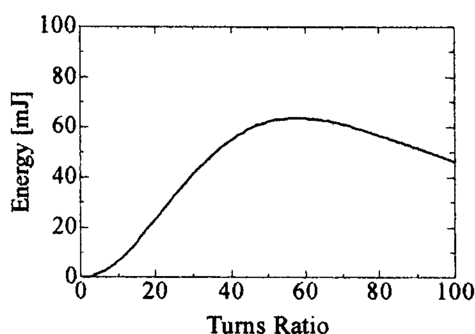

Fig.8 The influence of turns ratio for energy input.

The resistance of the copper particle is extremely small in comparison with the impedance of the discharge circuit, which is evident in the voltage signal in Fig. 3(a). Impedance matching in the powder discharge circuit is a critical issue to realize efficient power coupling between the energy storage capacitor to the copper particle. We made a circuit analysis with the P-Spice to examine the effect of a pulse transformer with a turn ratio of a:1 to improve the coupling efficiency as shown in Fig.7. For simplicity, we only consider the resistive component, where R_0 is circuit impedance, and R_p is powder impedance. Fig.8 shows the turn ratio dependence on the input energy. The input energy to the copper particle becomes a maximum when the turns ratio is 58.

IV. Conclusion

A microplasma is created with the single copper powder particle by relatively low energy pulsed discharges. The new method reported here is suitable for creating dense microplasmas. From the observation of discharge development process using voltage-current measurement and optical measurement, the phase transition was confirmed at the early stage of discharges. The phase transition in the particle develops heterogeneously and the three states: namely a solid, a liquid, and a gas, exist simultaneously. Since the impedance of the particle was

extremely smaller than that of the circuit, the sufficient energy was not supplied into the powder to be fully ionized. Impedance matching using the pulse transformer is effective to improve the power coupling.

References

(1) Kunihide Tachibana, Kaname Mizokami, Naoki Kosugi, Tetsuo Sakai: "Three-dimensional diagnostics of dynamics behaviors of exited atoms in microplasmas for plasma display panels", IEEE Transactions on Plasma Science, Vol.31, pp.68-73 (2003)

(2) H.Nozawa, H.Ishihara, Y.Kawasaki, J.Kuroda, S.Ibuka, Y.Liu, K.Yasuoka, S.Ishii : "High-Energy-Density Plasma Produced by Pulsed High Current Discharge of Powder", Jpn. J. Appl. Phys., Part I, Vol.40, No.2B, pp.1009-1012 (2001)

(3) T.Yokoyama, T.Kuraoka, K.Takano, S.Ibuka, K.Yasuoka, S.Ishii: "Early stage of pulsed high current discharge with copper powder", Transactions of the Institute of Electrical Engineers of Japan, Society A Fundamentals and Materials Society, Vol.124, No.1, pp.80-84 (2004)

(4) Michael J Taylor, "Formation of plasma around wire fragments created by electrically exploded copper wire", J. Phys. D: Appl. Phys., Vol.35, pp.700-709 (2002)

(5) K.M.Chandler, D.A.Hammer, D.B.S.Sinars, S.A.Pikuz, T. A. Shelkovenko : "The Relationship Between Exploding Wire Expansion Rates and Wire Material Properties Near the Boiling Temperature", IEEE Transactions on Plasma Science, Vol.30, pp577-587 (2002)

Development of Bipolar-pulse Accelerator for Intense Pulsed Ion Beam Acceleration

Katsumi Masugata, Yuichro Shimizu, Yuhki Fujioka, Iwao Kitamura
Hisao Tanoue, Kazuo Arai

Toyama University, 3190 Gofuku, Toyama 930-8555, Japan
National Institute of Advanced Industry Science and Technology,
1-1-1, Umezono, Tsukuba-shi, Ibaraki 305 -8568 ,JAPAN

ABSTRACT

To improve the purity of an intense pulsed ion beams a new type of pulsed ion beam accelerator named "bipolar pulse accelerator (BPA)" was proposed. To confirm the principle of the accelerator a prototype of the experimental system was developed. The system utilizes B_y type magnetically insulated acceleration gap and operated with single polar negative pulse. A coaxial gas puff plasma gun was used as an ion source, which was placed inside of the grounded anode. Source plasma (nitrogen) of current density ≈ 25 A/cm^2, duration ≈ 1.5 μs was injected into the acceleration gap by the plasma gun. The ions are successfully accelerated from the grounded anode to the drift tube by applying negative pulse of voltage 240 kV, duration 100 ns to the drift tube. Pulsed ion beam of current density ≈ 40 A/cm^2, duration ≈ 50 ns was obtained at 41 mm downstream from the anode surface. To evaluate the irradiation effect of the ion beam to solid material, amorphous silicon thin film of thickness ≈ 500 nm was used as the target, which was deposited on the glass substrate. The film was found to be poly crystallized after 4- shots of the pulsed nitrogen ion beam irradiation.

1. Introduction

Intense pulsed ion beams (PIB) of carbon, nitrogen or aluminum, have a wide area of applications including nuclear fusion, materials science, etc. For example, PIB is expected to be applied to a "pulsed ion beam implantation" to semiconductor since doping process and annealing process is expected simultaneously. The PIB is also expected to be use in a crystallization process of semiconductor thin films or surface modification process of metallic materials.

PIB can easily be generated in a conventional pulsed power ion diode using flashboard ion source[1)]. However, since many kinds of ions are produced in the same time in the flashboard ion source, the purity of the beam is usually very poor. For example, in a point pinch ion diode we found that produced PIB contains much kind of ions including protons, multiply ionized carbons, and organic ions[2)]. Hence an application of the PIB has been extremely limited.

To improve the purity a new type of pulsed power ion beam accelerator named "bipolar pulse accelerator (BPA)" was proposed [3-5]. As the first step of the development of the BPA, a prototype of the experimental system of the accelerator was constructed to confirm the principle. By using the system the acceleration of ion beam was successfully confirmed[6)]. In addition, the accelerated beam was used to irradiate amorphous silicon thin films to

evaluate the irradiation effects of PIB. In the paper the results of the experiments are described.

2. Bipolar Pulse Accelerator

Figure 1 shows the concept of the bipolar pulse accelerator[3]. A conventional PIB diode is also shown for comparison. As shown in Fig.1 (a), proposed ion accelerator consists of a grounded ion source, a drift tube and a grounded cathode. In the diode, bipolar pulse (V_1) is applied to the drift tube. At first the negative voltage pulse of duration τ_p is applied to the drift tube and ions on the grounded ion source are accelerated toward the drift tube. If τ_p is adjusted to the time of flight delay of the ions to pass the drift tube, the pulse is reversed and the positive voltage of duration τ_p is applied to the drift tube when top of the ion beam reaches the 2nd gap. As a result the ions are again accelerated in the 2nd gap toward the grounded cathode.

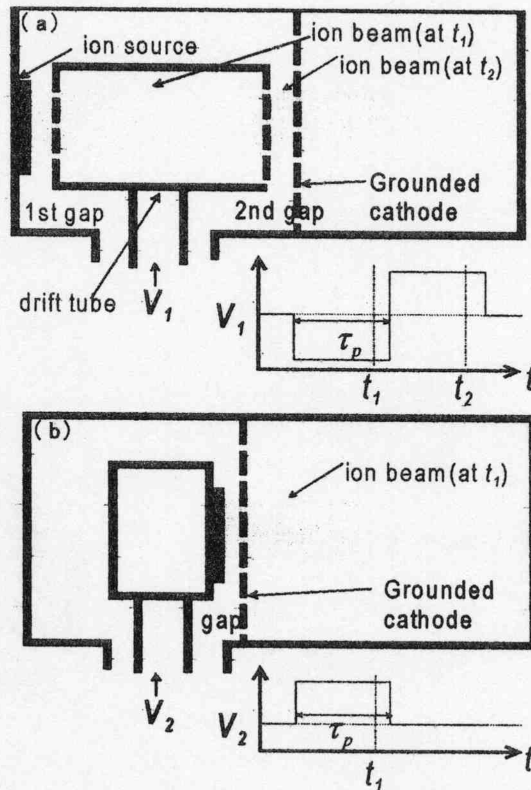

Fig.1. Conceptual drawing of (a) bipolar pulse accelerator and (b) conventional pulsed ion beam accelerator.

As seen in Fig.1 (b), in the conventional PIB diode, ion source is placed on the anode where high voltage pulse is applied, while in the proposed ion diode, ion source is on the grounded anode. This seems to be favorable for the active ion sources where ion source is powered by an external power supply.

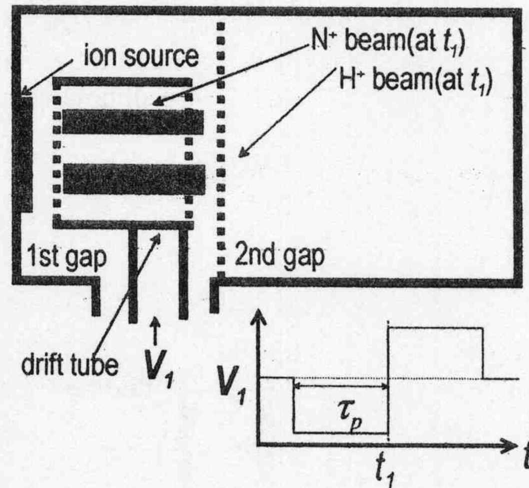

Fig.2. Principle of the improvement of the purity of the ion beam.

Here, considering the acceleration of ions in the case that ion source contains N^+ and impurity ions of H^+ in the proposed diode (see Fig. 2). In the case, ions of N^+ and H^+ are accelerated in the 1st gap toward the drift tube when negative voltage is applied. In Fig. 2, N^+ and H^+ beams are schematically described and as seen in the figure, due to the deference of the velocity the length of H^+ beam is much longer than that of N^+. Here assuming that the length of the drift tube is designed to be same as the beam length of N^+ of duration τ_p at acceleration voltage V_p. It is, for example calculated to be 7.8 cm when V_p = 500 kV, τ_p = 60 ns. When N^+ beam of length 7.8 cm is in the drift tube ($t = t_1$) the voltage is reversed and positive voltage is applied to the drift tube, which accelerate N^+ beam in the 2nd gap. In contrast, since length of H^+ beam at V_p = 500 kV, τ_p = 60 ns is 29.4 cm,

73 % of the beam is out of the drift tube at t_1 and it is not accelerated in the 2nd gap. Hence 73 % of H^+ beam is removed in the accelerator[4].

Figure 3 shows the conceptual design of the BPA. The accelerator consists of a grounded anode, drift tube and a grounded cathode. To produce insulating magnetic fields in both acceleration gaps, a magnetic field coil of grating structure is used to produce uniform magnetic field in vertical direction (y-direction).

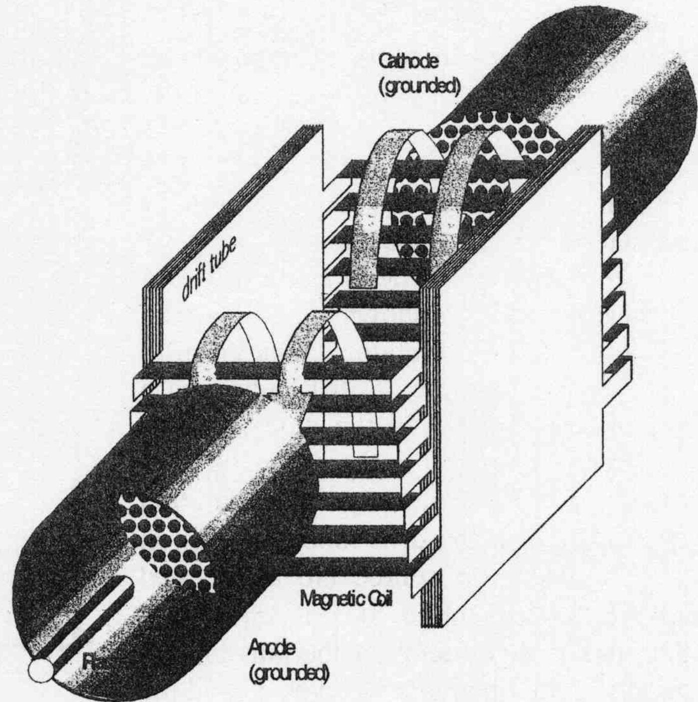

Fig.3. Conceptual drawing of B_y type magnetically insulated gap of the bipolar pulse accelerator.

3. Accelerator Experiment

Figure 4 shows the cross-sectional view of the experimental system. The system consists of a grounded anode (copper), a drift tube (stainless steel) and a magnetically insulated acceleration gap (MIG). The drift tube is connected to a high voltage terminal of a high voltage pulsed power generator. A Blumlein type pulse forming line (PFL) was used [7], which generate an output pulse of -300 kV, 48 kA, 60 ns. By applying negative pulse to the drift tube, ions on the anode are accelerated toward the drift tube. The magnetic coil of the MIG is installed on the rectangular drift tube where acceleration voltage is applied and produces magnetic field of vertical direction (y-direction). To obtain higher transmission efficiency of the ion beam, right and left sides of the coil (facing the anode or cathode) consist of 8 blades each and have a grating structure. Each of the blades (10 mm^W x 118 mm^L x 1 mm^T) is connected in series and constructs an 8-turn coil. Since high voltage pulse is applied to the drift tube,

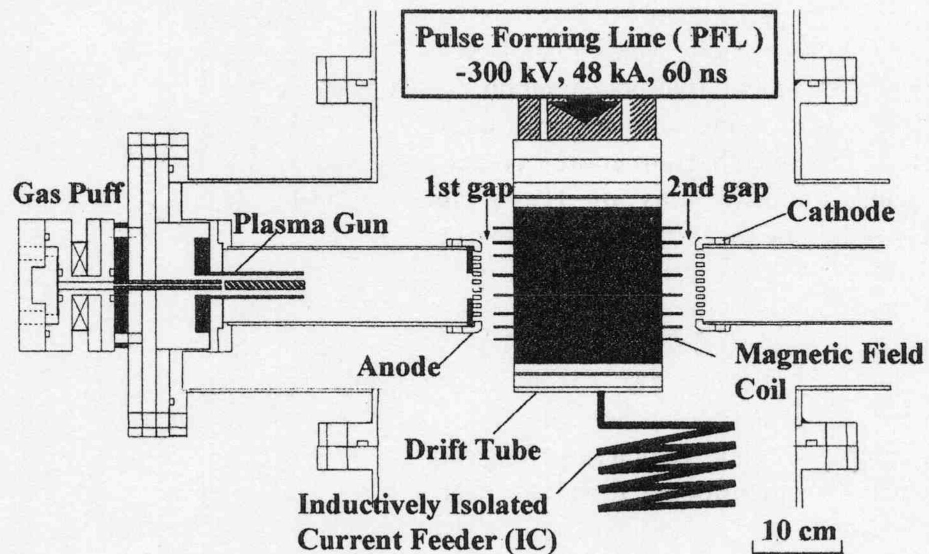

Fig.4. Cross-sectional view of the experimental system.

pulsed current produced by the capacitor bank (500 μF, 5 kV) is applied to the coil through an inductively isolated current feeder (IC). The IC is a helically winded coaxial cable and the outer conductor of the IC is connecting the grounded vacuum chamber and the drift tube with inductance of 12.4 μH.

The anode and the cathode are brass electrode of diameter 78 mm, thickness 5 mm. The electrodes are uniformly drilled with apertures of diameter 4 mm, giving beam transmission efficiency of 58 %. To produce anode plasma (source plasma of the ion beam) gas puff plasma gun was used, which was placed inside the anode.

Figure 5 shows the magnetic filed distribution in the gap. As seen in the figure uniform B_y field of strength 0.4 - 0.5 T is produced in the acceleration gap of $d_{A\text{-}K}$ = 10 mm.

Figure 6 shows the detail of the gas puff plasma gun used in the experiment. The plasma gun consists of a high-speed gas puff valve and a coaxial plasma gun. The gas puff valve consists of a nylon vessel, an aluminum valve and a drive coil and the vessel is pre-filled with N_2 gas. By applying pulse current to the drive coil, the magnetic stress produced by the pulsed magnetic field presses the aluminum valve to open the valve. As the results, filled gas in the vessel expands with a supersonic velocity and

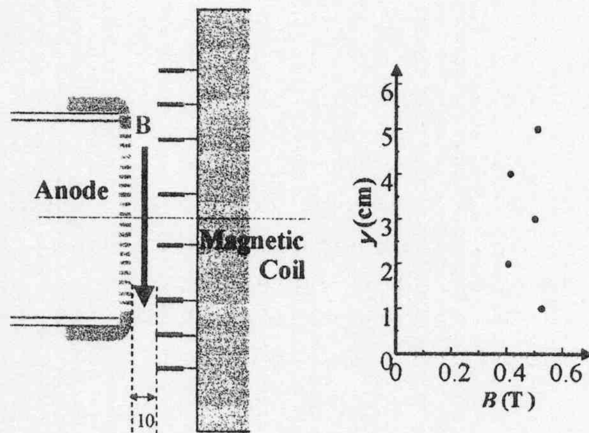

Fig.5. Magnetic field (B_y) distribution in the acceleration gap when charging voltage of the bank is 4.0 kV.

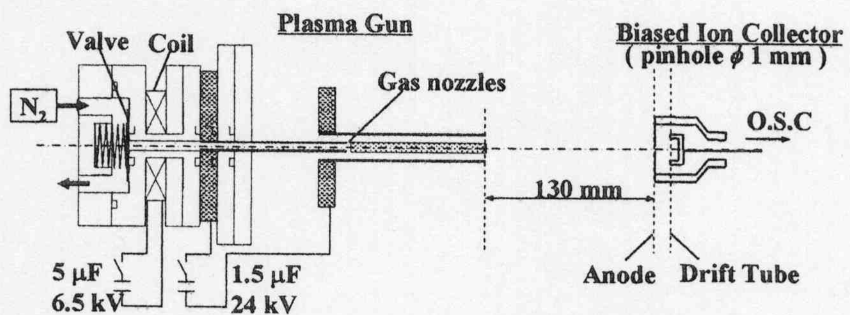

Fig.6. Cross-sectional view of the gas puff plasma gun.

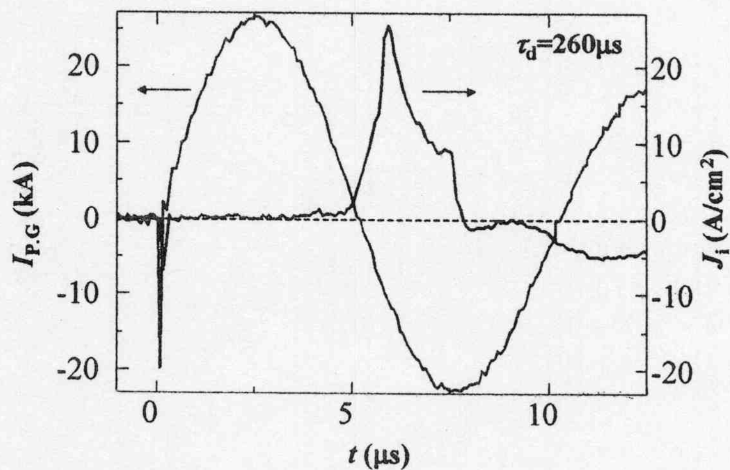

Fig.7. Typical waveforms of the discharge current of the plasma gun ($I_{P.G}$) and the ion current density (J_i). J_i was measured by BIC placed at 130 mm downstream from the top of the plasma gun.

reaches the gas nozzles on the inner electrode of the plasma gun.

The plasma gun has a pair of coaxial brass electrodes, i.e. an inner electrode of outer diameter 6 mm, length 65 mm, and an outer electrode of inner diameter 16 mm. Since it takes about a hundred μs to open the valve and several tens μs for N_2 gas to reach the gas nozzle of the plasma gun, the capacitor bank of the plasma gun is discharged with a delay time of τ_d around 200-300 μs. To apply pulsed current to the gas puff coil and the plasma gun, capacitor banks of 5 μF and 1.5 μF were used, respectively. Each capacitor was usually charged to 6.5 kV, and 24 kV, respectively.

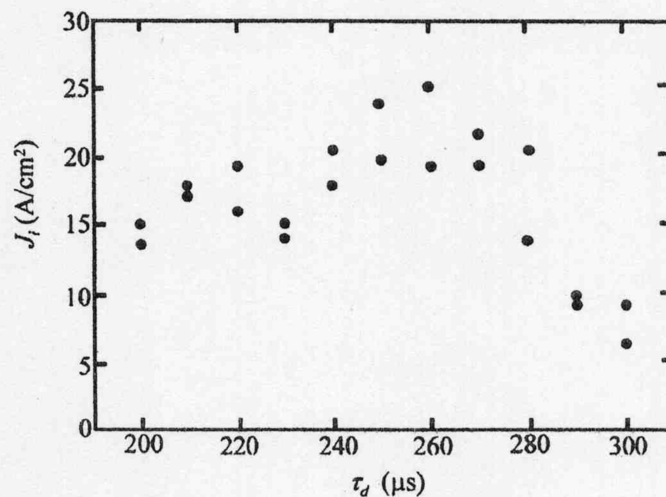

Fig.8. The dependence of the ion current density J_i on the delay time of the discharge current rise from the rise of gas puff current τ_d.

Figure 7 shows the waveforms of the discharge current of the plasma gun ($I_{P.G}$) and the ion current density (J_i) obtained by a biased ion collector (BIC) when τ_d = 260 μs. As seen in the figure $I_{P.G}$ rises in 2.5 μs and have a peak value of 27 kA. The peak value of J_i = 25 A/cm^2 was obtained at 130 mm downstream from the plasma gun on the axis at t = 7 μs after the rise of $I_{P.G}$.

Figure 8 shows the dependence of J_i on τ_d evaluated. As seen in the figure J_i rises at $\tau_d \approx$ 200 μs and have a peak around 260 μs, and after that decreased. The results suggest that it takes 200 μs after the election of gas puff coil for the gas to reach the nozzles.

4. Experimental Results

To confirm the acceleration of ions in the 1st gap negative pulse was applied to the drift tube. Figure 9 shows the set-up of beam acceleration experiment to measure the accelerated ion beam. To limit the beam diameter

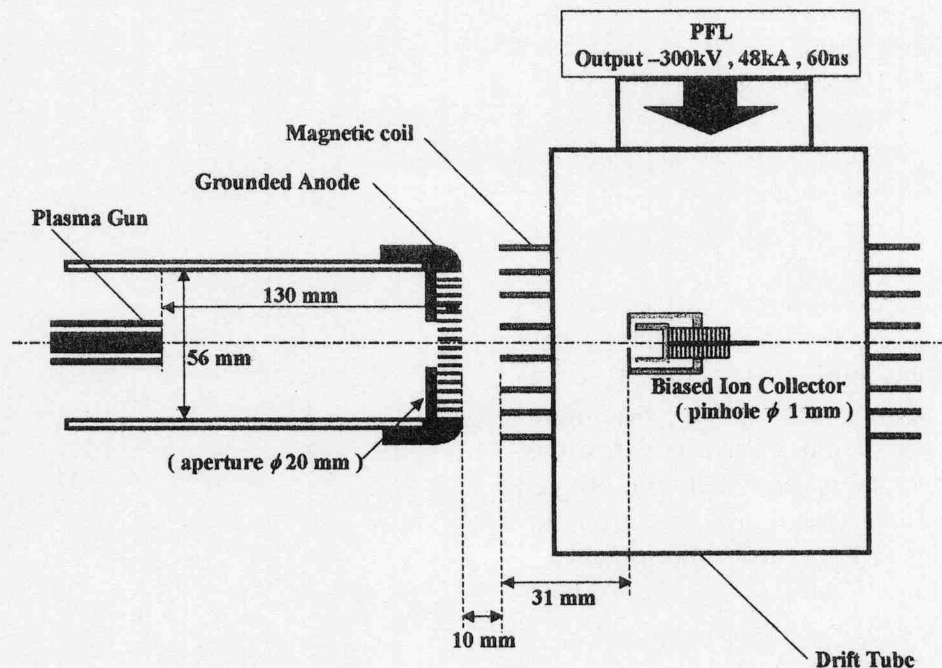

Fig.9. Experimental setup of beam acceleration experiment.

and enhance the beam current density on the axis, aperture plate of aperture diameter 20 mm is installed inside the anode. BIC was installed inside the drift tube to observe the ion current density (J_i). Since high voltage pulse is applied to the drift tube, inductively isolated coaxial cable of same structure as IC was used to transport the BIC signal. The system was operated at 80 % of the full charge condition of the PFL. Insulating magnetic field of 0.3 - 0.4 T was applied to the acceleration gap of gap length $d_{A\text{-}K}$ = 10 mm. The plasma gun was operated at the condition of ≈ 240 μs in advance to the PFL operation and the PFL was fired at τ_{pp} = 9-20 μs after the rise of the $I_{P.G}$ to apply negative high voltage pulse to the drift tube.

Figure 10 shows typical waveforms of the output voltage (V_g), the anode current (I_a) and the ion current density (J_i). They were obtained at the condition of τ_{pp} = 15.3 μs. Here, I_a was measured at the root of the anode and it is considered to be equivalent to the current flowing across the 1st gap. J_i was measured at 41 mm downstream from the anode surface. As seen in the figure, V_g rises at t = -10 ns and peak voltage of -240 kV was obtained. I_a rises with V_g and has a peak of 18 kA whereas J_i rises at t = 50 ns and have a peak of 27 A/cm^2.

Figure 11 shows the dependence of V_g, I_a and J_i on the delay time (τ_{pp}) for the fixed condition of τ_d, the insulating magnetic field and the charging voltage of the PFL. As seen in the figure J_i increases monotonically with increasing τ_{pp}. This seems to be due to that quantity of the plasma on the anode or in the 1st gap increases with

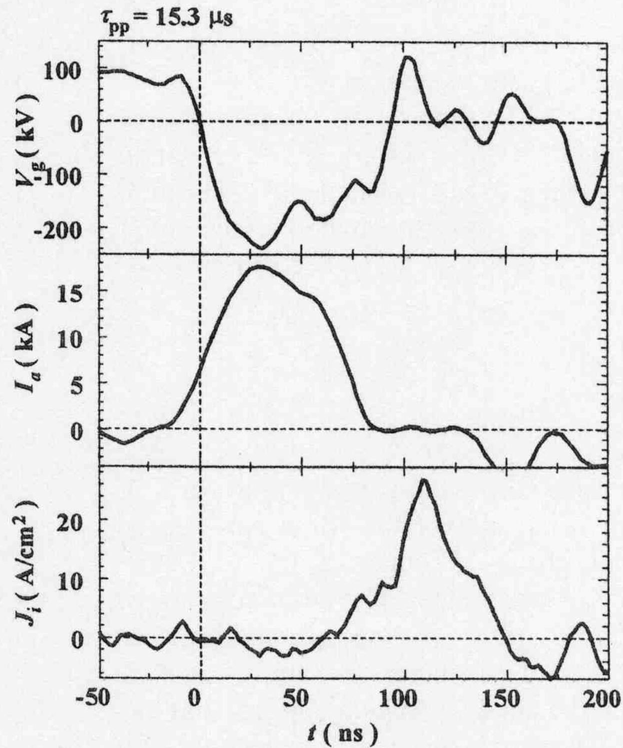

Fig.10. Typical waveforms of gap voltage (V_g), anode current (I_a) and ion current density observed at 41 mm downstream from the anode surface (J_i).

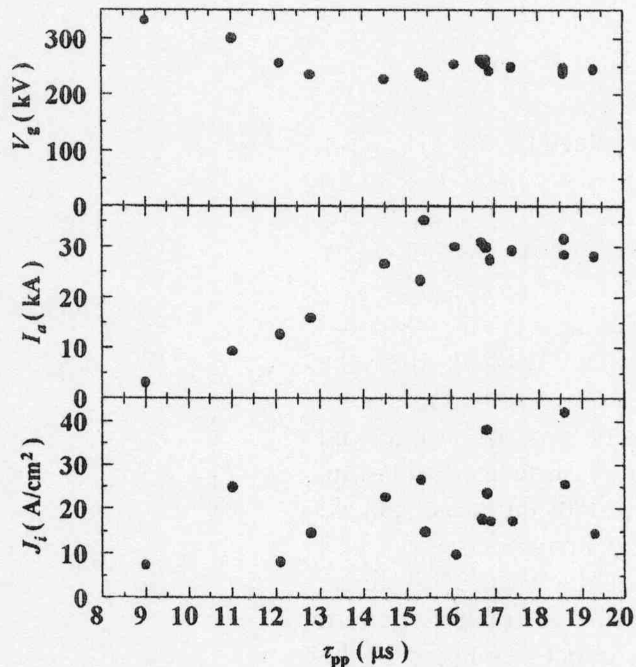

Fig.11. Dependence of the peak values of gap voltage (V_g) and ion current density (J_i) on the delay time (τ_{pp})

increasing τ_{pp}. Due to the increase of output current of the PFL with τ_{pp}, V_g decreases with increasing τ_{pp}.

Figure 12 shows the beam pattern obtained on the thermo sensitive paper. The paper was placed at 41 mm downstream from the anode surface and 4 shots of ion beams were fired to enhance the contrast of the pattern. As seen in the figure, round black pattern is observed with white central part around the beam axis. The white part is due to the ablation of the surface of the paper, hence indicating the strong irradiation of the beam. The size of the white part has an elliptic shape of long axis 60 mm short axis 45 mm. The size is much larger than the size of the plasma-limiting aperture of diameter 20 mm installed inside the anode. Which suggest that the size of source plasma expands in the acceleration gap after passing the aperture.

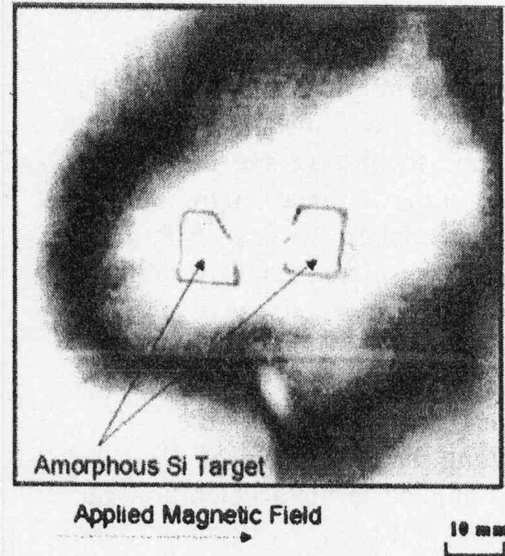

Fig.12. Beam pattern obtained on a thermo sensitive paper. The paper was placed at 41 mm downstream from the anode surface.

5. Beam irradiation Experiment

To evaluate the annealing effect of the pulsed ion beam to the materials, amorphous silicon thin films was used as a targets. The films have a thickness of 500 nm and fabricated on the glass substrate. Two targets was placed at 41 mm downstream from the anode and attached on the thermo sensitive paper as shown in Fig. 11. Here, the amorphous thin film placed at right-hand side was removed after the irradiation due to that beam intensity was too strong and cause surface ablation. Hence only the target placed at left-hand side was evaluated. Figure 13 shows the X-ray diffraction pattern of the target. As seen in the figure no diffraction peak is observed in the target before the irradiation. In contrast

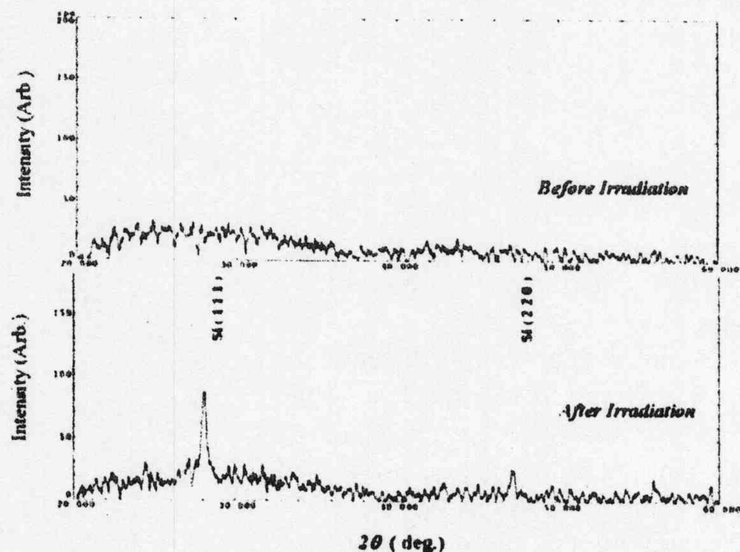

Fig.13. X-ray diffraction pattern of the amorphous silicon thin films before and after the ion beam irradiation.

clearer peaks of Si(111) and Si(220) were observed on the target after the irradiation. The results clearly indicate that the target of amorphous silicon thin film was poly-crystallized by the irradiation.

6. Conclusion

To confirm the principle of the bipolar accelerator a prototype of the experimental system was developed. The system utilizes B_y type magnetically insulated acceleration gap and operated with single polar negative pulse. A coaxial gas puff plasma gun was used as an ion source, placed in the grounded anode. Source plasma (nitrogen) of current density $\approx$ 25 A/cm^2, duration $\approx$ 1.5 μs was injected into the acceleration gap. The ions are successfully accelerated from the grounded anode to the drift tube by applying negative pulse of voltage 240 kV, duration 100 ns to the drift tube. Pulsed ion beam of current density $\approx$ 40 A/cm^2, duration $\approx$ 50 ns was obtained at 41 mm downstream from the anode surface. To evaluate the irradiation effect of the ion beam to solid material, amorphous silicon thin film of thickness $\approx$ 500 nm was used as the target, which was deposited on the glass substrate. The film was found to be poly-crystallized after four shot of irradiation.

References

1) E. Chishiro, A. Matsuyama, K. Masugata and K. Yatsui, "Dependence of characteristics of Br-type magnetically insulated diode on configuration of insulation magnetic field", Jpn. J. Appl. Phys., **35**(4A), pp.2350-2355 (1996).
2) K. Masugata, H. Okuda, K. Yatsui and T. Tazima, J. Appl. Phys. **80** pp. 4813-4818, 1996
3) K. Masugata, "High current pulsed ion beam accelerators using bi-directional pulses" Nuclear Instrum. & Methods in Phys. Res., **A 411**, pp.205-209, 1998
4) K. Masugata, K. Kinbara, T. Atsumura, Y. Kawahara, T. Takao, I. Kitamura, and T. Takahashi, *Proc. 12th Symp. on High Current Electronics (1st Int'l Congress on Radiation Physics, High Current Electronics, and Modification of Materials, Tomsk, Russia, 24-29 September 2000), ed. by G. Mesyats, B. Kovalchuk, and G. Remnev,* pp.111-114 (2000)
5) K. Masugata, I. Kitamura, T. Takahashi, Y. Tanaka, H. Tanoue, K. Arai, *Proc. 28th IEEE Int'l Conf. on Plasma Science and 13th IEEE Int'l Pulsed Power Conf., Las Vegas, Nevada, June 17-22 2001, ed. by R. Reinovsky and M. Newton,* pp. 1366-1369 (2001).
6) Y. Fujioka, C. Mitsui, I. Kitamura, T. Takahashi, K. Masugata, H. Tanoue, K. Arai, Development of Bipolar Pulse Accelerator for Intense Pulsed Ion Beam Acceleration, Research Report, **NIFS-PROC-54** (National Institute for Fusion Science, Nagoya, Japan, Workshop on Physics and Applications of Micro and Fast Z-Pinch Plasmas, Dec. 5-6, 2002) pp.38-44 (2003)
7) K. Masugata, S. Tsuchida, H. Saitou, K. Yatsui, K. Shibata and M. Shigeta, "Fast charging Blumlein pulse forming line" Laser and Particle Beams **15**(2) pp.249-258 (1997)

Characteristics of High Energy Ions Produced in Plasma Focus

Yoshikazu Kawaguchi, Kazuto Takao, Masaki Shiotani, Takeo Honda,
Iwao Kitamura and Katsumi Masugata

Faculty of Engineering, Toyama University, 3190 Gofuku, Toyama 930-8555 Japan

Abstract

Characteristics of ion beams produced in the Mather type plasma focus (PF) were studied experimentally to apply the beam to materials processing. The plasma focus was pre-filled with H_2 of 250 Pa, or mixture of H_2 (270 Pa) and Ne (30 Pa). At 218 mm downstream from the top of the anode on the electrode axis, ion beam of current density $\approx$ 4 kA/cm^2, pulse width $\approx$ 100 ns (FWHM) was observed when filling gas of H_2 was used. The ion species and energy spectra were evaluated by a Thomson parabola spectrometer. Protons of energy in the range of 0.1–1.4 MeV are observed when PF was filled with H_2. From the X-ray measurement pinch plasma column of 3–4 mm in diameter and 40 mm in length is observed and line emission of He-like and H-like K shell X-ray emissions were observed when PF was filled with mixture gas. Measurement of pinhole image and an incident angle resolved proton energy spectrum ion production is found to be axial symmetry and the ion energy decreases with increasing incident angle. To evaluate the irradiation effect amorphous silicon thin films of thickness 500 nm was irradiated by the ion beam. By the X-ray diffraction measurement of the films before and after the irradiation we found that the film was poly-crystallized by the irradiation.

1. Introduction

Strong emission of energetic ions, and x-ray are known to be emitted from the pinch plasma produced in plasma focus (PF). Especially, the energetic ions have following characteristics and expected to be applied to materials processing.[1-6]

a) High energy ions of energy ranging from 100 keV to several MeV are produced with relatively low voltage pulsed power systems.[7]

b) The power density and the brightness of the beams are very high. [1,3]

To clarify the mechanism of the production of the ion beams and to apply them to materials processing we have evaluated the characteristic of the ion beam. In addition, the beam was used to irradiate amorphous silicon thin film to evaluate the irradiation effect. In the paper the experimental results are described.

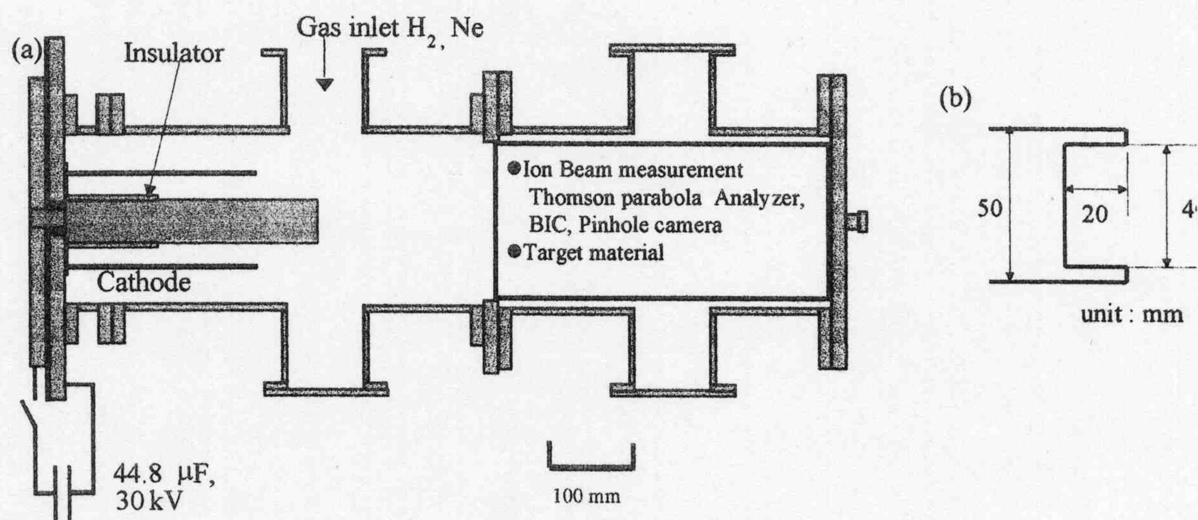

Fig. 1. a) Schematic of the experimental system. b) Detail of the anode top.

2. Experimental apparataus

Table I. Experimental condition.

Charging voltage Store energy	Base pressure	Filling gas/ pressure
44.8 μF, 30 kV / 20.2 kJ	< 7.0×10^{-3} Pa	H_2 250 Pa
		H_2 / Ne 270/ 30 Pa

Figure 1 shows the schematic of the experimental apparatus. Mather type PF was used in the experiment. The PF consists of an inner electrode (anode), an outer electrode (cathode), and a glass insulator. The anode is a cylindrical copper electrode and its length and the diameter are 280 mm and 50 mm, respectively. Figure 1 (b) shows the detail of the anode top. To reduce the production of impurity ions and to reduce the damage of the electrode, the anode has a hollow shape top and has a hollow of 40 mm in diameter and 20 mm.

The cathode consists of 24 copper rods of diameter 10 mm, length 230 mm and the effective inner diameter of the cathode is 100 mm. The insulator is made of glass and the length and the outer diameter are 125 mm and 60 mm, respectively.

A capacitor bank of capacitance 44.8 μF, maximum charging voltage 80 kV was used, which was connected to the PF through 224 of coaxial cables. In the experiment the charging voltage of the capacitor bank was fixed to 30 kV. The vacuum chamber was once evacuated to $< 7\times10^{-3}$ Pa and after that filling gas was introduced. In the experiment pure hydrogen (purity 99.9 %, 250 Pa), and mixture gas of hydrogen (purity 99.9 %, 270 Pa) and neon (purity 99.99 %, 30 Pa) were used as the filling gases. The experimental conditions are summarized in table I.

3. Experimental results

3-1. Ion beam measurement

Figure 2 shows typical waveforms of discharge current (I_{ch}) measured by a Rogowski coil, and ion current density (J_i) measured by a biased ion collector (BIC) at z = 218 mm downstream from the top of the anode on the electrodes axis. The BIC has a cup electrode inside the grounded body and the ions are injected into a cup electrode through an aperture of 0.3 mm in diameter. The electrode was biased to -300 V to remove co-moving electrons. In the experiment the PF was pre-filled with pure H_2.

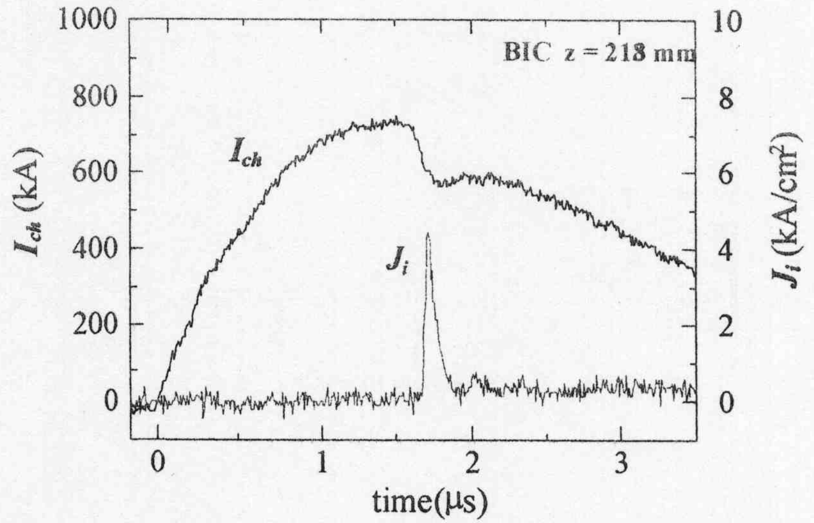

Fig. 2 . Typical waveforms of I_{ch} and J_i.

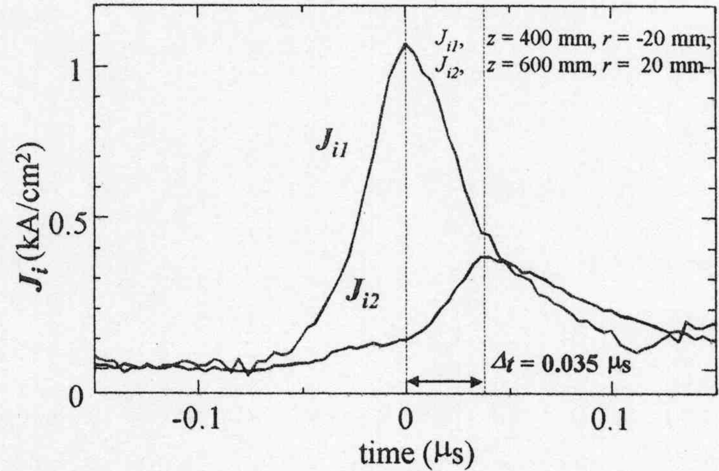

Fig. 3. Waveforms of J_i at different axial positions for TOF evaluation of ion velocity and energy.

As seen in the figure, I_{ch} has a peak of 750 kA at t = 1.6 μs and after that 150 kA of current dip is observed, which suggests the strong pinch of the plasma. In the figure, J_i rises sharply at the end of the current dip (at t = 1.7 μs) and has a peak of 4.5 kA/cm^2 with pulse width of 80 ns (FWHM). Considering the time of flight (TOF) delay of J_i, ions are accelerated at the dip phase of I_{ch}.

Figure 3 shows the waveforms of J_i at different axial positions (J_{i1} and J_{i2}) for TOF evaluation of ion velocity. Two BIC's fo J_{i1} and J_{i2} were placed at z = 400 mm, r (radial distance from the electrode axis) = -20 mm and z = 600, r = 20 mm, respectively. The ion velocity is evaluated to be 5.7×10^6 m/s from the time deference between the peaks of J_{i1} and J_{i2}. The velocity corresponds to the proton energy of 170 keV.

To evaluate the species of ions and their energy spectra, a Thomson parabola spectrometer (TPS) was used. The TPS consists of a pair of pinholes (1st and 2nd pinhole) to collimate the incident ion beam, a magnetic deflector, an electrostatic deflector, and an ion track detecting

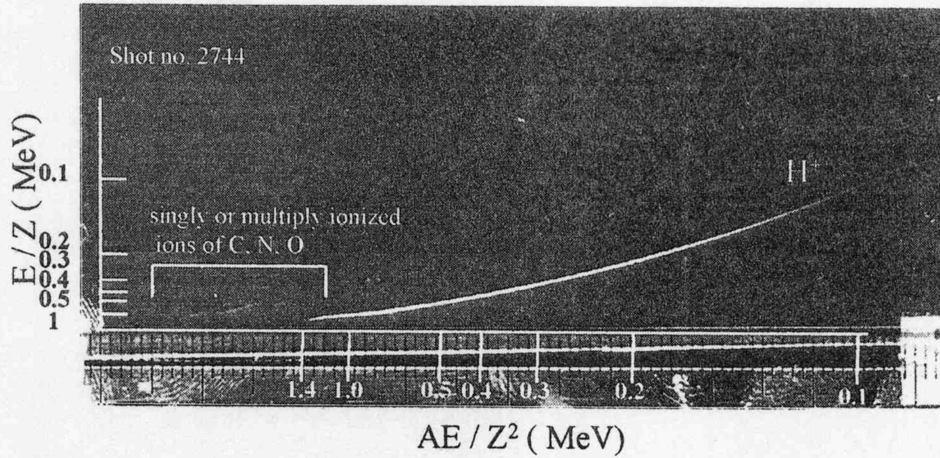

Fig. 4. The track pattern obtained by TPS. The filling gas of H_2 250 Pa was used. Here E, Z and A are the ion energy in MeV, charge state of ions and the mass number of ions, respectively.

film of CR-39, the detail of the TPS is shown in the literature[1]. Figure 4 shows the ion track pattern obtained by the TPS. As seen in the figure, strong trace of protons is observed with weak trace of impurities such as oxygen, nitrogen and carbon ions. The energy of the protons is in the range of 0.1 – 1.4 MeV. The source of the impurities seems to be the desorbed gas from the electrode surface.

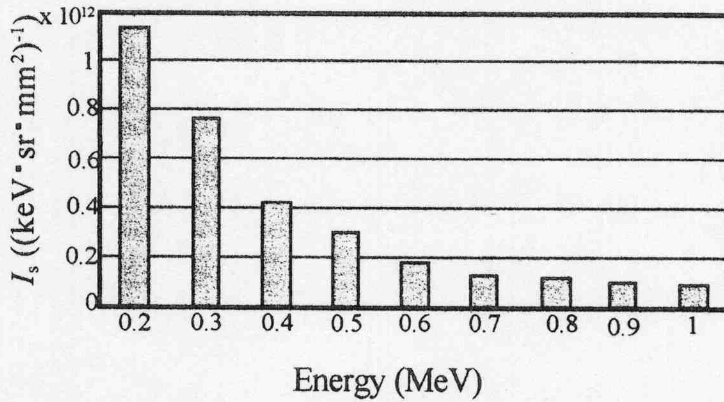

Fig. 5. Energy spectrum of protons evaluated from Fig. 4.

To evaluate the spectral intensities (I_s) of each beam energy from Fig. 4, line densities of the ion tracks (N_l, track number density along the parabola trace) of each energy were carefully evaluated. Here, I_s is evaluated by the following equation [7].

$$I_s \equiv \frac{1}{\Omega \cdot S} N_l \frac{dl}{dE} \cdot \qquad (1)$$

Here, l is the length of the parabola trace, E is the ion energy, S is the area of the 1st pinhole, Ω is the solid angle of the 2nd pinhole observed from the 1st pinhole. Figure 5 shows the result of the evaluation. As seen in the figure, I_s decreases with increasing energy.

Figure 6 (a) shows the particle pinhole image on CR-39 obtained by a particle pinhole camera. In the figure concentric circular patterns are observed, which suggest the axially

symmetric ion beam generation. Considering that ions passing off-axis are bended by the strong self-magnetic field of azimuthal- direction, the ions seem to be produced on the axis.

To evaluate the angular distribution of ion energy spectrum, electrostatic ion energy spectrometer was used, schematic of which is shown in Fig. 7. The spectrometer consists of a pinhole, fan-shaped electric deflector and an ion track detecting film of CR-39. The obtained track pattern is shown in Fig. 6 (b) with a pinhole image. From the pattern we see that the ion energy decreases with the incident angle.

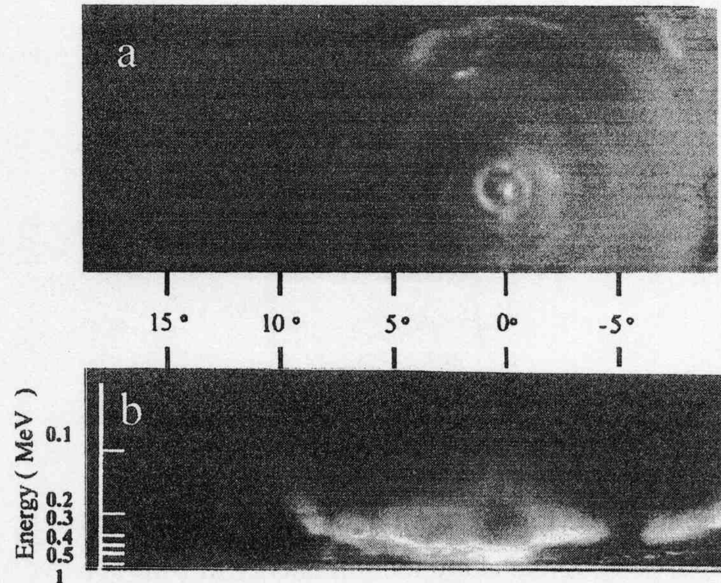

Fig. 6. Particle pinhole image (a) and an angular distribution of ion energy (b) obtained by a particle pinhole camera and an electric mass spectrometer, respectively. The incident pinholes for both measurement were placed at $z = 218$ mm on the electrode axis.

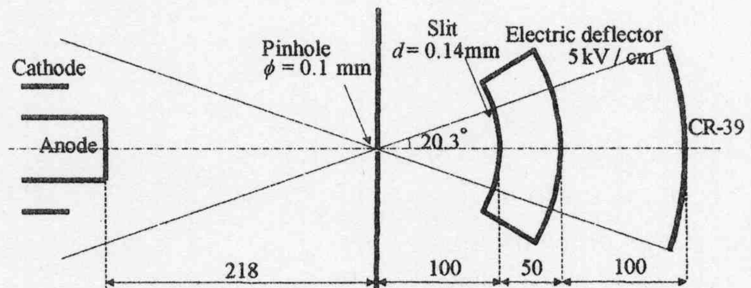

Fig. 7. Schematic of incident angle resolved electric ion energy spectrometer.

3·2. X-ray measurement

To evaluate the characteristics of hydrogen pinch plasma by X-ray observations, 10 % of neon was added as a seed gas (H_2/Ne = 270/30 Pa). Figure 6 shows time integrated X-ray image of the PF obtained by an X-ray pinhole camera. Be filter of thickness 30 μm was used in the camera to remove visible light. As seen in the figure, X-ray images are observed from a pinch column of the plasma and from the top of the hollow anode. The X-ray image of the pinch column has a size of 3-4 mm in diameter and 40 mm in length, hence we see that relatively uniform high temperature pinch column of that size is produced. In addition, some bright spots are also observed in the image, which indicate the existence of hot spot in the plasma. On the other hand, bright X-ray image of the electrode top seems to be due to the electron irradiation.

Hence strong electron beam seems to be produced in the pinch plasma. To evaluate the time variation of X-ray emission, X-ray PIN diode was used. The PIN diode was placed in the vacuum chamber at 110 mm from the axis of the PF. Be filter of thickness 35 μm was used to remove light signal.

Figure 9 shows the waveform of X-ray PIN diode output (V_{pin}). As seen in the figure, V_{pin} sharply rises with J_i and have a FWHM pulse width of less than 50 ns.

Figure 10 shows X-ray spectrograph obtained by a crystal spectrometer. In the measurement KAP crystal ($2d$ = 2.664 nm) was used with X-ray films of IP-21 (Kodak). Incident slit of width 0.25 mm was covered with Be foil. As seen from the figure K shell X-ray emission of H-like Ne and He-like Ne is observed, which indicate the existence of highly ionized Ne ions (Ne^{8+} and Ne^{9+}) in the pinch plasma.

3-3 Beam irradiation Experiment

To evaluate the annealing effect of the pulsed ion beam to the materials amorphous silicon thin films were used as targets. The films have a thickness of 500 nm and fabricated on glass substrates. The target was placed at z =500, r =30 mm, where J_i was evaluated to be 250 A/cm^2. Figure 11 shows the X-ray diffraction pattern of the target before and after one shot of

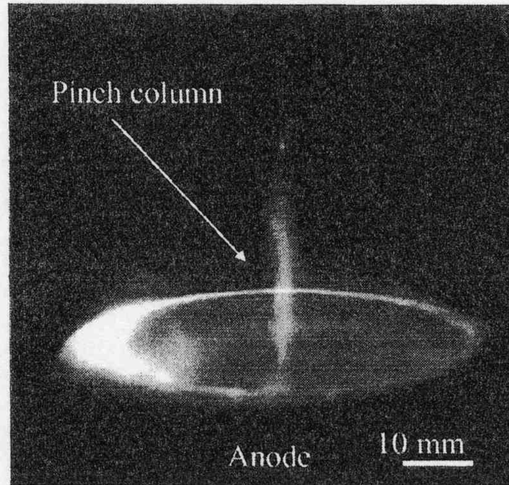

Fig. 8. X-ray pinhole image obtained on an X-ray film. The PF was filled with mixuture gas (H_2/Ne = 270/30 Pa).

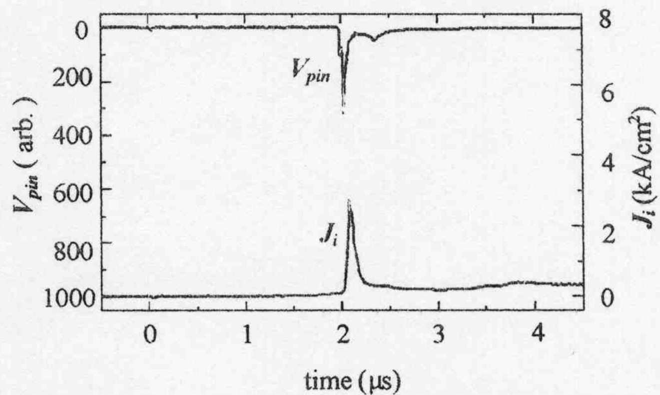

Fig. 9. Waveform of X-ray PIN diode output (V_{pin}) shown with J_i.

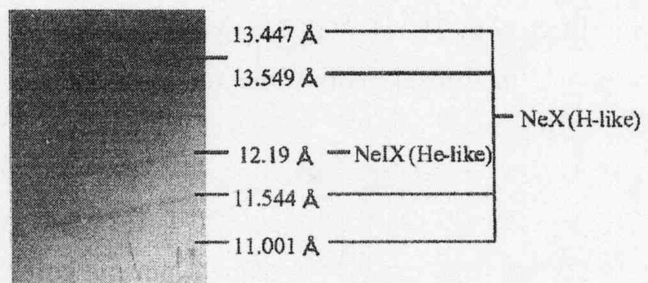

Fig. 10. X-ray spectrogrhaph.

irradiation. From the figure we see that clearer peaks of Si (111) and Si (220) appear by the irradiation of ion beam, which indicate that amorphous silicon thin film was poly-crystallized by the irradiation.

Due to the special characteristics of an intense pulsed ion beam, it is expected to applied for materials processes such as surface treatment, pulsed ion beam implantation, thin film deposition, etc. Pulsed power ion diode has been used for those applications[8]. However, from this experiment we see that the PF is the potential beam source for material processing since highly bright ion beam can easily be obtained by a low cost power supply of simple capacitor bank.

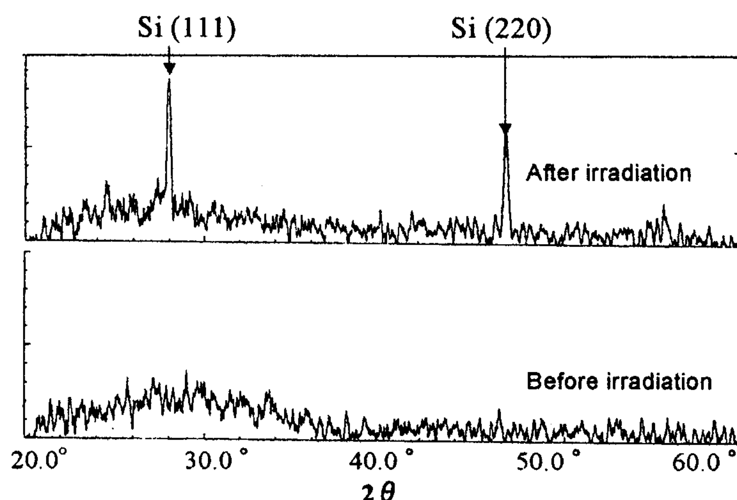

Fig. 11. X-ray diffraction pattern of amorphous silicon thin film before and after the ion beam irradiation.

4. Conclusion

Characteristics of ion beams produced in the Mather type plasma focus (PF) were studied experimentally to apply the beam to materials processing. The plasma focus was pre-filled with H_2 of 250 Pa, or mixture of H_2 (270 Pa) and Ne (30 Pa). At 218 mm downstream from the top of the anode on the electrode axis, ion beam of current density ≈ 4 kA/cm^2, pulse width ≈ 100 ns (FWHM) was observed when filling gas of H_2 was used. The species and energy spectra of ion were evaluated by a Thomson parabola spectrometer. Protons of energy in the range of 0.1–1.4 MeV are observed when PF was filled with H_2. From the X-ray measurement pinch plasma column of 3–4 mm in diameter and 40 mm in length is observed and line emission of He-like and H-like K shell X-ray emissions were observed when PF was filled with mixture gas. From the measurement of pinhole image

and an incident angle resolved proton energy spectrum we see that ion production is axial symmetry and the ion energy decreases with increasing incident angle.

To evaluate the irradiation effect, amorphous silicon thin film of thickness 500 nm was used as a target and irradiated by the ion beam. By the X-ray diffraction measurement of the thin films before and after the irradiation we found that the film was poly-crystallized by the irradiation.

References

1) K. Takao, Y. Doi, S. Hirata, M. Shiotani, I. Kitamura, T. Takahashi and K. Masugata, *Jpn. J. Appl. Phys.*, **40**, pp. 1013-1015 (2000)
2) T. Takao, M. Shiotani, T. Honda, I. Kitamura, T. Takahashi, K. Masugata, "Characteristics of the Nitrogen Ion Beam Produced in a Plasma Focus Device", *Proc. 28th IEEE Int'l Conf. on Plasma Science and 13th IEEE Int'l Pulsed Power Conf., Las Vegas, June 17-22, 2001*, pp.731-734 (2001)
3) K Takao, T Honda, I Kitamura and K Masugata, "Purity of nitrogen ion beams produced in plasma focus", *Plasma Sources Sci. Technol.* **12,** pp. 404-411 (2003)
4) J. N. Feugeas, E. C. Llonch, C. O. de Gonzalez and G. Galambos, *J. Appl. Phys.*, **64** p.2648 (1988)
5) H. Kelly, A. Lepone, A. Marquez, D. Lamas and C. Oviedo, *Plasma Sources Sci. Technol.*, **5,** p.704 (1996)
6) R.L. Gullickson and H.L. Sahlin, *J. Appl. Phys.*, 49, p.1099 (1978)
7) K. Masugata, H. Okuda, K. Yatsui and T. Tazima, "Evaluation of brightness of intense pulsed ion beam by a Thomson spectrometer" *Laser and Particle Beams* **15**, p.325 (1997)
8) For example H. A. Davis et al., *Matelials Chemistry and Physics* **54**, pp. 213-218 (1998)

Generation of Intense Pulsed Heavy Ion Beam by a B_y Type MID with Pulsed Plasma Gun

Jun Kawai, Rei Tejima, Iwao Kitamura, K. Masugata,
Hisao Tanoue*, and Kazuo Arai*
Faculty of Eng., Toyama Univ., Toyama, 930-8555 Japan
*National Institute of Advanced Industry Science and Technology,
1-1-4, Tsukuba, Ibaraki, 305-8568 Japan

ABSTRACT

Intense pulsed heavy ion beam (PHIB) of ion current density more than several tens of A/cm^2 can be applied to materials processes. To apply PHIB to materials processes purity of the beam is very important. For the purpose a new type of ion beam diode was developed. In the diode a new acceleration gap configuration is used with active ion source of pulsed plasma guns. Two types of plasma guns were developed to generate variety of ion beams, i.e. a gas puff plasma gun and a vacuum arc plasma gun. Two types of plasma guns were developed to generate variety of ion beams, i.e. a gas puff plasma gun and a vacuum arc plasma gun. With the gas puff plasma gun, source plasma of nitrogen ions was produced. The current density of the plasma was evaluated to be $\approx$ 28 A/cm^2 at 90 mm downstream from the top of the plasma gun. The plasma was injected into the acceleration gap of the diode and the ion diode was successfully operated at diode voltage $\approx$ 200 kV, diode current $\approx$ 2.0 kA, pulse duration $\approx$ 150 ns. Ion beam of ion current density $\approx$ 13 A/cm^2 was obtained at 55 mm downstream from the anode. The energy and species of the beam was evaluated by a Thomson parabola spectrometer and found that N^+ and N^{2+} beam of energy 60-300 keV were accelerated with impurity of protons of energy 60-150 keV. The purity of the nitrogen beam was estimated to be 87 %.

To generate metallic ions vacuum arc plasma gun was developed. The characteristics of the plasma gun were evaluated and source plasma of current density 8 A/cm^2, plasma drift velocity 4.7×10^4 m/s was found to be obtained.

1. Introduction

Intense pulsed heavy ion beams (PHIB) such as carbon, nitrogen, or aluminum have a wide area of applications including nuclear fusion, materials science, etc. For example, by the irradiation of PHIB on to the material, very attractive effects are expected as shown in the followings;

1) Pulsed surface heating,
2) Production of high dense ablation plasma,
3) Production of strong pressure and shock wave,
4) Deposition of atoms.

Hence it is expected to be applied to surface treatment[1,2], thin films deposition[3], or an implantation process. Especially for the implantation process, PHIB is expected to be used as a new type of ion implantation technology since the ion implantation and surface heat treatment or surface annealing are completed in the same time.[4,5]

Pulsed ion beams usually have been generated in pulsed power ion diodes with surface flashover ion sources. However, in the diodes producible ion species are limited. In addition the beams usually contains much quantity of impurity ions[6,7]. In the implantation process highly pure ion beam is required, hence conventional pulsed ion diode is not suitable for the process.

To produce pulsed heavy ion beam with acceptable purity a new type of pulsed ion beam source has been developed. In the ion souse B_y type magnetically insulated acceleration gap is used with active ion source of gas puff plasma gun. In addition to produce metallic ions, vacuum arc plasma gun was developed. In the paper preliminary results of the experiments are described.

2. Ion Diode Experiment

Figure 1 shows the schematic of the experimental system. The system consists of a high voltage pulsed power generator, a gas puff plasma gun, and a B_y type magnetically insulated ion acceleration gap (diode). The pulsed power generator used in the experiment consists of a fast capacitor bank and a step up transformer. The capacitor bank of maximum charging voltage 50 kV produces high power pulse of duration ~150 ns (FWHM). The pulse is voltage magnified by the multi-turn step up transformer using magnetic cores of amorphous metal. The output parameter of the generator is 200 kV, 2 kA, 150 ns, which is applied to the anode of the diode.

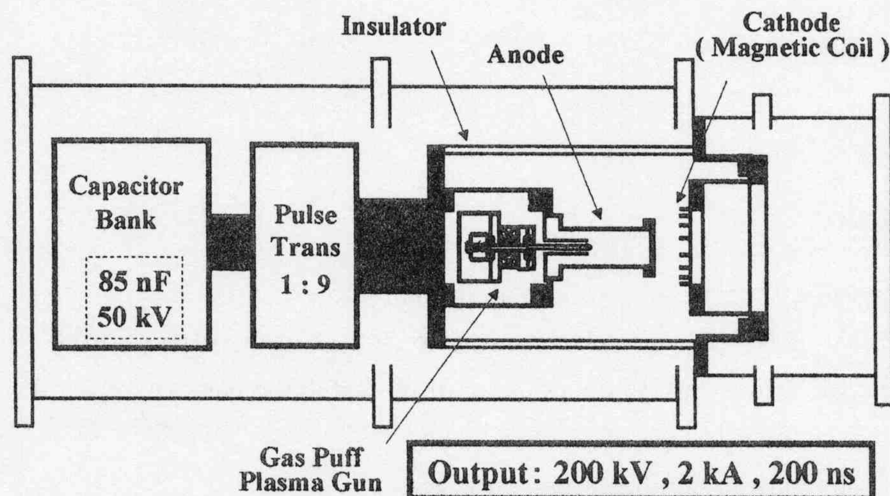

Fig.1. Schematic of the experimental system.

The diode consists

of a cylindrical anode of diameter 60 mm at the top, length 115 mm, and a cathode of grid structure. Inside the anode a gas puff plasma gun was installed to produce ion source plasma. In the experiment the gap length $d_{A\text{-}K}$ was adjusted to 10 mm and the vacuum chamber was evacuated to 5 x 10^{-3} Pa.

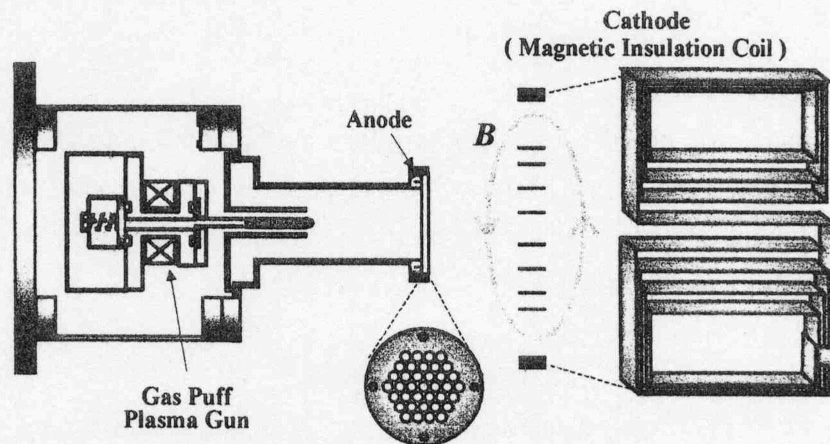

Fig. 2. Cross-sectional view of the B_y type magnetically insulated acceleration gap.

Figure 2 shows the detail of the diode. The top of the anode is a copper plate of diameter 60 mm. To introduce the source plasma to the acceleration gap, the copper plate is drilled with apertures of 5 mm in diameter in the central area of 40 mm in diameter. The cathode has a grid structure to pass through the accelerated ions. To produce a magnetic field in the acceleration gap for insulating electron flow the cathode also acts as a multi-turn magnetic field coil. The coil is made of phosphor bronze strip of thickness 1 mm, width 10 mm and has an 8-character like shape. A capacitor bank of 250 μF, 5 kV is used to apply a pulse current of rise-time 50 μs to the coil. By applying a pulse current of 10 kA to the coil, uniform magnetic field of 0.8 T is produced in the gap.

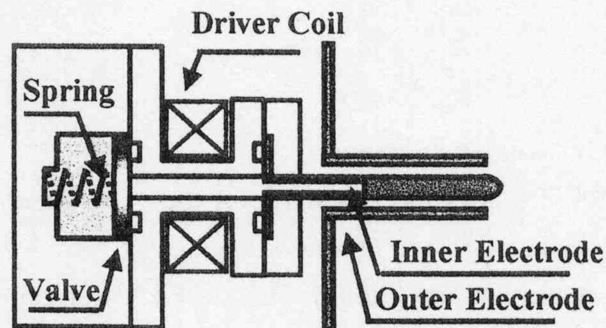

Fig.3. Cross-sectional view of the gas puff plasma gun.

Figure 3 shows the cross-sectional view of the gas puff plasma gun. The plasma gun consists of a high-speed gas puff valve and a coaxial plasma gun. The gas puff valve consists of a nylon vessel, an aluminum valve and a driver coil. The vessel is pre-filled with 2 atm of N_2 gas. By applying pulse current to the driver coil, the magnetic pressure pushes the valve to open. By the opening of the valve the gas expands and reaches to the electrode of the plasma gun.

The plasma gun has a pair of coaxial electrodes, i.e. an inner electrode of outer diameter 6 mm, length 80 mm, and an outer electrode of inner diameter 18 mm. Since it takes ≈ 150 μs

to open the valve and several tens μs for N_2 gas to reach the gas nozzle on the inner electrode of the plasma gun, the capacitor bank of the plasma gun is discharged with a delay time of τ_{gp} = 236 μs. Capacitor banks of 20 μF and 3.3 μF are used for the driver coil and the plasma gun, respectively. Both banks were charged to 5.5 kV, and 17 kV, respectively. Since the plasma gun is placed inside the anode where high voltage pulse is applied, pulsed currents generated by the capacitor banks are fed through inductively isolated coaxial cable.

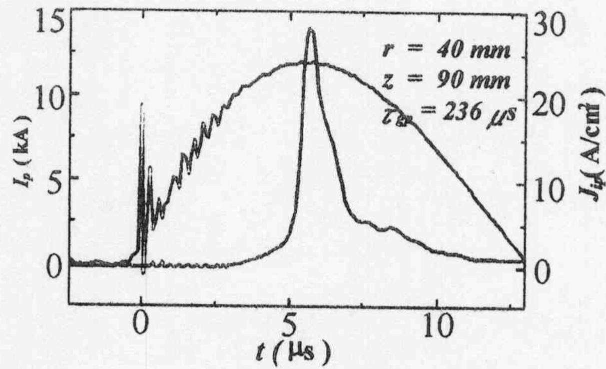

Fig.4. Typical waveforms of discharge current (I_p) and ion current density (J_{ip})

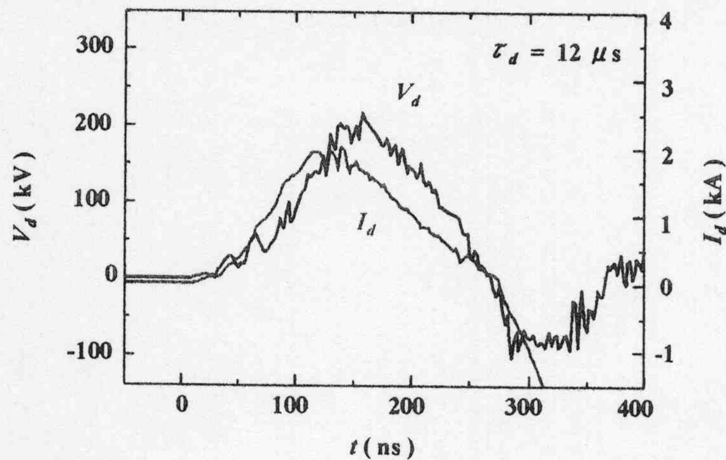

Fig.5. Typical waveforms of diode voltage (V_d) and diode current (I_d).

The ion current density of the plasma (J_{ip}) was evaluated by a biased ion collector (BIC) placed at z = 90 mm downstream from the top of the plasma gun where anode is placed in the experiment. Figure 4 shows typical waveforms of the discharge current (I_p) and J_{ip}. As seen in the figure J_{ip} rises to 12 kA in 6 μs. I_p of 28 A/cm^2 was obtained at 6 μs after the rise of I_p.

3. Experimental results

In the experiment the pulse power system was fired at delay time of τ_d after the rise of the discharge current of the plasma gun. Figure 5 shows typical waveforms of diode voltage (V_d) and diode current (I_d) at τ_d = 12 μs. As seen in the figure, V_d rises in 150 ns and has a peak of 220 kV. On the other hand I_d rises with V_d and have a peak of 2.0 kA at t = 125 ns and after that decreases. Figure 6 (a) shows the ion current density of the accelerated beam J_i measured by BIC placed on the axis at z = 55 mm downstream from the surface of the anode. The waveform of V_d is shown as the reference. As seen in the figure J_i of 12 A/cm^2 was observed at 130 ns after the rise of V_d. Considering the time of flight delay, the ions corresponding the peak of J_i seems to be accelerated before the peak of V_d.

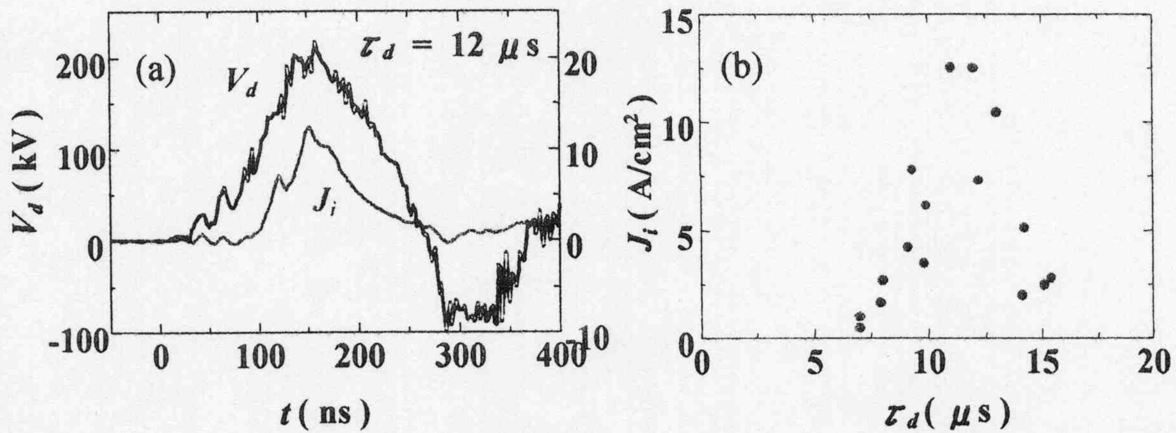

Fig. 6. Dependence of J_i on the delay time of the rise of the main pulse from the rise of the discharge current of the plasma gun (τ_d).

Figure 6 (b) shows the dependence of J_i on τ_d. As seen in the figure J_i rises at τ_d = 6 μs and has a clear peak at τ_d around 12 μs. Figure 7 shows the damage pattern of the ion beam recorded on the thermo-sensitive paper. Position of the anode is shown in the figure as the reference. As seen in the figure the beam tends to sift to the direction of $\boldsymbol{E}\times\boldsymbol{B}$ drift.

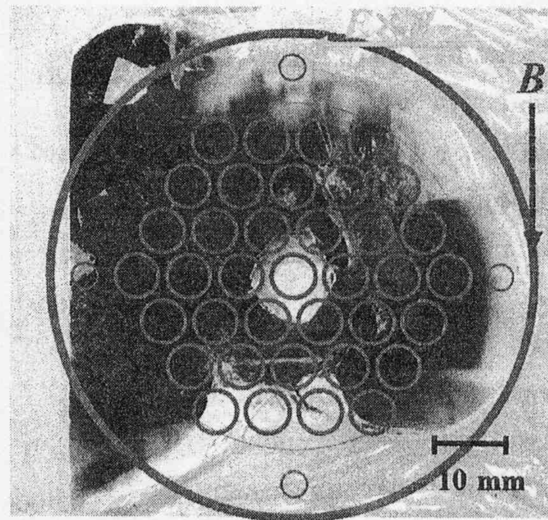

Fig. 7. Damage pattern of the ion beam recorded on the thermo-sensitive paper.

To evaluate the species and the energy spectrum of the ion beam Thomson parabola spectrometer was used. Figure 8 shows the example of the track pattern recorded on the ion track detecting plate of CR-39. In the

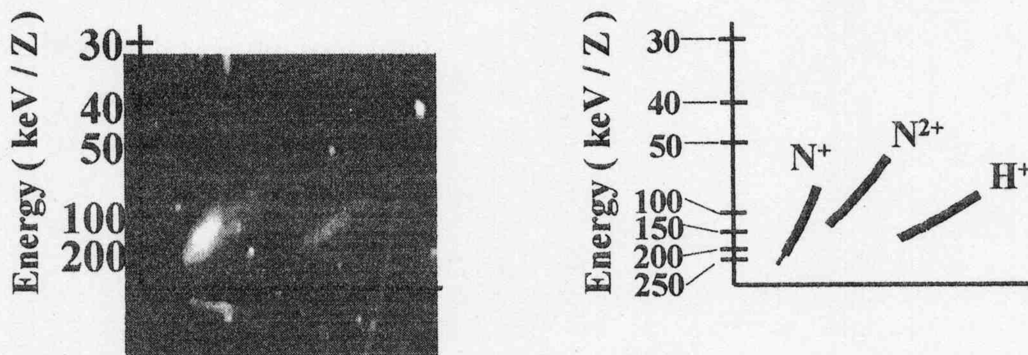

Fig. 8. The example of ion track pattern obtained by the Thomson parabola spectrometer.

Table I. Energy and the number ratio of each ion species evaluated by TPS measurement.

Ion specie	N^+	N^{2+}	H^+
Energy (keV)	60-300	100-300	60-150
Percentage	86.5		13.5

figure, singly and doubly ionized nitrogen ions are observed with impurity of hydrogen ions. The energy range and the number ratio of each ion species evaluated from the track pattern and listed in table I. From the table the purity of the beam was evaluated to be 86.5 %.

4. Development of vacuum discharge metallic ion source

Pulsed ion beams of metallic ions are attractive for materials processes, however they cannot be obtained yet. To develop an intense pulsed metallic ion source we are developing vacuum discharge ion source[8]. Figure 9 shows the experimental setup to evaluate the characteristics of vacuum discharge. Self breakdown type capacitor bank of capacitance 1 μF, maximum charging voltage 35 kV was used in the experiment. As the discharge electrode a pair of aluminum rod of diameter 6 mm was used, which was placed face to face with gap length 1 mm. To measure the ion current density BIC was placed at 100 mm apart from the gap. The experiment was done in the vacuum of 4×10^{-3} Pa.

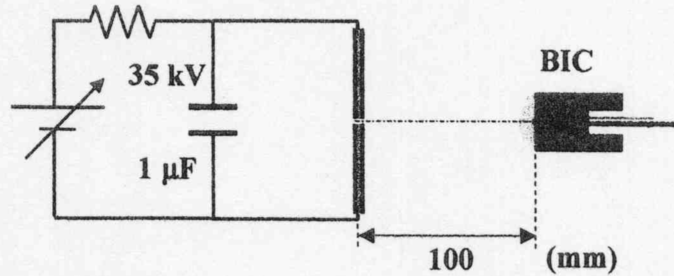

Fig. 9. Experimental system of self-breakdown type vacuum discharge ion source.

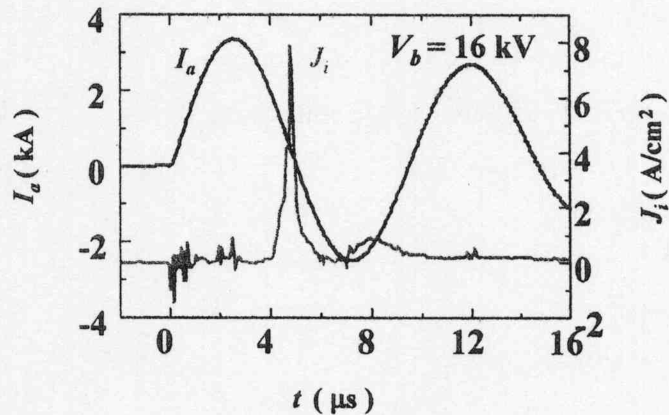

Fig. 10. Typical waveforms of discharge current (I_a) and ion current density (J_i).

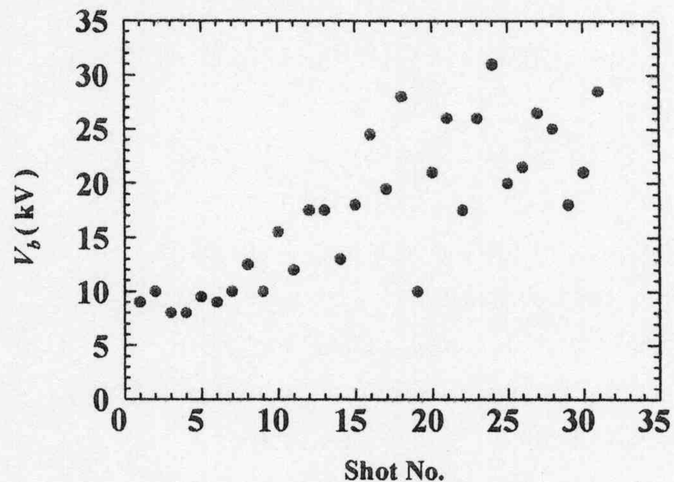

Fig. 11. Dependence of V_b on the shot number.

Figure 10 shows the typical waveforms of discharge current (I_a) and ion current density (J_i) at 29th shot after the exchange of the electrodes. At the shot the electrodes was

self-broken at charging voltage V_b = 16 kV. As seen in the figure sinusoidal waveform of I_a of quarter cycle 2.5 μs, peak current 3.4 kA was observed. 4.8 μs after the rise of I_a, J_i of 8 A/cm^2 was observed with pulse width 240 - 320 ns.

Figure 11 shows the dependence of V_b on the shot number. As seen in the figure the V_b has a strong dependence on the shot number. In the first 7 shots V_b is around 10 kV however, the V_b gradually increases after 7th shot and reaches 30 kV around 25th shot. The V_b still increases and it exceeds the maximum charging voltage of 35 kV after 32nd shot.

To evaluate the drift velocity of the plasma by a time of flight method (TOF), a pair of BIC's is placed. The distances of the BIC's from the discharge gap was 112 and 206 mm, respectively. Figure 12 the result of the evaluation. As seen in the figure TOF delay time τ of 2 μs was observed between the signal of two BIC's, which corresponds the drift velocity of 4.7×10^4 m/s. Assuming the aluminum ions the velocity corresponds to the ion energy of 311 eV.

To apply the ion source to the intense pulsed ion diode synchronized operation of the ion source is required. For the purpose, a trigger able capacitor bank was used with a vacuum discharge ion source, which is shown in Fig. 13. In the system a Blumlein type capacitor bank using two capacitors of 0.5 μF, 35 kV each was used. The geometry of the electrodes and the BIC was same as shown in Fig. 9. The capacitors are pre-charged to 27 kV each before the discharge.

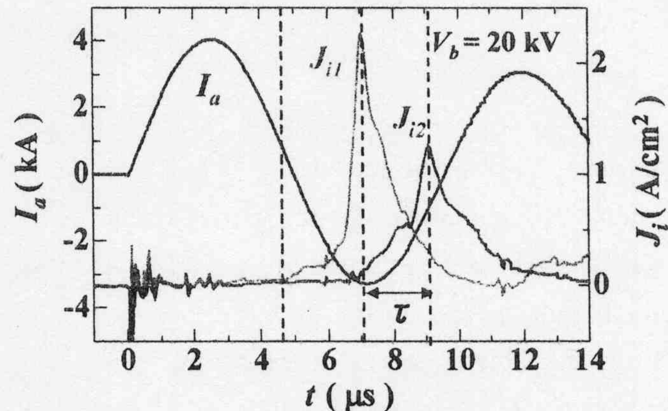

Fig. 12. Result of the time of flight evaluation of the drift velocity of the plasma.

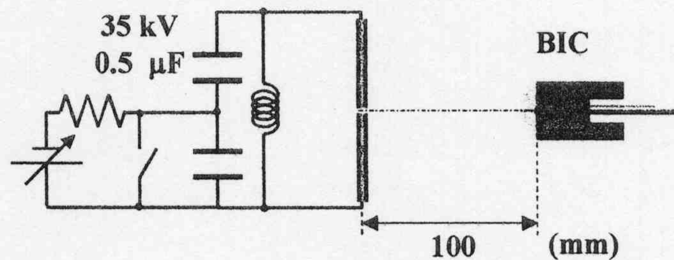

Fig. 13. A vacuum discharge ion source using triggerable capacitor bank.

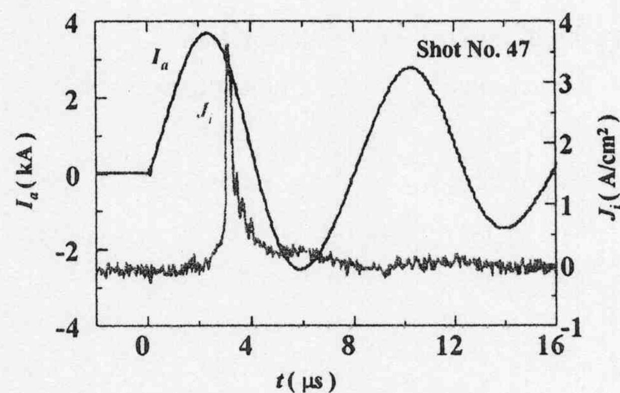

Fig. 14. Typical waveforms of discharge current (I_a) and ion current density (J_i).

Figure 14 shows the typical waveforms of I_a and J_i at 47th shot after the exchange of the electrodes. As seen in the figure I_a has a sinusoidal waveform of current rise time 2.3 μs, peak current 3.7 kA. Ion current density J_i of the plasma was evaluated to be 3.6 A/cm^2 at the point of 100 mm apart from the discharge gap. The arrival time of the plasma at the point is 3.1 μs after the rise of I_a.

5. Summary

To apply PHIB to materials processes purity of the beam is very important. For the purpose a new type of ion beam diode was developed. In the diode a new acceleration gap configuration is used with active ion source of pulsed plasma guns. Two types of plasma guns were developed to generate variety of ion beams, i.e. a gas puff plasma gun and a vacuum arc plasma gun. With the gas puff plasma gun, source plasma of nitrogen ions was produced. The current density of the plasma was evaluated to be ≈ 28 A/cm^2 at 90 mm downstream from the top of the plasma gun. The plasma was injected into the acceleration gap of the diode and the ion diode was successfully operated at diode voltage ≈ 200 kV, diode current ≈ 2.0 kA, pulse duration ≈ 150 ns (FWHM). Ion beam of ion current density ≈ 13 A/cm^2 was obtained at 55 mm downstream from the anode. The energy and species of the beam was evaluated by a Thomson parabola spectrometer and found that N^+ and N^{2+} beam of energy 60-300 keV were accelerated with impurity of protons of energy 60-150 keV. The purity of the nitrogen beam was estimated to be 87 %.

To generate metallic ions vacuum arc plasma gun was developed. The characteristics of the plasma gun were evaluated and source plasma of current density 8 A/cm^2, plasma drift velocity 4.7×10^4 m/s was found to be obtained.

References

1) K. Masugata, Y. Shimizu, Y. Fujioka, I. Kitamura, H. Tanoue, K. Arai "D evelopment of Bipolar-pulse Accelerator for Intense Pulsed Ion Beam Acceleration", Nuclear Instruments & Methods in Physics Research, Section A, (accepted for publication)
2) H.A.Davis, et al., Matelials Chemistry and Physics **54**, pp.213-218 (1998)
3) K. Yatsui, X. Kang, T. Sonegawa, T. Matsuoka, K. Masugata, Y. Shimotori, T. Satoh, S. Furuuchi, Y. Ohashi, T. Takeshita, and H. Yamamoto, "Application of intense pulsed ion beam to materials science" Phys. Plasma **1**(5), pp.1730-1737 (1994).
4) K. Masugata, K. Takao, M. Shiotani, T. Honda, R. Tejima, I. Kitamura, and T. Takahashi Application of Intense Pulsed Ion Beam to Materials Processes, Proc. Int'l Power Modulator Conf., Hollywood, CA, USA, June 30-July3, 2002, pp. 552-555 (2002)

5) K. Masugata, Y. Kawahara, C. Mitsui, I. Kitamura, T. Takahashi, Y. Tanaka, H. Tanoue, K. Arai, Development of Bipolar Accelerator for Pulsed Ion Beam Implantation, ibid, pp.334-337 (2002)
6) E. Chishiro, A. Matsuyama, K. Masugata and K. Yatsui, "Dependence of characteristics of Br-type magnetically insulated diode on configuration of insulation magnetic field", Jpn. J. Appl. Phys., **35**(4A), pp.2350-2355 (1996).
7) K. Masugata, H. Okuda, K. Yatsui and T. Tazima, "Diagnosis of high-brightness ion beams produced in point pinch diodes", J. Appl. Phys. **80**(9) pp. 4813-4818 (1996)
8) I. Brown, "Vacuum arc ion sources" Rev. Sci. Instrum. **65** (10), pp. 3061-3081 (1994)

Droplet Generation Mechanism by Intense Pulsed Ion-Beam Evaporation

Hiroaki Shishido*,[1], Hideki Kawahara[1], Hideki Yanagi[1], Tsuneo Suzuki[1], Takashi Yunogami[1,2], Hisayuki Suematsu[1], Weihua Jiang[1] and Kiyoshi Yatsui[1]

[1]Extreme Energy-Density Research Institute, Nagaoka University of Technology Nagaoka, Niigata 940-2188, Japan

[2] ITEC, Doshisya University, Imadegawa-dori, Kamigyo-ku, Kyoto 602-8580, Japan

ABSTRACT

Droplet generation mechanism was clarified by observing a surface morphology of target which was irradiated by intense pulsed ion-beam evaporation (IBE). A lot of spherical projections were observed on an Al target after ion beam irradiation. The size of these projections was 70 μm in diameter, which was almost the same size as droplets on a thin film. Therefore, it was thought that these projections were the origin of droplets. The droplet generation model was considered as follows. First, the target surface layer was melted by ion beam irradiation. Secondly, the melting layer was waved. Thirdly, spherical projections were formed by surface tension of liquid. Finally, some spherical projections leave the surface, and become droplets. In addition, the objections which are not able to leave the surface solidify were observed. This model was validated by the experimental results of ion beam irradiated Ag and Ti targets.

I. Introduction

When an intense pulsed light ion beam (LIB) is irradiated on a solid target, high-density ablation plasma is generated. Utilizing the plasma, thin films can be deposited on a substrate which is facing the target. This method was termed pulsed ion -beam evaporation (IBE) [1-6]. Various thin films including $B_{12+x}C_{3-x}$ [4], $SrAl_2O_4$: Eu [5] and TiFe [6] were successfully prepared by IBE.

However, many droplets existed on some of thin films prepared by IBE method. The droplet generation becomes a serious problem in other physical vapor deposition method, such as laser ablation methods or ion plating methods, as well as IBE method. Until now, several groups have suggested various approaches to suppress the droplet formation. For example, it was pointed out that the droplet was shielded by a shadow mask placed between the target and the substrate [7]. However, this method has a problem that the film deposition rate is significantly reduced. In other words, physical vapor deposition methods with little droplet at high speed has not be realized. In order to develop the physical vapor deposition method with little droplet at high speed, it is necessary to clarify the droplet generation mechanism.

The purpose of this study is to clarify the droplet generation mechanism of thin films prepared by IBE method. A reason to use IBE method for this study is as follows. In IBE method, the LIB gives a target the very high energy in a short time. As a result, a lot of droplets are generated. Therefore, it is easy to study the droplet generation mechanism in detail compared with other physical vapor deposition method.

To realize the purpose as mentioned above, three kinds of targets, such as Al, Ag, and Ti,

were irradiated by the LIB to prepare thin films. The following experiments were performed. (1) The relation between the surface roughness of target and the decrease in target mass was clarified. (2) The relation between the surface roughness of target and the amount of droplet on the thin film was clarified. (3) Surface morphology of Al target after the LIB irradiation was observed. From the results in the case of Al target, the droplet generation model was proposed in IBE method. This model was applied to explain the number of droplets on thin films prepared using Ag and Ti targets.

II. Experimental details

II-1. Experimental setup

Figure 1 shows the experimental setup of the IBE process. Experiments were carried out using an intense, pulsed power generator, "ETIGO-II [8]." The LIB was produced by a magnetically insulated ion beam diode, where the motion of electrons was insulated by the transverse magnetic field. By using a polyethylene sheet as a flashboard anode, proton content in the LIB was more than 75 %, which was diagnosed with an energy spectrometer. Table I summarizes the experimental conditions. The operating conditions for the ion beam evaporation were accelerating voltage of 1MV (peak), current of 80 kA and pulse width of 70 ns (full width at half-maximum). An Al target was inclined by 30 degrees to the ion beam axis. The distance from anode surface to the target, and the distance from the target to the substrate are defined as d_{AT} and d_{TS} respectively. The thin film preparation chamber was evacuated to $\sim 10^{-4}$ Torr.

Table 2 shows properties of targets. In order to elucidate of droplet generation mechanism, three kind of metals (Al, Ag, Ti) were used for the target.

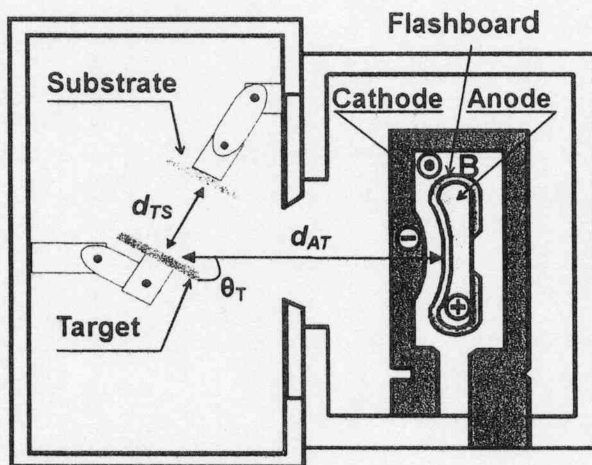

Fig. 1 Schematic of ion beam diode and thin film preparation chambers.

Table I Experimental condition

Accelerating voltage (peak)	1 MV
Pulse width (FWHM)	70 ns
Energy density of ion beam	30 J/cm^2
Ion species	H^+ (75%)
Number of shots	1～10
Pressure	2×10^{-4} Torr
Targets	Al, Ag, Ti
Angle of target (θ_T)	30 deg.
Substarate	Si (100)
Substarate temperature	R.T.
d_{AT}	200 mm
d_{TS}	100 mm

Table II Properties of targets

Material	Range[μm]	Melting point[K]	Boiling point[K]	Thermal conductivity[W/mK]
Al	14.4	933	2793	237
Ag	6.95	1235	2435	429
Ti	10.4	1939	3562	21.9

II-2. Experimental method

For paying attention to the increase in surface roughness of the target by the increase in the number of LIB irradiation, the following experiments were carried out. (1) The Al target before irradiation was observed with an optical microscope and the surface roughness and the target mass were also measured. (2) An Al thin film was prepared on a Si substrate by irradiation of the LIB on the Al target. (3) The irradiated Al target was observed again with the optical microscope. The surface roughness and the target mass were also measured. Ablated mass was calculated from a difference between the target masses before and after the LIB irradiation. (4) The prepared Al thin film was observed with the optical micrograph. (5) A new Si substrate was placed instead of the former substrate. The same Al target was used. The process of (2)-(5) was repeated for 10 times.

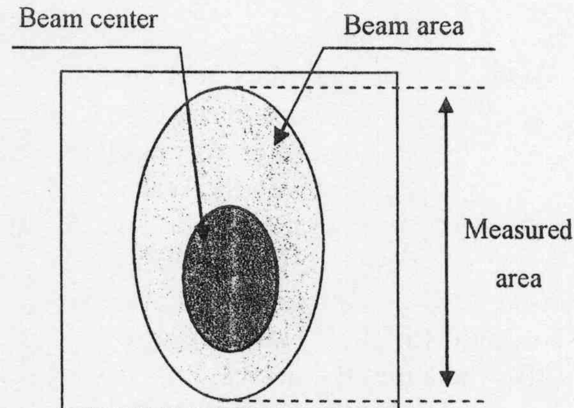

Fig. 2 Area of surface roughness measurements on irradiated target.

The ablated mass was measured using an electronic balance. Figure 2 shows the schematic damage pattern of target irradiated by an LIB. The target roughness (R_a) was measured using a surface profiler. Furthermore, the surface morphology of the ten LIB irradiated Al target observed by a scanning electron microscope (SEM) operated at acceleration voltage of 5.0 kV. The produced thin film was observed by an optical microscope.

III. Experimental results

III-1. Relation between surface roughness of target and number of LIB irradiation

Figure 3 shows the relation between surface roughness of target and the number of LIB irradiation. From this result, in the case of Al target, the surface roughness of the Al target increased linearly with increasing the number of shots. In the case of Ag target, the surface roughness of Ag target increased with increasing the number of shot until 4th shot. However, after 5th LIB irradiation, the surface roughness of Ag target saturated about Ra = 5 μm. Moreover, in the case of Ti target, the surface roughness of Ti target after 5th LIB irradiation also saturated about R_a = 2 μm.

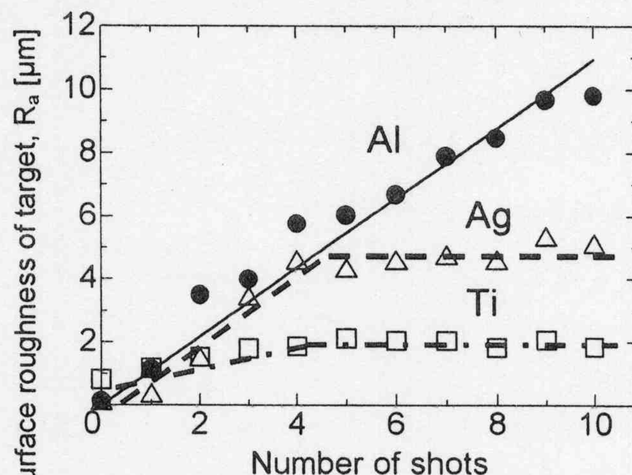

Fig. 3 Target surface roughness as a function of number of LIB irradiations.

Ⅲ-2. Relation between decrease in target mass and number of LIB irradiation

Figure 4 shows the relation between the decrease in target mass and the number of LIB irradiation. In the case of Al target, the decrease in Al target mass increased linearly with increasing the number of shots. In the case of Ag target, the decrease in Ag target mass increased with increasing the number of shot until 4th shot. However, after 5th LIB irradiation, the decrease in Ag target mass saturated (~ 26 mg). In the case of Ti target, the decrease in Ti target mass was constant (~ 8 mg).

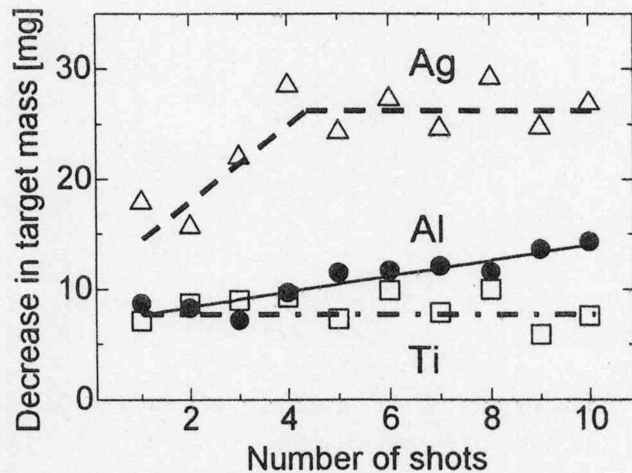

Fig. 4 Decrease in target mass as a function of number of LIB irradiations.

Ⅲ-3. Relation between decrease in target mass and surface roughness of target

From the both results of Figs. 3 and 4, the decrease in target mass was plotted as a function of the surface roughness of the target as in Fig. 5. From Fig. 5, in the case of Al and Ag, the decrease in target mass on one shot increased with increasing the roughness of target (R_a). On the other hand, in the case of Ti target, the above-mentioned phenomenon was not observed.

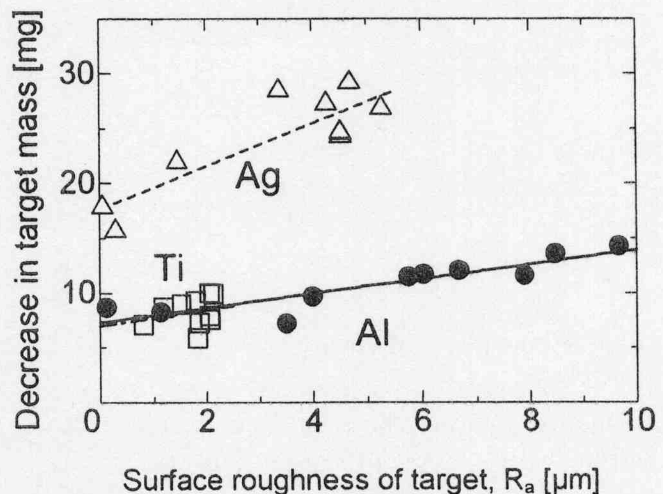

Fig. 5 Decrease in target mass as a function of surface roughness of the target.

Ⅲ-4. Relation between amount of droplet and surface roughness of target

Figure 6 shows optical micrographs on thin films with 1st, 5th and 10th LIB irradiation. From the observation, the huge droplets were observed on the Al thin film. In addition, the number of huge droplets increased with increasing the number of LIB shots. In the case of Ag thin films, the droplet size was smaller than that on the Al thin films. In addition, the number of small droplets increased with increasing the number of LIB shots. In the case of Ti thin film, the droplet was not almost observed.

Moreover, occupied areas of droplets on the Al thin films are shown in Fig. 7. From Fig. 7, in the case of Al thin films, the amount of droplet increased with increasing the number of LIB shots.

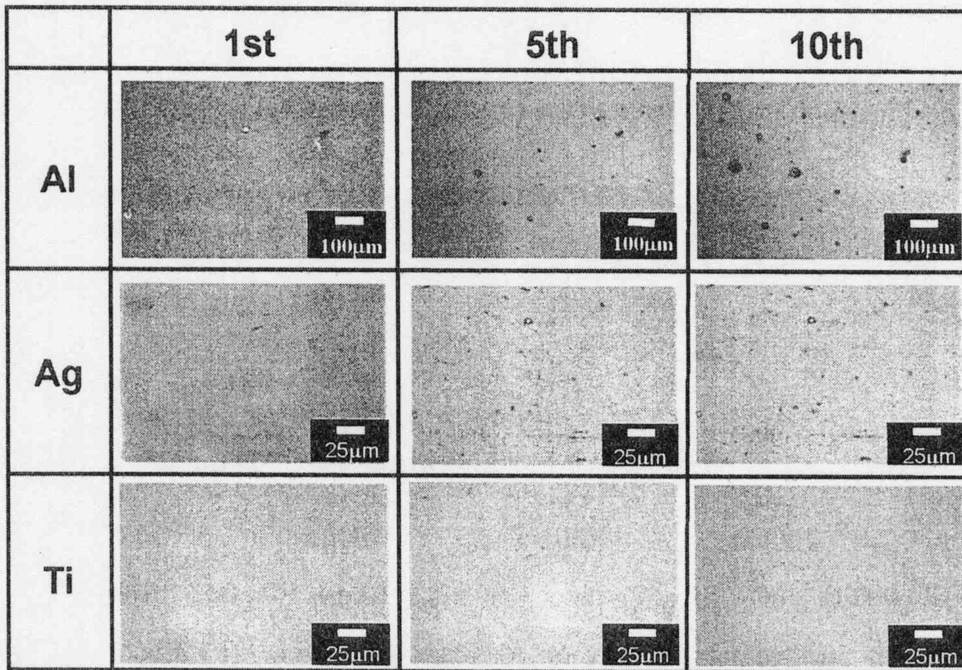

Fig.6 Optical microscope picture of Al thin film

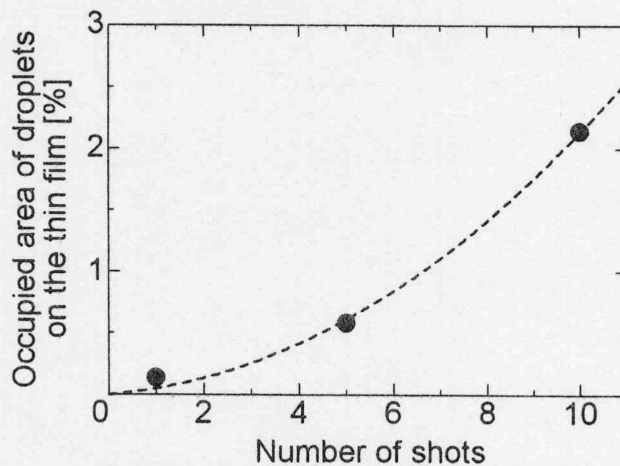

Fig. 7 Occupied areas of droplets on the Al thin films as a function of number of shots..

Ⅲ-5. Surface morphology of the target

Figure 8 shows optical micrographs of Al target surface (a) before, (b) after one, (c) after two and (d) after ten shots of LIB irradiations. As in Fig. 8 (a) the scratches that were produced by polishing as pretreatment was observed. In Fig. 8 (b) the scratches were disappeared and the surface of Al target were wrinkled by an LIB irradiated. In Fig. 8 (c) projections spherical objects appeared. In Fig. 8 (d) the projection of surface became bigger, the spherical objects was seen more clearly. An enlarged optical micrograph of one of the spherical objects is shown in Fig. 9.

A scanning electron micrograph of the spherical objects is shown in Fig. 10. Many

spherical objects exist. Enlarged scanning electron micrograph of this spherical object is shown in Fig. 11. The diameter of the spherical object is about 70 μ m and there are horizontal stripes in the lower half of the spherical object. As shown in Fig. 6, the diameter of droplets on the Al thin film which was prepared at the tenth LIB irradiation was about 10 -50 μm.

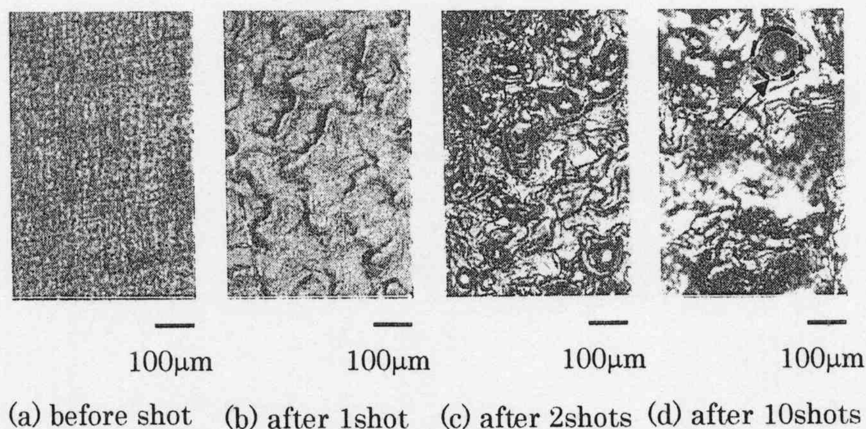

Fig. 8 Surface morphology of Al target (a) before, (b) after one, (c)after two and (d) after ten LIB irradiations.

Fig. 9 Spherical projection on Al target after ten LIB irradiations.

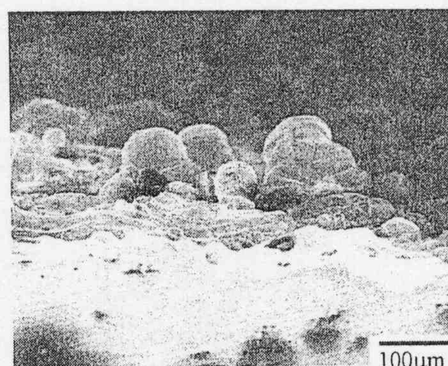

Fig. 10 A scanning electron micrograph of many spherical objects on Al target after ten LIB irradiations.

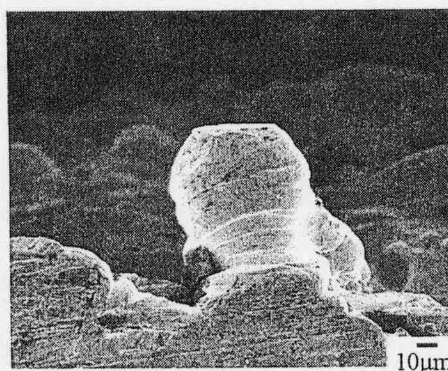

Fig. 11 A scanning electron micrograph of the spherical object on Al target after ten LIB irradiations.

Ⅳ. Discussion

Ⅳ-1. Al droplet generation model

From the above experimental results, the droplet generation mechanism with the Al target was considered.

A model is proposed as shown in Fig. 12. (1) LIB irradiated the Al target. The ion penetrates the target to the depth of the range (14.4 μm) while losing its energy. At the bottom of the range, the ion delivers most of the energy. (2) The energy that the target received is converted into heat. By this heat, the target surface layer melts, boils and generates plasma. The plasma is generated from the bottom of the range so that most of the energy is given to the bottom of the range. (3) When this plasma ablates from the bottom of the range in the target, the melting surface layer is waved. (4) The tip of the wave becomes spherical by surface tension of liquid Al. (5) LIB irradiates again. The ablation plasma is generated from the bottom of the range again. Some spherical objects leave the surface together with the ablation plasma, and become droplets. (6) The objects which are not able to leave the surface solidify, and become spherical objections, which are observed by scanning electron micrograph of target surface after LIB irradiation.

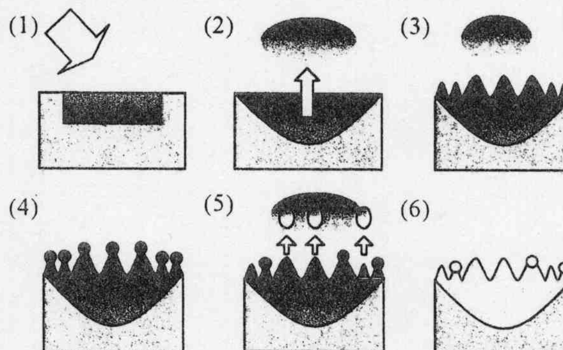

Fig. 12 A model of the droplet generating process on the thin film prepared by IBE. (1) LIB irradiation on a target, (2) melting and evaporating the target, (3) application of recoil from the ablation plasma, (4) splashing of the liquid surface, (5) formation of liquid drops and (6) cooling of the target to form spherical objects on the target.

Ⅳ-2. The validity of this model

In the former section, a droplet generation model on Al thin films prepared by IBE method was proposed. In this section, this model was applied to explain droplet formation process in the preparation of Ag and Ti thin films by IBE method.

According to the above model, when LIB is irradiated onto the target, the surface layer of the target melts, melting layer is waved, the tip of the wave becomes spherical by surface tension, and these spherical objects become droplets.

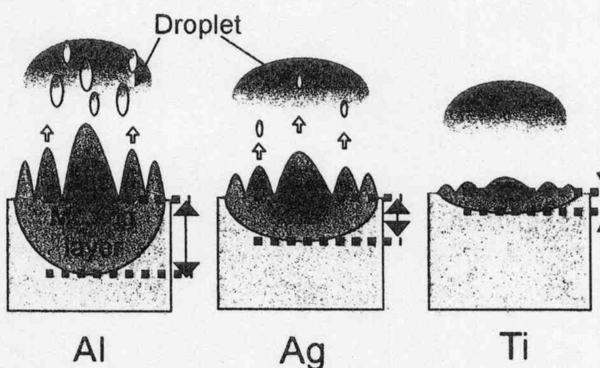

Fig. 13 A model of the melting layer on target surface

It is thought that amplitude of the wave and diameter of the spherical objects increase with increasing the melting layer.

Then, thickness of the melting layer is estimated in the case of Al, Ag and Ti. First, melting point of each material is compared (Ti : 1939 [K] > Ag : 1263 [K] > Al : 933 [K]). Secondaly, ion range of each material are compared (Al : 14.4 [μm] > Ti : 10.4 [μm] > Ag : 6.95 [μm]). Finally, thermal conductivity of each material are compared (Ag : 429 [W/mK] > Al : 237 [W/mK] > Ti : 21.9 [W/mK]).

The range of proton in Al is the longest, while, the melting point of Al is the lowest. Therefore, Al is easy to melt. It is thought that the melting layer of Al is the thickest. On the other hand, the melting point of Ti is the highest and the thermal conductivity of Ti is the lowest. Therefore, it is thought that the melting layer of Ti is the thinnest though the range of Ti is bigger than the range of Ag.

As the result, order of the melting layer thickness is as follows; Al>Ag>Ti. Therefore, the order of size of droplets should follow the same order, too, as shown in Fig. 13.

From Fig. 6, it is known that the droplet of Al is the biggest, the droplet of Ag is smaller than Al, and there are few droplets in the case of Ti. It was concluded that this model may be proven by the above-mentioned consideration.

V. Concluding remarks

LIB irradiates on the three kind of targets (Al, Ag, and Ti) in order to elucidate droplet generation mechanism in IBE method.

(1) In the case of Al and Ag, the decrease in the target mass increased with increasing the surface roughness of the target. On the other hand, in the case of Ti, even if the target was irradiated by LIB, the surface roughness does not change.

(2) In the case of Al, big droplets which are 10 -50 μm in size was generated. The number of big droplets increased with increasing the LIB shot. In the case of Ag, the droplet generated from Ag target was smaller than that generated from Al target. The number of small droplet increased with increasing the LIB shot, too. In the case of Ti, the droplets were not generated.

(3) After LIB irradiation on the Al target, surface morphology was changed. When LIB was irradiated, at first, the surface wrinkled. With increasing the number of LIB shot, the wrinkle grew big, and the spherical projections were generated on the target. The size of spherical projection was 70μm in diameter, it was almost the same size as droplets.

(4) It was thought that these spherical objections were the origin of droplets. The droplet generation model was considered as follows. First, the target surface layer was melted by ion beam irradiation. Second, the melting layer was waved. Third, spherical objects were formed by surface tension of liquid. Fourth, some spherical objects leave the surface, and become droplets. The objections which were not able to leave the surface were solidified, and were left on the target surface.

(5) According to the above model, a high-amplitude wave should be formed when the melting layer is thick, and spherical objection formed by surface tension should be big when the amplitude of wave is large. The order of the melting layer thickness is as follows; Al>Ag>Ti. Therefore, size of droplet should follow the same order, too, as shown in Fig. 13.

References

[1] Y. Shimotori, M. Yokoyama, H. Isobe, S. Harada, K. Masugata and K. Yatsui, *J. Appl. Phys.*, **63,** 968-970 (1988).

[2] Y. Shimotori, M. Yokoyama, S. Harada, K. Masugata and K. Yatsui, *Jpn. J. Appl. Phys.*, **28,** 468-472 (1989).

[3] K. Yatsui, *Laser and Particle Beams*, vol. **3,**part 2, 119-155 (1989).

[4] K. Kitajima, T. Suzuki, W. Jiang and K. Yatsui, *Jpn. J. Appl. Phys.*, **40**, 1030-1034 (2001).

[5] M. Sengiku, Y. Oda, W. Jiang, K. Yatsui, Y. Ogura, K. Kato, K. Shinbo and F. Kaneko, *Jpn. J. Appl. Phys.*, **40,** 1035-1037 (2001).

[6] T. Suzuki, T. Saikusa, H. Suematsu, W. Jiang and K.Yatsui, *Transactions of the Materials Research Society of Japan* **28**[2] 433-435 (2003).

[7] M. Tachiki and T. Kobayashi, *Jpn. J. Appl. Phys.*, **38**, 3642-3645 (1999).
[8] A. Tokuchi, N.Nakamura, T. Kunimatsu, N. Ninomiya, M. Den, Y. Akira, K. Masugata, and K. Yatsui, Proc. 2nd Int'l Top. Symp. on ICF Res. by High-Power Particle Beams, ed. K. Yatsui, 430 (1986).

DIESEL FLUE GAS TREATMENT BY PULSED, INTENSE RELATIVISTIC ELECTRON BEAM

Go Imada*, Tomoki Sakurai, and Kiyoshi Yatsui

Extreme Energy-Density Research Institute, Nagaoka University of Technology
Nagaoka, Niigata 940-2188, JAPAN
*e-mail: imada@nagaokaut.ac.jp

ABSTRACT

Diesel flue gas in a chamber spatially isolated from electron-beam source has been treated by pulsed, intense relativistic electron beam (IREB). The chamber is filled up with the diesel flue gas, and is irradiated by IREB (2 MV, 2.6 kA, 95 ns (FWHM)). The diesel flue gas is supplied from a diesel generator (3 kVA) with and without 1.3-kW load. When the flue gas exhausted from the diesel generator without load is irradiated by firing 10 shots of IREB, the concentration of NO_x, SO_2, and CO are decreased from 77, 14, and 770 ppm to 5, 11, and 690 ppm, respectively. It is found that ~ 96 % of NO_x is removed by firing 10 shots of IREB with the load of 1.3 kW in the diesel generator. The reduction of CO_2 has not been observed in this experiment.

I. Introduction

NO_x (Nitrogen oxide; NO (nitric monoxide) and NO_2 (nitric dioxide)) and SO_2 (sulfur dioxide) have induced acid rain that causes environmental problem in the earth such as deforestation. To reduce the NO_x and SO_2 in atmosphere, flue gas treatment by electron beam has been attracting attention. Pulsed, intense relativistic electron beam (IREB), in particular, is a promising candidate for the electron beam source of the gas treatment due to the high current density and the long range. For example, the range of IREB at 2 MeV is calculated to be ~ 9 m in atmosphere[(1)]. Therefore, the IREB irradiation is able to apply to flue gas treatment in long chimney and tunnel.

In previous research, dry-N_2/O_2-balanced NO_x gas mixture has been successfully treated by the IREB irradiation within a long chamber and a chamber spatially isolated from electron beam source[(2,3)]. However, there is very little data on NO_x and SO_2 treatment by IREB irradiation in diesel flue gas which contains a lot of components such as NO_x, SO_2, H_2O (water vapor), HC (hydrocarbon), CO (carbon monoxide), and CO_2 (carbon dioxide).

In this study, the diesel-flue-gas treatment within distant gas chamber spatially isolated from the IREB source has been demonstrated. The diesel flue gas is supplied from a diesel generator (3 kVA), and is irradiated by the IREB passing through a 1.6-m-long room air. In the above-mentioned experiments, a pulsed-power generator, "ETIGO-III" is used for generating the IREB.

II. Principle of flue gas treatment by electron beam

Figure 1 shows the process diagram of NO_x and SO_2 treatment by electron beam(4). The diesel flue gas generated by the combustion of light oil consists of principal species of N_2 (nitrogen), O_2 (oxygen), CO_2, and H_2O, and a little dose of poisonous species such as CO, NO_x, and SO_2. These species are ionized and dissociated by irradiation of the electron (*e*), and then the free radicals (*e.g.* N, O, OH, HO_2, and S) will be generated. The NO_x and SO_2 are resolved by the collision with the free radical species into N_2 and O_2. In this treatment process, unfortunately, HNO_3 (nitric acid) and H_2SO_4 (sulfuric acid) are produced as by-products. If adding NH_3 (ammonia) into the flue gas, HNO_3 and H_2SO_4 are converted into NH_4NO_3 (ammonium nitrate) and $(NH_4)_2SO_4$ (ammonium sulfate) which can be used as a chemical manure for agriculture.

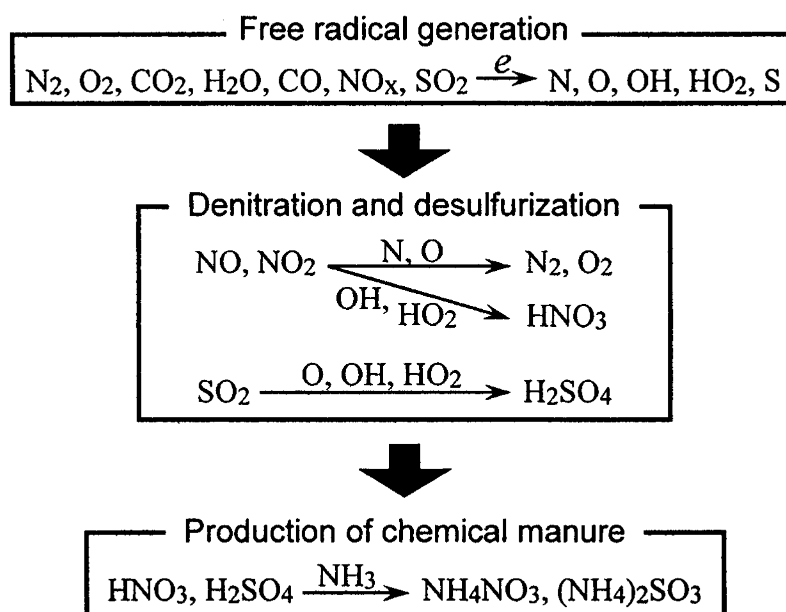

Fig. 1 Process diagram of NO_x and SO_2 treatment by electron beam.

III. Experimental apparatus

Figure 2 shows the schematic diagram of pulsed-power generator, "ETIGO-III"(5). It consists of a Marx generator, a pulse forming line, and induction acceleration cells of four stages. The output voltage of the pulse forming line is ~ 670 kV, which is fed to the four acceleration cells through the transmission lines in parallel. Three amorphous-metallic magnetic cores are installed in each cell, producing approximately 2 MV per cell (670 kV×3). The electron beam with the energy up to 2 MeV is generated by an electron-beam diode set at the first acceleration cell. The field-emission foilless diode with a hollow cathode is used to generate the electron beam. The inner and outer diameters of the hollow cathode are 59.5 mm and 60 mm, respectively. This electron beam is accelerated by each acceleration cell, and the maximum energy of the IREB increases up to ~ 8 MeV. In this study, the first acceleration cell is used as an IREB source for the diesel-flue-gas treatment.

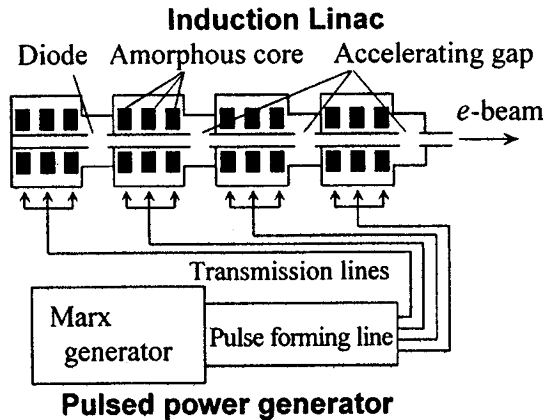

Fig. 2 Schematic diagram of "ETIGO-III".

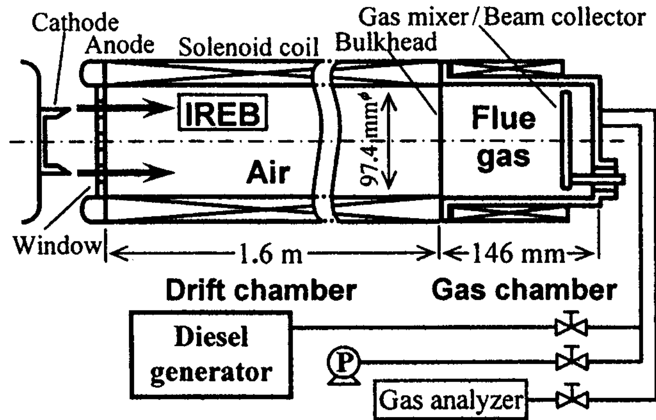

Fig. 3 Cross-sectional view of flue gas treatment chamber.

Figure 3 shows the cross-sectional view of flue gas treatment chamber. It consists of an electron-beam diode, window, drift chamber, bulkhead, gas chamber, external magnetic field, gas mixer, and gas system. The gas chamber is made of a stainless-steel pipe with the volume of ~ 1.1 ℓ. After the gas chamber is evacuated to ~ 20 Pa by the rotary vacuum pump, it is filled up with a diesel flue gas with the pressure of 200 kPa. The diesel flue gas is supplied from a diesel generator (KDG3500E-BL, Komatsu Ltd.) with and without 1.3-kW load. The IREB generated by "ETIGO-III" is injected into the gas chamber through not only the window and bulkhead but also the 1.6-m-long drift chamber filled up with room air. The window consists of a titanium foil with the thickness of 40 μm and a stainless-steel honeycomb flange with the optical transparency of ~ 53 %. The IREB is guided by an external, axial magnetic field (~ 0.5 T) through the drift chamber and gas chamber. At the IREB energy of 2 MeV, the kinetic-energy loss of the electron through the titanium foil and the 1.6-m-long room air are calculated to be ~ 26 keV and ~ 447 keV, respectively[(1)], where the path length of the electron in the air is estimated to be 2.2 m because the trajectory of the electron becomes helical in the axial magnetic field. The concentrations of NO, NO_2, SO_2, CO, CO_2, and O_2 in the flue gas are measured by a controlled potential-electrolysis gas analyzer (GSV-350M/XL, testo AG) after mixing up the gas mixture for 3 minutes.

IV. Results and Discussion

(a) Accelerating voltage and current of IREB

Figure 4 shows the typical time evolution of acceleration voltage of IREB (V_a) and IREB current (I_b and I_c), where I_b and I_c are measured by a Faraday cup with a Rogowski coil placed at the inlet of the drift chamber and the gas chamber, respectively. It is found that the IREB propagates up to the gas chamber. At $V_a \sim 2$ MV, however, we found that the peak current of the IREB decreases form $I_b \sim 2.6$ kA to $I_c \sim 0.1$ kA due to the kinetic-energy loss and scattering of the electrons within the window, bulkhead, and air. It does not matter in practical application, because part of current loss is effective for the flue gas treatment if the drift chamber is also filled up with the flue gas. The pulse width of I_b and I_c are estimated to

Table I Composition of flue gas generated by diesel generator.

Species	Load of generator none	1.3 kW
NO	45 ppm	192 ppm
NO_2	30 "	63 "
SO_2	14 "	6 "
CO	770 "	401 "
CO_2	1.5 %	2.9 %
O_2	18.5 "	16.0 "

be ~ 95 and ~ 65 ns (FWHM), respectively. It indicates that the electrons, which have the kinetic energy less than the energy loss in the window, bulkhead, and 1.6-m-long air, may not arrive in the gas chamber.

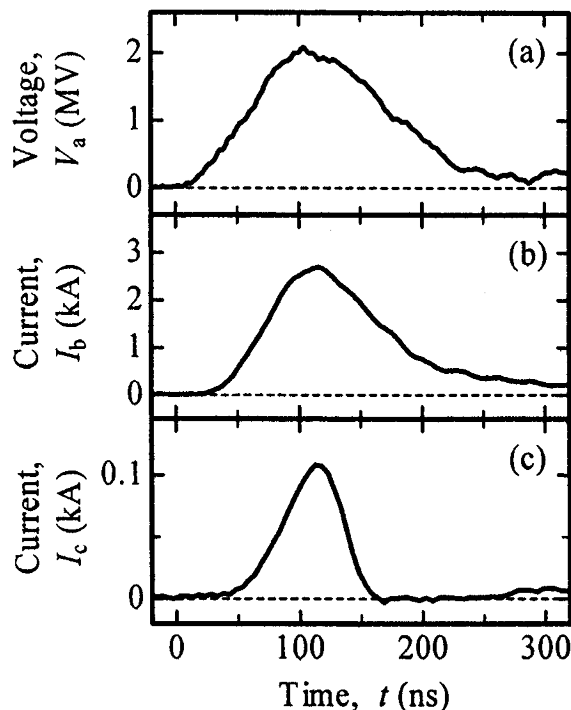

Fig. 4 Time evolution of IREB acceleration voltage V_a (a), IREB current at drift chamber I_b (b), and IREB current at gas chamber I_c (c).

(b) Composition of flue gas generated by diesel generator

Table I summarizes the composition of flue gas generated by the diesel generator with and without 1.3-kW load. It is found that the concentrations of NO and NO_2 increase with connecting the load to the diesel generator. Since the number of revolution of diesel engine will be increased by connecting the load, the temperature in the combustion chamber of the diesel engine rises. It induces to activate the chemical reactions of NO_x generation such as $N_2 + O_2 \rightarrow 2NO$ and $2NO + O_2 \rightarrow NO_2$.

(c) Treatment of diesel flue gas by IREB irradiation

Figure 5 shows the concentrations of NO_x (sum of NO and NO_2), SO_2, CO, and CO_2 in the diesel flue gas as a function of number of IREB irradiation in cases without and with the 1.3-kW load of the diesel generator. It is found that the concentrations of NO_x are successfully reduced by irradiating the IREB regardless of the load of the diesel generator. We also found that ~ 94 and ~ 96 % of NO_x are treated by firing 10 shots of the IREB irradiation in cases with and without the 1.3-kW load of the diesel generator, respectively. Although concentration of SO_2 decreases from 14 to 11 ppm by firing 10 shots of IREB irradiation in case without the load, the SO_2 is not treated by the IREB irradiation in case with the 1.3-kW load. The detailed discussion of this characteristic is found later (see Chap. IV (d)). We can not recognize the treatments of CO and CO_2 in our experimental conditions except for the

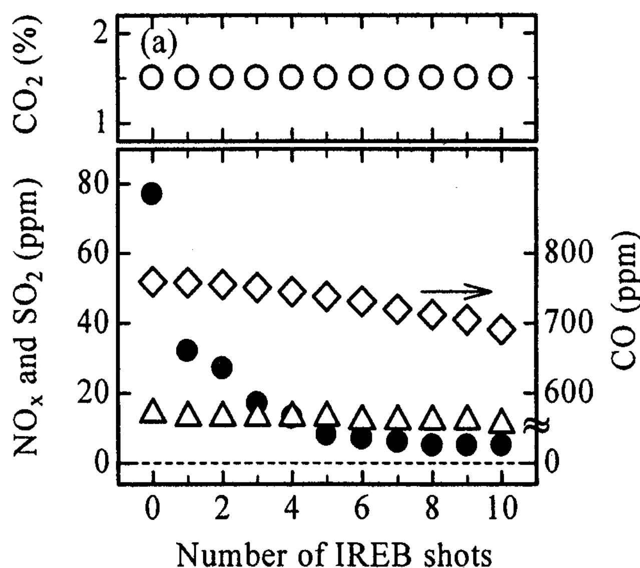

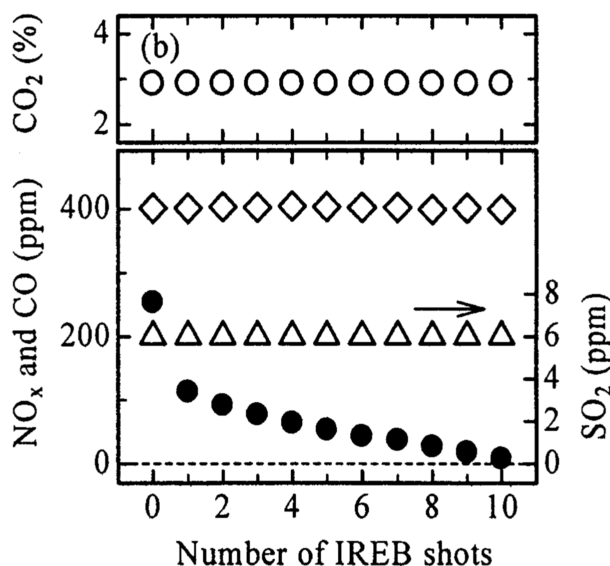

Fig. 5 Concentrations of NO_x, SO_2, CO, and CO_2 as a function of number of IREB shot in cases without load (a) and with 1.3-kW load (b) of diesel generator. ●: NO_x, △: SO_2, ◇: CO, and ○: CO_2.

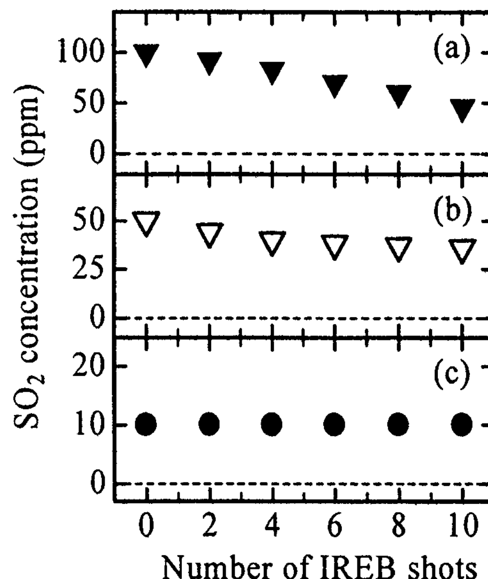

Fig. 6 Concentration of SO_2 as a function of number of IREB shot at various initial SO_2 concentrations of simulated flue gas (σ). (a) σ = 100 ppm, (b) σ = 50 ppm, (c) σ = 10 ppm.

CO treatment in case without the load of the diesel generator.

(d) Characteristics of SO_2 treatment by IREB irradiation

The SO_2 is not treated by the IREB irradiation in case with the 1.3-kW load of the diesel generator. The characteristics of SO_2 treatment seem to depend on the composition of the flue gas. Therefore, the characteristics of SO_2 treatment are investigated by using various simulated flue gases having the initial SO_2 concentrations of σ = 10, 50, and 100 ppm. The simulated flue gases are the dry-N_2/O_2-balanced SO_2 gas mixture with the composition of N_2 : O_2 = 8 : 2, and are made by the commercial cylinder gases which have no impurities.

Figure 6 shows the concentration of SO_2 as a function of number of the IREB shot at various initial SO_2 concentrations of simulated flue gas. It is found that the concentration of SO_2 decreases with every shot of the IREB irradiation at σ = 100 and 50 ppm. At σ = 10 ppm, on the other hand, the concentration of SO_2 does not decrease in spite of irradiating the IREB. These results prove that the characteristics of SO_2 treatment by the IREB irradiation

depend strongly on the initial concentration of SO_2 in the diesel flue gas.

(e) Characteristics of NO_x treatment in diesel flue gas by IREB irradiation

It is found form Fig. 5 that the concentration of NO_x decreases dramatically at the first two shots of IREB irradiation, and then that decreases slightly as the number of IREB shot increases. It is known that OH (hydroxyl radical) is efficient to treat the NO_x. Here, OH is generated by the collision between electron and H_2O molecule which is contained within the diesel flue gas[(6)]. Table II shows the typical reaction rate constant of NO_x treatment in diesel flue gas. It is found that the reactions concerned with OH, Reaction (1) and (2), have a high rate constant in comparison with the other reactions. The rate constants of Reaction (1) and (2) are of the order of 10^{-11} – 10^{-10} cm³/s. To confirm the effects of OH (*i.e.* H_2O) for the sudden NO_x reduction at the first

Table III Composition of simulated flue gas.

	Gas A	*Gas B*
NO	44 ppm	180 ppm
NO_2	35 〃	63 〃
SO_2	14 〃	6 〃
CO	760 〃	400 〃
CO_2	1.5 %	2.9 %
O_2	18.5 %	16.0 %
N_2	balanced	
H_2O	insignificant	
HC	none	

Table II Typical reaction rate constant of NO_x treatment in diesel flue gas.

	Reaction	Rate constant k (cm³/s)	Ref.	
(1)	$OH + NO \rightarrow HNO_2$	1.2×10^{-11}	7	
(2)	$OH + NO_2 + N_2 \rightarrow HNO_3 + N_2$	1.3×10^{-10}	8	*
(3)	$NO + NO_2 + N_2 \rightarrow N_2O_3 + N_2$	1.5×10^{-14}	9	*
(4)	$O + NO \rightarrow O_2 + N$	5.3×10^{-14}	10	
(5)	$N + NO \rightarrow N_2 + O$	1.9×10^{-11}	11	
(6)	$O_3 + NO_2 \rightarrow O_2 + NO_3$	3.5×10^{-17}	12	
(7)	$H_2O + NO + NO_2 \rightarrow 2HNO_2$	2.2×10^{-20}	13	*

* Since it is three-body reaction, the unit of the rate constant is reduced to two-body reaction where the number density of the third body is assumed to be 4.9×10^{19} particles/cm³ (200 kPa, 293 K).

two shots of IREB irradiation, the characteristics of NO_x treatment are investigated by using various simulated flue gases which have the insignificant amount of H_2O. The compositions of simulated flue gas are summarized in Table III. Here, *Gas A* and *Gas B* are simulated as the diesel flue gases with and without 1.3-kW load of the diesel generator, respectively. The simulated flue gases are the dry-N_2-balanced gas mixture, and are made by the commercial cylinder gases which have no impurities.

Figure 7 shows the concentrations of NO_x as a function of number of the IREB shot on the simulated gases (*Gas A* and *Gas B*) having the insignificant amount of H_2O, where the results for the diesel flue gas are also plotted. It is found that the quantities of NO_x reduction (ε) in the diesel flue gas are larger in comparison with those in the simulated gas at the first two shots of IREB. In the diesel flue gas in case with the 1.3-kW load, in particular, ε becomes twice in comparison with that in *Gas B*. It becomes clear from these experimental results and the theoretical knowledge on the rate constants mentioned above that the sudden reduction of NO_x at the first two shots of the IREB irradiation is caused by the effect of H_2O. Since the H_2O in the diesel flue gas is consumed in the first two shots of the IREB irradiation,

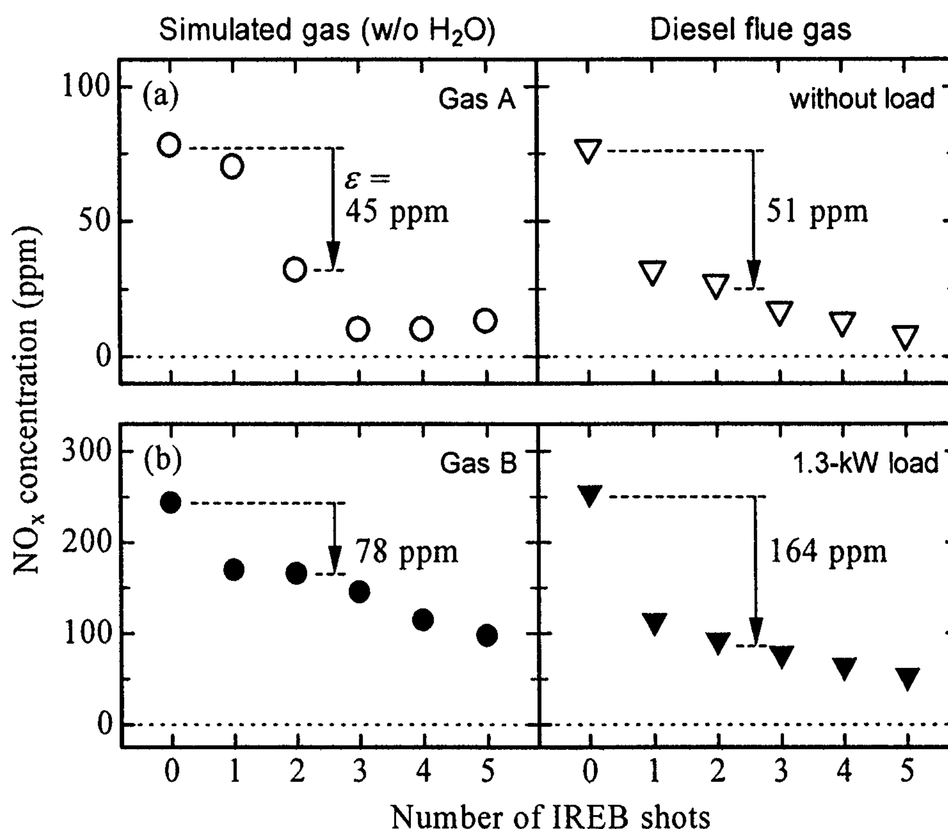

Fig. 7 Concentrations of NO_x as a function of number of IREB shot on simulated gases *Gas A* (a) and *Gas B* (b). Comparison between simulated gas (without H_2O) and diesel flue gas in cases without and with 1.3-kW load of diesel generator.

the concentration of NO_X tends to decrease slightly as the number of IREB shot increases after the third shot of the IREB irradiation.

V. Conclusions

Conclusions obtained from the studies of the treatment of diesel flue gas by the IREB irradiation can be summarized as follows.

(1) The poisonous species (NO_X, SO_2, and CO) in the flue gas generated by the diesel generator have been successfully treated by the IREB irradiation (2 MV, 2.6 kA, 95 ns (FWHM)) at the chamber 1.6-m isolated from the IREB source. We have obtained that 94-96 % of NO_X is removed by firing 10 shots of the IREB.

(2) The characteristics of SO_2 treatment by the IREB irradiation depend strongly on the initial concentration of SO_2 in the diesel flue gas.

(3) The sudden reduction of NO_X at the first two shots of the IREB irradiation is caused by the effect of H_2O in the diesel flue gas.

Acknowledgements

This work was supported in part by the Ministry of Education, Culture, Sports, Science, and technology in Japan under a Grant-in-Aid for the Scientific Research.

References

(1) M. Berger, S. Couresy, and A. Zucker: ESTAR; Computer program for calculating stopping-power and range tables for electrons (Ver. 1.21), Nat. Inst. Standards and Technol., Gaithersburg, MD., [Online Available: http://phisics.nist.gov/Star] (1999).

(2) G. Imada and K. Yatsui: *IEEJ Trans. FM*, **122**, 302 (2002) [in Japanese].

(3) G. Imada and K. Yatsui: *IEEE Trans. Plasma Sci.*, **31**, 295 (2003).

(4) T. Kojima: *OYO-BUTURI*, **72**, 405 (2003) [in Japanese].

(5) A. Tokuchi, N. Ninomiya, K. Yatsui, G. Imada, Q. Zhu, W. Jiang, and K. Masugata: *Proc. 12th Int'l Conf. on High-Power Particle Beams* (Haifa, Israel, June 1998), **1**, 175 (1998).

(6) A. Chminelewski, Y. Sun, Z. Zimek, S. Bulka, and J. Licki: *Radiation Phys. Chem.*, **65**, 397 (2002).

(7) R. Cox, R. Derwent, and P. Holt: *J. Chem. Soc. Faraday Trans.*, **72**, 2031 (1976).

(8) W. Demore, S. Sander, D. Golden, R. Hampson, M. Howard, A. Ravishankara, C. Kold, and M. Molina: *JPL Publication*, 97-4, 1 (1997).

(9) R. Atkinson, D. Baulch, R. Cox, R. Hampson, J. Kerr, M. Rossi, and J. Troe: *J. Phys. Chem. Ref. Data*, **26**, 1329 (1997).

(10) W. Tsang and T. Herron: *J. Phys. Chem. Ref. Data*, **20**, 609 (1991).

(11) K. Sugawara, K. Ishikawa, and S. Sato: *Bull. Chem. Soc. Jpn.*, **53**, 3159 (1980).

(12) R. Cox and G. Coker: *J. Atmos. Chem.*, **1**, 53 (1983).

(13) W. Kaiser and H. Wu: *J. Phys. Chem.*, **81**, 1701 (1977).

Pulsed Operation of an Inertial Electrostatic Confinement Fusion Device and its Applications

Kunihiko Tomiyasu, Kunihito Yamauchi, Atsushi Tashiro,
Masato Watanabe, Akitoshi Okino, Toshiyuki Kohno, Eiki Hotta

Department of Energy Sciences, Tokyo Institute of Technology
Nagatsuta 4259, Midori-ku, Yokohama 226-8502, Japan

ABSTRACT

An Inertial Electrostatic Confinement Fusion (IECF) device is a compact fusion neutron/proton source with an extremely simple configuration, and a project using IECF neutron source for landmine detection is ongoing now. In this paper, a new power system taken a pulse forming into account is suggested, and a number of fundamental discharge characteristics of pulsed IECF operation was yielded up using the fabricated power supply system. The validity of this new system was proved, and the neutron production rate has increased to 1.25×10^8 n/s at 48.3 kV and 6.2 A of short-pulse operation, and a prospect of success to achieve $> 10^8$ n/s, which is required for landmine detection, was cleared up.

I. Introduction

Inertial Electrostatic Confinement Fusion (IECF) is a scheme to confine ions electrostatically with two spherical electrodes. Ions are accelerated toward the origin with sufficient energy to cause fusion reactions, and recirculate inside the anode through a highly transparent grid cathode (see Fig. 1). Because of such a simple configuration and compactness of the device, IECF is expected to be a safe, portable, and well controllable neutron source as a near-term application.

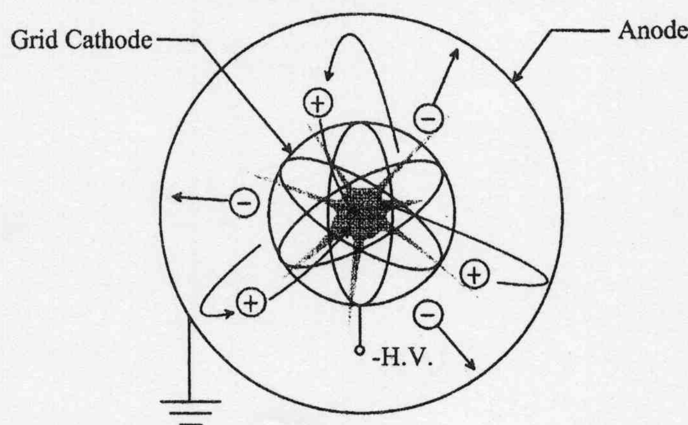

Figure 1: Principle of Inertial Electrostatic Confinement Fusion

Now, a project, which is making use of IECF neutron source on landmine detection, is ongoing in cooperation with other institutes. It is one of the projects for developing humanitarian demining

technologies supported by Japan Science and Technology Agency. In this project, our research group, Tokyo Tech., in charge of developing a high voltage pulse and DC power supply system for IECF neutron source. Hence the object of this work is to develop such a power supply system where pulse forming is taken into account, and to reveal the characteristics of pulsed IECF operation using the fabricated system are focused on this paper.

I.A. Principle of Landmine Detection using Neutron

It is possible to detect landmines by taking advantage of back-scattering reaction and/or neutron capture reaction on hydrogen and nitrogen in the explosives of landmines (see Fig. 2).

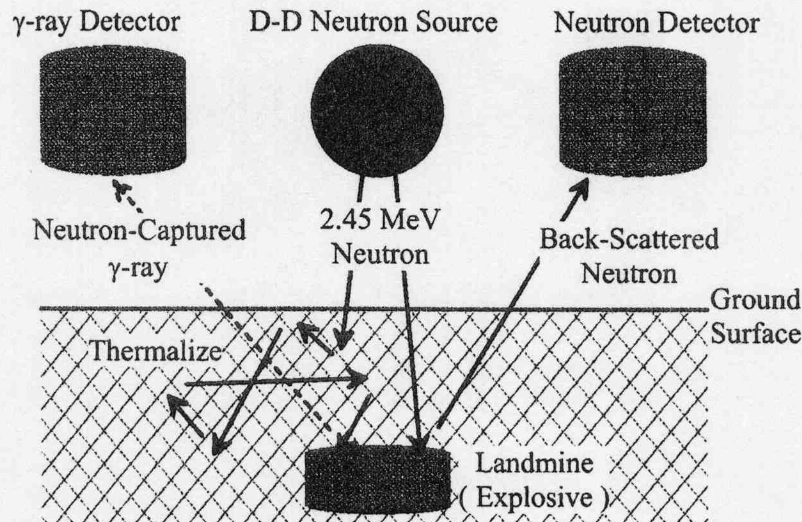

Figure 2: Principle of Landmine Detection using Neutron [1]

The existence of landmines are determined via detecting the back scattered neutron on the hydrogen because landmines are rich in hydrogen. Also, the kind of explosives can be identified by detecting neutron-capture γ-ray on hydrogen and nitrogen, and analyzing the ratio of them because the atomic ratio of explosives is fixed (see Table 1).

Table 1: Atomic Ratio of Major Explosives

explosive	Atom			
	H	C	N	O
TNT	3	7	3	6
Pentrite	8	5	4	12
Hexogen	2	1	2	2
Ammonium nitrite	4	–	2	3

In addition to determining the existence and identifying landmines, it is also possible to know how deep the landmines are buried by using pulsed neutron flux. While the cross section of neutron capture reaction is larger for thermal neutron, the time when the thermal neutron flux reaches a peak depends on the depth where the landmines are. Hence, the depth is estimated by measuring the time evolution of the neutron-capture γ-ray or back scattered neutron.

II. Experimental Setup

Figure 3 shows an experimental setup of this work. A spherical gridded cathode and a mesh–type spherical anode, which diameters are 70 mm and 300 mm, respectively, are set in the center of a cylindrical vacuum chamber which diameter is 450 mm and is 300 mm high. It is connected to a power supply system through a 30-m coaxial cable. The power supply system is composed of a CVCC power supply, a storage capacitor, four ballast resisters, and two high voltage semiconductor switches (SSW1 and 2). A high voltage pulse is applied to the cathode by discharging the storage capacitor via SSW1.

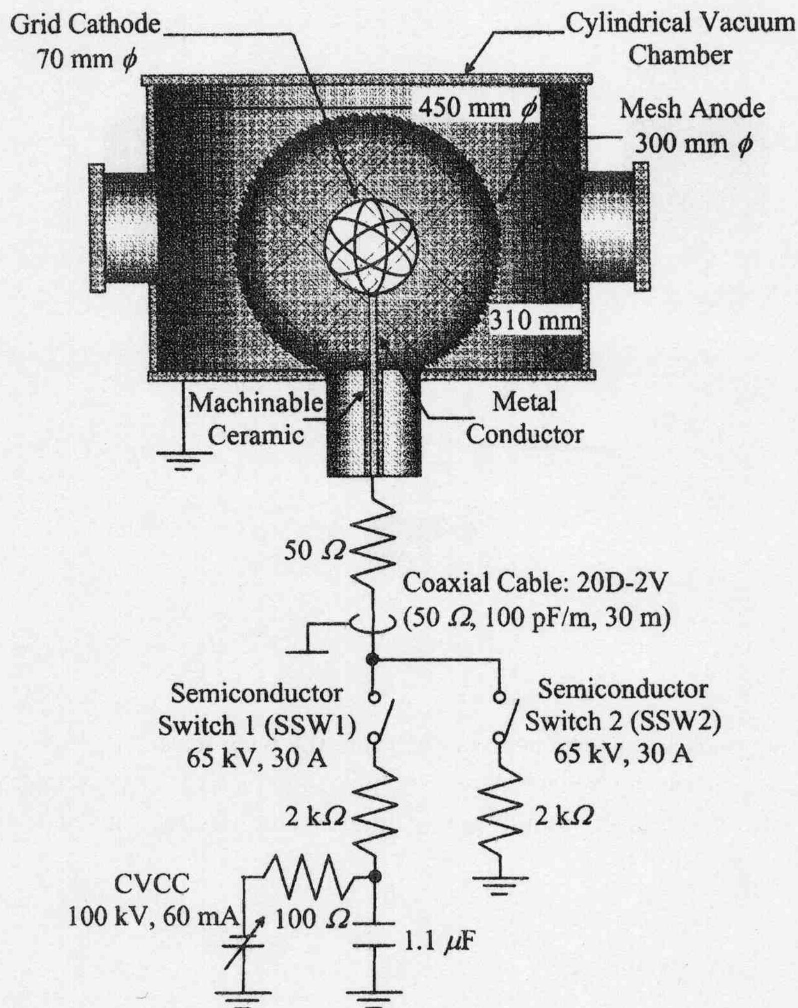

Figure 3: Schematic of an IECF device

In the former power supply system which consists of just one SSW, however, an afterglow shows up as the SSW turns off because the coaxial cable, which connects the chamber and power supply system, discharges through the cathode. Then another semiconductor switch (SSW2) was added to a new power supply system to degrade such an afterglow and to generate rectangular discharge waveforms. As the SSW2 turns on when the SSW1 turns off, the coaxial cable discharges through SSW2 and an afterglow is to be degraded.

III. Results and Discussion

III.A. Evaluation of Power Supply System

Validity of a suggested power supply system was evaluated by way of comparing the current and voltage waveforms of each system. Figures 4 and 5 show the waveforms of discharge current and cathode voltage for hydrogen discharge at 14.0 mTorr. Charging voltage of the capacitor is 20.0 kV.

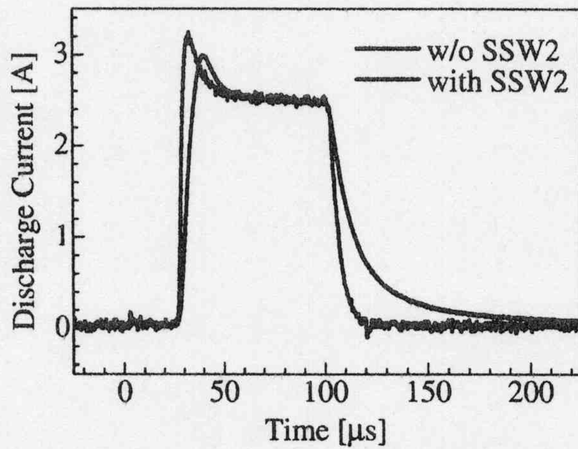

Figure 4: Comparison of Discharge Current Waveform

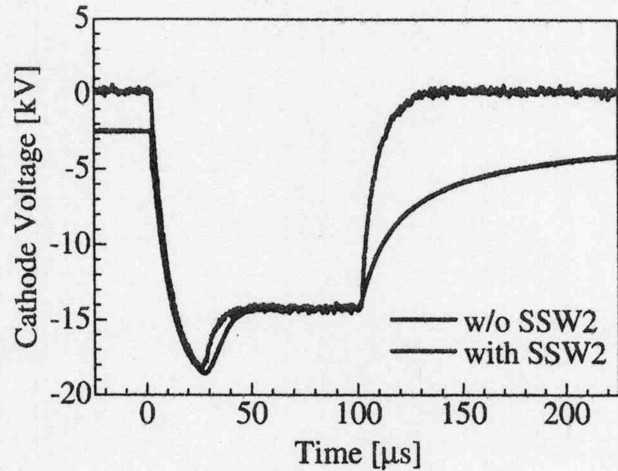

Figure 5: Comparison of Cathode Voltage Waveform

By the improvement of the power supply system, both discharge current and cathode voltage fall down faster as the SSW1 turns off. Comparing the fall time in discharge current, it is shortened from 46.2 μs to 10.0 μs. Hence, the validity of the power supply system was confirmed.

III.B. Discharge Characteristics of Pulsed IECF

Figure 6 shows the I–V characteristic in pulsed operation of IECF Device. Peak current increases with square of peak voltage and gas pressure. While a plasma produced in DC discharge of the IECF

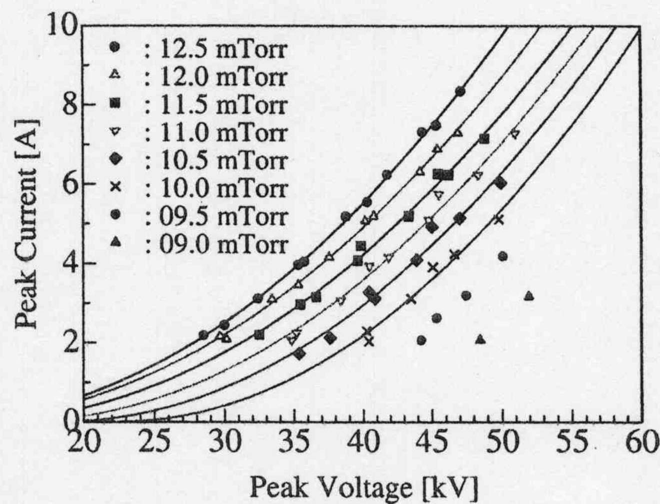

Figure 6: I–V Characteristic

device belongs almost to a normal glow region [2], that in pulsed discharge is found to belong to an abnormal glow region because the relation between the current and voltage in an abnormal glow region is expressed as

$$V_K = V_0 + \frac{K\sqrt{j}}{p_0} \tag{1}$$

where V_K is a voltage drop in the vicinity of the cathode, V_0 and K are specific constants determined by the kind of gas, j is a current density, and p_0 is a gas pressure.

Figures 7 and 8 show the dependence of delay time and rise time of discharge current on discharge conditions where delay time is the time needed the current starts flowing and rise time, respectively. Both delay time and rise time shortens as the peak voltage and gas pressure increase. In general, spark-forming-delay time, t_f, shortens as the overvoltage rate, ΔV $(= (V_p - V_s)/V_s)$, increases, where V_p is a peak voltage of the pulse, and V_s is a static breakdown voltage. Increase of the gas pressure corresponds to the decrease of the static breakdown voltage because the low pressure plasma produced by IECF device belongs to the left side of the Paschen's curve. Hence, overvoltage rate increases with peak voltage and gas pressure, then spark–forming delay time decreases and discahrge current rises faster. Also, it is found that the higher charging voltage is, the more stable pulsed discharges are. This is because that variance of stochastic-spark-delay time, t_s, is small in case that an overvoltage rate is large.

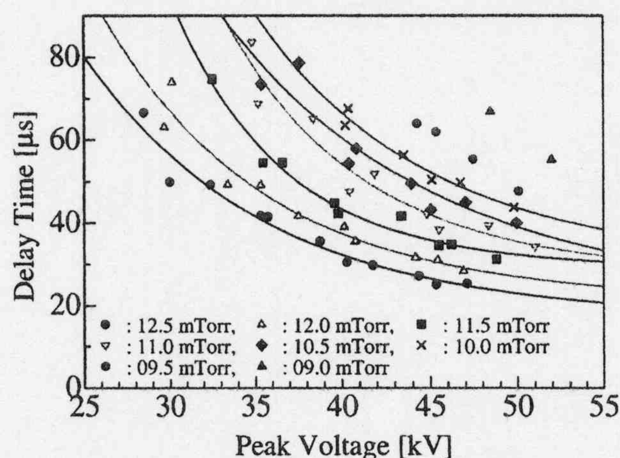

Figure 7: Dependence of Delay Time on Discharge Condition

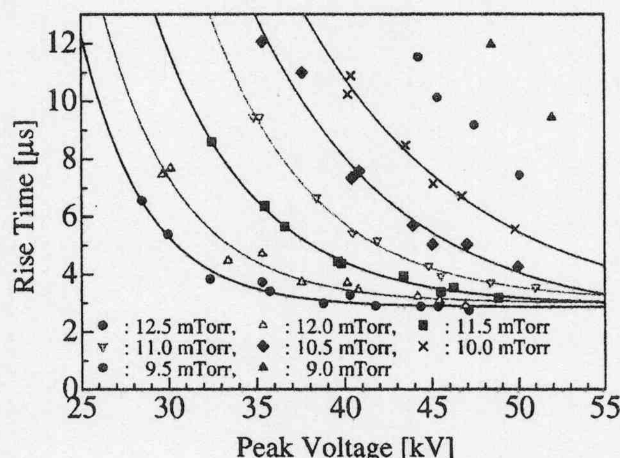

Figure 8: Dependence of Rise Time on Discharge Condition

III.C. Neutron Production

Figure 9 shows current dependence of neutron production rate at constant voltage. Neutron production rate is proportional to $I^{0.8} \sim I^{1.3}$. Figure 10 shows voltage dependence of neutron production rate at constant current. Neutron production rate increases with $\sigma_{DD}v$, where σ_{DD} is the cross section for D–D fusion reaction and v is ion velocity, in case that the ion energy is assumed to correspond to applied cathode voltage. These dependences are reasonable because fusion reaction rate, R, is denoted as

$$R = n_a n_b < \sigma v > V \tag{2}$$

where n_a and n_b is a number density of particle a and b, respectively, σ is a fusion cross section, v is an ion velocity, and V is a volume. If flowing ions collide and fuse each other, which is called Beam–Beam

reaction, fusion reaction rate, R, is proportional to the square of the current because the current is proportional to the number density in eq. (2). Also, if a flowing ion collides a cold neutral, which is called Beam–Background reaction, fusion reaction rate is proportional to the current. Hence, Beam–Background reaction seems to be dominant rather than Beam–Beam reaction in our IEC device from Fig. 9. Also, current and voltage dependences enable to optimize the discharge condition in pulsed operation.

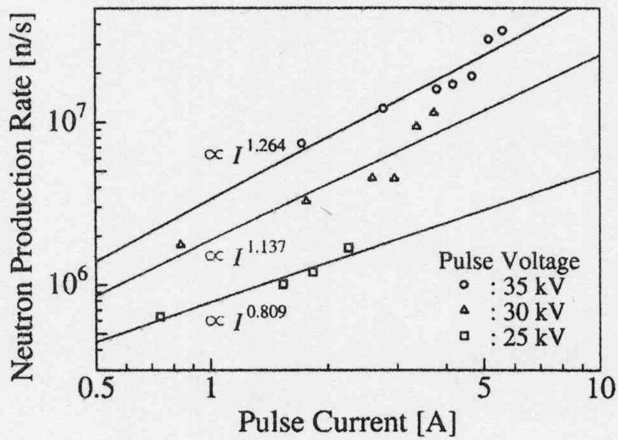

Figure 9: Current Dependence of Neutron Production Rate

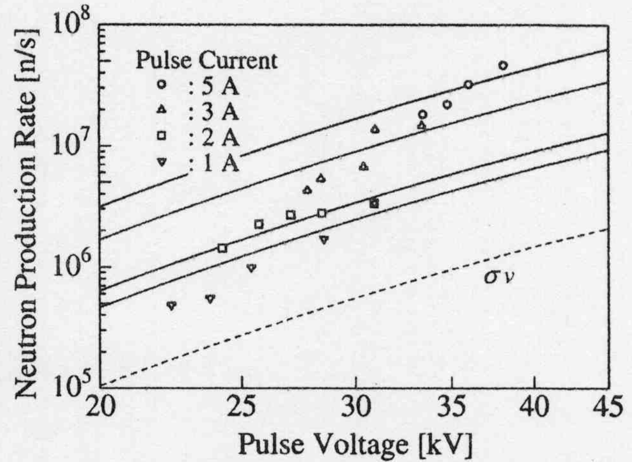

Figure 10: Voltage Dependence of Neutron Production Rate

Pulse width dependence of neutron production rate was measured changing pulse width at a constant discharge condition, then time dependence of neutron production rate was calculated shown in Fig. 11. It indicates that neutron production rate is the highest at the time when discharge current reaches its peak. One of the reasons is that both current and voltage reaches their peak at a moment the current rises. Also, it implies that shorter pulse which is turned off as the current reaches its peak, is more effective. Then short-pulse operation, where pulse width is $10 \sim 20$ μs, was carried out, and the result is shown in Fig. 12. Neutron production rate is higher than that in long-pulse one shown in Fig. 10. A maximum rate of 1.25×10^8 n/s was obtained at 6.2 A of peak current and 48.3 kV of peak voltage.

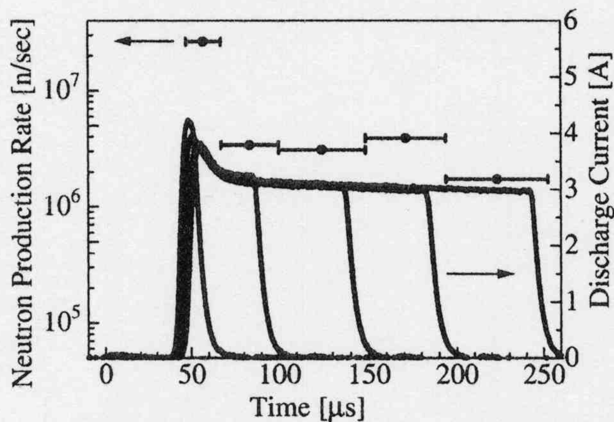

Figure 11: Time Dependence of Neutron Production Rate

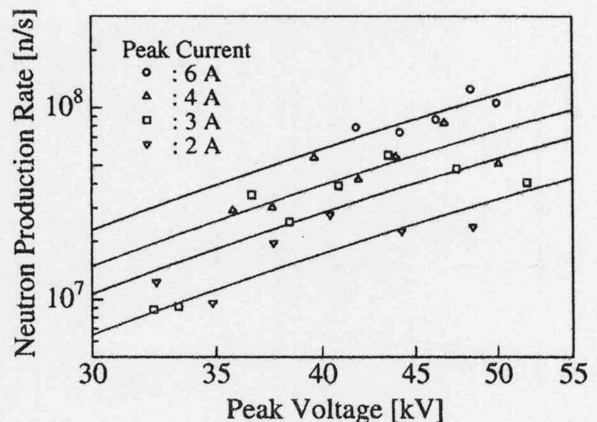

Figure 12: Neutron Production Rate in Short-Pulse Operation

Discharge condition dependences of neutron production rate in pulsed operation are compared with

those in DC operation, and are shown in Figs. 13 and 14. "Pulse(a)", "Pulse(b)", and "DC" in figures mean the results on this experiment, those on previous pulsed operation by our group, and those on DC operation, respectively. Figures 13 and 14 indicate that voltage and current dependence of neutron production rate in pulsed operation are almost consistent with that in high current region which is predicted by that in DC operation.

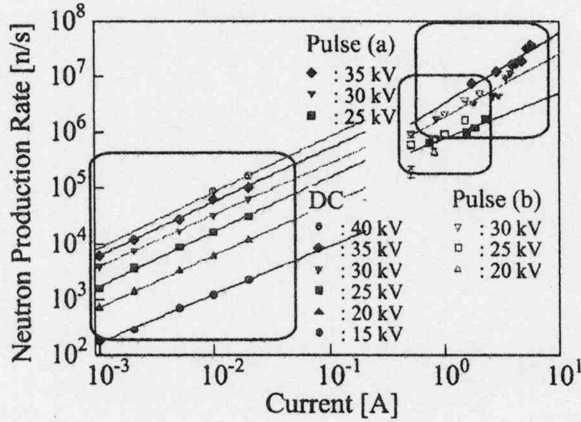

Figure 13: Comparison of Current Dependence of Neutron Production Rate between Pulse and DC

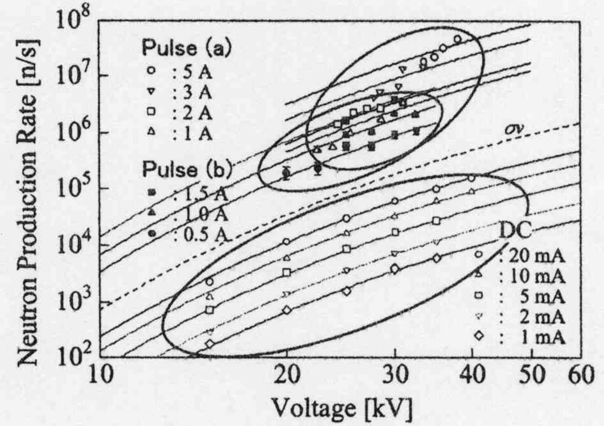

Figure 14: Comparison of Voltage Dependence of Neutron Production Rate between Pulse and DC

IV. Conclusions

It was confirmed that the suggested new power supply system for pulsed IECF operation was effective by way of comparing the pulse waveforms. Then fundamental discharge characteristics of pulsed IECF operation, such as I–V characteristics, discharge condition dependence of current rising, were yielded up. From the measurements of neutron production rate, it was found that the neutron production rate increases with $I^{0.8} \sim I^{1.3}$, and with $\sigma_{\mathrm{DD}} v$. From the measurement of time evolution of neutron production rate, it was found that the rate was the highest at the time the current rises and reaches its peak. Then a maximum rate of 1.25×10^8 n/s was obtained in short-pulse operation. From a comparison between pulsed and DC operation, it was cleared out that current and voltage dependence of neutron production rate were almost the same.

Acknowledgement

This work is supported by Japan Science and Technology Agency.

References

[1] K. Yoshikawa *et. al*, "Research and Developement of Landmine Detection System by a Compact Fusion Neutron Source", the 6$^{\mathrm{th}}$ US–Japan Workshop on Inertial Electrostatic Confinement Fusion", Yokohama, Japan, p. 7 (2003).

[2] Y. Ogino, "Study of Plasma Characteristics on Spherically Convergent Beam Fusion", Bachelor Thesis, Tokyo Institute of Technology, p. 30 (1999).

Development of Compositionally Gradient Thin Films by Intense, Pulsed Ion-Beam Evaporation

Makoto Hirai[1], Takehiko Honzawa[1], Naoya Honda[1], Tsuneo Suzuki[1], Hisayuki Suematsu[1], Takashi Yunogami[1,2], Weihua Jiang[1], and Kiyoshi Yatsui[1]

[1] *Extreme Energy-Density Research Institute, Nagaoka University of Technology, 1603-1 Kamitomioka, Nagaoka, Niigata 940-2188, Japan*

[2] *Institute for Technology, Enterprise and Competitiveness, Doshisha University, Imadegawa-Karasuma, Kamigyoku, Kyoto 602-8580, Japan*

ABSTRACT

Until now, without mask control by intense, pulsed ion-beam evaporation (IBE) method, the compositionally gradient thin films have been successfully prepared by irradiating an ion beam on two plates with different compositions. This investigation was carried out to explain the deposition process of ablation plasma emitted from Cu and W plates, and to reduce the compositional gradient (a) of the compositionally gradient Si-Ge thin films. From the results of high-speed photographs and Rutherford backscattering spectroscopy (RBS), the ablation plasma emitted from the Cu plate was clarified to reach to the substrate before that of the W plate. Additionally, to optimize the experimental conditions, a of the compositionally gradient Si-Ge thin films reduced from 6.4 to 0.8 at. %/mm.

I. INTRODUCTION

In recent years, functional thin films as semiconductive, fluorescent and magnetic materials have been used in wide area. The functional thin films, which consist of many elements, have been known to indicate excellent properties. To discover novel electronic, optical and magnetic properties, it is necessary to optimize the composition of thin films with many elements. Combinatorial methods, by which the optimization of the composition can be achieved more efficiently and systematically, have become of major interest lately.

In the combinatorial methods, to utilize pulsed laser deposition or sputtering, compositionally gradient thin films have been prepared on substrates by controlling masks that are located between targets and the substrates.[1,2] However, these methods have several problems that an experimental apparatus is expensive, and the system of the apparatus is very complicated.

Without the mask control by intense, pulsed ion-beam evaporation (IBE) method, we have successfully synthesized compositionally gradient Si-Ge thin films,[3,4] in which the ratio of Si atoms for Ge ones changed from 0 to 100 % on substrates. The thin films were obtained to simultaneously irradiate an ion beam on Si and Ge plates, which have melting point (T_m) as 1414 and 938 $^{\circ}$C, respectively. In contrast, the deposition process of ablation plasma emitted from two plates has not been clarified until now. However, it is very important to elucidate such process, since we are quite possible to synthesize compositionally gradient thin films with two plates having the larger difference in T_m.

Additionally, the compositional gradient (a) of the compositionally gradient Si-Ge thin film has been reported to be large value as 6.4 at. %/mm.[3] When the phases in the thin films are identified by X-ray diffraction (XRD), the irradiation area of X-ray is

approximately 6 mm under the conditions as divergence angle of 0.5 °, diffraction angle of 30 ° and goniometer radius of 185 mm. In the compositionally gradient Si-Ge thin film with a = 6.4 at. %/mm, the composition differs approximately 38 at. % at the irradiation area of X-ray. Therefore, to clarify each phase in the compositionally gradient Si-Ge thin films, it is necessary to reduce a in such thin films.

Therefore, this investigation was undertaken for (1) the explanation of the deposition process of ablation plasma emitted from two plates, and (2) the reduction in a of the compositionally gradient Si-Ge thin films. For the former purpose, to elucidate the influence induced by the difference in T_m, Cu and W plates, which the difference in T_m was very large value as approximately 2300 °C, were used as target.

II. EXPERIMENTAL SETUP

Figure 1 shows schematic illustration of the experimental setup of the IBE system. An intense pulsed ion beam was extracted from a magnetically-insulated diode, which was connected to a pulse power generator "ETIGO-II". A polyethylene flashboard was attached to an anode as an ion source. The high voltage of 1 MV (peak) was applied between the anode and cathode with the pulse width of approximately 50 ns. To prevent a current of electrons between the anode and cathode, the transverse magnetic field of approximately 1 T was generated by the cathode as a theta-pinch coil. The ions, which were produced by flashover of polyethylene flashboard, were mainly composed of protons (more than 85 %) and some carbon ions. The ion beam passed through the cathode with vane structure, and was geometrically focused on a target. When one of the targets was set at the distance (d_{AT}) of 180 or 230 mm from the anode, the energy density (E_d) of the ion beam on the targets was approximately 80 or 10 J/cm^2

respectively. Ablation plasma induced by the ion beam irradiation was deposited on substrates that were kept at RT in a vacuum of 1×10^{-2} Pa.

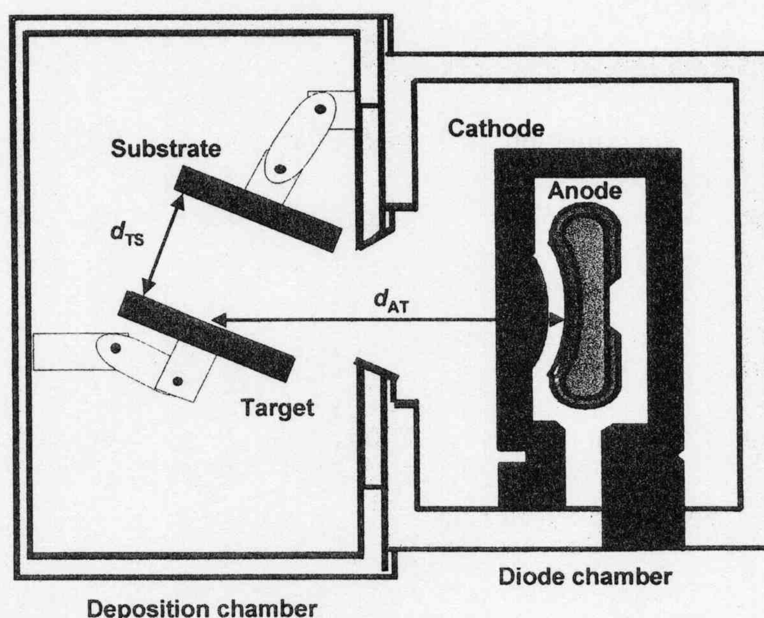

FIG. 1 Schematic illustration of the experimental setup of the IBE system.

For the preparation of thin films, Cu, W, Si and Ge plates were used as targets, as could be seen in Fig. 2 (a) and (b). In Fig. 2 (a), using the Cu and W plates as the target, the thin film was prepared on single crystal Si substrate. Furthermore, the incident angle (θ) of the ion beam and the distance (d_{TS}) between the target and substrate were 30 ° and 70 mm, respectively. A high-speed camera (Ultra NAC FS501) was used to record the deposition process of ablation plasma emitted from the Cu and W plates, and the photographs were taken under the conditions as the photographing interval of 3 μs and the exposure time of 50 ns. In addition, the time after camera operating was defined

as t. In Fig. 2 (b), to irradiate the ion beam on the Si and Ge plates, the compositionally gradient Si-Ge thin film was prepared on a stainless steel (SUS304) substrate under the conditions as $\theta = 40^{\circ}$ and $d_{TS} = 120$ mm. Experimental conditions are listed in Table I.

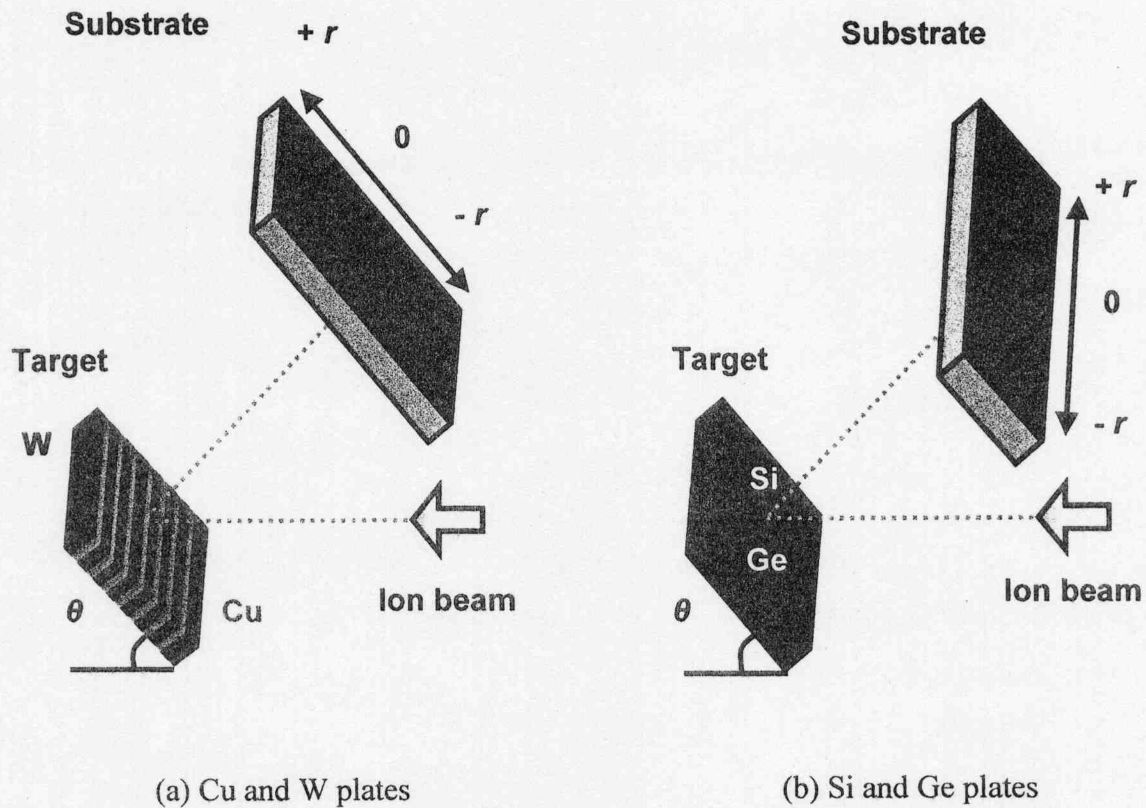

(a) Cu and W plates

(b) Si and Ge plates

FIG. 2 Schematic illustration of configuration of target and substrate. Cu and W plates are used as target in Fig. 2 (a). In contrast, in Fig. 2 (b), the target is comprised of Si and Ge plates.

A Rutherford backscattering spectroscope (RBS) was applied to measure the composition of the thin film, which was prepared by using the Cu and W plates. The

composition of the compositionally gradient Si-Ge thin film was determined by an energy dispersive X-ray spectroscope (EDS). The EDS was equipped with a scanning electron microscope (SEM), which was operated at the acceleration voltage of 10 kV. By this voltage, the incident depth of electrons corresponded to the thickness (approximately 300 nm) of the compositionally gradient Si-Ge thin film. Thus, the intensity of X-ray from the substrate was almost same as that of the background of EDS spectra. Moreover, the composition of the thin films was determined by $\Phi(\rho, z)$ method using a Cliff-Lorimer factor,[5] which was obtained from the spectrum of a standard Si-50 at. % Ge bulk.

Table I Experimental conditions

Main component of ion beam	H^+
Energy density (E_d)	10, 80 J/cm^2
Targets	Cu, W, Si and Ge plates
Substrates	Si, SUS304
Distance from anode to target (d_{AT})	180, 230 mm
Distance from target to substrate (d_{TS})	70, 120 mm
Incident angle of ion beam for target (θ)	30, 40 $^\circ$
Number of shot	1 shot
Substrate temperature	RT
Pressure	1×10^{-2} Pa

III. RESULTS AND DISCUSSION

A. Preparation of thin film with Cu and W plates

Figure 3 shows high-speed photographs of ablation plasma emitted from composite target that Cu and W plates are placed at the interval of 0.5 mm. The ablation plasma, which appeared $t = 3$ μs after camera operating, reached to the substrate at $t = 6$ μs. In t ranging from 6 to 30 μs, dark and light stripes were observed in the photographs of the ablation plasma. This result was induced by the difference in T_m of approximately 2300 °C between the Cu and W plates. In our previous works, when ion beam was simultaneously irradiated on two plates, the ablation plasma was firstly emitted from a plate having lower melting point.[6] Therefore, in Fig. 3, the ablation plasma emitted from the Cu plate is conjectured to reach to the substrate before that of the W plate.

Figure 4 shows depth profile of composition of thin film that is prepared by irradiating ion beam on Cu and W plates. The thin film was found to consist of W, Cu and O atoms. The O atoms in the thin film are probably incorporated the residual oxygen in the deposition chamber. In Fig. 4, the Cu content in the thin film increased with increasing in depth from thin film surface to Si substrate surface. Thus, in the early stage of deposition, a greater part of ablation plasma could be provided from the Cu plate. Additionally, when it is integrated along the lines attributed to Cu and W in Fig. 4, the integral value of Cu is larger than that of W. Accordingly, the ablation plasma of larger amount was emitted from the Cu plate than from the W one.

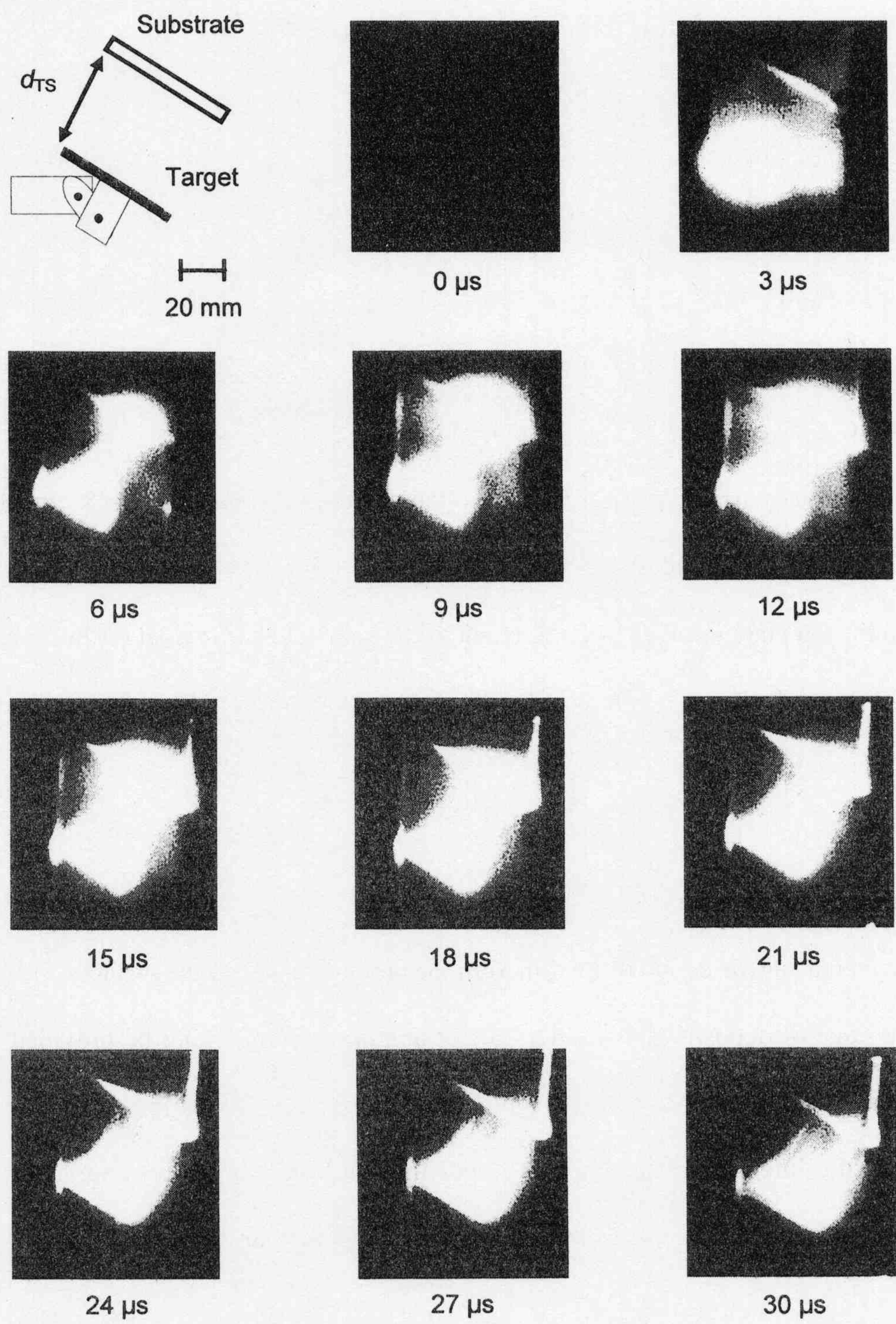

FIG. 3 High-speed photographs of ablation plasma emitted from composite target that Cu and W plates are placed at the interval of 0.5 mm.

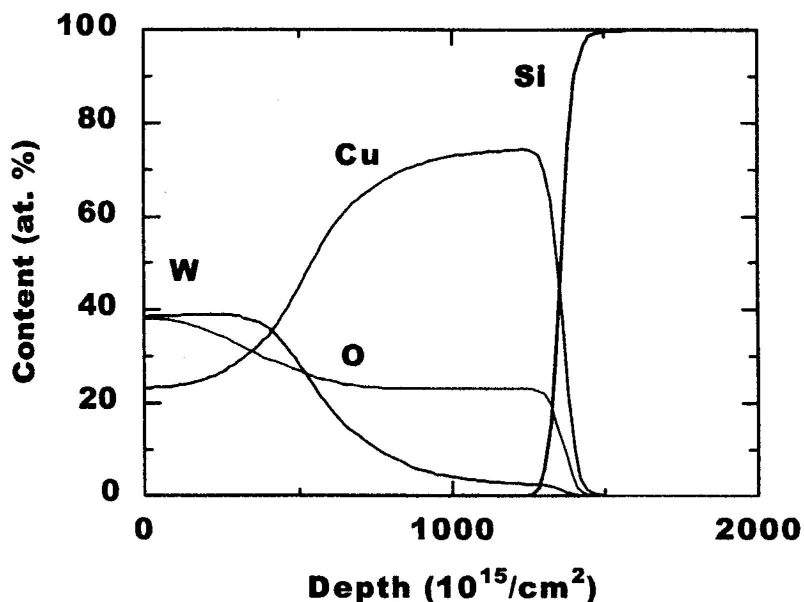

FIG. 4 Depth profile of composition of thin film that is prepared by irradiating ion beam on Cu and W plates.

From the results of Figs. 3 and 4, using two plates, the thin film, which contained the component of each plate, was synthesized for the irradiation of ion beam at once. This fact indicated that a compositionally gradient thin film can be prepared by the IBE method. Until now, although the compositionally gradient Si-Ge thin films were prepared by using Si and Ge plates, one of the thin films showed large values as a = 6.4 at. %/mm.[3] The result was considered due to that it is difficult to control the amount of ablation plasma emitted from each plates. Therefore, we proposed the configuration of the Si and Ge plates as could be seen in Fig. 2 (b), since the ion beam is quite possible to be uniformity irradiated on each plate.[4]

B. Preparation of compositionally gradient thin film with Si and Ge plates

Figure 5 shows substrate position (r) dependence of the composition of thin film that is prepared by irradiating ion beam on Si and Ge plates. As a result, since the ratio of Si atoms for Ge ones changed continuously in r ranging from 0 to 80 mm, the compositionally gradient Si-Ge thin film was confirmed to be prepared for the irradiation of ion beam at once. Additionally, in Fig. 5, the Si content in the thin film changed from 0 to 70 at. % on a substrate, and the compositionally gradient Si-Ge thin film was observed to have low value as a = 0.8 at. %/mm. Therefore, in the XRD measurement of the thin film, the difference in composition is approximately 5 at. % at the irradiation area of X-ray. This value was found to become an eighth of that of the previous work.[3]

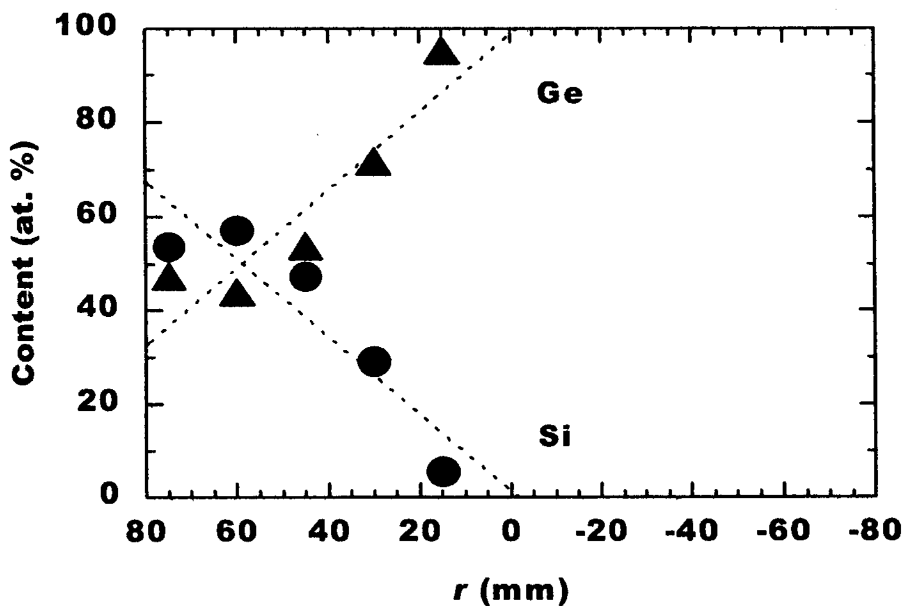

FIG. 5 r dependence of the composition of thin film that is prepared by irradiating ion beam on Si and Ge plates.

IV. CONCLUSIONS

From these experimental results, we have obtained the following conclusions:

(1) Using the IBE method, it is undertaken for the explanation of the deposition process of ablation plasma emitted from Cu and W plates. As a result, in t ranging from 6 to 30 μs, dark and light stripes are observed in the photographs of the ablation plasma. This result is induced by the difference in T_m of approximately 2300 °C between the Cu and W plates.

(2) The thin film, which is prepared by irradiating ion beam on Cu and W plates, consists of W, Cu and O atoms.

(3) The ablation plasma emitted from Cu plate reaches to the substrate before that of W plate. Additionally, the ablation plasma of larger amount is emitted from Cu plate than from W one.

(4) Without mask control, the compositionally gradient Si-Ge thin film is synthesized for irradiation of ion beam on Si and Ge plates. The compositionally gradient Si-Ge thin film has low value as $a = 0.8$ at. %/mm.

ACKNOWLEDGEMENTS

The authors appreciate M. Obata, Y. Sekimoto and K. Katagiri of Nagaoka University of Technology for the RBS measurement. The authors also thank S. Kitayama for the preparation of Cu-W thin film. This work was partly supported by the 21st COE Program of Ministry of Education, Culture, Sports, Science and Technology, Japan.

REFERENCES

[1]X.-D. Xiang, X. Sun, G. Briceño, Y. Lou, K.-A. Wang, H. Chang, W. G. Wallace-Freedman, S.-W. Chen, and P. G. Schultz, Science, **268**, 1738 (1995).

[2]H. Koinuma, Solid State Ionics, **108**, 1 (1998).

[3]H. Suematsu, T. Honzawa, M. Hirai, T. Suzuki, W. Jiang and K. Yatsui, Trans. Mater. Res. Soc. Jpn., **28**, 425 (2003).

[4]T. Honzawa, T. Suzuki, M. Hirai, T. Yunogami, H. Suematsu, W. Jiang and K. Yatsui, Submitted to Trans. Mater. Res. Soc. Jpn. (2004).

[5]D. B. Williams and C. B. Carter, *Transmission Electron Microscopy, Spectroscopy IV,* (Plenum Press, New York, 1996) p. 599.

[6]S. Kitayama, K. Ide, W. Jiang and K. Yatsui, Proc. Symposium on Extremely High Energy Density Plasmas and Their Diagnostics, (NIFS-PROC-50) p.198 (2001).

C-band intense microwave radiation with a cylindrical corrugated waveguide

Keiichi Ishibana, Takashi Nishiguchi, Naru Tomisawa, Kensho Yamamoto, Ritoku Ando and Keiichi Kamada

Graduate School of Natural Science and Technology, Kanazawa University, Kanazawa 920-1192, Japan

ABSTRACT

Generation of microwave pulse with frequency of 5 GHz, output power of 100 MW and duration of 5 ns was demonstrated using an intense relativistic electron beam with current of 5 kA, energy of 550 keV and duration of 12 ns, passing through cylindrical corrugated structure. The illumination of fluorescent tubes showed structured pattern corresponding to the excitation of TM_{01} mode. These results were compared with the results of PIC simulation. The simulation suggested that the output power of the radiated microwave was sensitively affected by energy and current waveforms of the beam. The radiation mechanism of the microwave was supposed to come from the superradiance. Preliminary experiments were carried out to transform the waveforms using a coaxial cavity and a cavity with large radius for enhancement of the microwave radiation.

1 Introduction

Intense pulses of electromagnetic radiation are required for applications in nuclear fusion, particle accelerators, radars, etc. Nearly continuous power output of ~1 MW is achieved by Gyrotron. On the other hands, the microwave devices with output power over 1GW are still in an experimental stage. Usually, the devices with output power of over 1 GW employ the conventional mechanisms for microwave radiation, which are applied to the low power devices. An intense pulsed electron beam with duration of less than 500 ns is used as an energy source. Because of strong electric field of the radiated microwave, the breakdown limits the microwave duration less than 100 ns, and the radiation efficiency decreased dramatically. Stimulated emission from extended electron bunches - superradiance (SR) [1] can be considered as effective method of generation ultra short intense electromagnetic pulses with output power over 1 GW. Different types of SR emission (bremsstrahlung, Cherenkov, cyclotron) were studied theoretically and were observed experimentally [2-4]. The most effective generation of SR pulses at Ka and X bands was obtained using Cherenkov mechanism for short electron beam moving in corrugated waveguide. It should be noted that increasing operating wavelength leads to

increasing of the electron pulse total duration, which can be involved in formation of a single SR pulse. In Ka band optimal pulse duration is about 1 ns. The transition to the C band makes it possible to employ a quite long electron beam with duration exceeding 10 ns. We report experimental and simulation results on the C-band superradiance.

In difference from the case of steady state generation, the electron pulses with a top plate waveform cannot be optimal for production of SR pulses. When a short SR pulse occurs and propagates inside interaction space, it is appropriate to feed this pulse by electrons with longitudinal velocities more and more exceeding phase velocity of the wave. Using an electron beam with increasing energy and current, it is possible to increase the SR pulse peak power [5-6]. The trapezoidal (nearly flat top) energy and current pulse profiles can be transformed to the profiles increasing in time using additional cavities. The experimental results of the transformation of waveforms are discussed.

2 Experimental setup

An intense relativistic electron beam (IREB) with energy of 580 keV was utilized as an energy source. A cylindrical corrugated waveguide structure for microwave radiation with frequency of 5 GHz was designed for the IREB. The final structure is shown in Fig.1. The mean radius and periodic length are decided to be 25 mm and 30 mm, respectively, by approximate dispersion relation for 4.9 GHz microwave radiation with the IREB. As the backward wave of TM_{01} mode was expected, the inner radius of the waveguide was decreased to be 22 mm (cut off frequency of 5.2 GHz) to reflect the wave to the downstream side at the entrance of the corrugated part (indicated by A in Fig.1). Therefore, the outer radius of corrugated part was set to be 28 mm. The beam radius was decided to be 20 mm.

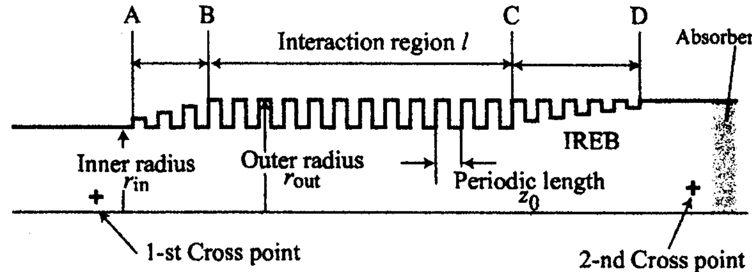

Fig. 1: Cross section of the cylindrical corrugated waveguide where r_b = 20 mm, r_{in} = 22 mm, r_{out} = 28 mm, z_0 = 30 mm and l = 300 mm. At the part indicated by A-B and C-D, the radius is gradually increased to prevent the beam and microwave from reflection. In the simulation, an absorber was set at the end of the tube and output microwave was observed at 2-nd cross point.

We set the distance between the beam and inner wall, 2 mm, as small as possible. We also used Particle-In-Cell simulation code KARAT [7] to optimize the parameters. The difference between the inner and outer wall radii, 6 mm, was simulated to be an optimum

depth. Gradually increasing radius regions were added at both sides of the interaction region to prevent from the reflection of an electron beam and radiated microwave. The output power of the radiated microwave was saturated at the length of 30 cm in the simulation.

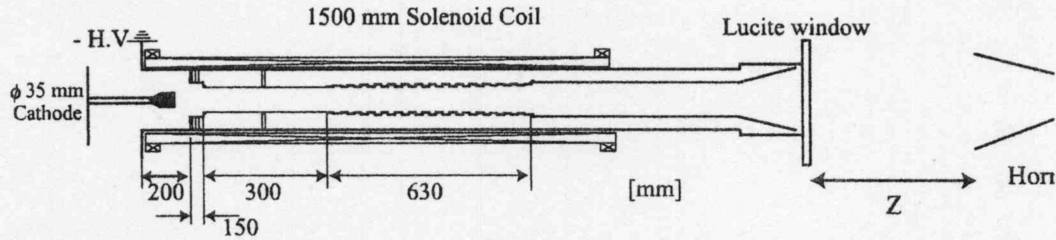

Fig. 2: Experimental setup

Figure 2 shows the experimental setup. An IREB with energy of 580 keV, current of 5.7 kA and duration of 12 ns was injected from a cold emission cathode into a drift tube with radius of 20 mm. The cylindrical corrugated waveguide was located 30 cm apart from the anode. A solenoid coil along the beam axis applied pulsed magnetic field with strength of 1 T. The IREB was diverged to the wall at the end of the solenoid coil. At the end of the drift tube, a horn was set. The microwave was radiated into the air through a Lucite window. The radiated microwave was detected by a horn located more than 1 m far from the Lucite window. The microwave detection system is shown in Fig. 3. The microwave received by a horn was attenuated by two variable attenuators. Five low pass filters with frequencies from DC - 4 GHz to DC - 8 GHz were utilized after 8-way power divider. Tunnel detectors detected microwaves passing through l the ow pass filters. The variable attenuators, low pass filters and tunnel detectors were calibrated. As examples, the output power of a tunnel detector was plotted against the output voltage (Fig. 3 (a)) and the output power of DC - 5 GHz low pass filter was plotted against the frequency with the same output power (Fig. 3 (b)).

3 Experimental results and discussions

The waveforms detected by tunnel detectors are shown in Fig. 4. No signal was detected without the corrugated waveguide. With corrugated waveguide, similar waveforms through all low pass filters except the DC-4 GHz low pass filter were observed. The vertical ranges of output power of all detectors except the DC-4GHz were comparable to each other. It was suggested that the microwave with frequency of nearly 5 GHz was radiated. The pulse width of the microwave of 5 ns is shorter than that of the beam current (Fig. 5). This very short radiation pulse is considered to be one of the typical characteristics of the superradiance.

The angular distribution of the radiated microwave was observed. The horn was moved along the circumference with radius of 1500 mm as shown in Fig. 6. The microwave

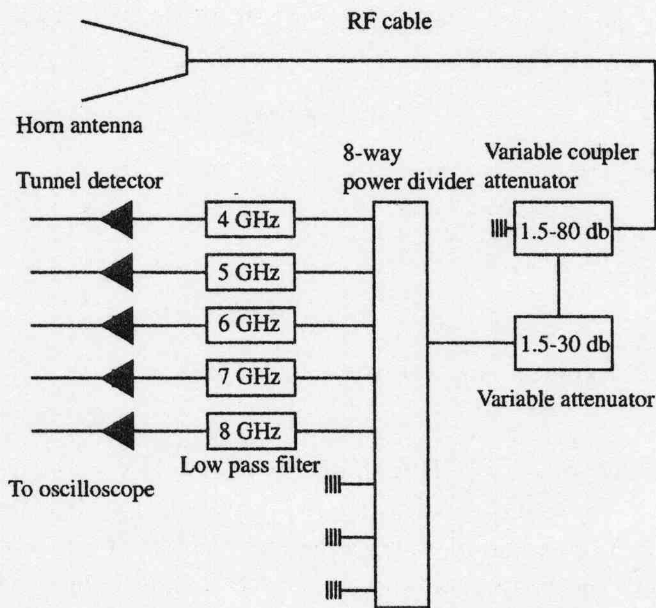

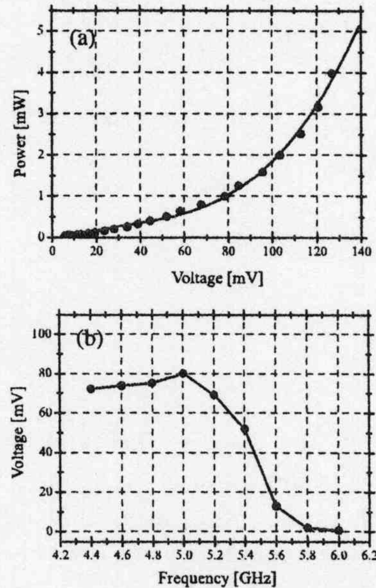

Fig. 3: Microwave detection system. (a) The output power vs. the output voltage of tunnel detector. (b) The output voltage vs. frequency of 5 GHz low pass filter.

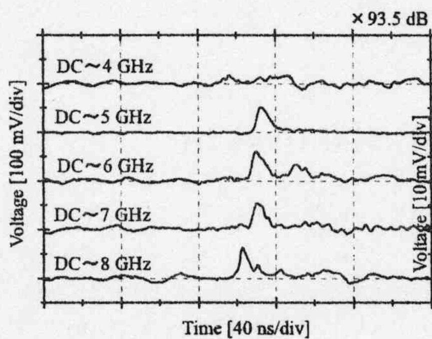

Fig. 4: Signals through low pass filters with cylindrical corrugated waveguide.

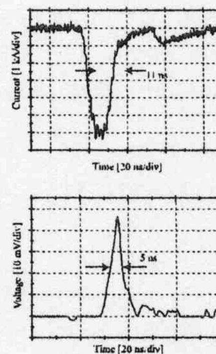

Fig. 5: Waveforms of beam current (upper) and tunnel detector through DC-5 GHz low pass filter (lower).

output has one peak around 15 degrees from the beam axis. The distribution of radiated microwave shown in Fig. 6 suggested the TM_{01} mode as expected. Fluorescent tubes were located 550 mm far from the Lucite window to observe the radiation pattern directly. The observed pattern shown in Fig. 7 was donuts like pattern that was consistent with the above result.

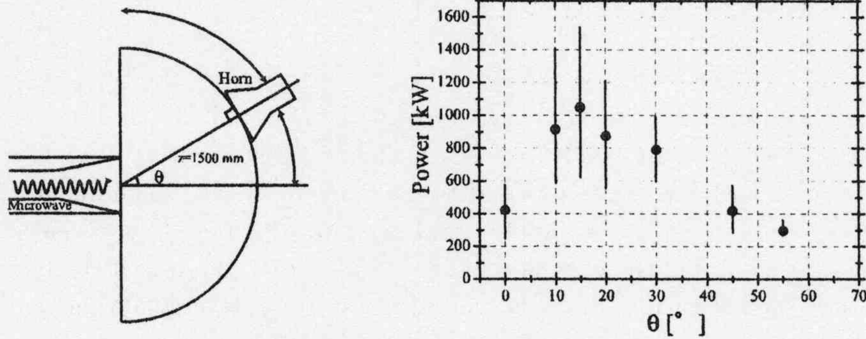

Fig. 6: The horn was moved along the circumference with radius of 1500 mm (left). The output power was plotted against the angle from the beam axis (right).

The observed output powers detected at each angle were sum up to estimate the total output power. The estimated total output power was about 50 MW. With the elongation of output horn, the total output power was increased to be 100 MW. Now we try to increase the output power with some arrangements of the apparatus.

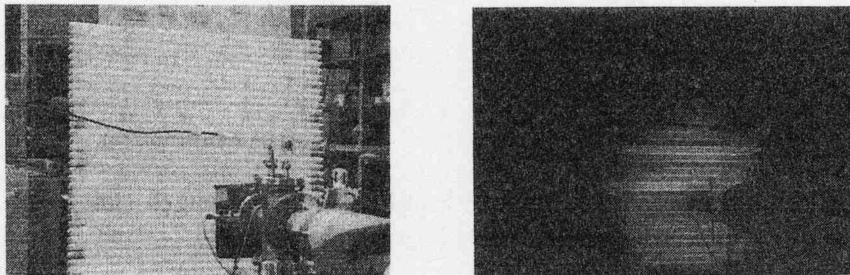

Fig. 7: Fluorescent tubes were located 550 mm far from the Lucite window (left). The donuts like pattern was observed (right).

It is difficult to declare that the microwave radiation described above is identified to be SR. When the mechanism of microwave radiation came from the SR, the duration of the beam pulse has the appropriate length for the maximum output power. We utilized the code KARAT to investigate the relation between the beam duration and the microwave output power. The simulation shows how the beam duration influences on the microwave output. In Fig. 8, the simulated results of microwave outputs with different beam duration using the parameters of the cylindrical corrugated waveguide and the

IREB described above are shown. The microwave output shows the maximum value with the beam duration of 8 ns.

In the experiment, the duration of the beam was 12 ns. The output power of the experiment is about several times less than the simulation result. Experimental result was shown with solid curve on the 12.5 ns simulation result (Fig. 8 left, the vertical scale is not comparable with each other.). The microwave duration of 5 ns observed in the experiment is comparable with the simulated one. The simulation results showed that the microwave output was very sensitive to the beam duration and the SR theory also indicates that the beam length affects the output power strongly. As we considered that the simulation results qualitatively agreed with the experimental ones, the microwave radiation in the experiment was supposed to come from the SR mechanism.

The physics of these results can be explained by the behavior of electrons in the simulation as below. When the duration of the beam is 8 ns, the tail of the beam electrons has already passed the entrance of the corrugated part at the time when the backward wave arrived at the entrance. On the other hands, the beam electrons are present together with the microwave at the entrance of the corrugated part when the beam duration is longer than 8 ns. It is supposed that the reflected microwave has a chance to be absorbed by the electrons in case of the longer beam. The beam duration of 8 ns is the maximum duration that the tail of the electron beam goes ahead of the head of the reflected microwave.

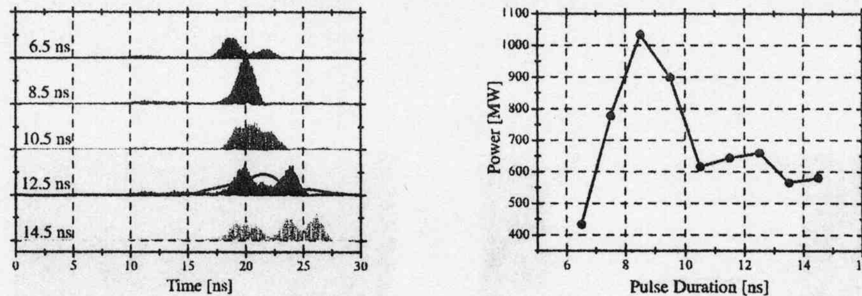

Fig. 8: The simulated microwave output for different beam length (left). The maximum microwave output is plotted against the beam length (right).

On the other hands, it was shown in [5,6] that due to nonstationary nature of SR emission an accelerating voltage should change over electron pulse duration to enhance peak amplitude of electromagnetic pulse. Optimization of profile of voltage and current pulses provided possibility for increasing peak power of SR pulses. In the case of cylindrical corrugated waveguide, the simulated results showed that the increasing energy and current waveforms made the microwave output twice larger than flat top waveforms. As the voltage between diode applied by a Marx generator and a pulse forming line is changed by the evolution of the diode impedance, it is technically difficult to control the waveforms at the diode. We carried out the experiments of reformation of IREB waveforms with a coaxial cavity and a cavity with large radius located at the drift tube. The experimental apparatus and results are shown in Fig. 9 and 10.

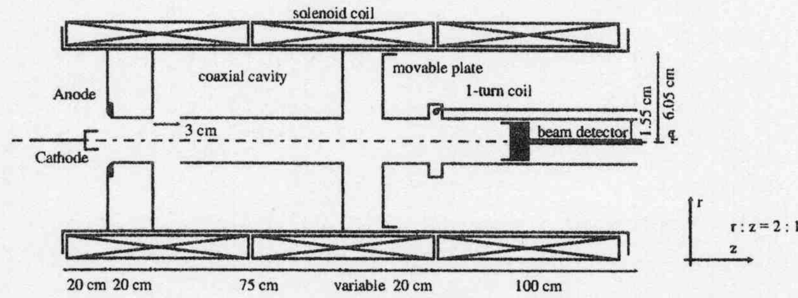

Fig. 9: The experimental apparatus of transformation of IREB waveforms. The coaxial cavity for energy transformation was followed by the cavity with large radius for current waveform transformation.

The principle of transformation of energy waveform is the same as that of the autoacceleration. The energy in the former part of the beam was transferred to the latter part of the beam through the cavity. The cavity length was the parameter to change the waveform. The transformed energy waveform can be estimated by transmission line theory. The current waveforms were a little changed by the coaxial cavity (Fig. 10 left). And if needed, the second coaxial cavity can be set after the cavity with large radius and the energy waveforme was transformed more strongly. The cavity with large radius transformed the current waveforms (Fig. 10 right). Increasing the radius decreases the space-charge limiting current. The length of the cavity arranged the transformed current waveform. In our case, the cavity with length of more than 30 cm resulted in the same current waveform. The energy waveform was little changed by the large radius cavity. The transformed time-increasing waveforms were obtained and the experiments on the SR with these waveforms will be carried out.

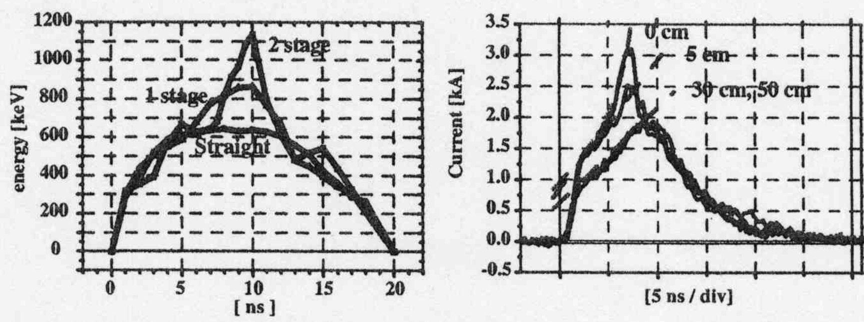

Fig. 10: The experimental results of transformed IREB waveforms. Energy waveforms after the coaxial cavity (left). The energy waveforms were transformed after one cavity. The second cavity after the large radius cavity transformed the energy waveform more strongly. Current waveforms after the cavity with large radius (right). The cavity length more than 30 cm showed little difference.

4 Conclusion

Microwave with frequency of 5 GHz, output power of 100 MW and duration of 5 ns was obtained with an IREB with energy of 580 keV, Current of 5 kA and duration of 12 ns using cylindrical corrugated waveguide. The simulation results suggested that the mechanism of the microwave generation came from the superradiance. Now, it becomes possible to change the time evolution of the beam energy and current using a coaxial cavity and a cavity with large radius within the limit of the injected waveforms. We will try the enhancement of the efficiency of the microwave output with the time-increasing waveforms.

Acknowledgement

A part of this work is supported by a Grant-in-Aid for Scientific Research from Ministry of Education, Science, Sports and Culture, Japan

References

[1] N. S. Ginzburg, I. V. Zotova, Sov. Tech Phys. Lett., 15, pp. 573-574, 1989.
[2] N. S. Ginzburg, I. V. Zotova A. S . Sergeev I. V. Konoplev A. D. R. Phelps A. W. Cross S. J. Cooke, V. G. Shpak, M. I. Yalandin, S. A. Shunalinov, and M. R. Ulmaskulov, , Phys. Rev. Lett., 78, pp. 2365-2368, (1997).
[3] M. I. Yalandin, V. G. Shpak, S. A. Shunailov, M. R. Ulmaskulov, N. S. Ginzburg, I. V. Zotova, A. S. Sergeev, A. D. R. Phelps, A. W. Cross, K. Ronald, S. M. Wiggins, IEEE, vol. 28, pp. 1615-1618. 2000.
[4] S. M.Wiggins , D. A. Jaroszynski, B. W. J. McNeil, G. R. M. Robb, P. Aitken, A. D. R. Phelps, A. W. Cross, K. Ronald, V. G. Shpak, M. I. Yalandin, S. A. Shunailov , M. R. Ulmaskulov, N. S. Ginzburg, Phys. Rev. Lett., vol. 84, pp. 2393-2396. 2000.
[5] N. S. Ginzburg, I. V. Zotova, R. M. Rozental, A. S. Sergeev, M. Kamada, K.Sugawara, K.Kurihara, H. Shirasaka, R. Ando, K. Kamada, Proc. 14th Int. Conf. High-Power Particles Beams, (Albuquerque USA, 2002), pp. 291-294, 2002.
[6] N. S. Ginzburg. I. V. Zotova, R. M. Rozental, A. S. Sergeev, M. Kamada, K. Kurihara, H. Shirasaka, R. Ando and K. Kamada, Nucl. Instrum. Methods Phys. Res. A, 507, pp61-64, 2003.
[7] V. P. Tarakanov, "Users manual for code KARAT", ver. 7.09, 1999.

Development of Virtual Cathode Oscillator for High-Power Microwave Generation

Syuhei Ohno, Kousuke Kanbara, Nami Shimada, Weihua Jiang, and Kiyoshi Yatsui

Extreme Energy-Density Research Institute, Nagaoka University of Technology

Nagaoka, Niigata 940-2188, Japan

Abstract

This paper describes virtual cathode oscillator (vircator) developed recently. The optimization of vircator was performed by both computer simulation and the experiment. At the simulation, the maximum output power of microwave and the conversion efficiency to microwave was 120MW and ~7.5%. Experimental studies were carried out by using the repetitive pulsed-power generator "ETIGO-IV". The maximum output power of microwave was 80MW, giving the conversion efficiency of ~2%.

I. Introduction

Development of high power microwave (HPM) generators is demanded from many fields. The virtual cathode oscillator (vircator) is one of the high power microwave generators. Since vircator has very simple geometry, high peak power capability and high tuning ability,[1)] practical applications of HPM generation can be expected. The microwave generation by vircator is attributed to the action of two mechanisms. One mechanism is an electrons reflexing between the cathode and the virtual cathode, and the other is an oscillations of the virtual cathode itself. Because these mechanisms coexist destructively and interfere, the microwaves generated by vircators are propagating in many electromagnetic modes.[2)] To improve the microwave generation efficiency, we were optimizing the vircator with a new configuration.

Figure 1 shows the vircator developed. This vircator system consists of the cylindrical cathode, mesh anode and anode rod which fixes the mesh. The computer simulation using simulation code "MAGIC" performed the optimization design of the vircator. Computer simulation is carried out on the generation of high-power microwaves by vircator using relativistic electron beam. The parameters used in the simulations are those corresponding to the operating parameters of the repetitive pulsed-power generator "ETIGO-IV".

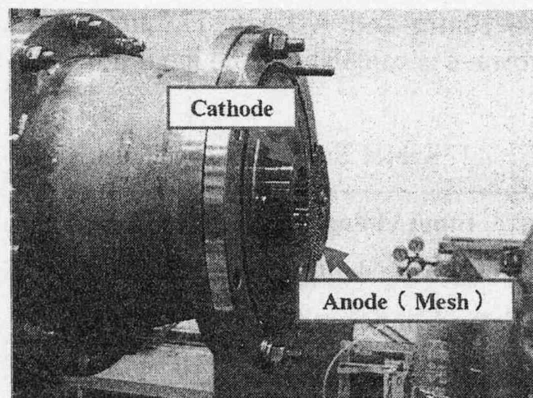

Fig.1 Vircator with the cylindrical cathode.

II. Simulation set up

II. I Simulation code "MAGIC"

The simulations are performed with "MAGIC", a fully electromagnetic, and relativistic particle-in-cell code.[4)] The vircator is modeled in 2.5-dimensional (two spatial and three velocity components) cylindrical coordinate system. Figure 2 shows the simulation model. This model expresses the upper half of vircator shown in Fig.1. The point in a figure shows the electrons. The particle trajectories in fig.2 show the beam flowing from the cathode to the anode. The figure shows that the reflected electron makes the virtual cathode. Moreover, other electrons spread to the waveguide.

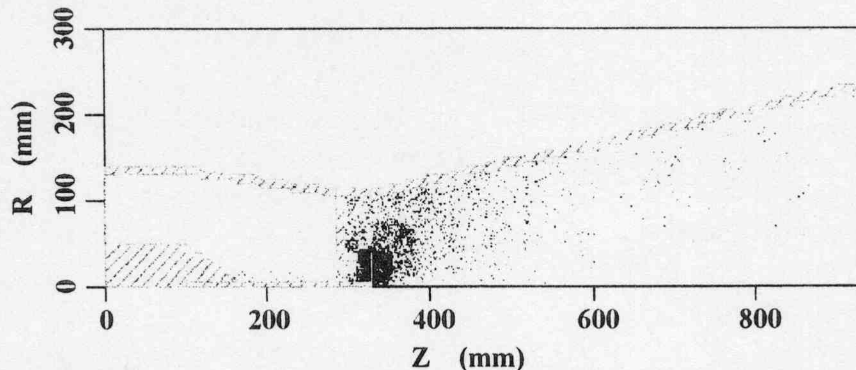

Fig.2 Simulation model of virtual cathode oscillator by 2D "MAGIC" simulation.

II. II Simulation Parameters

In the simulation, cathode and waveguide are perfect conductors. And the anode is an aluminum foil with thickness of 10 μm. Although the actual anode was made from the mesh, in the simulation, thin aluminum foil was used as the anode for simplification. The length of waveguide was set to 850mm and the radius was set to 105mm. These values are the sizes of waveguide actually used by "ETIGO-IV". Cathode width was changed by 10mm and 15mm. And the A-Kgap was changed from 10mm to 30mm. In the simulation, 400kV of the voltage rating of "ETIGO-IV" was impressed onto the A-K gap. Figure 3 shows the typical diode voltage and diode current waveform obtained by simulation. On the condition of cathode width=10mm and A-Kgap=17.5mm, 4kA current was obtained. Conversion efficiency to microwave is calculated from input power and microwave output.

Table1 Simulation conditions.

Input voltage	**400 kV**
Cathode width	**10 , 20 mm**
Cathode inner radius	**30 mm**
A-K gap	**10 ~ 30 mm**

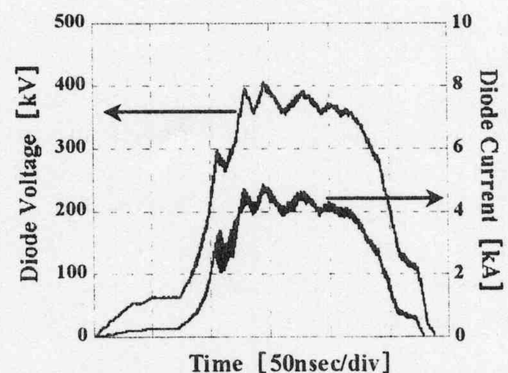

Fig.3 Typical voltage and current waveform.

Ⅲ. Simulation Results

Ⅲ. I Measurement of microwave power

Figure 4 shows the output microwave power obtained by simulation. The Poynting vector measured at the outlet of waveguide determined the microwave power. The maximum output of microwave was obtained with cathode width=10mm and A-K gap=18mm. Under this condition, the output power of microwave was 120MW and the conversion efficiency to microwave was 7.5%.

Figure 5 shows the conversion efficiency to microwave as a function of A-Kgap. From this result, the conditions of cathode width=10mm were higher efficiency than the conditions of cathode width=20mm.

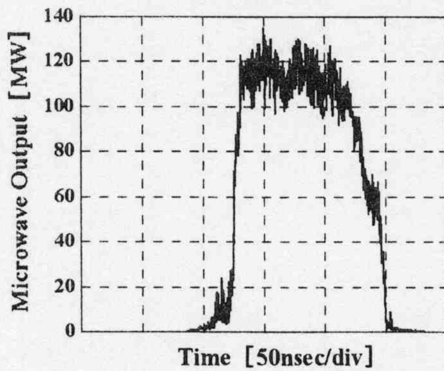

Fig.4 Microwave output waveform.
(Cathode width=10mm, A-Kgap=17.5mm)

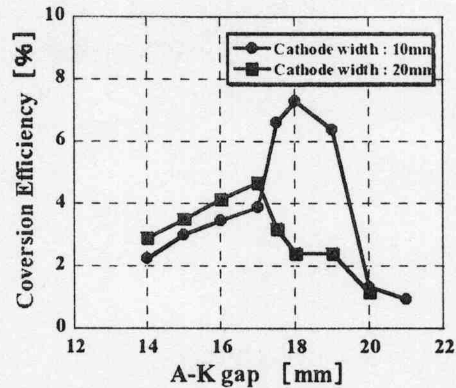

Fig.5 Conversion efficiency versus A-Kgap distance.

Ⅲ. Ⅱ Measurement of microwave frequency

The electric field was measured at the outlet of waveguide. Figure 6 shows the time history of the electric field E_z. Microwave generation is verified by the strong oscillatory behaviour of the electric field as depicted in Fig.6 (a).

Figure 6 (b) shows the frequency ingredient of microwave. The frequency of microwave was calculated by FFT of an electric field waveform. Frequency of the microwave obtained with this condition shows a strong peak at 2.9GHz.

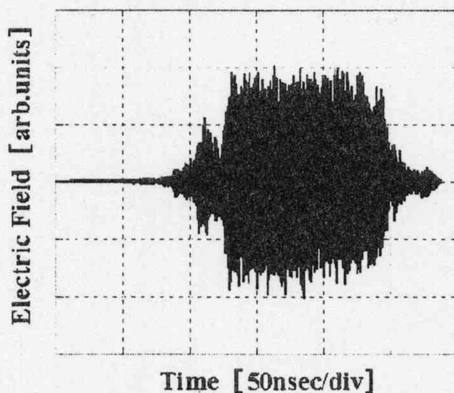

(a) Electric field waveform.

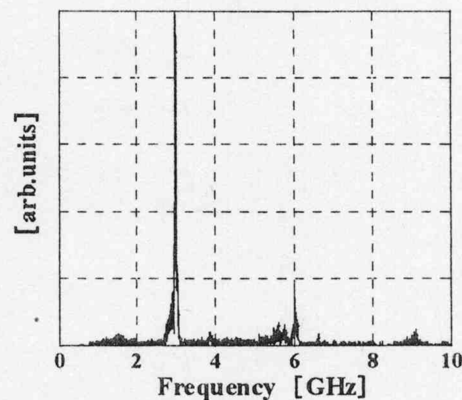

(b) Frequency spectrum of microwave.

Fig.6 Electric field waveform and frequency spectrum of microwave by simulation.
(Cathode width=10mm, A-Kgap=17.5mm)

Ⅲ.Ⅲ Measurement of microwave propagation mode

The situation of the electric field distribution within waveguide is shown in Fig. 7. These electric field distributions show that the dominant propagation mode of the microwave was found to be TM_{02}. Here, the microwave frequency of TM_{02} is 2.9 GHz as shown in Fig. 6 (b).

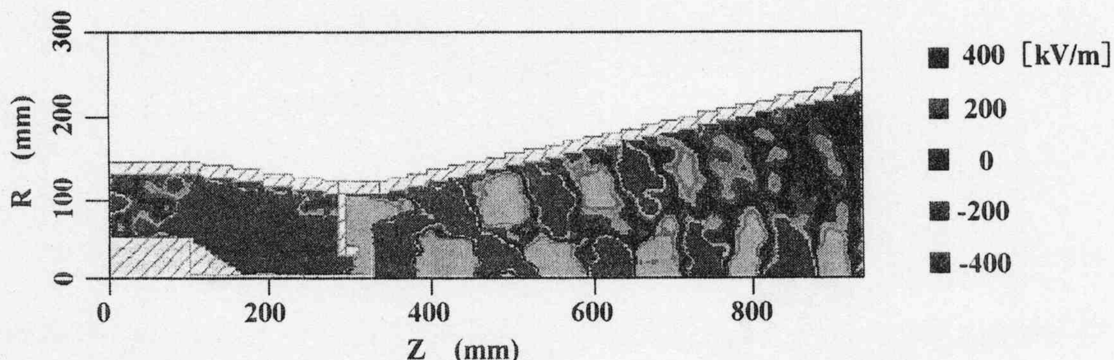

Fig.7 The electric field distribution within waveguide by 2D "MAGIC" simulation.

Ⅳ. Experimental configurations

Figure 8 shows the schematic of the experimental setup. The experimental system consists of the diode chamber, circular waveguide, receiving antenna and the repetitive pulsed-power generator "ETIGO-IV". The cylindrical cathode and anode rod are made from brass, and the mesh anode is made from the stainless steel. Velvet is stuck in order to support electronic discharge on the surface of cylindrical cathode. The diode voltage and diode current are measured by using capacitive divider and rogowski coil. The typical output waveforms obtained by experiment are shown in Fig.9 (a). In the experiment, the cathode width was set to 10mm, and A-Kgap was changed from 15mm to 25mm. If the voltage from "ETIGO-IV" is impressed to the diode, the virtual cathode is formed in the chamber, and microwave is emitted. In the meantime, the output microwave is measured by the receiving antenna. Typical microwave output waveform is shown in Fig.9 (b).

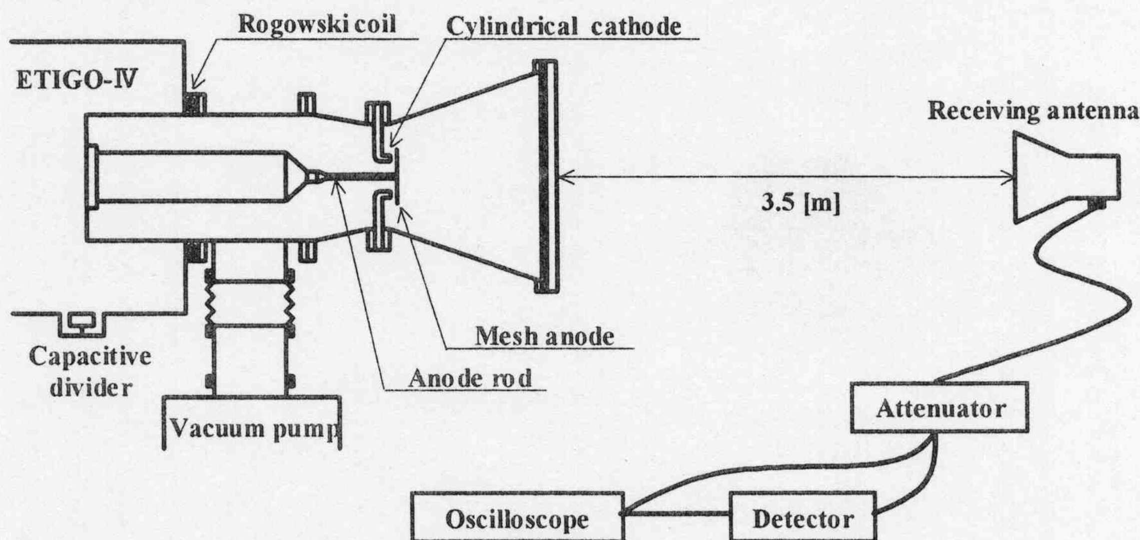

Fig.8 Schematic of experimental setup.

V. Experimental Results and Discussions

Figure 9 (a) shows the typical diode voltage and diode current waveform obtained by experiment. Moreover, Figure 9 (b) shows the microwave output waveform. The maximum output of microwave was obtained with cathode width=10mm and A-Kgap=17.5mm. Under this condition, the output power of microwave was 80MW and the conversion efficiency to microwave was 2 %. As a result of comparing the diode current value obtained by the experiment and the simulation, about 3kA difference was seen.

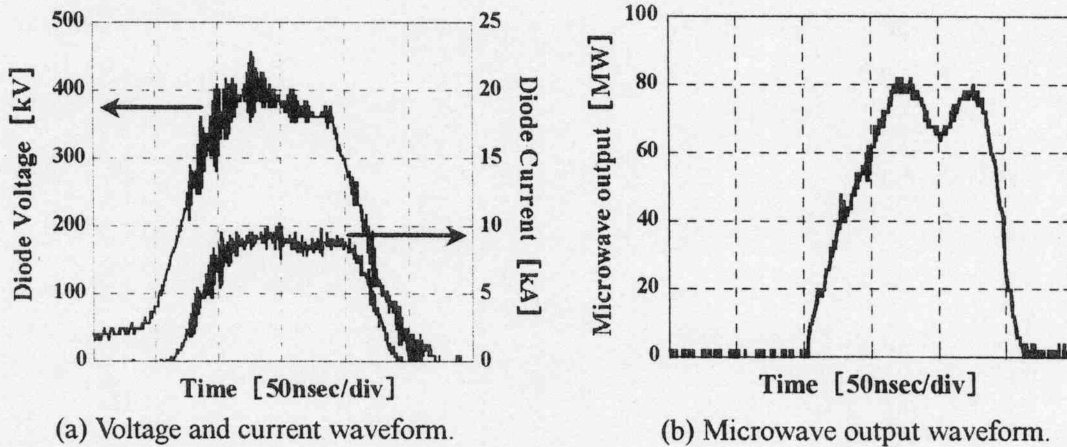

(a) Voltage and current waveform. (b) Microwave output waveform.

Fig.9 Typical output waveform by Experiment.
(Cathode width=10mm, A-Kgap=17.5mm)

Figure10 (a) shows the A-K gap dependence of microwave output power. In the simulation, the optimal condition of microwave output was found near A-Kgap=18mm. However, the optimal condition of microwave output was not obtained in the experiment result. This difference will be studied in detail by future investigations.

Figure10 (b) shows the A-Kgap dependence of microwave frequency. The frequency of microwave was calculated by FFT of the electric field waveform. Frequency of microwave output changed with variable of A-Kgap from 1.6GHz to 2.6GHz. From the result shown in Fig10 (b), the similar tendency by both simulation and experiment was seen.

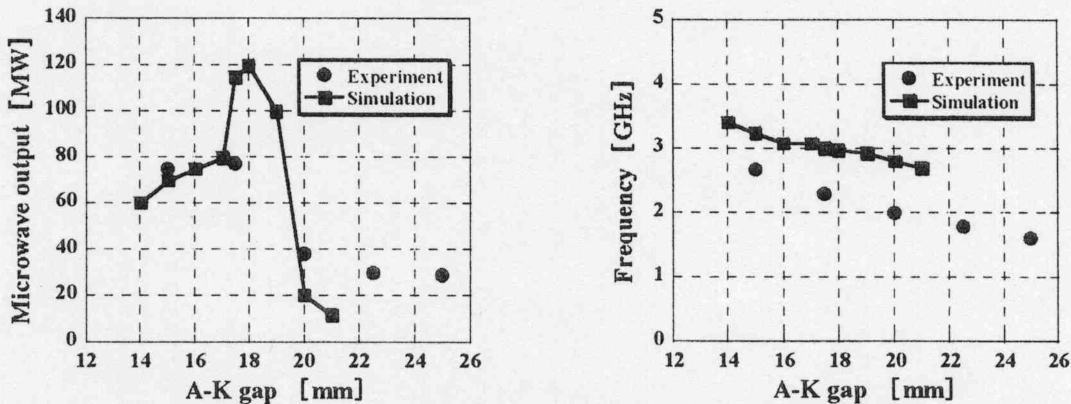

(a) Microwave power versus A-Kgap distance. (b) Microwave frequency versus A-Kgap distance.

Fig.10 Output microwave power and frequency versus A-Kgap distance.

VI. Conclusions

The computer simulation using simulation code "MAGIC" performed the optimization for the design of new vircator. As a result, the maximum output power of microwave obtained by simulation was 120MW, giving the conversion efficiency of ~7.5%. The frequency of microwave is calculated to be 2.9GHz and the dominant mode of propagation in the cylindrical waveguide was TM_{02}. In the meantime, high power microwave generation by vircator was studied by using the repetitive pulsed-power generator "ETIGO-IV". As the experimental results, the maximum output power of microwave was 80MW, giving the conversion efficiency of ~2%. The frequency of microwave depending on the A-K gap was in the range of 1.6~2.6 GHz.

VII. References

1. James Benford and John Swegle. "High Power Microwave Sources", Artech House (1991).
2. Weihua Jiang and Kiyoshi Yatsui. "High Power Microwave Generation by a Coaxial Virtual Cathode Oscillator", IEEE Trans. Pl. Sci. 27, 1538 (1999).
3. Weihua Jiang and Kiyoshi Yatsui. "Pulsed Power Technology and Its Applications at Extreme Energy Density Research Institute (EDI), Nagaoka", Jpn. J. Appl. Phys. 40, 921 (2001).
4. Weihua Jiang, Katsumi Masugata and Kiyoshi Yatsui. "Mechanism of microwave generation by virtual cathode oscillator", Physics of Plasmas, Vol.2, No.3, 982 (1995).
5. Weihua Jiang and Magne Kristiansen. "Theory of the virtual cathode oscillator", Physics of Plasmas, Vol.8, No.8, 3781 (2001).
6. Larry Ludeking, David Smithe, Mike Bettenhausen and Scott Hayes. "MAGIC USER'S MANUAL" (1999).

Modeling and Characterization for Low Temperature Operation of Power MOSFET

Miho Io, Takashi Kikuchi*, Mitsuo Nakajima, Kazuhiko Horioka
(Department of Energy Sciences, Tokyo Institute of Technology)
(*Center for Nuclear Study, University of Tokyo)

Abstract
A two-dimensional modeling of the operating characteristic of a Si-MOSFET at low temperature is discussed. In addition, a detailed measurement of the operating characteristic of Si-MOSFET at low temperature is performed. The device temperature is controlled actively using a liquid nitrogen cooling system. Comparing the experimental result with the simulation result, various fitting parameters and low temperature characteristic of the FET device are examined. Both theoretical and experimental results reveal that the on-resistance decreases and mobility increases, with decreasing the operation temperature.

1. Introduction

Power devices that offer great potential for high power, high voltage, high frequency, low resistance applicants are required in many field. However there is a trade-off between the operating frequency and current capacity of power devices, so operating frequency becomes lower while current capacity becomes larger. Although both operating frequency and current capacity of silicon power devices have been improved, improvement of trade-off between high frequency and high voltage, low resistance is upcoming to limit because of the intrinsic performance limit of silicon devices. Devices that hoped exceed the silicon's performance limit are based on wide band-gap materials such as SiC and diamond.

SiC has been recognized as a potential semiconductor material for advanced power devices owing to its large band-gap, high electron mobility and saturation drift velocity, high thermal conductivity, high breakdown electric field strength [1]. However, properties of experimental SiC devices have not achieved expected values because of various undeveloped technologies of crystal-substrate growth and device process. Therefore it's necessary to find out detailed characteristic of SiC devices and investigate to solve these subjects in order that SiC devices may reach to a level of practical applications.

Because SiC MOSFETs are made to replace Si by SiC, there is no intrinsic difference between a basic structure of SiC MOSFETs and that of Si MOSFETs, and they make it possible to apply a model of Si MOSFETs operating characteristic for a modeling of SiC MOSFETs. Among the characteristics of Si MOSFETs, the performance at low temperature as high frequency and low resistance switching devices is superior to that at room or high temperature. Especially the SiC performance at low temperature is expected to be useful for applications where high frequency and low

resistance are required. However behaviors of the SiC device at low temperature are expected to be significantly different from Si-based device because of interface trapped density [1]. So it's necessary to establish a Si MOSFETs characteristic model at low temperature first for SiC characteristic modeling.

We aimed to establish the model for MOSFETs operating characteristic at low temperature by comparing the characteristics of Si MOSFETs and that with simulation. In this paper, we briefly show preliminary results for the numerical modeling and the experimental results of FETs at low temperature.

2. MOSFETs Experiment

For this work, we used an n-channel power Si MOSFET [NEC 2SK2488]. To measure I-V characteristics at some temperature measuring points, we cooled MOSFET with a system using liquid nitrogen.

The field effect mobility was derived from the experimental I_D-V_G (drain current-gate voltage) characteristic, using the following equation,

$$\mu = \frac{\partial I_D}{\partial V_G} \frac{L}{C_{OX} V_D W} \qquad (1)$$

where L and W are the channel length and width, respectively, and C_{OX} is the capacitance of oxide layer per unit area. Fig. 1 shows I_D-V_G characteristic of the MOSFET as a function of the gate voltage at V_D=10V at some temperature points.

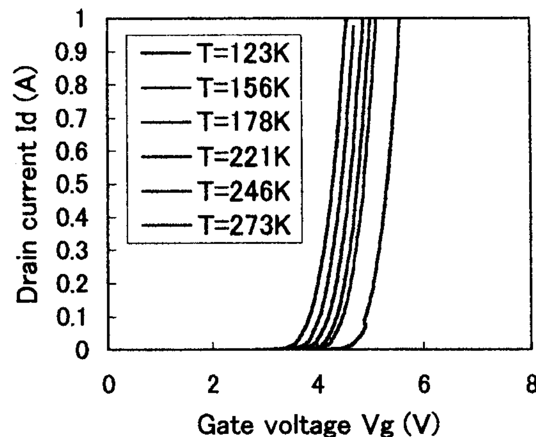

Fig. 1. Measured I_D-V_G characteristic at V_D=10V at some temperature points.

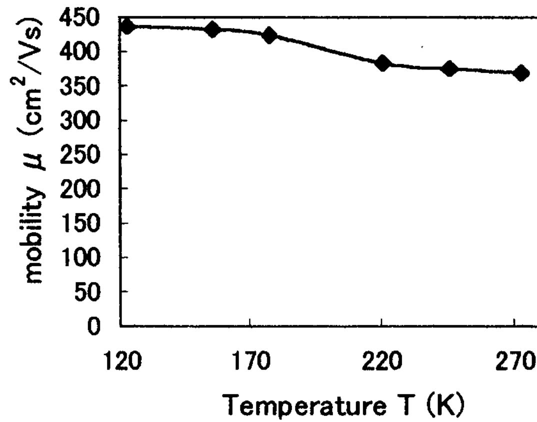

Fig.2. Extracted field effect mobility at some temperature points

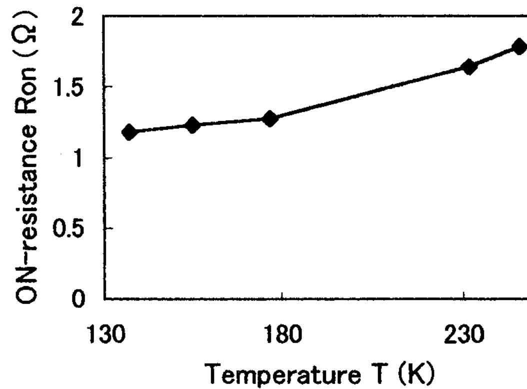

Fig.3. ON-resistance at some temperature points.

From the I_D-V_G characteristic we can derive the mobility. Fig. 2 shows the field effect mobility as a function of the temperature. Fig.3 shows ON-resistance as a function of temperature.

As shown in Fig.2 and 3, mobility increases and ON-resistance decreases with decreasing the operating temperature, and increase of mobility and decrease of ON-resistance are closing to saturation under around 180K. Although there are several scattering mechanisms to interrupt transfer of electrons, we use power MOSFET so we consider ionized impurity scattering as a cause of the saturation at lower temperature.

3. Numerical Simulation

3.1 Mobility model

Using the Mathiessen's rule [2], which implies that the local mobility is inversely proportional to the sum of individual scattering rates, we obtain the following general expression for the inverse of low-field mobility [3,4]:

$$\frac{1}{\mu_n} = \frac{1}{\mu_B} + \frac{1}{\mu_{sr}} + \frac{1}{\mu_{ac}} \quad (2)$$

where μ_B is the carrier mobility in bulk of the semiconductor, μ_{sr} is the carrier mobility limited by surface-roughness scattering, and μ_{ac} is the carrier mobility limited by lattice scattering (surface acoustic phonons).

Low-field bulk mobility depends largely on acoustic phonon and ionized impurity scattering. The bulk mobility μ_B is modeled using empirical model proposed by Caughey-Thomas for silicon[5,6], as follows.

$$\mu_B = \mu_{\min} + \frac{\mu_{\max}(T) + \mu_{\min}}{1 + \left(\frac{N_{total}}{N_{ref}}\right)^{\alpha}} \quad (3)$$

$$\mu_{\max} = \mu_{300} \times \left(\frac{T}{300}\right)^{-\gamma}$$

where N_{total} is the total doping concentration, and $\mu_{\max}$、$\mu_{\min}$、N_{ref}、α are fitting parameters. From the data in [3], we obtain $\mu_{300} = 1417$, $\mu_{\min} = 52.2 cm^2/Vs$, $N_{ref} = 9.68 \times 10^{16} cm^{-3}$, $\alpha = 0.68$, $\gamma = 2.5$ as initial parameters.

The surface roughness scattering mobility term is frequently expressed in the following equation [2,3,4]:

$$\mu_{sr} = \frac{D}{E_{\perp}^2} \quad (4)$$

where D is the fitting parameter. From the data in [3], we obtain $D = 5.82 \times 10^{14}$ as a possible value of initial estimate for D.

The acoustic phonon term has the following form [2,3]:

$$\mu_{ac} = \frac{B}{E_{\perp}} + \frac{C}{T\sqrt[3]{E_{\perp}}} \quad (5)$$

where B and C are fitting parameters. With the values given in [3], we obtain $B = 4.75 \times 10^7 cm/s$、$C = 1.74 \times 10^5 \times N_A^{0.125} K \cdot cm/s \cdot (V/cm)^{-2/3}$ as an initial estimate for the parameters B and C.

3.2 2-D simulation result

Having incorporated the mobility model into 2-D Poisson equation and drift-diffusion equation, we obtain 2-D field effect mobility. For convergence, numerical analysis is

performed with small doping density and gate voltage. Fig.4 shows a results of numerically obtained 2-D mobility as a function of temperature at V_G=0.8V. Fig.5 shows resistance as a function of temperature at V_G=0.8V.

From figures 4 and 5, we can see that the temperature dependency of the mobility and the resistance is corresponding to the experimental one, in terms of mobility increasing and resistance decreasing with decrease of temperature.

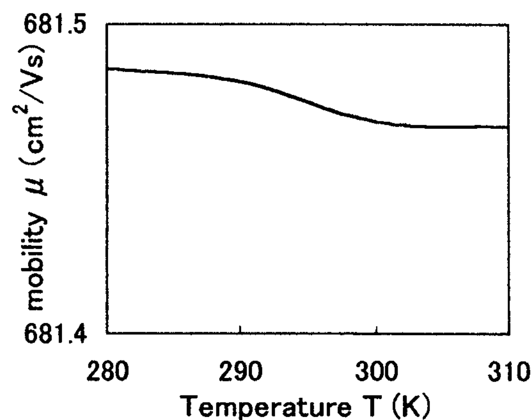

Fig. 4. 2-D mobility at V_G=0.8V.

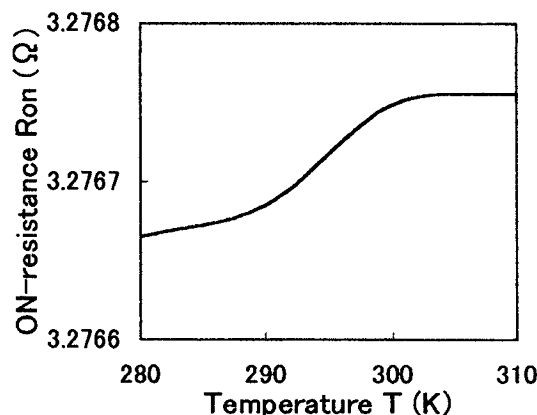

Fig. 5. Numerically estimated ON-resistance at V_G=0.8V.

4. Conclusion

From the experimental results, it was shown that mobility increases and ON-resistance decreases with decreasing the operating temperature. It means that switching frequency will be higher and power loss will be smaller with decreasing the operating temperature.

Experimental results also showed that increase of the mobility is closing to saturation under about 180K, therefore each temperature region that each scattering is dominant at, is different. Parameters of each mobility term can be obtained by measuring field effect mobility and by fitting them with simulation result at some temperatures.

The simulation results can predict the temperature dependence on mobility and ON-resistance corresponds to experimental results, so mobility model used in this work is available at low temperature.

2-D MOSFET simulation at same voltage and doping concentration and fitting with experimental results are required to establish mobility model at low temperature, and after that 2-D transit state analysis is necessary. In addition, we need to consider interface trapped density, which is especially important factor in modeling of SiC MOSFET, and incorporate it into Si model. We are going to apply the model established for Si-FET to SiC operation, and the final goal of us is to evaluate the potentiality of SiC MOSFET as a switching device for special application [7], where controllable power devices with high frequency, high voltage and low-loss are strongly desired.

Acknowledgment
A part of this work was supported by Grant-in-aid of the Ministry of Education. The authors thank Prof.K.Takayama of the High Energy Accelerator Research Organization (KEK) for valuable discussion and encouragement.

Reference

[1] Fundamentals and Application of SiC Devices,
Edited by Kazuo Arai, and Sadafumi Yoshida : *Ohmsha*, (2003) (in Japanese)

[2] Stephen K.powell, Neil Goldman, James M.Mcgarrity, Joseph Bernstein. :
Physics-based numerical modeling and characterization of 6H-sillicon-carbide metal-oxide-semiconductor field-effect transistors. J.Appl.Phys. **Vol.92**, No.7, p4053-4061, (2002)

[3] Claudio Lombardi, Stefano Manzini, Antonio Saporito, Massimo Vanzi. :
A Physically based Mobility Model for Numerical Simulation of Nonplanar Devices, IEEE Trans. Computer-Aided Design, **Vol.7**, No.11, p1164-1171, (1988)

[4] Handoko Linewih, Sima Dimitrijev, Kuan Yew Cheong. : Channel-carrier mobility parameters for 4H SiC MOSFETs. Microelectronics Reliability, **Vol.43**, p405-411, (2003)

[5] D.M.Caughey, R.E.Thomas. : Carrier Mobilities in Silicon Empirically Related to Doping and Field. Proc. IEEE, **Vol.55**, p2192-2193, (1967)

[6] Matthias Roschke, Frank Schwierz. : Electron Mobility Models for 4H, 6H, and 3C SiC. IEEE Trans Electron Dev, vol.48, p1442-1447, (2001)

[7] Y.Shimosaki, E.Nakamura, K.Takayama, K.Torikai, M.Watanabe, M.Nakajima, K.Horioka: Beam-dynamic effects od a droop in an induction accelerating voltage, Phys. Rev., Special Topics, **Vol.7**, 014201 (2004)

Breaking of Ice using Pulsed Power

Satoshi Ihara and Chobei Yamabe
Department of Electrical and Electronic Engineering,
Faculty of Science and Engineering, Saga University,
1 Honjo-machi Saga 840-8502, Japan

ABSTRACT

The breaking of ice using shock waves produced by a pulsed power generator is suggested as a new method for navigation of icebreakers in order to realize the safe and quick navigation in icebound sea. The shock wave can be produced by applying the voltage between the electrodes contacted to an ice sample. The ice breaking by the pulsed power was demonstrated in the tap water experimentally. During the experiments the ice sample was artificially made from pure water. In the salt water with salinity of 3.5 %, the ice sample was not broken according to the results obtained using the cylindrical electrode with flat tip. Using the conical electrode with the sharp-pointed tip, above ice sample was broken. The shockwave caused by the ionized region formed at the tip of conical electrode, and the localized intense stress at crack seem to be the important mechanisms of ice breaking in the salt water.

1. Introduction

Recently, the development of navigation system for icebreakers on icebound sea has been important for the advancement of the natural resources production. For example, in 1999 in the Northern Sakhalin in the Sea of Okhotsk, the commercial production of crude oil and gas started. At present, production during the winter season is not carried out. Year-round production, including the winter season, during which the Sea of Okhotsk is covered by the sea ice, is planned to start from 2004.[1-3]

To make possible the navigation in icebound sea, an icebreaker crushes the sea ice using the force generated by the ship's mass. As the ship advances into an unbroken ice field, crushing of ice begins to occur at the point of contact. A specially shaped hull made of high-strength material is required for the design of the icebreaker. Furthermore, in the regions, where the thick ice sheets exist, a navigation time is prolonged because continuous crushing is difficult or even impossible. If the worst comes to the worst, it is possible that the navigation is impossible. Realizing a new method of icebreaking to decrease the disadvantage points above is beneficial to the marine transport and shipbuilding.

In this research, the icebreaking using pulsed power is proposed as a new method for the operation of icebreakers in the icebound sea. [4] The ice is broken by shock wave produced by the pulsed power. The reasons for using pulsed power are as follows:

(1) The degree of damage to the hull can be significantly decreased.

(2) The continuous breaking can be realized because the pulsed power generator can be operated repetitively.

The overview of the icebreaking process using the pulsed power is shown in Fig. 1. The pulsed power generator is loaded on the ship, and the electrodes connected to the generator are guided to the ice surface from the bow using an insulated rod with several joints.

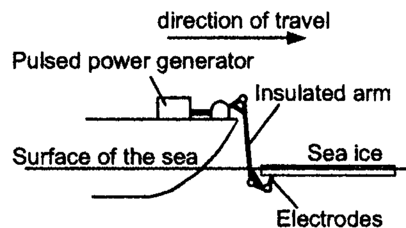

Fig. 1 Overview of the icebreaking process using pulsed power.

The fundamental researches on the destruction of solid materials using the pulsed power were carried out for the development of the new drilling and demolition technologies.[5, 6] On the works described in Ref. 6, the Marx generator was employed as an energy source, and granite was used as a sample of solid material. The rod electrodes were contacted to surface of sample, which was immersed in water. Although the destruction of solid materials such as rocks using the pulsed power was tested in detail until now, there was a lack of the experimental results for breaking of ice. Thus, the demonstration of the breaking of ice and the obtaining of the fundamental data were necessary.

The final purposes of this research are to evaluate the efficiency of ice breaking by pulsed power, and to discuss the usefulness of this method. In order to do that, the demonstration of ice breaking and the discussion of the breaking mechanisms are needed. In this research experiments on breaking of ice are carried out using the pulsed power generator and an ice sample. In these experiments ice samples were made from pure water, placed into a plastic vessel, which was filled with water or salt water. Also the shape of electrode was tested. In this paper, experimental results and mechanisms of breaking are described and discussed.

2. Experimental Apparatus and Method

Figure 2 shows a schematic diagram of the experimental apparatus.[4)] A Marx generator, with six capacitors with a capacitance of 0.2 μF, was used as a pulsed power generator. The capacitors of the generator were charged to a negative high voltage, and triggered by an external signal to a gap switch. The circuit parameters R_s, circuit inductance including L_s were estimated to be approximately 20 Ω and 1.5 μ F, respectively, assuming that C_s was 33 μ F. The ice sample was placed into a plastic vessel, which was filled with water. At first the tap water was used. On the next step salt water with salinity of 3.5% was used to simulate the actual condition. Ice samples were made from pure water. The electrodes were made of a dielectric material (Polyethylene) and metal (copper).

Figure 3 shows setup of the electrode system and the dimensions of the electrodes.[4)] The tips of electrodes contacted the surface of the ice sample. In this experiments, two kinds of shapes of electrodes, cylindrical and conical (shown in Fig. 4), were tested to investigate the electrode shape effects, especially in the case of using salt water.

In the experiments the voltage between the electrodes was measured using a high-voltage probe (EP-50K: Pulse Electric Engineering Co., Ltd.), and the current was measured using a current probe (Model 110A: Pearson Electronics, INC). The digital oscilloscope (DS4374: IWATSU) was used to observe the waveforms.

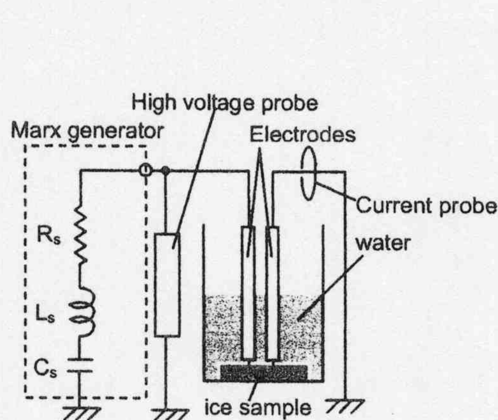

Fig. 2 Equivalent circuit and configuration of apparatus.

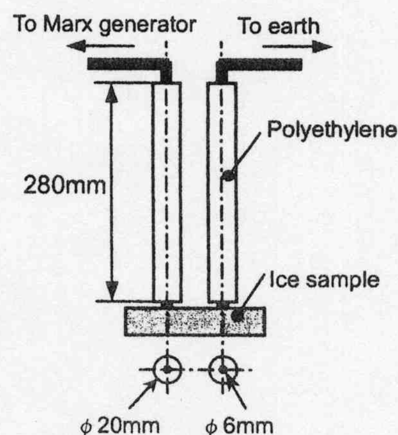

Fig.3 Configuration and dimensions of electrodes.

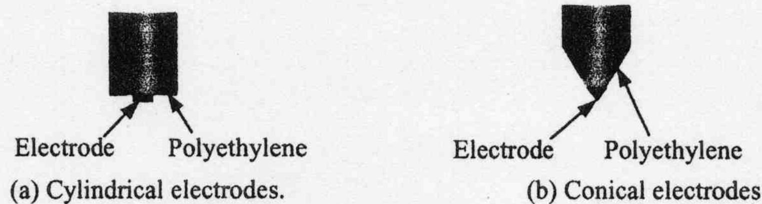

(a) Cylindrical electrodes. (b) Conical electrodes

Fig. 4 Cylindrical (a) and conical (b) electrodes.

3. Experimental Results and Discussions

3.1 Results in the case of using Tap Water[4)]

The experiments in the case of using the tap water were carried out. In this experiments, the cylindrical electrodes were used, and dimensions of ice sample were 95×82×28 mm (thickness of 28 mm). The experimental results were shown in Ref. 4. At t=0 a voltage of 50 kV was applied to the electrodes, and after 30 μs the discharge current started to rise. The photograph of discharge between the electrodes was taken. It was confirmed from this photograph that the discharge occurred on the surface between the electrodes. The photographs of the ice sample after applying the voltage, which were presented in Ref. 4, clearly showed that the ice sheet was broken by the discharge.

The power was calculated from the current and voltage waveforms, and the energy was calculated from the integral of the power. The inductance of the discharge region was neglected. It can be seen that the values of the maximum power and energy were 40 MW and 33 J, respectively. At that time the charging energy of the power supply, which was calculated from the measured voltage just before the discharge started, was 36 J. Therefore almost all charging energy was consumed by the discharge between the electrodes, the discharge led to the breaking of the ice.

The *V-I* characteristics obtained from voltage and current waveforms had two regions, which had negative and positive slopes (refer to Ref. 4). The negative slope denoted the formation of the arc discharge, and the positive slope denoted the decrease in the discharge current during a time constant for the parameters of the electric circuit including the discharge region. The resistance evaluated from positive slope in the *V-I* characteristic was approximately 9 Ω at a current less than 1 kA.

3.2 Results in the case of using Salt Water

In practice, the sea ice exists in a seawater or water with higher conductibility than the tap water. Thus, the experiments using the salt water with the salinity of 3.5 % were carried out in order to simulate the real conditions. The voltage and current waveforms in the case of the salt water are

shown in Fig. 5(a), where the cylindrical electrodes were used. In above case icebreaking was not confirmed. Also the discharge emission could be observed only at the tip of electrodes. The total charging energy of pulsed power generator was 60 J. On the other hand, using the conical electrodes the ice sample was successfully broken, with the same total charging energy. Fig. 5(b) shows the voltage and current waveforms in the case of conical electrodes. In this case also the discharge emission could be observed only at the tip of electrodes. Although the voltage waveforms were decreased in a certain time constant after the peak value in both cases, the clear difference was indicated in the current waveforms. The higher peak current was observed in the case of the conical electrodes than the cylindrical electrodes.

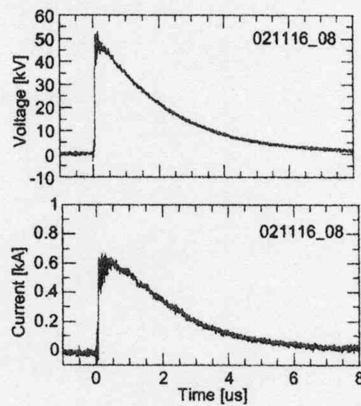

(a) Cylindrical electrodes

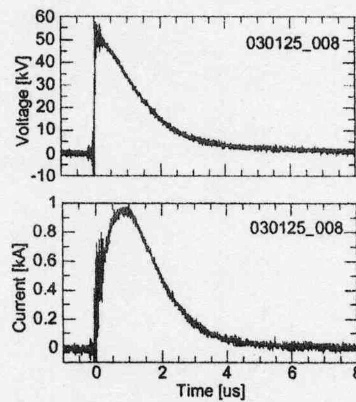

(b) Conical electrodes

Fig. 5 Voltage and current waveforms in cases of (a)cylindrical and (b)conical electrodes.

Fig. 6 shows the waveform of the discharge power calculated from the voltage and current waveforms presented in Fig. 5. The peak value of discharge power increased from 25 MW to 40 MW by changing the electrode shape from the cylindrical to the conical one. From the experimental results it was found that the conical electrode with sharp-pointed tip was effective for the breaking of ice.

Figure 7 shows the *V-I* characteristics obtained from Figs. 5(a) and (b). It can be seen from this figure that in the case of cylindrical electrode *V-I* characteristics had almost constant positive slope, what indicated that the current observed here was caused by the ions contained in the salt water. The resistance evaluated from this positive slope in Fig. 7 was approximately 63 Ω. In the other words, this current could be regarded as a leakage current because it did not contribute to the breaking of ice sample. Such a leakage current was consumed as a joule loss. In the case of the conical electrode the negative slope region was observed at voltage of 50 kV to 40 kV, and then the positive slope region appeared at less then 30 kV. The resistance evaluated from this positive slope was approximately 30 Ω.

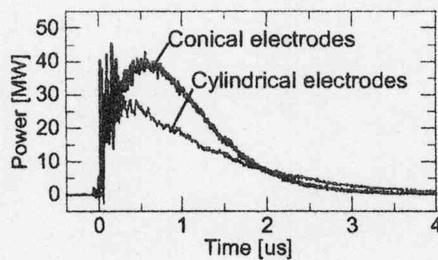

Fig. 6 Discharge power waveforms in cases of cylindrical and conical electrodes.

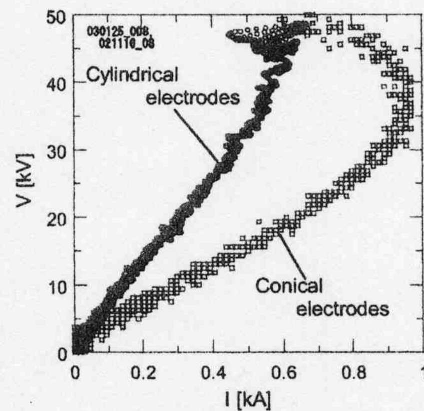

Fig. 7 *V-I* characteristics in cases of cylindrical and conical electrodes.

4. Discussions

In the tap water, formation of arc discharge between the electrodes was observed clearly, and the ice sample was broken, where the cylindrical electrodes were used. The negative slope region in *V-I* characteristic (shown in Fig. 7 of Ref. 4) indicates the formation of arc discharge. From these results, main phenomena for the discharge and icebreaking in the tap water was presumed as follows,

(1) By applying voltage across the electrodes the arc discharge starts to be formed at the surface of ice sample. This step corresponds to the negative slope region in *V-I* characteristics.

(2) Starting of arc discharge forms the shockwave.

(3) Local intense stress occurs in the cracks inside the ice during propagation of the shockwave, and then it is resulted in the break of the ice.

Using the conical electrodes the sharp-pointed tip of the electrode got into the ice sample, and the icebreaking was realized in the salt water, while in case of cylindrical it did not take place. The main effects of using the conical electrode were as follows:

(1) The energy loss by leakage current decreased because the tip of electrode got into the ice sample.

(2) The region with intense electric field was formed inside the ice.

Taking account of above effects, the following phenomena were supposed mechanisms for the icebreaking.

(1) Ionized regions are formed by the high electric field at the tip of the conical electrode. This step corresponds to the negative slope region in *V-I* characteristic shown in Fig. 7.

(2) The shockwave is induced by forming of ionized regions.

(3) Local intense stress occurs in the cracks inside the ice during propagation of shockwave, and then it is resulted in the break of the ice.

The difference of above phenomena between the cases of tap water and salt water is caused by resistivity of water. In the case of salt water no arc discharge path was observed between the electrodes because of leakage current caused by low resistivity of salt water. It suggests that the shockwave with enough pressure for icebreaking can be not generated in the case of salt water and cylindrical electrodes. Using the conical electrodes, the leakage current was decreased and ionized region was formed inside the ice sample. The formation of ionized region results in the formation of negative slope region in *V-I* characteristic. The peak value of discharge power increases rather then in the case of cylindrical electrodes. It seems that the ionized region promotes the formation of the shockwave with high pressure and realizes the icebreaking. In the medium with low resistivity, the following things are important for icebreaking.

(1) To decrease leakage current flow through the medium.

(2) To make a source of shockwave inside ice sample, for example using electrode with sharp-pointed tip.

Fulfilling above conditions causes that the peak value of the discharge power increases, and the formation of shockwave is promoted. In Fig. 6 the higher peak power, obtained in the case of conical electrode, is caused by the above conditions. In our results, threshold value of the discharge power for icebreaking was unknown. In order to evaluate the threshold value, the experiments in which the charging energy is changed, are necessary.

Figs. 8(a) and (b) shows the photographs before and after the discharge. Presented sample with the thickness of 40 mm was not broken during the first discharge. It could be seen from this photograph that the cracks were formed around the electrodes. This sample was broken after the third shot at the same charging energy of the capacitor. Fig. 9 shows the sample broken by the discharge. It was possible that the discharge power was slightly changed at every shot, while the charging energy of pulsed power generator was constant. In almost all cases the sample was broken along the line through the point of the electrodes contact, as shown in Fig. 9. It seemed from the observations shown in Figs. 8 and 9 that the cracks were formed by the discharge, and then these cracks induced the break of the ice sample. Also the observations confirmed the breaking mechanisms described above.

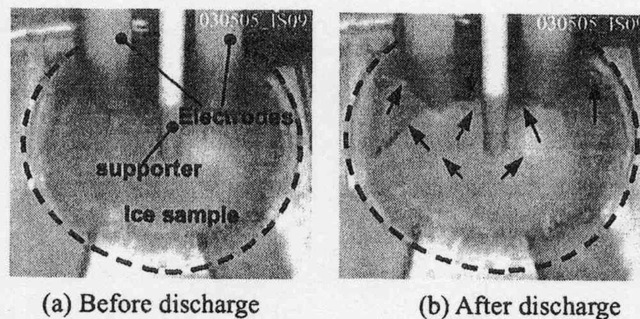

(a) Before discharge (b) After discharge

Fig. 8 Photographs before and after the discharge .

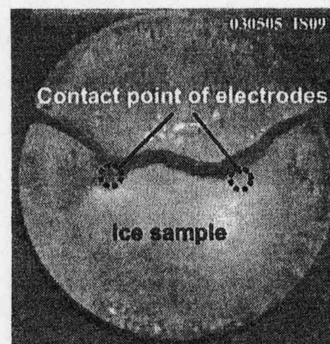

Fig. 9 Ice sample broken by discharge.

According to Ref. 6 it was found that on the destruction of granite with large number of voids, a partial discharge affected the energy efficiency of destruction. It is a localized discharge occurring at which the insulators with different dielectric constant are located. Generally, ice also has many small voids containing air. Therefore for the breaking of ice, although the partial discharge was not detected

directly, it was possible that the partial discharge inside the void was one of the important mechanisms of breaking of the ice sample

The sea ice contains brine, which is the seawater with high salinity. The brine is confined in the microscopic regions inside the sea ice. It is known that the brine strongly affects the mechanical strength of ice. Ref. 7 showed the empirical equation that indicated the relationship of mechanical strength and relative brine volume, as follows.

$$\frac{\sigma_f}{\sigma_0} = 1 - A\sqrt{V_b} \qquad (1)$$

where V_b is relative brine volume, A is constant number, σ_f and σ_0 are mechanical strength for sea ice with brine and pure ice without brine, respectively. According to above equation, increase of relative brine volume resulted in the decrease of strength in a function of $V_b^{1/2}$. Therefore it seemed that the energy for breaking of sea ice would decrease more than in the case of the experiment described here.

The relative brine volume depends on the ice salinity, ice temperature etc.[8] The crystal size and orientation also affect the mechanical strength. It is difficult to evaluate the mechanical strength of the ice quantitatively because of properties described above complexly change due to the way of freezing of the water, its quality, etc. In our experiment, all the ice samples were made in the same freezer and under the same conditions. Therefore each experimental data obtained here could be compared relatively. In the future works, the experiments taking account of the property of ice, and the experiments using the natural sea ice are planed.

5. Conclusions

In this research, the icebreaking using the pulsed power was proposed as a new method for operation of the icebreakers in icebound sea. In this research breaking of the ice sample artificially made from pure water by pulsed power was demonstrated in the tap water experimentally. In order to simulate actual condition, the ice sample in the salt water with salinity of 3.5 % was tested. From the results using the cylindrical electrode with flat tip, the ice sample was not broken. Using the conical electrode with sharp-pointed tip, the ice sample was successfully broken. It was found from the results that the conical shape is effective for icebreaking in medium with low resistivity. It seemed that the shockwave caused by ionized region at tip of conical electrode, and the localized intense stress at crack were important mechanisms of the ice breaking in the salt water.

The experiments taking account of the various properties of ice, and the experiments using the natural sea ice are necessary to be carried out as the next works in order to evaluate the efficiency of

breaking.

Acknowledgement

The authors would like to thank Dr. S. Uto from the National Maritime Research Institute and Dr. S. Ushio from the National Institute of Polar Research, for providing information for this research. This research was supported by the Fundamental Research Developing Association for Shipbuilding and Offshore (REDAS).

References

1) K. Izumiya, A. Konno and S. Sakai: Proc. 17th Int. Symp. Okhotsk Sea & Sea Ice, 2002 (Okhotsk sea & cold ocean research association, Mombetsu, Hokkaido, 2002) p. 267.

2) A. Konno and K. Izumiya: Proc. 17th Int. Symp. Okhotsk Sea & Sea Ice, 2002 (Okhotsk sea & cold ocean research association, Mombetsu, Hokkaido, 2002) p. 275.

3) K. Ogiwara, N. Otsuka, K. Kanaami, S. Takahashi, K. Maida and H. Saeki: Proc. 17th Int. Symp. Okhotsk Sea & Sea Ice, 2002 (Okhotsk sea & cold ocean research association, Mombetsu, Hokkaido, 2002) p. 290.

4) S. Ihara and C. Yamabe: Jpn. J. Appl. Phys. Vol. 42 (2003) pp. L 489-490

5) I. V. Lisitsyn, H. Inoue, I. Nishizawa, S. Katsuki and H. Akiyama: Journal of Applied Physics, Vol. 84, No. 11, pp.6262-6267, 1998.

6) I. V. Lisitsyn, H. Inoue, S. Katsuki and H. Akiyama: IEEE Trans. Dielectrics and Electrical Insulation, Vol. 6, No. 1, pp. 105-108, 1999.

7) Schwarz, J. and Week, W. F.: J. Glaciol., Vol. 19, pp. 499-530, 1977

8) Frankenstein, G. and Garner, R. : J. Glaciol., Vol. 6, pp. 943-944, 1967

RAIL GAP SWITCH USING POROUS METAL AS ELECTRODE

Seizo FURUYA, Hiroaki TANAKA, Saburo TAKANO and Juichi IRISAWA

Nagaoka University of Technology, Niigata 940-2188, JAPAN

ABSTRACT

As for a multichannnel gap switch, the shorter the formative and statistical time lags of each gap, the larger the number of arc channels. As we examined the breakdown characteristics of a sphere/plane gap using a mirror-finished brass plate and a porous metal as plane electrodes, we confirmed that the formative and statistical time lags decrease when porous metals are used as a discharge electrode, so we expect that the number of arc channels increases when porous metal is used as one of the electrodes of a rail gap. Therefore, we compared the experimental results to confirm it. As a result, in the case of the gap length of 1 mm, the number of arc channels increases when porous metal is used as an electrode.

1. Introduction

As for a multichannnel gap switch, the shorter the formative and statistical time lags of each gap, the larger the number of arc channels. As we examined the breakdown characteristics of a sphere/plane gap using a mirror-finished brass plate and a porous metal as plane electrodes, we confirmed that the formative and statistical time lags decrease when porous metals are used as a discharge electrode(1), so the number of arc channels of a rail gap with the porous metal is expected to increase. Therefore, we compared the results of the rail gap using a mirror-finished brass plate and a porous metal as one of the electrodes of the rail gap.

2. Experimental Setup

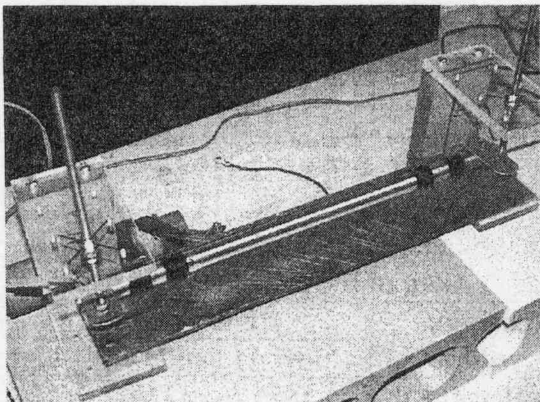

Fig. 1 Cylinder/mirror-finished plate

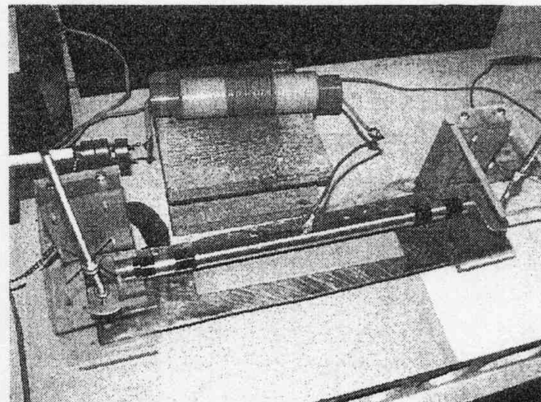

Fig. 2 Cylinder/porous metal

Figures 1 and 2 show cylinder/mirror-finished plate gap and cylinder/porous metal gap, respectively. The upper electrode is a brass cylinder of 18 mm in diameter and the lower electrode is a brass plate of 5 mm in thickness. When the lower electrode is a porous metal,

we put the porous metal on the brass plate shown in Fig. 2. The active length of the rail gap is 200 mm. The lower electrode was grounded and positive or negative voltage pulses were applied to the upper electrode. The experiments were carried out in air at 1 atm and UV irradiation was not carried out in our experiments. The porous metal we used is made of copper and its average pore diameter is 600 μm. Its size is 210×40 mm and thickness is 2 mm. It was manufactured by Mitsubishi Materials Corp.

The rectangular voltage pulses applied to the gap were generated by a 100-cm-long coaxial-type ferrite sharpener[(2)(3)]. Figure 3 shows the electrical circuit to generate the pulses. The input voltage pulse which has a slow rise time is steepened at the end of the sharpener due to its nonlinear effect. Figures 4(a)-(c) show the examples of voltage waveforms of open-ended ferrite sharpener applied to the rail gap. The charging voltage of the capacitor V_0 is +10 kV. The voltages become approximately twofold V_0. Figure 4(a) shows the waveform when dV/dt is high, using the circuit of Fig. 3. Figure 4(b) shows the waveform when dV/dt is middle, inserting ferrite beads between the sharpener and rail gap to decrease dV/dt of the pulses. Figure 4(c) shows the waveform when dV/dt is low, inserting 33-μH inductance between the sharpener and gap to decrease dV/dt more. dV/dt of the pulses are summarized in Tab. 1. Voltages were measured using a Tektronix high-voltage probe (P6015A) and a Hewlett-Packard digital oscilloscope (HP54542A).

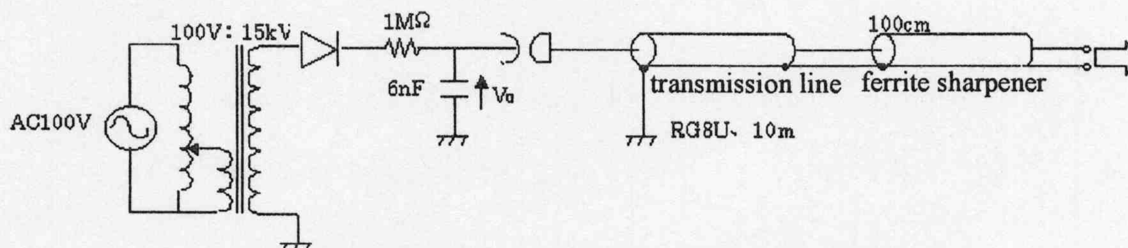

Fig. 3 Electrical circuit to generate the pulses applied to the gap

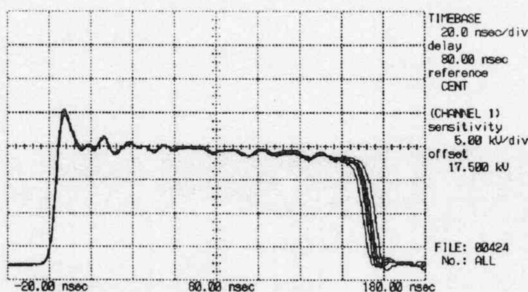

Fig. 4(a) dV/dt is high

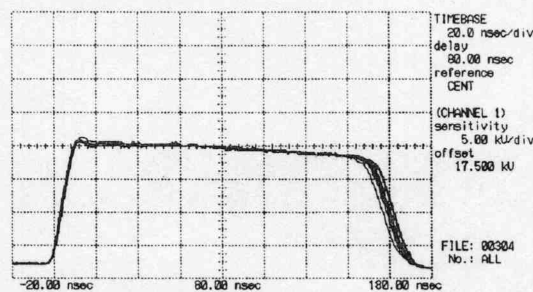

Fig. 4(b) dV/dt is middle

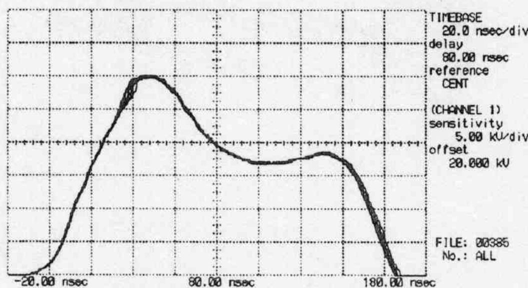

Fig. 4(c) dV/dt is low

Fig. 4 Examples of voltage waveforms of open-ended ferrite sharpener

Tab. 1 dV/dt of the pulses applied to the gap

charging voltage	dV/dt (kV/ns)		
	low	middle	high
positive10kV	0.75	1.70	2.50
positive15kV	1.43	2.50	5.09
positive20kV	1.90	4.19	6.88
negative10kV	-0.77	-1.69	-3.80
negative15kV	-1.60	-3.33	-6.50
negative20kV	-2.22	-4.29	-8.69

3. Experimental Results and Discussion

First, we examined the relation between the position where the voltage pulse is applied and the position where the arc channels are generated. Second, the number of arc channels is investigated when the polarity, rise time and amplitude of the applied voltage, and the gap length of the rail gap are changed. The number of arc channels was evaluated by open-shutter photographs of a digital camera. Under each condition 10 shots were performed.

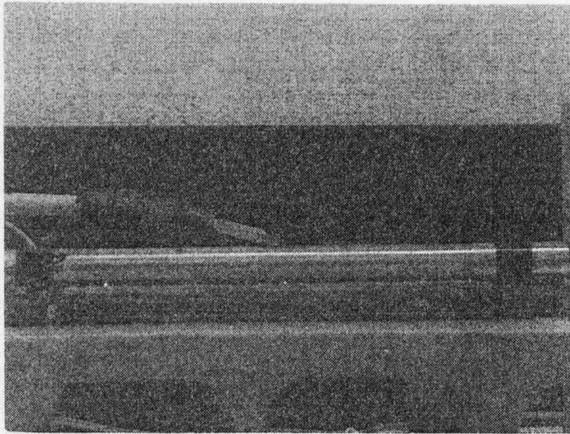

Fig. 5 First example of discharge photo

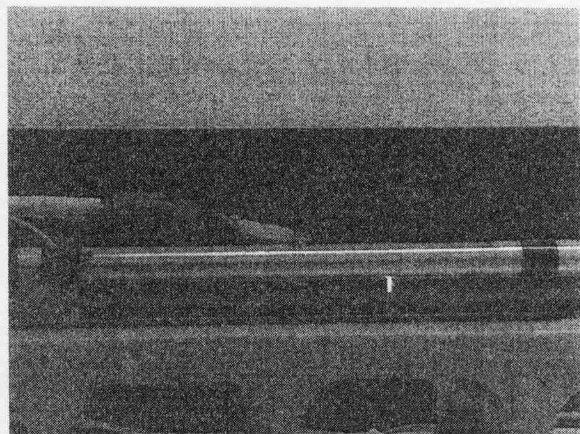

Fig. 6 Second example of discharge photo

Figure 5 shows the first example of discharge photograph. The lower electrode is porous metal and the charging voltage of the capacitor V_0 is +20 kV. dV/dt is low and the gap length of the rail gap is 1 mm. As shown in the figure, 3 arc channels were generated. Figure 6 shows the second example of discharge photograph. The lower electrode is mirror-finished plate and V_0 is +20 kV. dV/dt is low and the gap length of the rail gap is 5 mm. In this case, 1 arc channel was generated.

Figures 7(a)-(d) show the examples of voltage waveforms with breakdown. dV/dt is middle and 10 shots are superimposed in each figure as 10 shots were performed under each experimental condition.

3.1 Position where the voltage pulse is applied

First, we examined the relation between the position where the voltage pulse is applied and the position where the arc channels are generated. We investigated it under several conditions. Figures 8(a)-(c) show the example of results for (a) the position is left, (b) center and (c) right. The lower electrode is porous metal and the charging voltage of the capacitor V_0 is −20 kV. dV/dt is middle and the gap length of the rail gap is 3 mm. A number in the figures is a shot number and shows the position where the arc channels are generated. For example, in the second shot of Fig. 8(c), 3 arc channels were generated where '2' are written. From these experiments, arc channels did not concentrate at the position where the voltage

pulse is applied, so we concluded that there is no relation between the position where the voltage pulse is applied and the position where the arc channels are generated.

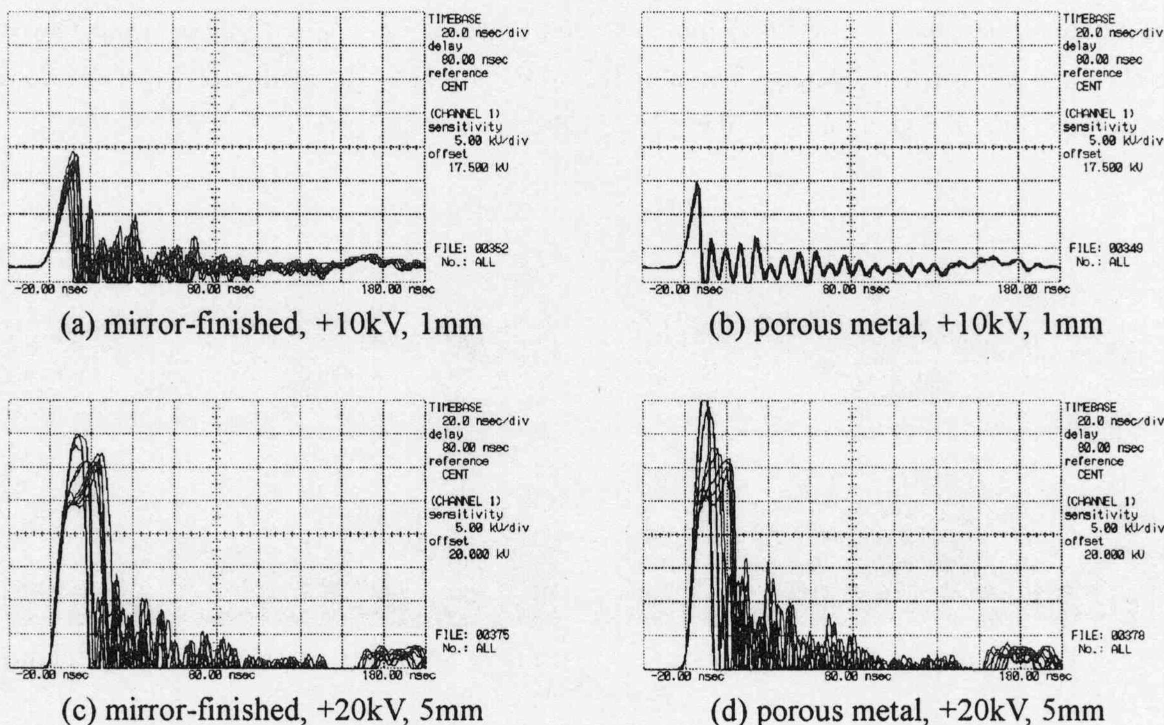

(a) mirror-finished, +10kV, 1mm (b) porous metal, +10kV, 1mm

(c) mirror-finished, +20kV, 5mm (d) porous metal, +20kV, 5mm

Fig. 7 Examples of voltage waveforms with breakdown

3.2 The number of arc channels when the parameters are changed

Second, the number of arc channels is investigated when the polarity, rise time and amplitude of the applied voltage, and the gap length of the rail gap are changed. We summarized the results in Tab. 2. The number of arc channels in the table is the average of 10 shots. H in the table means that dV/dt of the applied voltage pulse is high, M middle and L low. In the case of the gap length of 3 mm and 5 mm, a significant difference between the results of the mirror-finished plate and those of the porous metal was not observed. In the case of the gap length of 1 mm, the number of arc channels increases when porous metal is used as a lower electrode instead of the mirror-finished plate. The effect of dV/dt and polarity of the applied voltage pulse was not almost observed.

4. Conclusion

We expect that the number of arc channels increases when porous metal is used as one of the electrodes of a rail gap, so we compared the experimental results to confirm it. As a result, we obtained the following results:

(1) There is no relation between the position where the voltage pulse is applied and the position where the arc channels are generated.

(2) In the case of the gap length of 1 mm, the number of arc channels increases when porous metal is used as a lower electrode instead of the mirror-finished plate.

References

(1) S. Furuya, S. Takano and J. Irisawa: Jpn. J. Appl. Phys. **43** (2004) *to be published.*

(2) S. Furuya, H. Matsumoto, H. Fukuda, T. Ohboshi, S. Takano and J. Irisawa: Jpn. J. Appl. Phys. **41** (2002) 6536.

(3) S. Furuya, K. Tachi, S. Takano and J. Irisawa: Jpn. J. Appl. Phys. **43** (2004) 1131.

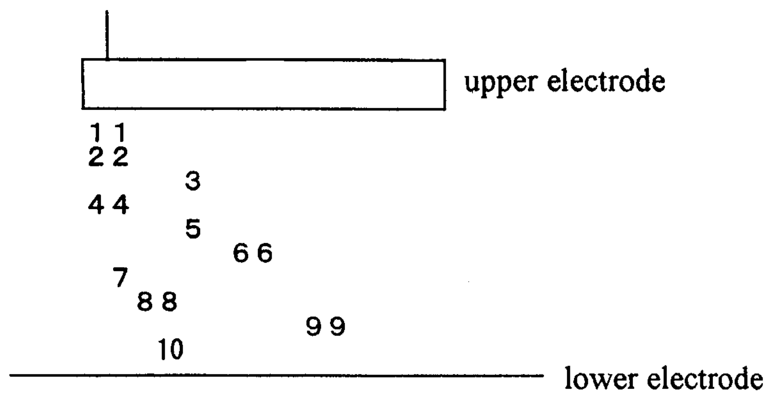

(a) left

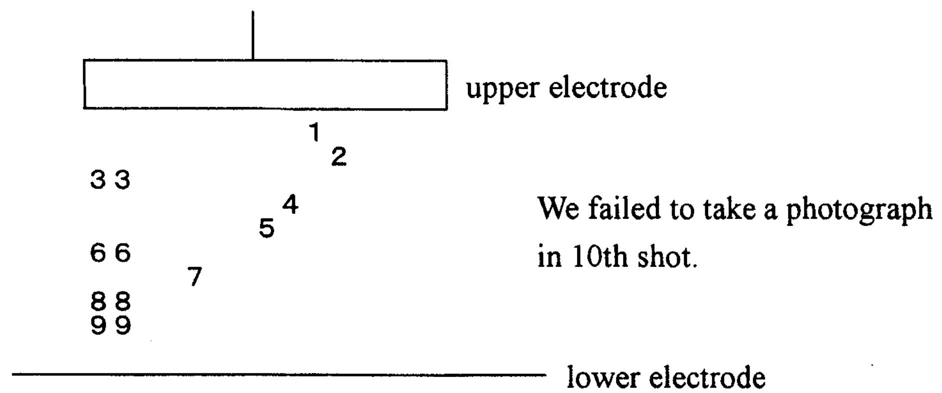

(b) center

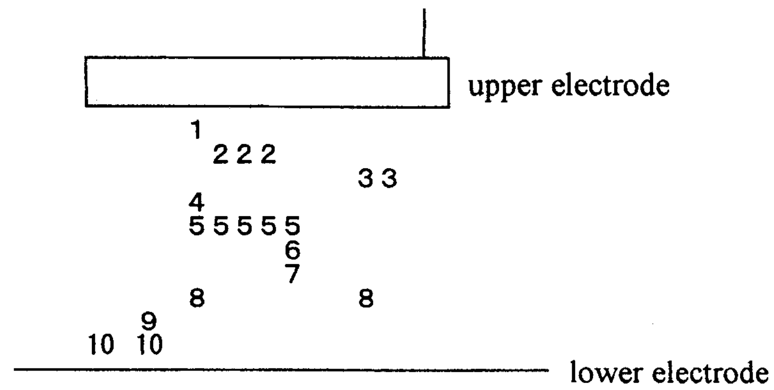

(c) right

Fig. 8 Relation between the position where the voltage pulse is applied and the position where the arc channels are generated

Tab. 2 Ten-shot average of the number of arc channels when the parameters are changed
H in the table means that dV/dt of the applied voltage pulse is high, M middle and L low

			1mm		3mm		5mm	
charging voltage			mirror-finished	porous metal	mirror-finished	porous metal	mirror-finished	porous metal
positive	10kV	**H**	1.1	1.5	1.1	1.0	0.0	0.0
		M	1.7	1.7	1.0	1.2	0.1	0.0
		L	1.0	1.0	1.0	1.0	0.8	1.0
	15kV		1.6	2.2	1.2	1.3	1.0	1.1
			1.0	2.7	1.1	1.4	1.3	1.0
			1.0	1.4	1.2	1.0	1.0	1.1
	20kV		1.3	2.3	1.6	1.7	1.3	1.5
			1.5	2.4	1.6	1.9	1.0	1.2
			1.3	1.5	1.1	1.1	1.1	1.2
negative	10kV		1.0	1.1	1.2	0.9	0.2	0.0
			1.0	1.3	1.0	0.9	0.1	0.0
			1.0	1.0	1.0	1.0	1.0	1.0
	15kV		1.0	2.2	1.0	1.1	1.1	1.0
			1.3	2.0	1.2	1.6	1.3	1.1
			1.0	1.1	1.0	1.0	1.1	1.0
	20kV		1.4	1.8	1.0	1.2	1.1	1.0
			1.8	2.1	1.2	2.1	1.0	1.3
			1.0	1.0	1.0	1.0	1.0	1.0

Pressure Measurement of the Shock Waves due to Pulsed Streamer Discharges in Water

Keiichi Tanaka, Manabu Jikuya, Taisuke Fudamoto, Sunao Katsuki and Hidenori Akiyama
Dept. Electrical and Computer Engineering, Kumamoto University,
39-1, Kurokami 2-chome, Kumamoto 860-8555, Japan

Hansjoachim Bluhm
Forschungszentrum Karlsruhe GmbH,
Hermann-von-Helmholtz-Platz 1, 76344 Eggenstein-Leopoldshafen, Germany

Abstract

Temporal development of shock waves generated from streamers discharges in water was observed by means of time resolved imaging based on laser Schlieren method. Pressure of shock wave was calculated by Hugoniot's equation, which utilizes the relation between the shock pressure and its propagation velocity. The streamer discharges were generated by pulsed positive voltages applied to a needle electrode. The measurements indicate that the pressure exceeding 1 GPa takes place only near the streamer discharges. Stronger shockwave was generated in more conductive water.

I. INTRODUCTION

A large volume plasma, which consists of a bunch of thin discharges like strings, is generated around an electrode with a sharp edge when a pulsed high voltage is applied to the electrode in water. (Fig. 1) The thin discharges are so called pulsed corona or streamer in some articles [1,2] because they resemble to streamers in gas discharges. The streamer discharges are coming to be used for chemical and biological decontamination in water environment [1,3,4].

However, their character seems different from the gas discharges with respect to the propagation mechanism, which is not still clear [2,3,5]. The streamers are accompanied by several physical events, such as extremely intense electric fields exceeding 1 MV/cm, ultra violet rays, free radical species, and shockwaves. Individual investigations of these events are attractive. Only a few papers reported the radiation of ultraviolet rays and the generation of free radical species [6,7]. However, there is no quantitative study on the electric field and the shockwave due to the streamers.

This paper tries to characterize the shockwaves caused by the streamers in water by means of framing and streaking photography based on the Schlieren method. The pressure of shock wave is calculated by Hugoniot's equation using the propagation velocity derived from the streaking photography. Streamers were produced by way of a pulsed voltage applied to a needle electrode which was placed in water. The pulse duration and the amplitude of the applied voltage were adjusted in order to make the discharges small enough to produce a single circular shockwave. The shockwave pressure and its propagation property in different conductive water are discussed.

II. EXPERIMENTAL SETUP AND PROCEDURE

Figure 2 shows the experimental setup including a pulsed high voltage generator, a glass made water container, the Schlieren imaging system and its timing control system. A needle to wire electrode set with a space of 14 mm is fixed in the middle of the thin water container, of which the dimension is 90 mm × 90 mm × 5 mm. The curvature of the needle tip is 5 μm and the diameter of

the wire electrode is 1 mm which is large enough for the discharge not to be produced on the surface. Positive pulsed voltages of 40 kV are given to the needle against the wire electrode. A relatively low voltage up to 20 kV is generated by a Blumlein type pulse forming network (PFN) and is stepped up to 60 kV by a transformer with ferromagnetic core. The pulse duration is adjusted by changing the number of stages in the PFN. Output impedance of the PFN is approximately 200 Ω. The water conductivity was set to 0.1 and 20 mS/m, which lead the gap resistance of approximately 40 kΩ and 200 Ω, respectively. A 200 Ω resistor was placed in parallel to the electrodes in the case of 0.1 mS/m water for the sake of impedance matching. The PFN starts operating with triggering a spark gap switch. The voltage across and the current flowing through the electrodes were monitored using a voltage divider (Pulse Electronics Co. Ltd, EP100K) and a current transformer (Peason 110). Figure 3 shows the voltage waveforms for different number of stages in the PFN. 2 and 5 staged PFNs generate a pulse duration of 120 and 250 ns, respectively.

The imaging system consists of a CW Ar ion laser (488 nm, 150 mW), an acoustic optical shutter (ISOMET, AOM1205C), a beam expander, lenses, a knife edge and imaging devices. A gated high speed digital camera (Stanford Computer Optics, 4 Quick) or a streak camera (Hadland Photonics, IMACON 790) were used as the imaging device. The laser beam with a diameter of 30 mmφ passes through the water container so as to include the needle tip in the view. A couple of μs

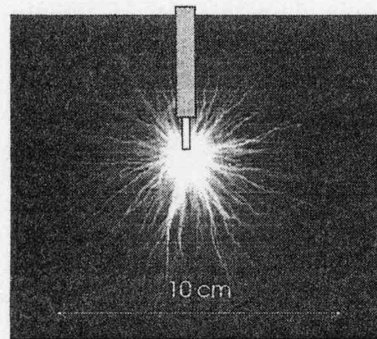

Figure 1. Typical appearance of streamer-like discharge in water with the conductivity of 20 mS/m. Positive pulsed voltage of 120 kV, 1.2 μs was applied to a rod electrode.

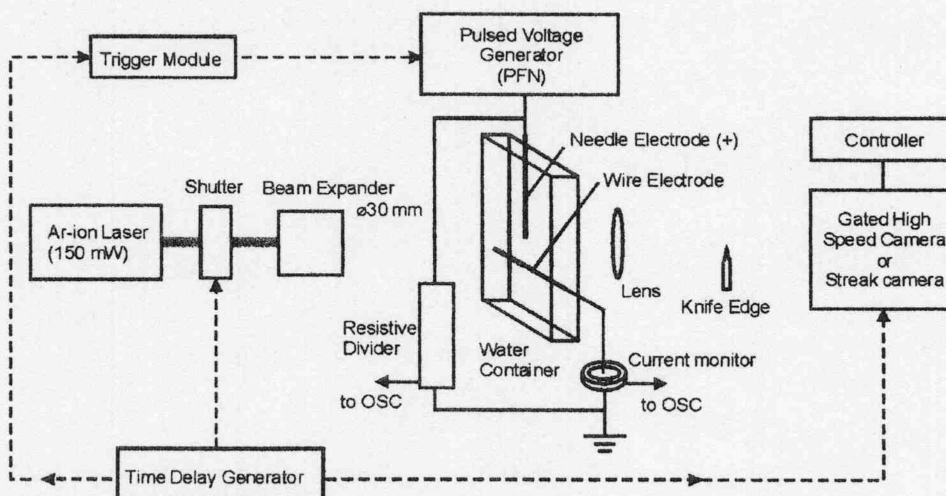

Figure 2. Schematic diagram of the experimental setup. Solid and dashed lines indicate the main discharge circuit and the timing signals.

after the optical shutter is open, the PFN is fired. And then a sparking noise of the gap switch was used for triggering the imaging system. The timing of the imaging system was precisely controlled by a delay generator (Stanford Research, DG535).

III. EXPERIMENTAL RESULTS AND DISCUSSION

A. Appearance of shock waves from streamers

Figure 4 shows the time-resolved images of light emission of the streamer discharge (left) and Schlieren images (right) at different *t*, which is the time from when the voltage starts. Although micro structure of the streamer discharges is different from shot to shot, the emission intensity and the spatial expanse of the discharge are similar. Therefore, the observation is appropriate to grasp a summary of discharge development. Amplitude of the pulsed voltage applied between electrodes is 40 kV. The exposure time of each frame is 5 ns which is small enough to observe the streamer behaviors since the streamer propagation velocity in water is approximately 30 km/s. For the light emission at t = 350 ns (a), several thin streamers emerging from the needle tip form a shape like a root of trees. Some of the streamers split into a couple of streamers. The diameter of the streamer tip is less than 100 μm, which is the spatial resolution of the imaging system. The lengths of all discharges are almost the same, which indicates the propagation velocity of each channel is the same. In Schlieren images at the same time, several bubble-like shades emerge from the electrode tip. Although the spatial expanse of the shade is similar to the light emission area, its structure does not appear to be like that of the emission. The light emission is no longer observed at t = 750 ns or later since no voltage remains after t = 500 ns. On the other hand, the thick shades in the Schlieren image are kept expanding since the beginning of the discharge. This is the evidence that the shock wave occurs by the "quiet" streamer discharges in water.

Let us look into the detailed structure of the streamer discharges. Figure 5 show the time-resolved Shadow image of the discharge at t = 1000 ns. Pulse duration of the applied voltage was 250 ns for this shot. Even 700 ns after the voltage ends, several streamer shadows remain where the streamers had existed. These streamer shadows stay for approximately 100 μs after the discharge. The streamer is thick near the needle electrode and is thin at the tip. The characteristics of the streamer propagation in water are described in [2]. Tens of shock waves are observed along each streamer path. These phenomena suggest that the streamer propagates with small steps and each step generates the shock wave independently. The step length, which is estimated by the gap between

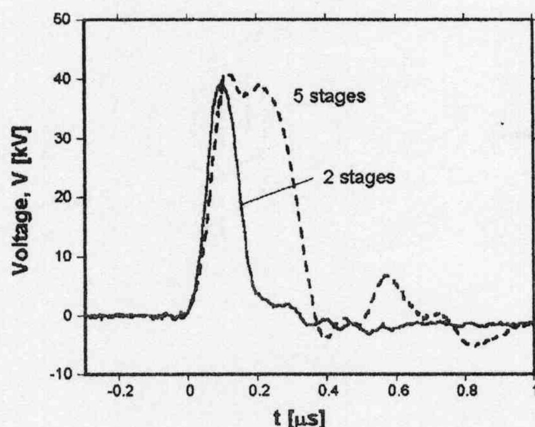

Figure 3. Voltage waveforms applied to the needle against the wire electrode. The numbers in the figure show the number of stages in the pulse forming network.

neighboring shock waves, is roughly 200 μm.

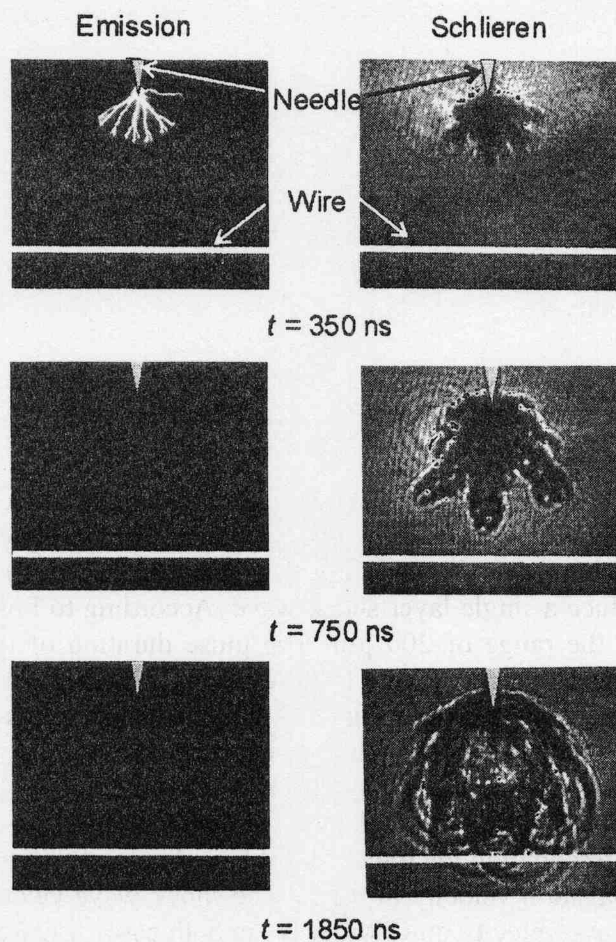

Figure 4. Emission photography and Schlieren image for different t, which are taken by a gated ICCD camera. Exposure time is 5 ns. Amplitude and duration of the voltage pulse are 40 kV and 500 ns, respectively.

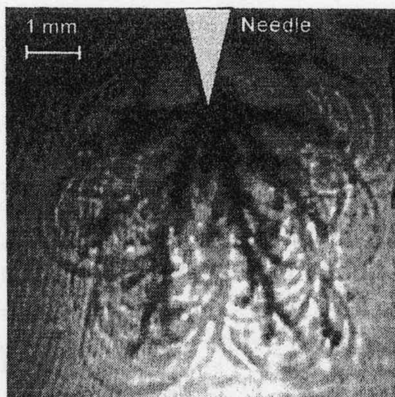

Figure 5. Time-resolved shadow photograph of the tree-like streamer discharge emerging from the positive needle electrode at t = 1000 ns. Exposure time is 5 ns.

B. Measurement of shock wave pressure

There are a number of studies on shock wave propagation in fluids, and its properties are well investigated. The shock pressure can be calculated from the Hugoniot equations, which are given by

$$P = \rho_0 u_s u_p \qquad (1)$$

$$u_s = A + B u_p \qquad (2)$$

where P is pressure of a shock wave, ρ_0 is density of water (1 g/cm^3), u_S is the shock wave speed, u_p is the particle velocity, A is 1.45 km/s (acoustic sound velocity in water). B is 1.99, which is experimentally provided by [8]. Therefore, the shock pressure P can be expressed as a function of the measurable shock velocity u_S

$$P = \rho_0 u_s \frac{u_s - A}{B} \qquad (3)$$

The shock front is precisely marked by the Schlieren method and its movement is traced by using a streak camera (Hadland Photonics, IMACON790). However, the multiple shock waves, which are generated by the usual discharges as shown in Fig. 5, can not be traced. Only the chance to trace the one shock wave is to produce a single layer shock wave. According to Fig. 5, the step length of the discharge seems to be in the range of 200 µm. The pulse duration of the voltage must be short enough to obtain such a tiny discharge. Figure 6 shows a single layer shock wave produced by using the 120 ns duration voltage pulse shown in Fig. 2. A slit of 100 µm is placed at the entrance of the camera. The streak speed is 80 ns/mm, which is calibrated. The voltage applied to the electrodes was 40 kV. The shock velocity was obtained by differentiating the trace.

Figure 7 shows the shock propagation velocities in water of different conductivity (ρ = 0.1 and 20 mS/m), obtained by differentiating the trace. The obtained velocity is at most 6 km/s that is much slower than streamer propagation velocity in water. The shock wave velocity depends on the water conductivity. The shock wave velocity quickly decays in both cases. Figure 8 shows the shock wave pressure as a function of distance from the needle tip, which are derived from Fig. 7. Shock wave velocity in 0.1 mS/m water exceeds 2 km/s, that leads the pressure exceeding 1 GPa. The pressure decays quickly and settles down to the acoustic velocity in water. In the case of 20 mS/m water, the velocity reaches 4.5 km/s, which leads the pressure of 6 GPa. The range where the pressure exceeds 1 GPa is more extensive than that in 0.1 mS/m water.

IV. CONCLUSION

Behavior of shock waves due to streamer discharges in water was investigated with the framing and streak cameras combined with Schlieren method. The measured pressure exceeds 1 GPa in the case of high resistive water, and quickly decays during its propagation. The pressure depends on the water conductivity, which can be explained by the energy deposition into the discharges.

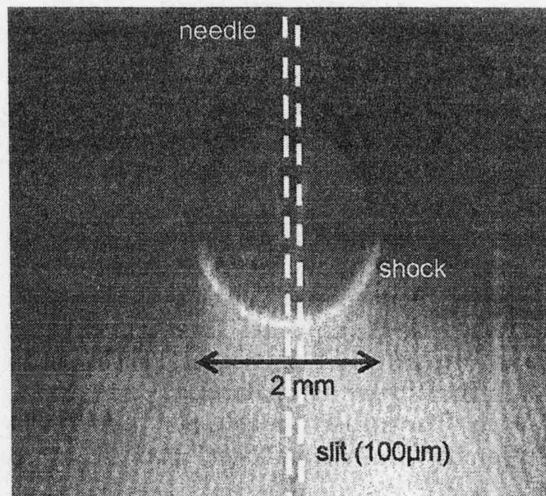

Figure 6. Single circular shockwave generated by a tiny discharge at the needle tip, where the 120 ns duration voltage pulse was applied. White dotted lines indicates the 100 μm slit, which determines the visible range in the streak photography.

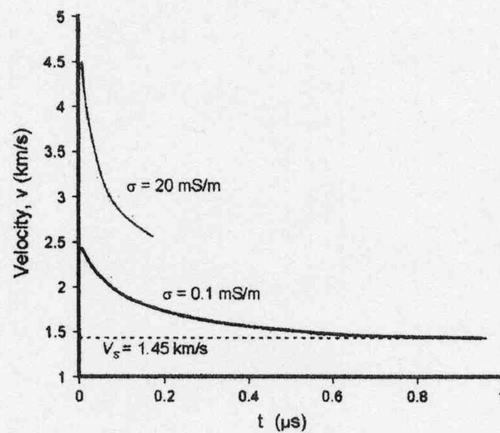

Figure 7. Propagation velocity of the shock front due to the discharge as a function of time.

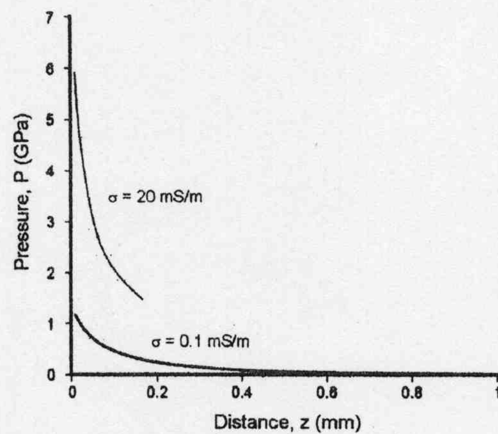

Figure 8. Calculated pressure of the shock wave as a function of the distance from the needle tip.

V. REFERENCES

[1] M. Sato, B. Sun, T. Ohshima and Y. Sagi, "Characteristics of active species and removal of organic compound by a pulsed corona discharge in water," J. Adv. Oxid, Technol., vol. 4, no. 3, pp.339-342, 1999.

[2] A. Beroual, M. Zahn, A. Badent, K. Kist, A.J. Schwabe, H. Yamashita, K. Yamazawa, M. Danikas, W.G. Chadband and Y. Torshin, "Propagation and structure of streamers in liquid dielectrics," IEEE Electr. Insulat. Magazine, Vol. 14, No. 2, pp.6-17, 1998.

[3] H. Akiyama, "Streamer discharges in liquids and their applications", IEEE Trans. Dielectr. Electr. Insulat., Vol. 7, No. 5, pp. 646-653, 2000.

[4] M. Sato, T. Ohgiyama, J.S. Clements, "Formation of Chemical Species and Their effects on Microorganisms Using a Pulsed High –Voltage Discharge in Water," IEEE Trans. Ind. Appl., vol. 32, no. 1, pp.106-112, 1996.

[5] S. Katsuki, H. Akiyama, A. Abou-Ghazala, K.H. Schoenbach, "Parallel streamer discharges between wire and plane electrodes in water", IEEE Trans. Dielectr. Electr. Insulat., Vol. 9, No. 4, pp. 498-506, 2002.

[6] J.S. Clements, M. Sato, R.H. Davis, "Preliminary Investigation of Prebreakdown Phenomena and Chemical Reactions Using a Pulsed High-Voltage Discharge in Water," IEEE Trans. Ind. Appl., vol. IA23, pp.224-235, 1987.

[7] P. Sunka, V. Babicky, M. Clupek, P. Lukes, M. Simek, J. Schmidt, M. Cernak, "Generation of chemically active species by electrical discharges in water," Plasma Sources Sci. Technol., Vol. 8, No. 2, pp.258-65, 1999.

[8] K. Nagayama, Y. Mori, K. Shimada, M. Nakahara, "Shock Hugoiot compression curve for water up to 1 GPa by using a compressed gas gun," J. Appl. Phys., Vol. 91, pp.476-482, 2002.